Design of Single-Shot Longitudinal Bunch Profile Monitor Based on Analysis of Coherent Smith-Purcell Radiation

Hannah Harrison

St Cross College, Oxford

Thesis submitted in fulfilment of the requirements for the degree of Doctor of Philosophy at the University of Oxford

Trinity Term, 2018

Abstract

The spectral analysis of coherent Smith-Purcell radiation (cSPr) is a promising new longitudinal diagnostic technique. This thesis presents a conceptual design for a single-shot, non-destructive, coherent Smith-Purcell radiation monitor and investigates the challenges of realising this type of diagnostic.

It is proposed to use the polarization of coherent Smith Purcell radiation in order to distinguish it from background radiation. A series of experimental studies are carried out at the 8 MeV electron accelerator LUCX (KEK, Japan) in order to measure the polarization of cSPr.

An experimental setup is developed for measuring the frequency and polarization of low intensity THz frequency signals in accelerator environments. The frequency measurements are made with a Fabry-Pérot interferometer, using wire grid polarizers as beamsplitters. The operation of this interferometer is shown to be comparable to classic interferometer designs.

The results show cSPr to be highly polarized and easily distinguishable from unpolarized background radiation. Suggestions are made to improve the experimental setup in order to obtain more detailed measurements in the future.

An investigation into the number and distribution of detection channels required in the cSPr monitor is also carried out. This demonstrates that significant savings in space and cost can be made by optimising the design for specific accelerator environments.

To the students who are just beginning.

Acknowledgements

I would like to acknowledge the following colleagues without whom this thesis would not have been finished. Firstly, thanks go to my supervisor Dr Ivan V. Konoplev, for his guidance and support over the last four years. I would also like to thank him for his MAGIC PIC simulations. I must also thank Dr George Doucas who always made time to help and advise me. I have relied on his expertise and knowledge, particularly about the surface current model and phase recovery methods. I thank Dr A. J. Lancaster for his dedication and drive over the couple of years we spent working together and from whom I learnt a great deal about rigorous analysis. I would like to acknowledge his work on the design of the single-shot cSPr monitor, the FPi scheme and the polarizer-rotation scan methodology. I an indebted to our collaborators at KEK, without whom the experimental results contained within would not have been obtained. In particular to Dr Alexander Aryshev for the many hours spent tirelessly guiding us around the accelerator and Dr Mikhail Shevelev for the vast quantity time he spent tuning the laser. There is a strong correlation between the time you spent working late at night and the quantity of analysis work in this thesis. My thanks go to Dr P. G. Huggard for his great supply of wisdom about all things interferometer and exceedingly patient corrections to my calculations. His help was invaluable and has vastly improved the quality of the work presented. I would also like to specifically acknowledge his work calculating the transmission properties of doped and high resistivity silicon beamsplitters.

Additionally, this thesis could not have happened without the support of all the family and friends who provided sympathetic ears, hugs and a lot of cake. I cannot name you all, so I'm carefully balancing the probabilities of who is most likely to read this. I would like to thank my mother for being so patient when explaining the purpose of the comma and

for always being on the end of the phone when needed. I would like to thank my father for applying his eye for detail to my work and for the sage advice on all things PhD. A special thanks go to James who was with me every step of the way, although I'm not sure I'll ever forgive you for finishing first. And of course, Sam, who I thank most sincerely for the infinite supply of patience both with me and with this project - especially over the last few months. You have made completing this thesis so much easier and smoother than it might have been. I promise to stop moaning about it now.

Contents

1 Introduction to the Project **1**

1.1 The Demand for Longitudinal Bunch Diagnostics 2

1.1.1 High Energy Physics 2

1.1.2 Light Sources 4

1.1.3 Accelerator Research and Development 5

1.2 Types of Longitudinal Bunch Diagnostics 5

1.2.1 Transverse Deflecting Cavities 6

1.2.2 Electro-Optic Techniques 6

1.2.3 Coherent Radiative Techniques 7

1.3 The Objectives of this Thesis 9

2 The Theory and Simulation of Smith-Purcell Radiation **11**

2.1 A Theoretical Overview of Smith-Purcell Radiation 12

2.1.1 Discovery and Early Theories 12

2.1.2 Evanescent Wave Description 15

2.1.3 High Energy Smith-Purcell Radiation 16

2.1.4 The Electric-Field Integral Equation Model 17

2.1.5 The Surface Current Model 19

2.2 Coherent Smith-Purcell Radiation 22

2.2.1 Radiative Processes Induced by Electron Beams 22

2.2.2 Using the Surface Current Model 25

2.3 The Polarization of Smith-Purcell Radiation 26

2.4 Simulating Smith-Purcell Radiation 29
2.4.1 Code Development 29
2.4.2 Limitations of the Simulations 32
2.4.3 Recent Updates 34
2.5 Summary 40

3 Overview of the Single-Shot Monitor Design 42
3.1 The Multi-Shot Design 43
3.2 Challenges of Multi-shot to Single-Shot 47
3.2.1 The Use of Multiple Gratings 47
3.2.2 Background Elimination 49
3.3 Design of the Single-Shot Monitor 51
3.4 Design Aspects Covered in this Thesis 54
3.4.1 Using Polarization to Eliminate Background Radiation 54
3.4.2 Distribution of Detection Channels 55
3.5 Summary 55

4 The LUCX Accelerator 57
4.1 Overview of the Accelerator 58
4.1.1 Bunch Generation and Propagation 59
4.1.2 Charge Measurements 60
4.1.3 γ Detection 61
4.1.4 Imaging the Transverse beam 61
4.2 THz experiments at LUCX 62
4.2.1 The THz Chamber 62
4.2.2 THz Detectors 64
4.2.3 cSPr Generation 67
4.2.4 Michelson Interferometry Scheme 69
4.2.5 Moving Detector Scheme 72
4.3 Preliminary Simulations 73

4.4 Initial Investigations 75
4.4.1 Detecting cSPr 76
4.4.2 Preliminary Polarization Measurements 82
4.4.3 Improving the Polarization Measurements 87
4.5 Summary 88

5 Experimental Design and Interferometer Study **90**
5.1 The New Experimental Scheme 91
5.2 Design of the Fabry-Pérot Interferometer 94
5.2.1 Interferometer Layout 94
5.2.2 Discussion of Beamsplitters 96
5.3 Experimental Configuration during the Interferometer Study 102
5.4 Results of the Interferometer Study 103
5.5 Summary 113

6 Measurement and Analysis of the Polarization of cSPr **114**
6.1 Polarization Measurements 115
6.1.1 Rotation Scans 115
6.1.2 Analysis Procedure 118
6.1.3 Raw Measurements 124
6.2 Comparison with Simulation 128
6.2.1 Simulations with LUCX Parameters 128
6.2.2 The Sawtooth Gratings 133
6.2.3 The Strip Grating 136
6.3 Analysis of Discrepancy between Simulation and Experiment 138
6.3.1 Limitations of the GFW Simulations 138
6.3.2 Limitations of the Experimental Apparatus 142
6.3.3 Conclusions of the Polarization Study 144
6.4 Summary 145

7 An Overview of Phase Recovery Techniques **147**

7.0.1 The $\boldsymbol{\rho}$ Function . . . 147

7.1 Reconstruction Methods . . . 148

7.1.1 The Library Search Method . . . 149

7.1.2 The Kramers-Kronig Method . . . 149

7.1.3 Iterative Solutions . . . 151

7.2 Summary . . . 153

8 Optimizing the Number and Distribution of Detection Channels **154**

8.1 Reconstruction of the Longitudinal Bunch Profile . . . 155

8.1.1 Case Study of the Gaussian Profile . . . 155

8.1.2 Method of Reconstruction . . . 157

8.1.3 Optimised Detector Layout . . . 158

8.2 Methodology . . . 162

8.2.1 Generating a ρ Profile . . . 162

8.2.2 Analysing the Success of Profile Reconstruction . . . 164

8.2.3 Introducing Variable Parameters . . . 166

8.3 Results . . . 167

8.3.1 The Zero Noise Scenario . . . 169

8.3.2 The Low Noise Scenario . . . 173

8.3.3 The High Noise Scenario . . . 177

8.3.4 Discussion . . . 181

8.4 Future Work . . . 182

8.5 Summary . . . 183

9 Overview and Future Work **185**

9.1 The Polarization Study . . . 186

9.2 The Optimization Study . . . 187

A Charge Measurements at LUCX **189**

Bibliography **195**

List of Publications

Journal Publications

H. Harrison, A. J. Lancaster, I. V. Konoplev, G. Doucas, A. Aryshev, M. Shevelev, N. Terunuma and J. Urakawa, "A Fabry-Prot interferometer with Wire-Grid Polarizers as Beamsplitters at Terahertz Frequencies," *Rev. Sci. Instrum.* vol 89(4), 2018

H. Zhang, I. V. Konoplev, A. J. Lancaster, H. Harrison, G. Doucas, A. Aryshev, M. Shevelev, N. Terunuma and J. Urakawa, "Non-destructive measurement and monitoring of separation of charged particle micro-bunches," *Appl. Phys. Lett.* vol 111(4), 2017

Conference Proceedings

H. Harrison et al., "First Steps Towards a Single-Shot Longitudinal Profile Monitor: Study of the Properties of Coherent Smith-Purcell Radiation Using the Surface Current Model," *in Proc. of IPAC '16*, Busan, 2016

H. Harrison et al., "Novel Approach to the Elimination of Background Radiation in a Single-Shot Longitudinal Beam Profile Monitor," *in Proc. of IBIC '16*, Barcelona, 2016

H. Harrison et al., "The Design of a Non-Destructive Single-Shot Longitudinal Bunch Profile Monitor using Smith-Purcell Radiation," *in Proc. of IPAC '17*, Copenhagen, 2017

Glossary of Abbreviations

CDR Coherent Diffraction Radiation

cSPr Coherent Smith-Purcell Radiation

CSR Coherent Synchrotron Radiation

CTR Coherent Transition Radiation

DAQ Data Aquisition Unit

DoP Degree of Polarization

FCT Fast Current Transformer

FPi Fabry-Pérot Interferometer

GFW Grating Finite Width (simulation code)

ILC International Linear Collider

KK method Kramers-Kronig method (for phase recovery)

LHC Large Hadron Collider

LUCX Accelerator facility at KEK (Japan)

Mi Michelson Interferometer

PCI method Phase Constrained iterative method (for phase recovery)

RF Radio-Frequency

SCM Surface Current Model

SLAC Linear Accelerator at Stanford (USA)

WAP (Filters) Waveguide Array Plate Filters.

WGP Wire Grid Polarizers

Chapter 1

Introduction to the Project

Particle accelerators are machines capable of accelerating bunches of particles to high energies. They are an essential tool for conducting research into the fundamental nature of matter and are also widely used as drivers for photon factories, in industry and for medical applications [1, 2]. In hospitals, particle accelerators are used to generate the radiation for imaging, radiotherapy and sterilisation[2, 3]. Researchers from many fields - such as biologists [4, 5] and archaeologists [6] - use the radiation generated at photon factories for the imaging of samples.

Modern radio-frequency (RF) particle accelerators operate by accelerating groups of particles (as opposed to DC accelerators), these groups are known as bunches. A typical bunch at the Large Hadron Collider (LHC), for example, contains 1.15×10^{11} protons. When considering the propagation of the accelerated particles and their interaction with targets it is useful to consider the properties and dynamics of the whole bunch. The successful operation of a particle accelerator relies on a good understanding of the properties of the bunches. The bunch energy, position, charge and shape are among the parameters of most importance. High quality measurements of these parameters are essential to the commissioning and stable operation of particle accelerators.

Beam diagnostics are a group of techniques used to measure a range of bunch properties. The diagnostic equipment installed at any accelerator, and its specifications, are dependent

on the type of facility, for example, different diagnostic tools are used in proton and electron accelerators. The demand for improved accelerator specifications - including higher energies, higher luminosities and steeper accelerating gradients - drives the development of new facility designs. As the properties of accelerators change, it is essential that the corresponding beam diagnostics are improved and adapted.

This thesis is concerned specifically with the development of a diagnostic tool for the measurement of the longitudinal bunch profile of electron bunches. The longitudinal (or temporal) profile of a bunch of particles, describes the variation of charge along the length of the bunch or, equivalently, the variation observed over time as the bunch passes a fixed point. The knowledge of the longitudinal profile of a bunch is essential for determining the behaviour and dynamics of the accelerator. In particular, the recent development of accelerator facilities capable of generating bunches with lengths on the order of a few fs, for high energy colliders and next generation light sources, makes the need for accurate diagnostics more acute. For example, in colliders, accurate assessment of the beam-beam effects - which requires high quality measurements of the longitudinal profile - are needed to maximise the luminosity.

In this chapter the role of longitudinal diagnostics at a range of different types of accelerator are discussed and the challenges in their implementation for future accelerator projects are introduced. Several techniques for measuring the longitudinal bunch information are outlined, with the advantages and disadvantages of each highlighted.

1.1 The Demand for Longitudinal Bunch Diagnostics

1.1.1 High Energy Physics

High energy colliders are often used to investigate fundamental questions in physics research. Impacts between particles are brought about by colliding two beams of particles which are travelling in opposite directions. There are many colliders worldwide, with a wide variety of

parameters. Colliders can be either circular or linear and are used to accelerate electrons, positrons, hadrons and heavy ions.

An important property of a collider is its luminosity, a measure of how many collisions are taking place between the colliding beams. It is desirable to have a high luminosity as this increases number of collisions and hence the number of events that can be detected. The luminosity of a collider, assuming a collision between two (transverse) Gaussian bunches, is given in Eq. 1.1 in units of $\mathrm{cm}^{-2}\mathrm{s}^{-1}$ [7],

$$L = \frac{N_1 N_2 f}{4\pi\sigma_x\sigma_y}\eta_l(\phi_c, A) \tag{1.1}$$

where η is given by Eq. 1.2,

$$\eta_l(\phi_c, A) = \frac{1}{\sqrt{\pi}A_{x,y}}\exp\left(-\frac{1+c_\phi^2/4}{2A_{x,y}^2}\right)K_0\left(\frac{1+c_\phi^2/4}{2A_{x,y}^2}\right), \quad c_\phi = \frac{\phi_c}{\sigma_x/\sigma_z} \tag{1.2}$$

In Eq. 1.1, $N_{1,2}$ gives the number of particles in each bunch, $\sigma_{x,y}$ describe the dimensions of the transverse bunch profile and f the frequency of collisions. η_l, which is defined in Eq. 1.2, is an efficiency factor which depends on the finite crossing angle of the two beams ϕ_c ($\phi_c = 0$ for a head on collision) and the parameter A, which is defined in Eq. 1.3 - where $\beta^*_{x,y}$ is the β function at the collision point [8]. (The β function is a measure of the transverse dimensions of the bunch, related by $\sigma_{x/y} = \sqrt{\epsilon\beta_{x/y}}$, where ϵ is the bunch emittance.)

$$A_{x,y} = \frac{\sigma_z}{\beta^*_{x,y}} \tag{1.3}$$

Eqs 1.1, 1.2 and 1.3, illustrate the complex dependency of the luminosity on the longitudinal bunch length σ_z. It is, therefore, essential to have high quality measurements of the longitudinal bunch properties when attempting to optimise the luminosity of a collider.

The International Linear Collider (ILC) is a proposed 1 TeV electron-positron collider

which could be built in the next decade [9]. The design of this accelerator includes a high operating luminosity ($\approx 1 \times 10^{34}\,\mathrm{cm}^{-2}\mathrm{s}^{-1}$) and very short bunch lengths (sub-ps). This presents a challenge for longitudinal beam diagnostics, as accurate measurements will be needed to maintain the luminosity requirement, however, conventional diagnostics struggle at short bunch lengths (see Section 1.2).

1.1.2 Light Sources

In light sources (or photon factories), such as synchrotrons and free electron lasers (FELs), it is also important to understand the dynamics of the bunches used to create the radiation (typically X-rays). Users often have specific requirements for the intensity and frequency distribution of the radiation delivered.

Many synchrotron facilities have detected micro-bunch instabilities, manifesting as filamentation of the bunch, which produce coherent synchrotron radiation (CSR). The CSR generated by the micro-bunch instabilities is at a higher frequency than that generated by the bunch as a whole [10, 11]. Diagnostics which provide continuous monitoring of the longitudinal profile and which are able to resolve intra-bunch features are required to understand this type of instability. This may enable the elimination of the instability, or alternatively, its exploitation to access a wider range of frequencies at a given light source.

FELs are a tunable source of radiation, providing broader frequency coverage than other light sources. The emission of radiation is stimulated by the passage of an accelerated bunch of electrons through an undulator magnet. FELs are gaining popularity as light sources due to their tunable frequency range and high intensity emission. In particular, ultrashort photon pulses offer the possibility of researching fast dynamic processes (for example, in biomolecular imaging [12]). In order to achieve this, however, bunch lengths on the order of 10 fs are required [13]. To monitor the behaviour of this type of facility, longitudinal beam diagnostics capable of measuring fs timescales are needed.

1.1.3 Accelerator Research and Development

Looking further into the future, facilities which use plasma wakefields to accelerate particles [14, 15] will also require appropriate diagnostic tools. Plasma wakefield acceleration is capable of producing accelerating gradients orders of magnitude higher than conventional RF acceleration schemes. The possibility of reaching higher energies and reducing the space needed for acceleration has attracted a large amount of research interest. The AWAKE project (based at CERN) proposes to accelerate 10 GeV electron bunches to 500 GeV in only 500 m (an average accelerating gradient of $1\,\mathrm{GeVm^{-1}}$) using a proton bunch to drive the wakefield [16]. Previous proof-of-principle experiments, carried out at SLAC (USA), have demonstrated accelerating gradients of up to $4.4\,\mathrm{GeVm^{-1}}$ [17].

The proposed plasma wakefield schemes will generate bunches with significant bunch-to-bunch variation due to the chaotic nature of the plasma environment. These bunches will need individual monitoring to understand their production mechanisms and to enable their use downstream. Many of the current longitudinal bunch diagnostic techniques are destructive, which poses a problem if continuous monitoring is required. This is particularly problematic if there is a large amount of bunch-to-bunch variation and the bunches are intended for use after generation (either for collision or radiation generation).

1.2 Types of Longitudinal Bunch Diagnostics

The previous section outlined several key accelerator areas where the development of longitudinal beam diagnostics is required. Some of the key challenges facing this research area are the ability to:

- Measure short bunches (sub-ps lengths)
- Resolve intra-bunch features
- Measure bunches without destroying them (non-destructive)

- Monitor bunch-to-bunch variation (single-shot)

This section discusses a variety of longitudinal diagnostic techniques, considering their advantages and disadvantages with respect to this list of desirable qualities.

1.2.1 Transverse Deflecting Cavities

Transverse deflecting cavities are found in many accelerators, they provide a time dependent deflection of charged particles which can be used to measure the longitudinal bunch profile (among other applications) [18]. The deflection is induced by the application of a transverse electric field. When measuring the longitudinal bunch properties, phase variation is used to introduced a correlation between the transverse momentum and relative longitudinal bunch position for each particle. The deflected bunch is then incident on a screen, where the intensity (a voltage) and the distribution of the bunch are used to calculate the longitudinal bunch length [19].

Whilst this method requires only minimal analysis, it does, however, have several disadvantages. The device is expensive, requires a power supply to deflect the beam and occupies a large footprint along the beamline. Additionally, only information about the length of the bunch is easily obtained and information about the profile distribution or any intra-bunch features requires the observation of many bunches. Crucially, this method is destructive and therefore not appropriate for continuous monitoring.

1.2.2 Electro-Optic Techniques

The optical properties, in particular the refractive index, of electro-optical materials are modified by the presence of an electric field. The passage of a charged particle bunch through an electro-optical crystal (such as ZnTe), induces birefringence in the crystal. This provides an opportunity to detect the electric field associated with the charged particle bunch at a fixed point over a period of time. Typically, laser pulses are used to probe the changes induced

in the crystal; successful measurements require high levels of synchronization between the bunches and the laser. The length and longitudinal profile of the bunch are then decoded from measurements of the laser pulse after it has travelled through the electro-optical material. This can be done either by spectral or time domain analysis [20, 21].

When spectral analysis is used the electric field of the bunch, which is encoded in the intensity of a chirped probe pulse, is decoded by examining the spectrum of the resultant pulse [21, 22]. Although this technique provides single-shot measurements of the longitudinal bunch profile, the resolution in the time-domain is limited due to distortion in the frequency domain [21].

Direct measurement of the longitudinal bunch information in the time domain can be obtained, by measuring the intensity modulation of the probe pulse as a function of time. This is done by cross correlating the modulated pulse with a secondary laser pulse.

Electro-optical techniques are a highly promising area for high quality longitudinal bunch diagnostics. In particular they can provide measurements with high temporal resolution (of the order of tens of fs [23]), which are both single-shot and non-destructive. However, these techniques require the use of a laser system and, in the case of spectral decoding, a spectrometer. Depending on the existing resources at specific facilities, this could make the installation of electro-optical diagnostics complex and expensive.

1.2.3 Coherent Radiative Techniques

Bunches of charged particles can be induced to emit coherently using a variety of methods. Coherent emission can be caused by the interaction of charged particle bunches with structures placed inside the beam pipe of an accelerator. The longitudinal bunch profile information is encoded in the resulting frequency spectrum. Coherent methods perform well for short bunches and have the potential to provide highly resolved, single-shot longitudinal profile measurements. Several methods for inducing coherent radiation with charged particle bunches are presented, however, this is not an extensive list.

Coherent Diffraction Radiation

Coherent diffraction radiation (CDR) is generated when a bunch of charged particles passes close to a target. The interaction of the electric field generated by the bunch and the boundary of the target causes diffraction radiation to be emitted [24]. CDR generation has been successfully demonstrated as a diagnostic technique in several independent experiments [25, 26].

CDR generation provides single-shot, non-destructive method for extracting the longitudinal bunch profile information. The signal produced has a very low intensity and whilst this can make detection challenging, the low energy exchange means that the effect on the bunch as it propagates downstream is negligible. This method requires a spectrometer to decode the resultant frequency spectrum.

Coherent Transition Radiation

Coherent transition radiation (CTR) is produced when a bunch of charged particles passes through the boundary between two media with different permittivities. This is typically achieved by colliding the bunch with a metal or dielectric target in the beam pipe [27]. The signal produced has a much higher intensity than CDR for the same bunch properties, making detection of CTR less challenging [20]. However, the impact of the bunch and the target is destructive, which prohibits any further use of the bunch after measurement.

CTR generation is the most developed coherent radiation technique for longitudinal bunch diagnostics. Not only have proof-of-principle experiments been carried out by independent groups [27, 28], but CTR diagnostic tools have also been installed at several facilities [29, 14]. This method requires a spectrometer in order to analyse the frequency spectrum produced.

Coherent Smith-Purcell Radiation

cSPr is generated when a bunch of charged particles passes in the vicinity of the surface

of a periodic (typically metal) grating. The electric field of the bunch interacts with the surface of the grating, resulting in the emission of radiation. The intensity of the emitted radiation is dependent (among other parameters) on the number of periods of the grating [30, 24]. Unique among the coherent radiative techniques, the frequency of cSPr is spatially dispersed (see Chapter 2), therefore, a spectrometer is not required to measure the resultant spectrum. cSPr generation is a non-destructive technique and the interaction has a negligible effect on the bunch as it propagates downstream.

Proof-of-principle experiments have been carried out, demonstrating the applicability of this technique to longitudinal bunch measurements [31, 32]. As of yet, however, no diagnostic using this technique has been developed.

1.3 The Objectives of this Thesis

This thesis looks specifically at the development of a single-shot, non-destructive longitudinal bunch profile monitor using cSPr. In particular, research is carried out in the following areas:

- Development of a conceptual design for a single-shot diagnostic based on the analysis of cSPr.
- Extending the capabilities of software for the simulation of the intensity and polarization of cSPr and using it to make predictions about the expected behaviour in experiments.
- Investigating the proposed background elimination method, by comparing measurements and simulations of the polarization of cSPr.
- Developing a method for the measurement of both the frequency and polarization of cSPr in the THz frequency range.
- Optimizing the distribution of the frequency sampling for the single-shot, cSPr monitor and for other coherent radiative techniques.

The work carried out in the proof-of-principle cSPr experiments is expanded upon to create a design for a single-shot diagnostic monitor (Chapter 3). The design relies upon the ability to accurately predict and measure the polarization of cSPr, which is the motivation for a series of experimental studies. Initially, the generation of cSPr is verified and preliminary measurements are taken for one frequency point (Chapter 4). Experimental apparatus is then designed which is capable of measuring the frequency and polarization of cSPr at a range of observation angles. The challenges of working in the THz frequency range are explored and suitable optical devices are identified (Chapter 5). An extensive investigation into the polarization of cSPr is carried out, using a range of frequencies and several gratings. The results are compared with the theoretical model using a simulation code (Chapter 6). Finally, the retrieval of the longitudinal bunch information from coherent radiative processes is investigated from the perspective of optimizing sampling of the frequency spectrum.

Chapter 2

The Theory and Simulation of Smith-Purcell Radiation

To use Smith-Purcell radiation to measure the longitudinal profile of a bunch of charged particles, a good understanding of the properties of this type of radiation is required. It is important to be able to accurately predict the features of Smith-Purcell radiation and to understand how its parameters relate to the properties of the bunch being measured. This chapter discusses some of the theoretical approaches that have been used to describe Smith-Purcell radiation and looks in detail at the surface current theory. The link between coherent radiative processes and the extraction of information about the longitudinal bunch profile is discussed. An original numerical code (GFW) has been modified and is used to simulate the intensity and degree of polarization (DoP) of coherent Smith-Purcell radiation (cSPr) over a range of observation angles, investigating the dependencies of the radiation on a range of electron bunch parameters.

2.1 A Theoretical Overview of Smith-Purcell Radiation

Smith-Purcell radiation is emitted when charged particles pass close to the surface of a periodic structure, such as a metal grating. Smith-Purcell radiation is spatially distributed according to the well known dispersion relation given in Eq. 2.1.

$$\lambda = \frac{p}{n}\left(\frac{1}{\beta} - \cos\theta\right) \tag{2.1}$$

In Eq. 2.1, λ is the measured wavelength, θ is the observation angle, $\beta = \frac{v}{c}$ is the normalized electron velocity, p is the period of the grating and n is the diffraction order of the radiation.

Fig. 2.1 is a schematic representation of the emission of Smith-Purcell radiation and its dispersion by the grating. The colours represent the different wavelengths of light, going from longer wavelengths (red) in the backwards direction to shorter wavelengths (blue) in the forwards direction. The axis along which the electron travels will be referred to as the z-axis throughout this thesis. Similarly, the angle θ is used to refer to position of observation in the x-z plane and the azimuthal angle ϕ is defined as observation position in the x-y plane.

The key feature of Smith-Purcell radiation is its spectral distribution, which is dependent on the observation angle along the θ axis. When generated by an electron of known energy, using a grating with a specific periodicity, the frequency of the observed radiation measured is determined by the location of the detector.

2.1.1 Discovery and Early Theories

The existence of Smith-Purcell radiation was first suggested by Frank [33, 34, 24] in 1942, via the derivation of an equation for radiation due to the Doppler effect when a charge moving in a vacuum induces a current on the surface of a nearby periodic metallic grating. When

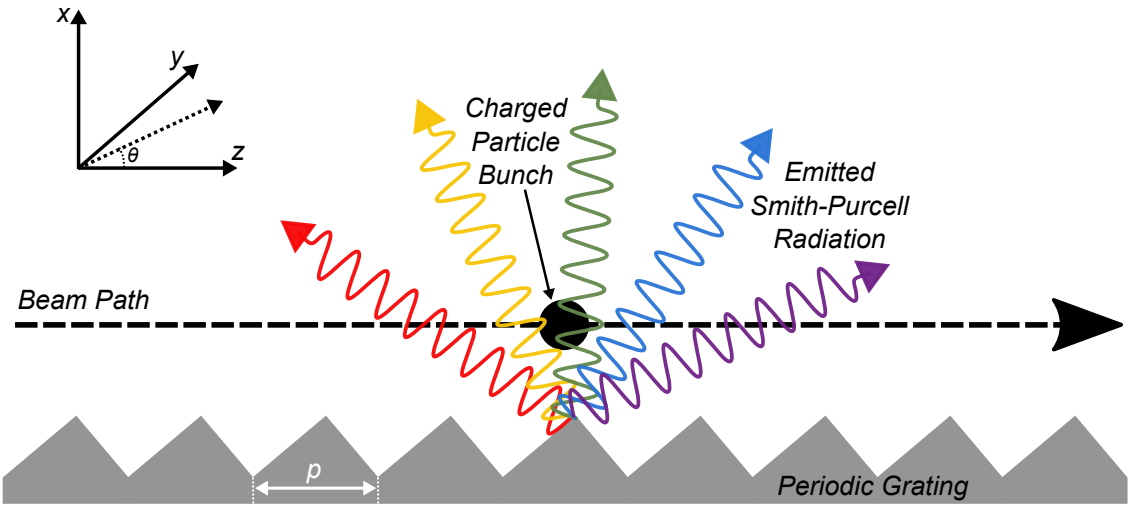

Figure 2.1: This schematic demonstrates the spatial distribution of Smith-Purcell radiation emitted due to the interaction of a charged particle bunch and a periodic grating. The angle θ refers to the observation position in the x-z plane.

the effects of refraction are neglected this can be written as shown in Eq. 2.2, where $\Omega = \frac{2\pi\beta c}{p}$ is the eigenfrequency of the electric dipole created by a charge moving with velocity βc.

$$\omega(\theta) = \frac{\Omega}{1 - \beta\cos\theta} = \frac{2\pi\beta c}{p(1 - \beta\cos\theta)} \tag{2.2}$$

Although a similar analysis was carried out by Motz in 1951 [35], no experimental evidence had been published confirming the observation of this type of radiation.

In 1953 Smith and Purcell [36] independently hypothesised -

> *"...if an electron passes close to the surface of a metal diffraction grating, moving at right angles to the rulings, the periodic motion of the charge induced on the grating should give rise to radiation."*

- and demonstrated the existence of their eponymous radiation. They used a Huygens construction to derive an expression for the fundamental wavelength λ at the angle θ between the direction of motion and the light ray. In Fig. 2.2 a construction of this type is shown.

The difference in path length Δd_1 travelled by photons emitted from consecutive facets,

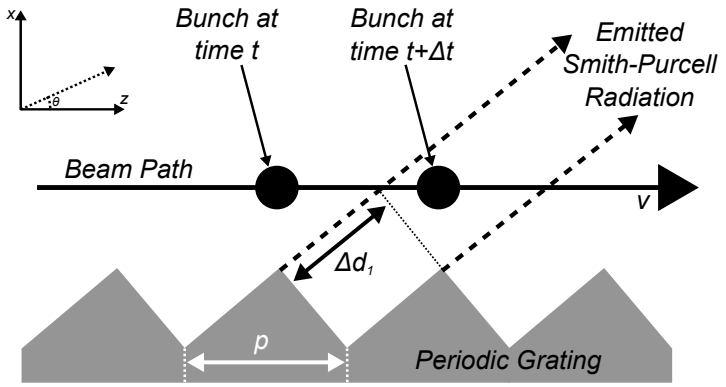

Figure 2.2: A typical Huygens construct for a SPr scheme is shown, where the two dashed arrows represent the paths of SPr emitted by consecutive facets of the grating, travelling parallel (constant θ) to observation in the far field. δd_1 is the path difference caused by the geometry of the grating, and δt is the time it takes an electron travelling at v to travel a distance equivalent to one period of the grating p. This geometric formulation can be used to derive the dispersion equation (Eq.2.1) as described in the text.

separated by the grating periodicity p, is given for each angle θ in Eq. 2.3.

$$\Delta d_1 = p \cos\theta \tag{2.3}$$

The time delay, $\Delta t = \frac{p}{v}$, in the emission from consecutive facets is due to the finite velocity v of the charged particle. This delay in time can be considered a change in the path length travelled by the photons from the second facet, Δd_2, as shown in Eq. 2.4, where c is the speed of light and $\beta = \frac{v}{c} < 1$.

$$\Delta d_2 = \Delta t c = \frac{pc}{v} = \frac{p}{\beta} \tag{2.4}$$

This makes it possible to calculate the total path difference for photons emitted from consecutive facets (Eq. 2.5) and therefore the fundamental wavelength λ_f that could be detected at an angle θ.

$$\lambda_f = |\Delta d_2 - \Delta d_1| = \left| \frac{p}{\beta} - p\cos\theta \right| = p\left(\frac{1}{\beta} - \cos\theta\right) \tag{2.5}$$

This expression is equivalent to that obtained by Smith and Purcell in their paper on the discovery of the phenomena [36]. By considering that the total path difference as shown in Eq. 2.5 can be equal to a multiple of n wavelengths $\lambda_n = \frac{\lambda_f}{n}$ we can retrieve the commonly

used dispersion relation for Smith-Purcell radiation from Eq. 2.1. This is also equivalent to Frank's equation (Eq. 2.2) when rearranged to give the wavelength.

Smith and Purcell detected Smith-Purcell radiation for the first time; they used electrons travelling at 300 keV and an optical grating with a periodicity of 1.67 µm. The resultant radiation was in the visible wavelength region, as predicted by Eq. 2.1. They detected radiation that varied in "colour" depending on the angle of observation, and was strongly polarized (with the electric field vector of the detected light perpendicular to the grating grooves).

Smith and Purcell explained the generation of the radiation as being due to the periodic motion of the charge induced on the surface of the grating by the beam of charged particles [37]. Competing explanations were soon proposed, in the early 1960's Ishiguro and Takeo [38] described the radiation as being generated by a vibrating electric dipole consisting of an electron in the charged particle beam and its image, which oscillate with respect to the periodic grating surface. Whilst both of these descriptions can lead to the derivation of the dispersion relation (Eq. 2.1), neither are suited to calculating the properties of the radiation in the far field, such as the intensity of the radiation at all angles with respect to the direction of motion of the charged particle beam [37].

2.1.2 Evanescent Wave Description

The first attempt at a rigorous theoretical model of Smith-Purcell radiation was by Toraldo di Francia in 1960 [39]. In this work, the situations in which radiation is generated by a charged particle with "uniform and straight motion" are grouped together as "Cerenkovian effects" as they share many properties with Cherenkov radiation. It is proposed to consider the field generated by the charged particle as a set of evanescent waves. In the case of Smith-Purcell radiation, the evanescent waves get scattered on the discontinuities of the surface, becoming ordinary plane waves which carry energy away from the grating. Using the model of evanescent waves, the fields incident on and reflected from the grating can be calculated and so the intensity of the field at various detection locations can be predicted.

This description of Smith-Purcell radiation as evanescent waves was extended by Van den Berg in 1973 [37, 40, 41]. Here the problem is solved more rigorously, so that it can be applied to a wider variety of grating surfaces (in particular sinusoidal grating surfaces) and so that the boundary of the grating is appropriately handled. This method uses a Green's function to create an integral representation of the field; these integrals are solved numerically to make predictions about the behaviour of Smith-Purcell radiation, including the total radiated power due to the interaction and the dependence on distance between the charged particle beam and the grating [37]. This work was later extended to calculate the power losses of the charged particles due to the emission of Smith-Purcell radiation [40].

2.1.3 High Energy Smith-Purcell Radiation

By the 1990's high energy electron sources were increasing available. In 1992 a demonstration of Smith-Purcell radiation generated by 3.6 MeV electrons was reported, producing radiation in the far-infrared (GHz) region [42]. Around about this time two pivotal ideas for the application of Smith-Purcell radiation - especially that generated by the new higher energy electron sources - were first proposed. Firstly, the lack of sources of radiation in this region of the electromagnetic spectrum attracted interest in using Smith-Purcell radiation as an intense and coherent source in the GHz and THz regions [43, 44]. Secondly, it was proposed that a grating could be placed next to the beam in an electron accelerator and the radiation generated could be used as a diagnostic tool for the measurements of the longitudinal properties of the bunches [42].

The possibility of Smith-Purcell radiation generation in experiments with higher energy electrons prompted an extension of the theory developed by Toraldo di Francia and Van den Berg for energies up to 100 MeV; this was carried out by Haeberlé et al. in 1994 [45]. Key developments included solving the integrals developed by Van den Berg for the intensities of Smith-Purcell radiation in the energy range of 1 to 100 MeV, to make explicit predictions. This work predicted a sharp decrease in the intensity of emitted Smith-Purcell radiation at ultrarelativistic beam energies. While good agreement with experimental findings was

shown up to 10 MeV, significant discrepancies were seen at higher energies [42]. Haberlé et al. pointed out some of the limitations of the Van den Berg model model they were using. These limitations include: the assumption that the grating has an infinite conductivity which fails at very short wavelengths (i.e. ultraviolet and x-ray regions), the failure of the integral method when the ratio $\frac{\lambda}{p}$ (where p is the periodicity of the grating used) is very small for some types of grating. This places some restrictions on the range of wavelengths for which they can carry out these calculations and the type of grating that they are able to model.

2.1.4 The Electric-Field Integral Equation Model

The increasing availability of computational power, in the early 2000's, allowed the integral method of evanescent waves to be examined and tested more rigorously. The EFIE (a frequency domain Electric-Field Integral Equation) formulation, developed by Kesar et al. in 2005 [46], modelled bunches of many charged particles. A crucial advance compared to Van den Berg's (and Haberlé et al's) models is the consideration of finite length gratings instead of infinite length gratings. The EFIE model was initially used to calculate the field produced by a 2D [46] charged particle bunch and the formulation was later extended to a 3D charged particle bunch [47].

The EFIE model solves the electric-field integral equation along the surface of the periodic grating used to generate Smith-Purcell radiation. For each frequency, the "tangential incident field" at the point of observation is obtained from a Fourier transform of the time domain electric field integral, as created by the source fields incident on the grating. Solving the electric field in the frequency domain required consideration of the current induced on the surface of the grating. As the Fourier harmonic of the current was unknown, the grating was divided into pieces of Δ_n length and it was assumed that there was a constant current ($\vec{J_c}(\vec{r},\omega)$) across each piece. The expression for the current is given in Eq. 2.6, where a_n is the Fourier coefficient, $\vec{g_n}(\vec{r}) = 1$ in the n^{th} segment and zero outside of it, and $\vec{r}$ gives the observation point of the field.

$$\vec{J}_c\left(\vec{r},\omega\right) \approx \sum_{n=1}^{N} a_n \vec{g_n}\left(\vec{r}\right) \tag{2.6}$$

This approximation allows the electric field integral equations to be written as a set of N linear equations. A Hankel function is used to calculate the far-field vector potential ($\vec{A}$), providing a solution at realistic observation points. The solution for $\vec{A}$ in the 3D model for a grating which has finite length and width is given in Eq. 2.7.

$$\vec{A}(\vec{r},\omega) = \int_C \int_{-\frac{W}{2}}^{\frac{W}{2}} \vec{J}_c(\vec{r}\,',\omega) G^{3D}(\vec{r}-\vec{r}\,',\omega)\, dy'\, dc' \tag{2.7}$$

In Eq. 2.7, $G^{3D}(\vec{r}-\vec{r}\,',\omega)$ is a three-dimensional Green's function, $\vec{r}'$ is the source of the radiation on the surface of the grating, the W in the integration limits refers to the grating width and the C to the integration path along the xz plane [47]. This integral can then be solved numerically; it should be noted that significant computational power is required to solve for the surface current ($\vec{J}_c(\vec{r}',\omega)$) [48].

In its 2D form, the solutions provided by the EFIE model were compared both with a finite-difference time approach and with the conventional Van den Berg integral solution for infinite length gratings [49]. EFIE compares favourably with the finite-difference time approach; as the time domain approach is a near field particle-in-cell calculation, which must be transferred to the far-field, it is preferable to use the frequency domain approach. The comparison with Van den Berg shows considerable difference between the two methods, although the EFIE model converges to the Van den Berg solution as the length of the grating tends to infinity. This demonstrates the importance of considering the finite length (and width) of the gratings.

A power measurement of Smith-Purcell radiation was carried out, using electrons of energy 15 MeV which travelled over a grating with a periodicity of 2.54 mm; the results showed good agreement with solutions provided by the EFIE model [50]. In 2010, extensions were made to the EFIE model to formalise the inclusion of the finite width of the grating

into the calculations [51]. This method provides a rigorous solution for the electric field and has had success at predicting the intensity of Smith-Purcell radiation over a range of frequencies. The large quantity of computing resources required to solve these equations, however, is a significant limiting factor to the EFIE model.

2.1.5 The Surface Current Model

The models discussed up to this point have all be variations on the principle first proposed by Van den Berg - solving an integral containing a Green's function which describes the electric field at the surface of the grating. Although this provides a good method for making predictions about the behaviour of Smith-Purcell radiation, it is very time consuming to calculate the electric field propagation in this way. In the late 1990's an alternative approach was suggested by Brownell *et al.* [52], the Surface Current Model (SCM), which had significantly reduced calculation times compared to methods discussed previously.

In the SCM the electrostatic forces generated between the relativistic charged particle bunch and the grating induce an image charge on the surface of the grating which travels along its surface at the same velocity as the charged particle bunch moving above it. Smith-Purcell radiation is emitted when the image charge passes over variations (or discontinuities) on the grating surface and accelerates [30].

The moving image charge can be considered to be a current on the surface of the grating, $\vec{J}(\vec{r})$. The surface current can be related to the electric field of the charged particles which induced it by reference to Gauss's Law ($\sigma(y,z) = \epsilon_0 E$). This relationship is shown in Eq. 2.8, where $\sigma(y,z)$ is the surface charge on the grating, E is the magnitude of the electric field on the surface of the grating, $\vec{v}(\vec{r})$ is the velocity of the surface charge and ϵ_0 is the permittivity of free space.

$$\vec{J}(\vec{r}) = \sigma(y,z)\vec{v}(\vec{r}) = \epsilon_0 E\vec{v}(\vec{r}) \tag{2.8}$$

The velocity $\vec{v}(\vec{r})$ is described by its three components v_x, v_y and v_z, which describe the motion of the induced charge over the surface of the periodic grating. The expressions for

this will vary depending on the shape of the grating profile, for a typical grating (such as the one shown in Fig. 2.3) the expressions given by Eqs. 2.9, 2.10 and 2.11 respectively can be used.

$$v_x = \frac{dx}{dt} = v \tan \alpha \tag{2.9}$$

$$v_y = \frac{dy}{dt} = \frac{y}{x} v_x \tag{2.10}$$

$$v_z = \frac{dz}{dt} = v \tag{2.11}$$

In Eqs. 2.9, 2.10 and 2.11, v is the velocity of the electron bunch and α describes the incline of a particular facet of the grating (see Fig. 2.3). The x-axis and y-axis, relate to the axes perpendicular to the grating plane (height above the grating) and the axis in the plane of the grating which describes the grating width respectively. In Fig. 2.3 the orientation of the x, y and z axes are shown in relation to a periodic grating.

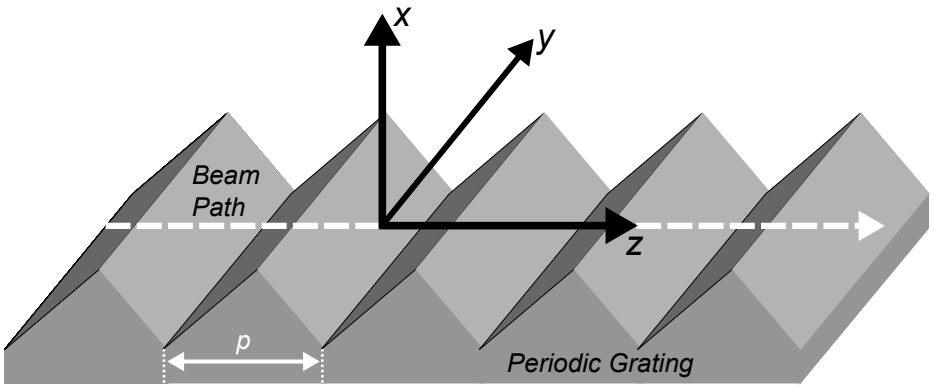

Figure 2.3: The x, y and z axes are defined in relation to the direction of the electron beam and a periodic grating used for the generation of Smith-Purcell radiation.

The field generated by a single relativistic electron E_{elec} is used to derive an expression for the surface charge generated by that electron (see Eq. 2.8). An expression for the electric field, E_{elec}, generated by a relativistic charged particle transformed into the laboratory frame, can be obtained by reference to Jackson [53]. These relationships are shown in Eq. 2.12, where

b is the height of the electron above the grating and $v = \beta c$ is the velocity of the electron.

$$\sigma(y,z) = 2\epsilon_0 E_{elec} = \frac{2\epsilon_0 \gamma e b}{[b^2 + y^2 + \gamma^2(z - vt^2)]^{\frac{3}{2}}} \tag{2.12}$$

The expression for the surface current on the surface of the grating can be used to obtain an expression for the intensity distribution of Smith-Purcell radiation. Equation 2.13 gives an expression for the energy radiated by a continuous distribution of charge in motion, per wavelength $d\omega$, per unit solid angle $d\Omega$, with respect to the surface current $\vec{J}(\vec{r})$.

$$\frac{d^2I}{d\omega d\Omega} = \frac{\omega^2}{4\pi^2 c^3}\left|\int_{-\infty}^{\infty}\int_{-\infty}^{\infty}\int_{-\infty}^{\infty} \vec{n} \times (\vec{n} \times \vec{J}) e^{i\omega(t - \frac{\vec{n}\vec{r}}{c})} dy dz dt\right|^2 \tag{2.13}$$

There are three infinite integrals, in the x, y and z directions. However, as the current is induced (and hence the integration is performed) across the grating surface, it is possible to describe one direction (the x direction) entirely in terms of the other two directions (the y and z directions). For this reason, in Eq. 2.13, there are integrals over y and z but not over x. It is also necessary to integrate over the time it takes for the electron to pass over the grating dt.

Substitution of the expressions given in Eqs. 2.8 to 2.12 into Eq. 2.13, gives an integrable expression for the intensity distribution due to the generation of Smith-Purcell radiation. In order to perform this calculation, however, the surface current $\vec{J}(\vec{r})$ must be calculated for every electron in the bunch. Typically accelerator facilities will have bunches containing on the order of 1×10^{10} electrons, making the calculation very computationally expensive in this form. This expression can, however, be calculated for a single electron $\left(\frac{d^2I}{d\omega d\Omega}\right)_1$ easily and in the next section a method for extending the single electron expression to the whole bunch is outlined.

2.2 Coherent Smith-Purcell Radiation

2.2.1 Radiative Processes Induced by Electron Beams

In this section, the theory of radiative processes induced by electron beams will be used to show how the theory of SCM can be applied to bunches of charged particles. Although here the theory of coherent radiative processes it is described as applicable to Smith-Purcell radiation in the SCM approach, this theory is also relevant to the other coherent radiative processes: including coherent diffraction radiation (CDR), coherent transition radiation (CTR) and coherent synchrotron radiation (CSR). The description of coherent radiation from a bunch of N electrons has been discussed in a number of places [54, 55, 30, 56]. The derivation here is drawn largely from the work by Grimm and Schmüser; however, as that work specifically deals with CTR some modifications have been made to handle Smith-Purcell radiation.

The electric field generated by a bunch of N electrons, when considered in the time domain, can be written as shown in Eq. 2.14. It is assumed that the time dependence of the field is identical for all of the electrons, excepting the time delay caused by their distinct spatial positions. If this is the case, it is possible to write the total field generated by N electrons as $\sum_{i=1}^{N} \vec{E}_i(t)$ considering only the time difference caused by the distance between each electron and a reference electron $\vec{E_1}(t)$ at a position of (0, 0, 0) within the bunch.

$$\vec{E}(t) = \sum_{i=1}^{N} \vec{E}_i(t) = \sum_{i=1}^{N} \vec{E_1}(t + \Delta t_i) \tag{2.14}$$

The spectrum generated by the electric field, $\vec{E}(\nu)$, is calculated by taking the Fourier transform of the time-domain electric field as shown in Eq. 2.15. In accordance with the relationship shown in Eq. 2.14, this is expressed in relation to the time domain electric field of the reference electron.

$$\vec{E}(\omega) = \frac{1}{\sqrt{2\pi}} \int_{-\infty}^{\infty} \vec{E}(t) e^{-i\omega t} dt = \sum_{i=1}^{N} \frac{1}{\sqrt{2\pi}} \int_{-\infty}^{\infty} \vec{E_1}(t + \Delta t_i) e^{-i\omega t} dt \tag{2.15}$$

By introducing a term $t' = t + \Delta t_i$, where t_i is constant for each electron in the bunch, we can rearrange Eq. 2.15 to separate out the expression for the electric field of a single electron as in Eq. 2.16.

$$\begin{aligned}\vec{E}(\omega) &= \sum_{i=1}^{N} \frac{1}{\sqrt{2\pi}} \int_{-\infty}^{\infty} \vec{E_1}(t') e^{-i\omega(t'-\Delta t)} dt' \\ &= \sum_{i=1}^{N} e^{i\omega\Delta t_i} \frac{1}{\sqrt{2\pi}} \int_{-\infty}^{\infty} \vec{E_1}(t') e^{-i\omega t'} dt' = \vec{E_1}(\omega) \sum_{i=1}^{N} e^{i\omega\Delta t_i}\end{aligned} \tag{2.16}$$

The idea of calculating the value of the electric field for a bunch of electrons if the electric field of one reference electron is known is a very powerful one. As the energy of radiation is proportional to the square of the electric field and given the expression in Eq. 2.16, it is possible to extend the expression for the intensity of Smith-Purcell radiation observed for a single electron $\left(\frac{d^2I}{d\omega d\Omega}\right)_1$ to a bunch of electrons. The expression given in Eq. 2.13 can be substituted into Eq. 2.17, joining the SCM description for a single electron with the theory of coherent radiative processes for N electrons. It must also be noted that since $\frac{d^2I}{d\omega d\Omega}$ is dependent on the distance between the electron and the grating surface (x_0 is the distance from the grating to the reference electron), an extra term is added to Eq. 2.17.

$$\left(\frac{d^2I}{d\omega d\Omega}\right)_{total} = \left(\frac{d^2I}{d\omega d\Omega}\right)_1 \left\langle \left| \sum_{i=1}^{N} e^{i\omega\Delta t_i} e^{-2x_0/\lambda_e} \right|^2 \right\rangle \tag{2.17}$$

The large angular brackets in Eq. 2.17 refer to this being a macroscopic average over microscopic fields generated by different electrons [56]. The time delay Δt_i can be rewritten in terms of the distance between the electrons in the bunch $\vec{r_i} - \vec{r_0}$ and the wavevector $\vec{k} = \frac{2\pi}{\lambda}\vec{k_0}$. The substitution $\omega\Delta t = \vec{k}(\vec{r_i} - \vec{r_0})$ can be used to achieve this. The introduction of the wave vector shows that the time delay between the reference electron and the i^{th} electron results in a phase shift between the electromagnetic waves generated.

The sum over all N electrons in the bunch can be expanded as shown in Eq. 2.18. At this point the use of the reference electron position r_0 is replaced by a second indexed electron position r_j. In this way the relationships of all the electrons in the bunch to each other

are considered. In Eq. 2.18 the reference positions x_i and x_j also account for the distance between the electrons and the grating. The origin of the x-axis is at the surface of the grating.

$$\left(\frac{d^2I}{d\omega d\Omega}\right)_{total} = \left(\frac{d^2I}{d\omega d\Omega}\right)_1 \left(\sum_{i=1}^{N} e^{-\frac{2x_i}{\lambda_e}} + \sum_{i=1}^{N}\sum_{j\neq i}^{N} e^{-\frac{x_i+x_j}{\lambda_e}} e^{ik(r_i-r_j)}\right) \tag{2.18}$$

In the case that $N >> 1$ the electrons in the bunch can be treated as a continuous distribution, and the sums are converted to integrals over the two transverse directions x and y, as well as in the longitudinal direction $t = \frac{z}{v}$. The two terms in Eq. 2.18 become the incoherent S_{inc} and coherent integrals S_{coh} (given in Eqs. 2.20 and 2.21), which are proportional to N and $N(N-1)$ respectively; for large N the coherent integral can be said to be proportional to $N(N-1) \approx N^2$.

$$\left(\frac{d^2I}{d\omega d\Omega}\right)_{total} = \left(\frac{d^2I}{d\omega d\Omega}\right)_1 (NS_{inc} + N(N-1)S_{coh}) \tag{2.19}$$

$$S_{inc} = \int_{-\infty}^{\infty} Xe^{-2\frac{x-x_0}{\lambda_e}} dx \tag{2.20}$$

$$S_{coh} = \left|\int_{-\infty}^{\infty} Xe^{-\frac{x-x_0}{\lambda_e}} dx\right|^2 \left|\int_{-\infty}^{\infty} Ye^{-ik_y y} dy\right|^2 \left|\int_{-\infty}^{\infty} Te^{-i\omega t} dt\right|^2 \tag{2.21}$$

In Eqs. 2.20 and 2.21 X, Y and T refer to the bunch distributions in the x, y and t ($\frac{z}{v}$) directions. For ease of calculation it is assumed that the bunch distribution in each direction is uncorrelated with the distribution in the other two directions. The x coordinate is now defined as 0 on the surface of the grating and the constant x_0 gives the distance between the reference electron (in the centre of the bunch) and the grating surface.

Although the total energy is a sum of the incoherent and coherent terms, under certain circumstances one or the other will dominate. The coherent term is so named as this deals with the fraction of the particles which are emitting coherently; the electric fields generated by the coherently emitting particles add constructively. The coherent term will dominate - with the majority of electrons emitting coherently - if the condition $\lambda >> l_B$ is satisfied,

where l_B is the length of the bunch [24]. As the wavelengths generated by Smith-Purcell radiation are determined by the dispersion relation (Eq. 2.1) - and if it is assumed for an experiment that β and the range of observation angles θ are fixed - an appropriate grating periodicity can be selected to ensure coherence. In this thesis we will consider exclusively coherent Smith-Purcell radiation (cSPr) from this point onwards.

The coherent integral, Eq. 2.21, which dominates the emission of cSPr shows that it is dependent on the shape of the bunch in all three dimensions. As accurate measurements can be made of the transverse dimensions (X and Y) by other methods, measuring the cSPr emitted by a bunch can yield information about the longitudinal bunch distribution (T). This measurement will also require a good understanding and calculation of the emission by a single electron $\left(\frac{d^2I}{d\omega d\Omega}\right)_1$, which can be done using the SCM (see Eq. 2.13).

2.2.2 Using the Surface Current Model

SCM, using the theory of radiative emission to describe collective emission from a bunch, was successfully compared to experimental measurements of cSPr generated with electron bunches of energy of 3.6 MeV in 1997 [52, 30]. The model was then used to predict high intensity radiation at higher energies for echelle gratings [30] and for lamellar gratings [57]. In 2002 the theory was used for the first time to determine the longitudinal bunch profile of electron bunches. The experiment used 1.8 MeV electrons to generate cSPr; the cSPr was detected and an approximately triangular longitudinal bunch profile was inferred from the measurements [58]. A later experiment with higher energy electrons (855 MeV) measured incoherent Smith-Purcell radiation and the results showed considerable disagreement with the SCM [59], with the authors suggesting that this discrepancy could be due to their assumption of infinite conductivity for the grating. Following this, a succession of experiments at energies ranging from MeV to GeV (15 MeV, 28.5 GeV, 20.35 GeV) were carried out, with increasingly short bunches (14 ps, 2.5 ps, 350 to 600 fs) which ensured the generation of Smith-Purcell took place in the coherent regime. All of these experiments showed very good agreement with SCM [60, 31, 32].

The success of the SCM (measured by agreement between theoretical predictions and experimental data), led to the development of experiments specifically for the purpose of making measurements of cSPr in order to reconstruct the longitudinal bunch profiles. Initial experiments using energies of 28.5 GeV measured bunch lengths in the region of 2 ps. Estimates were made of the longitudinal bunch profiles, however, the authors caution that due to experimental limitations this should only be treated as an order of magnitude measurement [31]. Subsequently an experiment, known as E203, was installed at FACET, SLAC (USA) in 2011 [61]. The experiment used 11 detection channels and three gratings to build up a frequency spectrum sufficiently broad to reconstruct the longitudinal profile of the bunch. Measurements were carried out with electrons at energies of 20.35 GeV and using sub-pico second bunches (356 to 606 fs) in 2014. The profiles taken for each run are shown to be highly self consistent, with variation between runs likely due to changes to the accelerator parameters [32]. The ability of the E203 experiment to measure not only bunch lengths, but also longitudinal bunch features, provides a strong argument for the development of a diagnostic tool using cSPr.

2.3 The Polarization of Smith-Purcell Radiation

Smith-Purcell radiation, like all forms of electromagnetic radiation, can be thought of as a transverse electromagnetic wave. While in previous sections we have discussed the magnitude of the electric field, which determines the intensity measured at any given observation location, the orientation of the electric field is also an important property of the radiation. This orientation is commonly referred to as the polarization of the radiation. There are several states of polarization, including linear, circular and elliptical. This thesis considers the linear polarization of Smith-Purcell radiation.

Linearly polarized (or plane polarized) radiation has an electric field with a constant orientation. If two in-phase electromagnetic waves, propagating in the same direction, have the same electric field orientation then the resultant wave will be linearly polarized in the

same direction as the two original waves. Alternatively, if two in-phase electromagnetic waves, propagating in the same direction, have electric fields with different orientations they combine to form a linearly polarized wave with an electric field orientation different from the original two waves. The resultant orientation is determined by summing the electric field vectors of each electromagnetic wave, so both their amplitude and orientation effects the resultant polarization. If the two electromagnetic waves are not in phase the resultant radiation will be circularly or elliptically polarized.

When discussing Smith-Purcell radiation, the orientation of the electric field vectors in every observation position is resolved along the two orthogonal directions, parallel and perpendicular to the grating grooves. In order to follow convention, the two orientations are referred to with respect to their respective magnetic field vectors (perpendicular to the electric field vectors) as follows:

(i) Radiation polarized parallel to the grating grooves, has its magnetic field vector perpendicular to the grating grooves.

(ii) Radiation polarized perpendicular to the grating grooves, has its magnetic field vector parallel to the grating grooves.

As shown in Fig. 2.4, observed Smith-Purcell radiation will have a field vector which is a combination of the parallel and perpendicular components. By measuring its polarization it is possible to compare the ratio of the intensities in the two orientations. Experiments either compare the two orientations of interest directly or take a measurement that allows for the recovery of the angle a°, which represents the direction of the field vector of the resulting linearly polarized radiation. Comparing the intensities of the radiation emitted in both orientations allows for a calculation of the degree of polarization (DoP), as shown in Eq. 2.22, where $I_{\parallel}$ and $I_{\perp}$ represent the intensity of the radiation emitted parallel and perpendicular to the grating grooves respectively.

$$DoP = \frac{I_{\parallel} - I_{\perp}}{I_{\parallel} + I_{\perp}} \tag{2.22}$$

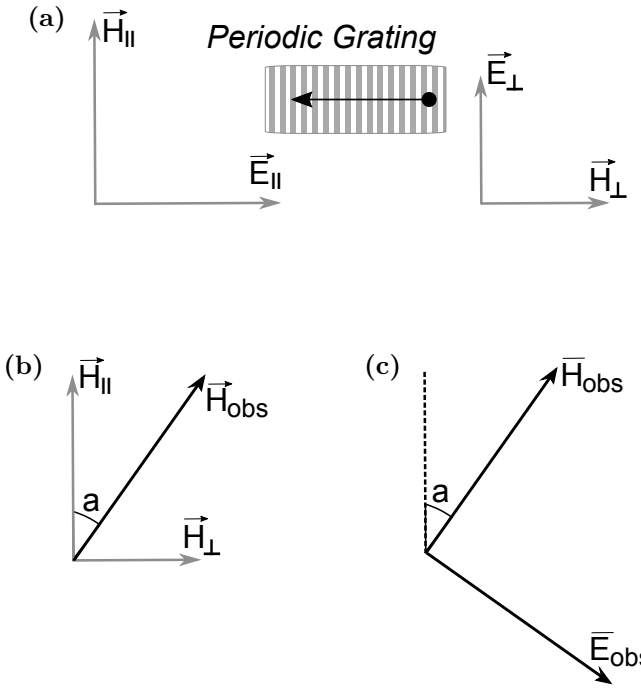

Figure 2.4: The (a) field vectors orientated parallel and perpendicular to the grating grooves, the (b) summation of two field vectors and the (c) resultant field vector. The angle a° gives the orientation of the resultant magnetic field vector with respect to the magnetic field vector parallel to the grating grooves. Note that the electromagnetic waves represented have a direction of propagation into the page (perpendicular to plane in which the electric and magnetic field vectors lie).

When the DoP is equal to 1 all the radiation is polarized parallel to the grating grooves, when it is equal to -1 all the radiation is polarized perpendicular to the grating grooves and if it is equal to 0 then the radiation is polarized in equal quantities in the two orientations (experimentally indistinguishable from unpolarized radiation). In an experimental environment it is important to also consider any background radiation, this radiation should be measured separately and the polarization determined before attempting polarization measurements of Smith-Purcell radiation. Techniques for carrying out this type of measurement are described in Chapter 3.

A small collection of studies have been carried out to investigate the polarization of Smith-Purcell radiation. In 1998, Shibata et al. [55] studied the Smith-Purcell radiation generated by a 40 MeV electron beam by measuring it along two orientations, described as H- and V-polarized components, normal to grating grooves and normal to the electron beam trajectory respectively. The study found that the H-polarized component dominated the total intensity of the detected Smith-Purcell radiation. This study did not use cSPr and only a small range of frequencies were considered, however, a substantial amount of data was collected measuring the intensity and polarization variation over a range of azimuthal (ϕ) angles.

In 2014, Andrews et al. [32], investigated the polarization of cSPr generated by a 20.35 GeV electron beam at the SLAC facility. This experiment found a variation in the polarization of cSPr with frequency, and some agreement was found with simulation results, however, the high levels of unpolarized background radiation could not be separated from the signal during experiment which was an impediment to accurate measurements.

2.4 Simulating Smith-Purcell Radiation

2.4.1 Code Development

Throughout this thesis simulation results will be used to predict both the intensity and DoP

of cSPr, generated under a wide variety of parameters. For these simulations an in-house code called GFW (Grating Finite Width), which provides solutions using the SCM method will be used. The methodology, code specific solutions and its limitations will be discussed in this section.

GFW was developed using the C programming language by Dr G. Doucas in the early 2000's; the code remains in use and is subject to continual development. Earlier versions of the code and resultant simulations are discussed in V. Blackmore's thesis [61]. The main task of this code is to produce solutions to the integrals shown in Eq. 2.13 and propagate them to far field solutions. The results of the code should ideally be comparable to experimental results and a variety of modifications have been carried out (as part of the work in this thesis) to achieve this.

The solutions to the integrals shown in Eq. 2.13 are provided by using Bessel function approximations. The x, y and z components of the surface current (J) as shown in Eq. 2.21, are first integrated over t and are then rearranged separately to give expressions in terms of a modified Bessel function of the second kind K_1 [62]. The resulting expressions can be written as four integrals over y and z along the surface of the grating. One of these integrals is shown in Eq. 2.23. The other three have the same structure but with different permutations of the sine and cosine terms.

$$I_1 = \frac{2}{\pi}\int_{z_s}^{z_f} \cos\left(Dz - k_x + \psi\right)dz \int_0^{w/2} \frac{kb}{\beta\gamma\sqrt{b^2+y^2}} K_1\left(\frac{k\sqrt{b^2+y^2}}{\beta\gamma}\right)\cos\left(k_y y\right)dy \qquad (2.23)$$

In Eq. 2.23 it has been assumed that the electron is travelling along the line defined as $y = 0$, and therefore that the expression for J can be considered to be symmetrical along the y-axis. This assumption results in the y-integral having limits of 0 to $\frac{w}{2}$ (where w is the grating width), which halves the computation time needed to solve these integrals. If these integrals are solved for an infinite width grating, then the y-integral will go from 0 to ∞ and the expression can be evaluated analytically, greatly simplifying the solution. Although this was done for early versions of the code, this was ultimately decided to be an inappropriate

approximation for the typical parameters used in experiments (for example, grating widths of 20 mm and periodicities of 1.0 mm). If the finite width of the grating is considered, it is necessary to solve the integrals numerically using, in this case, NAG library routines [63].

In Fig. 2.5, GFW is used to compare the total energy of the generated cSPr per electron bunch for gratings of varying width. The energy generated by the finite gratings is compared to the energy generated by a grating of infinite width. Although the generated energy tends towards the infinite grating value as the width is increased, for the 20 mm width grating used in experiments, the total energy emitted is approximately 60% of the infinite grating energy. This plot demonstrates the need for a simulation that can handle finite width gratings, as there is expected to be a significant impact on the emitted cSPr.

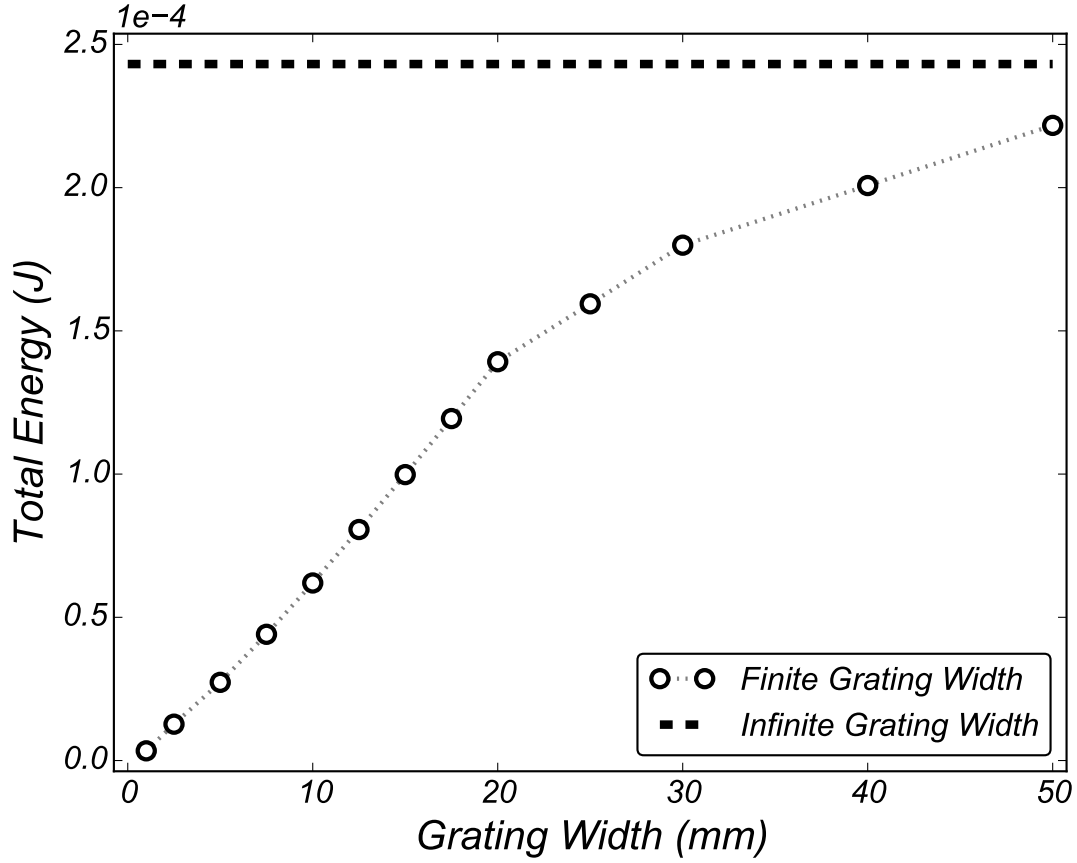

Figure 2.5: The calculated total energy of cSPr generated is plotted for varying grating widths. This simulation is carried out for electron bunches, energies of 20.35 GeV and a charge of 1.2 nC. In each case the grating has a length of 60 mm and a periodicity of 1.0 mm. The thick dashed line gives an estimate of the total energy emitted for a grating of infinite width.

The NAG Numerical library is a software library that provides a large number of numerical analysis routines in both C and Fortran. Crucially, it provides functions which evaluate multidimensional integrals as well as functions which evaluate modified Bessel functions. It should be noted that these numerical algorithms give approximate solutions to the integrals, not analytic solutions. The errors in the solutions provided by the software are considered to be small enough to ignore in subsequent calculations [63].

The GFW code takes a large number of input parameters, with the result that it can simulate cSPr production in a wide variety of accelerator environments. It is possible to vary basic accelerator parameters (such as electron energy and charge), the properties of the gratings used (shape, periodicity, length and width) and the longitudinal bunch properties (shape and length).

2.4.2 Limitations of the Simulations

The predictions made by the GFW code have several limitations. These limitations can be divided up into:

- those which are caused by the assumptions in the model of SCM
- those caused by the assumptions of the model of radiative processes
- those due to the numerical routines specific to the GFW code

As the limitations of the numerical algorithms have already been discussed, here only the limitations of the model that GFW is based on are considered.

The SCM, while providing a good description of the radiation generated by a single electron, ignores several physical aspects of the problem. The assumption that the periodic grating has infinite conductivity ignores any energy losses which will occur in a real metal and is only valid when the emitted frequency of cSPr is less than the plasma frequency of the metal [64]. For a metal such as aluminium, which has a high conductivity and a plasma frequency in the visible spectrum, this assumption is valid for the all of the experiments considered in

this thesis. Experiments with metals that have a higher resistivity, with dielectric materials or at significantly higher frequencies, however, would not necessarily be able to rely on the predictions made by the SCM.

Another consideration is that the SCM does not account for any additional effects due to the interaction of the surface current with the edges of the grating. The introduction of finite grating dimensions into the integrals cuts the current on the grating surface at the boundaries. In an experiment there may be reflections from the boundaries or radiation losses as the current is dissipated abruptly at the edge and transverse modes are formed, these phenomena are not considered by the current model. For the aluminium gratings used in this thesis, all of length 60 mm and a width 20 mm, the electron beam is presumed to be propagating above the centre of the grating. The surface current is, therefore, much larger in the central region, close to the electron beam, than at the edges of the grating. For this reason the boundary effects are considered to be negligible. Using smaller gratings (in particular gratings with a smaller width) may increase the chances of an edge effect being seen experimentally.

The derivation laid out in Section 2.2.1 assumes that the radiation is being observed in the far field and that the grating can be considered as a point source. This condition is also applicable to the dispersion relation of Smith-Purcell radiation as shown in Eq. 2.1. For experiments taking place in the far field any observations of the cSPr would have to satisfy the conditions $d_f >> D$ and $d_f >> \lambda$, where d_f is the distance from the source to the observation point, D is the largest dimension of the emitter (here the grating) and λ is the wavelength of the radiation being detected. We should expect some discrepancy between the simulations and experimental results due to detector location in the intermediate field for some frequencies.

We must also consider the parameters that GFW has been designed to simulate. In its current version GFW can accept a range of set grating profiles (sawtooth, strip) and bunch shapes (Gaussian, Lorentzian). It cannot, however, take as its input for either of these an arbitrary function. This inherently limits the scope of the simulations, however, the range of

grating profiles and bunch shapes available provides sufficient options to simulate a variety of accelerator environments.

2.4.3 Recent Updates

Simulations using GFW will be presented throughout this thesis, with the purpose of predicting the intensity and DoP of cSPr. Part of the research contribution of this thesis has been to maintain and update the GFW code. The code has been modified to accept input files, which streamlines the comparison of various parameters.

The output of the GFW code is large arrays, containing predicted intensity or DoP values, where each position in the array corresponds to an observation location. The range and resolution of the location coordinates, θ and ϕ, are input parameters selected by the user. GFW is used to generate the high density θ and ϕ maps shown in Fig. 2.6. The two plots give the (a) cSPr intensity and the corresponding (b) DoP respectively. These simulations are based on a series of experiments carried out at SLAC in 2012 -2013, which are discussed at length in published literature [32].

The intensity distribution (Fig. 2.6(a)) is given in $\mathrm{J\,sr^{-1}\,m^{-1}}$, which can be converted into energy (J) by integrating over the solid angle Ω and the length of the grating. Whilst the grating length is a constant, in an experimental context the solid angle would be defined by the acceptance of the detector and its distance from the grating. For a detector - with a radius of acceptance, r, located a distance, R, from the grating - the solid angle, Ω, is given by Eq. 2.24.

$$\Omega = \frac{\pi r^2}{R^2} \tag{2.24}$$

It is also possible to calculate the angular aperture, A, of the detector at a given position from the grating, which gives the detector acceptance in θ and ϕ, as shown in Eq. 2.25. In order to calculate the energy reaching a detector, all the values within a given aperture must

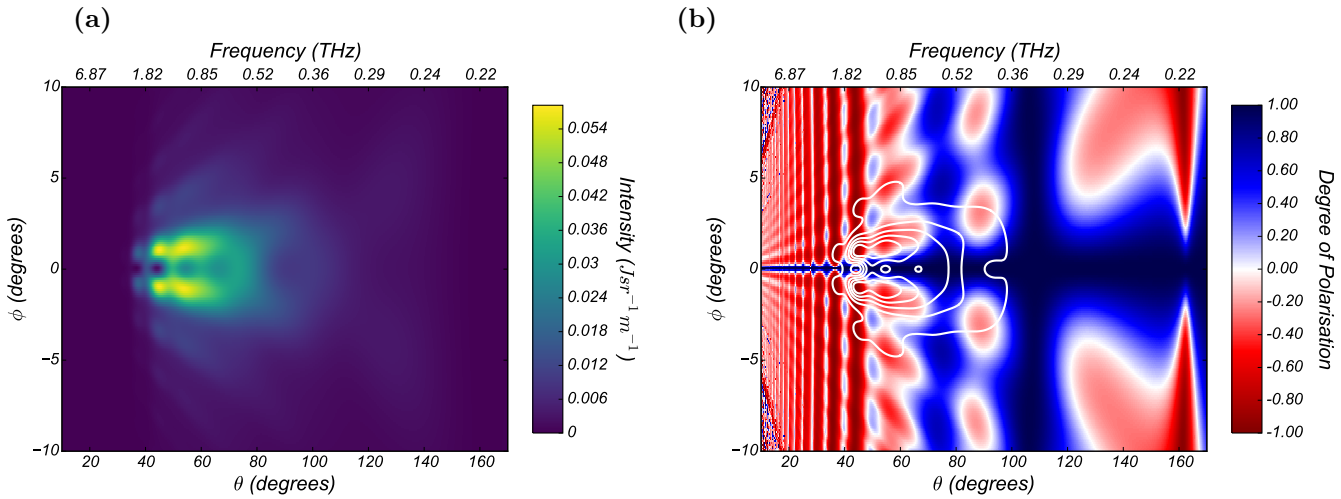

Figure 2.6: These figures show the (a) intensity and (b) DoP over a range of observation locations defined by the θ and ϕ coordinates. Key parameters for this simulation are an electron energy of 20.35 GeV, a charge of 1.2 nC, a bunch length of 450 fs and a grating periodicity of 1 mm. In (a) the intensity is given in $\mathrm{J\,sr^{-1}\,m^{-1}}$, in (b) the DoP is given in a range from -1 to 1, where 1 indicates radiation polarized with the electric field perpendicular to the grating grooves. The contours (b) indicate the intensity distribution of the radiation, they indicate the intensity levels from the lowest to highest value in 15% intervals.

be averaged then multiplied by the solid angle Ω and the length of the grating l.

$$A = \arctan\left(\frac{r}{R}\right) \tag{2.25}$$

The DoP given in Fig. 2.6(b) shows that the cSPr generated is expected to be highly polarized in the direction of the grating grooves. In particular, we see high levels of polarization along the ϕ=0 axis, where the detectors are typically placed. To calculate the DoP of the radiation reaching the detector, d_{dect}, a weighted average (which considers the intensity of the radiation, I) must be carried out, as shown in Eq. 2.26.

$$d_{dect} = \frac{\sum_i^A d_i I_i}{\sum_i^A I_i} \tag{2.26}$$

A Python code has been developed to carry out the post-processing of the results produced by the GFW code. The post-processing code simulates experiments by taking an array

of detector positions as inputs, and calculating the intensity (in J) and DoP of the radiation that reaches each detector. The simulations in this section use GFW to predict the effect of varying parameters associated with the generation of cSPr and the post-processing code to model the associated experimental outcomes. In each simulation the radiation is calculated for an array of 11 detectors positioned (centrally) from $\theta = 30°$ to $130°$ (at $10°$ intervals) and at $\phi = 0$. All of the simulations use the parameters listed in the caption of Fig. 2.6, except those which have been deliberately varied. In Fig. 2.7, the electron energy is varied from 10 MeV to 5 GeV.

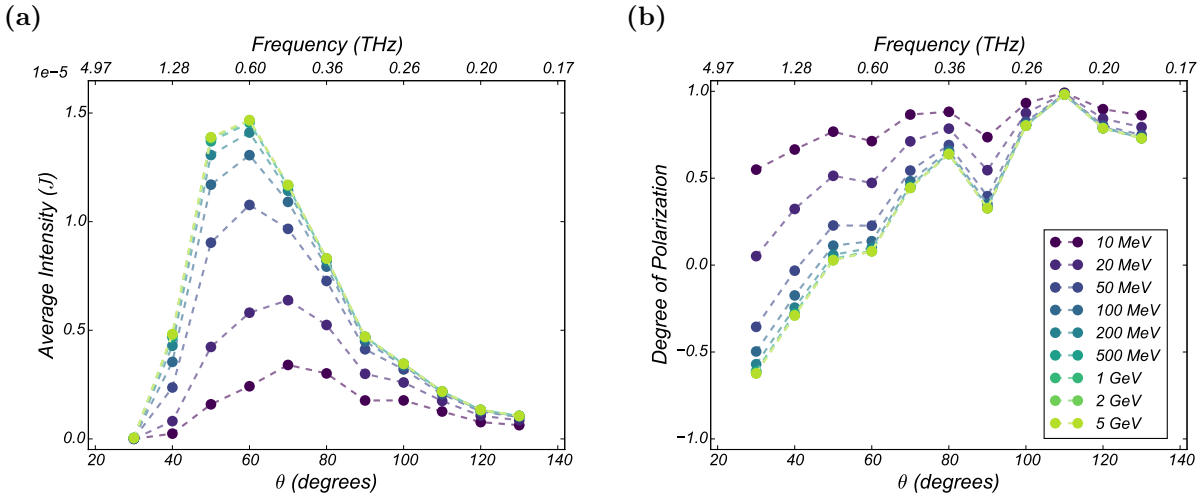

Figure 2.7: These figures show the calculated (a) intensity and (b) DoP of cSPr generated by bunches of varying electron energy. The markers on each graph represent the location of detectors with respect to the θ axis (all detectors are located at $\phi = 0$). The values given for intensity are in units of J and each has been integrated over a detector aperture of ± 6 mm. The legend shown applies to both (a) and (b).

The simulations, in Fig. 2.7(a), show a clear dependence between the energy of the electrons in the bunch and the intensity of the emitted radiation. The SCM model is known to predict a large increase in intensity as the energy of the electrons goes from relativistic to ultra-relativistic. The DoP, in Fig. 2.7(b), shows an increase in variation, and a general decrease in DoP, as the energy increases. Both the intensity and the DoP show a stronger dependence on energy for the lower values of energy (MeV), with the variation of intensity becoming less notable as the energy rises (GeV). The response, therefore, of both the intensity and DoP to energy fluctuations would be weaker at higher energy accelerators.

In order to understand why the measurements of DoP are predicted to vary so strongly with the electron energy, it is necessary to compare the overall intensity and DoP distributions for high energy electrons (20.35 GeV) - shown in Fig. 2.6 - with similar maps for low energy. In Fig. 2.8 the θ and ϕ distributions of intensity and DoP are given for cSPr generated by 10 MeV electrons (all other parameters are the same as in Fig. 2.6).

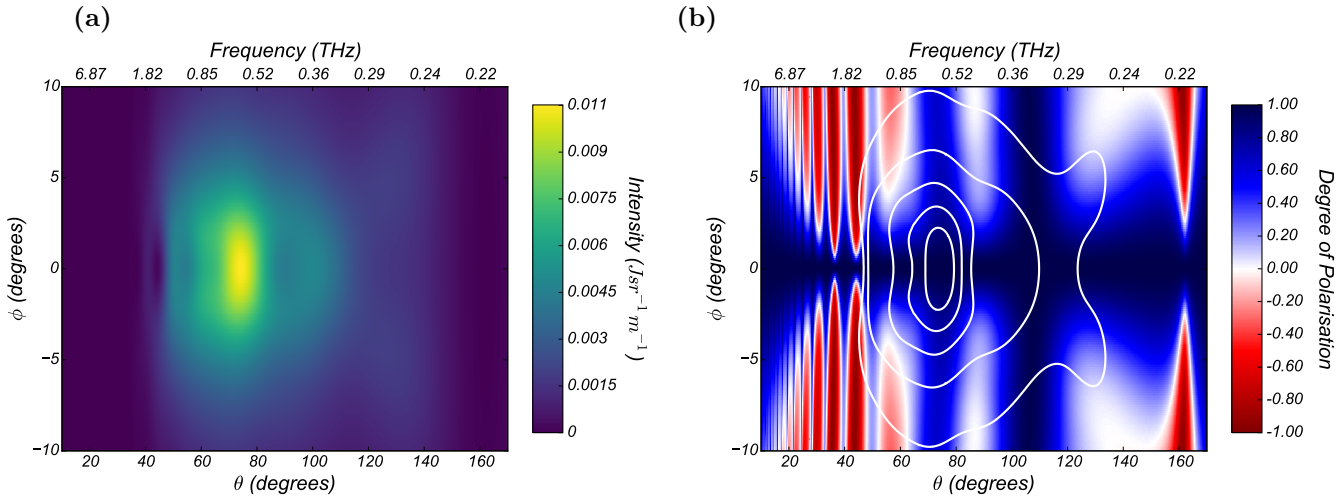

Figure 2.8: These figures show the (a) intensity and (b) DoP over a range of observation locations defined by the θ and ϕ coordinates. Key parameters for this simulation are an electron energy of 10 GeV, a charge of 1.2 nC, a bunch length of 450 fs and a grating periodicity of 1 mm. In (a) the intensity is given in J sr^{-1} m^{-1}, in (b) the DoP is given in a range from -1 to 1, where 1 indicates radiation polarized with the electric field perpendicular to the grating grooves. The contours (b) indicate the intensity distribution of the radiation, they indicate the intensity levels from the lowest to highest value in 15% intervals.

As the energy of the electrons increases, the intensity distribution of cSPr becomes narrower around the ϕ axis. This corresponds to low DoP values (<0) being found closer to the ϕ axis for some frequencies. For an experiment where the aperture of the detectors is centred around ϕ =0, an increase in energy corresponds to a decrease in the observed DoP, although the extent of the decrease varies across the frequency range considered in these simulations.

The impact of other parameters on the results of the GFW simulations is also considered. In Fig. 2.9 a simulation looking at the variation of the charge of the electron bunch is shown.

The simulations, shown in Fig. 2.9(a), show a very strong dependence between the charge of the electron bunch and the intensity of the emitted radiation (note the log scale on the

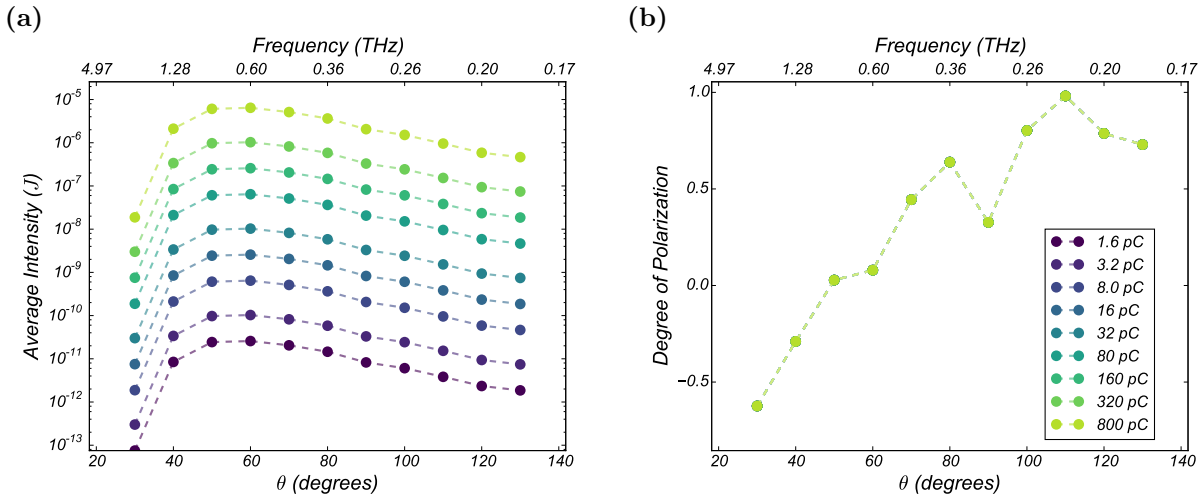

Figure 2.9: These figures show the calculated (a) intensity and (b) DoP of cSPr generated by electron bunches of varying charge. The markers on each graph represent the location of detectors with respect to the θ axis (all detectors are located at $\phi = 0$). The values given for intensity are in units of J and each has been integrated over a detector aperture of $\pm 6\,\text{mm}$. The legend shown applies to both (a) and (b). Note the log scale used in (a), required due to the significant variation in the predicted intensity values.

y-axis). This is to be expected, as the intensity of cSPr has a quadratic dependence on the number of particles in the bunch (see Eq. 2.19). Interestingly, the DoP shows no dependence on the charge of the bunch, predicting no variation in DoP measurement even for large charge fluctuations.

The post-processing code, developed to extract predicted detector measurements from GFW results, is particularly useful for designing experiments and testing their robustness. The next set of simulations analyses the effects, on cSPr measurements, of variations in the properties of the detectors arrays. In the first case, the aperture of the detector is varied, with the values of the radius of acceptance, r, ranging from 1 mm to 15 mm. The results of this simulation are shown in Fig. 2.10.

Unsurprisingly, the intensity of the radiation reaching the detector increases as the detector aperture increases (as shown in Fig. 2.10(a)). The dependence of the DoP on the detector, on the other hand, requires some further consideration. In Fig. 2.10(b), it is shown that larger apertures cause a decrease in the DoP for almost all of the detector positions considered. The extent of that decrease is variable and sensitive to the θ position of the

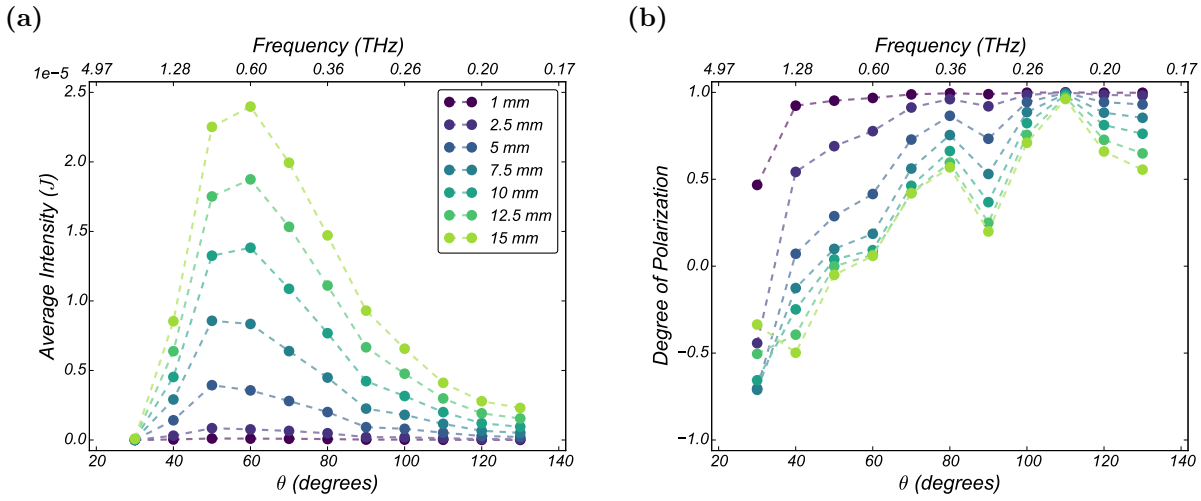

Figure 2.10: These figures show the calculated (a) intensity and (b) DoP of cSPr measured for varying detector acceptance angles. The markers on each graph represent the location of detectors with respect to the θ axis (all detectors are located at $\phi = 0$). The values given for intensity are in units of J and each has been integrated over its given detector aperture. The legend shown applies to both (a) and (b).

detector. As the aperture becomes increasingly large, with values of r above 10 mm, this variation slows considerably. Examination of the DoP map, shown in Fig. 2.6(b), shows that the central line ($\phi = 0$) of the distribution has very highly polarized radiation. The simulations with smaller detector apertures are highly influenced by this effect, but its influence decreases as the apertures increase.

When conducting experiments, it is useful to consider the impact of uncertainties and errors. In Fig. 2.11, the effect of incorrect alignment of the detectors along the ϕ=0 axis is considered. The simulation shows the measured intensity and DoP for varying ϕ location coordinates, this variation is given as a deviation $\delta\phi$ from the nominal location of $\phi = 0$.

In Fig. 2.11(a), a strong dependence on the ϕ observation angle is seen, there is a significant reduction in the expected signal for $\delta\phi > 1°$. This highlights the importance of correctly aligning the detectors with respect to the grating (and vice versa) in experiments. Interestingly, only small changes are seen to the DoP, in Fig. 2.11(b), as the position of the detector is shifted along the ϕ axis.

Throughout this thesis, the GFW code and the post-processing code, are used to predict the outcomes of various different experimental schemes for the generation of cSPr. This

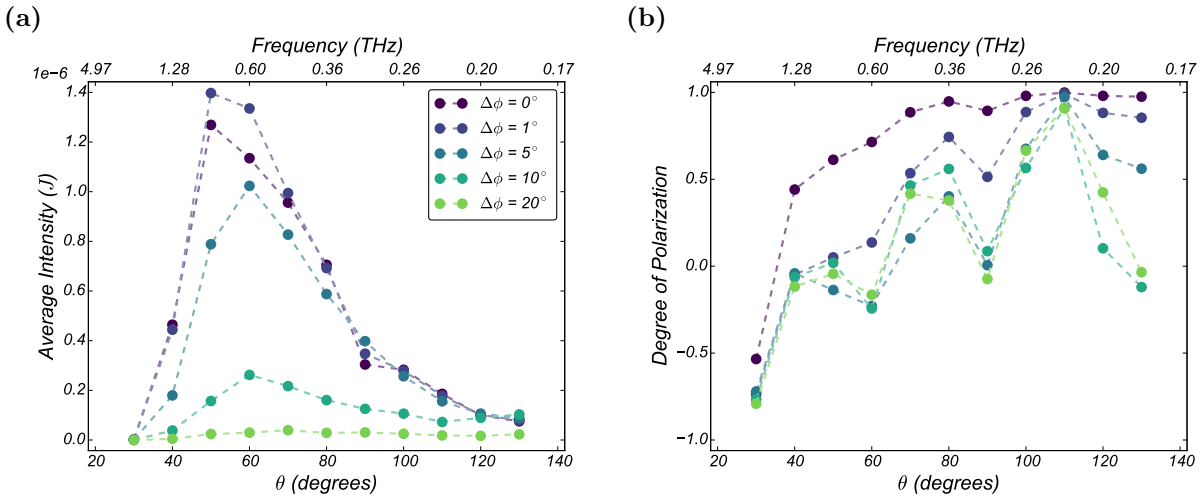

Figure 2.11: These figures show the calculated (a) intensity and (b) DoP of cSPr measured for varying ϕ location coordinates. The markers on each graph represent the location of detectors with respect to the θ axis. The values given for intensity are in units of J and each has been integrated over a detector aperture of ± 6 mm. All parameters in this simulation are equivalent to those used to generate Fig. 2.6.

section serves to highlight some of the features and new developments to this code, providing readers with an idea of its capabilities and limitations.

2.5 Summary

This chapter outlines the discovery and research surrounding the phenomena known as Smith-Purcell radiation. A selection of theoretical approaches are outlined, such as the evanescent wave description, the EFIE model and the surface current model (SCM). The advantages and disadvantages of each method are described, with particular attention paid to the surface current model. The extension of the surface current model, or similar models, to deal with large numbers of particles is described using the theory of coherent radiative emission. Coherent Smith-Purcell radiation (cSPr) is shown to be generated when the wavelength of the radiation generated by the Smith-Purcell mechanism is shorter than the length of the charged particle bunch. When the radiation is coherent it is possible to extract information about the longitudinal bunch profile by measuring the intensity of the radiation at a range of frequencies. This chapter also outlines the code used to simulate the generation of

cSPr throughout this thesis. The code is based on the SCM and requires a numerical library in order to solve for a grating of finite width and length. Recent improvements to the code allow for easy comparison of a wide variety parameters, including the testing of experimental robustness by varying detector position and acceptance. Examples of the results provided by the simulations are given to demonstrate the capability of the code.

Chapter 3

Overview of the Single-Shot Monitor Design

In this chapter the specific challenges of designing a single-shot, non-destructive cSPr monitor for longitudinal bunch diagnostics are introduced. The basic design of the pre-existing multi-shot cSPr device and the successful proof-of-principle experiments carried out with it are discussed, outlining the starting point upon which the new design is based. The success of the proof-of-principle, multi-shot system with fs resolution motivated the design of a new single-shot device capable of operating as a diagnostic. The proposed single-shot monitor must be able to reconstruct the longitudinal bunch profile on a bunch-to-bunch basis and also be able to meet the needs, such as high accuracy and resolution, of potential users in the accelerator community. A conceptual design for the single-shot monitor, which meets these requirements, is presented.

Focus is given to elements of the design which present particular challenges for a single-shot monitor and require further investigation prior to construction and installation. This includes discussion of the background radiation, including proposed methods to evaluate the background component and eliminate it from the measured signal. Other aspects of the design, including the size of the proposed diagnostic and effective distribution of detection channels are considered.

The conceptual design of the single-shot monitor provides the unifying context for the research presented in upcoming chapters.

3.1 The Multi-Shot Design

The single-shot cSPr monitor design is largely based on the multi-shot monitor successfully used in proof-of-principle experiments. This outline of the multi-shot device provides the context and background for the design of its single-shot successor.

The multi-shot proof-of-principle experiments were conducted over a number of years by the Oxford Smith-Purcell group and their collaborators. Initially installed at FELIX (Netherlands) in 2005 [60], the experiment was later moved to SLAC (USA) in 2007, first to End Station A and then later to FACET, where the experiment ran until 2014 [31, 32]. Whilst installed at the FACET facility, the device was known as the "E203" experiment. It was used to successfully demonstrate longitudinal bunch profile reconstruction from measurements of cSPr.

All the reconstructions carried out with the E203 experiment required multiple bunches (>100) to gather sufficient data. The beam parameters at FACET were: electron beam energy of 20.35 GeV, charge of 1.6 nC and bunch length < 0.5 ps [32]. A labelled photograph of the E203 set-up installed in the accelerator tunnel is shown in Fig. 3.1 and a cross-sectional schematic of the monitor is shown in Fig. 3.2.

The fundamental concept of the cSPr longitudinal bunch profile monitor is to reconstruct the longitudinal bunch profile through analysis of the frequency spectrum of cSPr. In order to measure the frequency spectrum, an array of detectors are positioned at varying θ positions around a periodic grating. The multi-shot schematic shown in Fig. 3.2 consists of 11 detectors spaced at 10° intervals around the interaction region. Due to the dispersion relation of Smith-Purcell radiation (Eq. 2.1), the array of detectors at different observation angles samples the frequency spectrum at 11 points per grating. The array of detectors, as well as their corresponding optics and metal holders, are collectively referred to as a detector arc. When

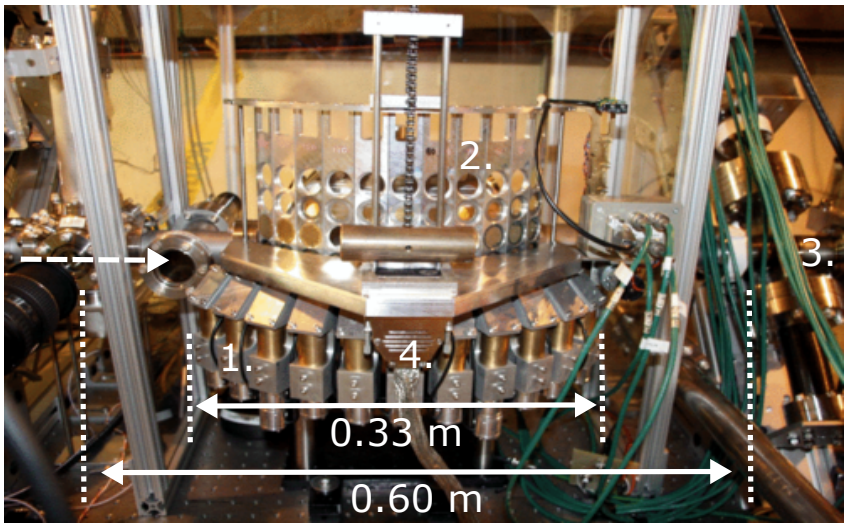

Figure 3.1: Photograph of the multi-shot cSPr monitor, installed in the beamline at FACET. The components are labelled as follows: 1. Detection Channels, 2. Filter Mechanism, 3. Beampipe, 4. DAQ Cable. The direction of travel of the electron beam is shown by an arrow. The insertion length of the monitor in the beam line (0.60 m) and the length of the detector array (0.33 m) are both marked.

developing the multi-shot experiment it was decided that three periodic gratings - with different periodicities - would be required to sufficiently sample the frequency spectrum for longitudinal profile reconstruction. The sampling must cover a broad frequency range and provide a reasonable resolution, enabling accurate interpolation and extrapolation over the whole frequency domain. The gratings are attached to a grating carousel which can be remotely rotated between measurements, allowing each grating to be placed alongside the beam in turn. The use of the grating carousel makes the monitor inherently multi-shot, as the measurements taken with each periodic grating involve different electron bunches.

In order to ensure coherent generation of Smith-Purcell radiation appropriate grating periodicities must be selected. As outlined in Section 2.2.1, when the condition $\lambda >> l_B$ is satisfied (where λ is the wavelength of the generated radiation and l_B is the length of the bunch) coherent emission occurs. The three grating periodicities used in E203 - 0.05 mm, 0.25 mm and 1.50 mm - cover an approximate frequency range of 0.1 to 20 THz (equivalent to 14 to 3000 µm). This range of periodicities is selected to induce cSPr when interacting with bunches of sub-pico-second length.

In addition to the three gratings, there is also a “blank” grating attached to the grating

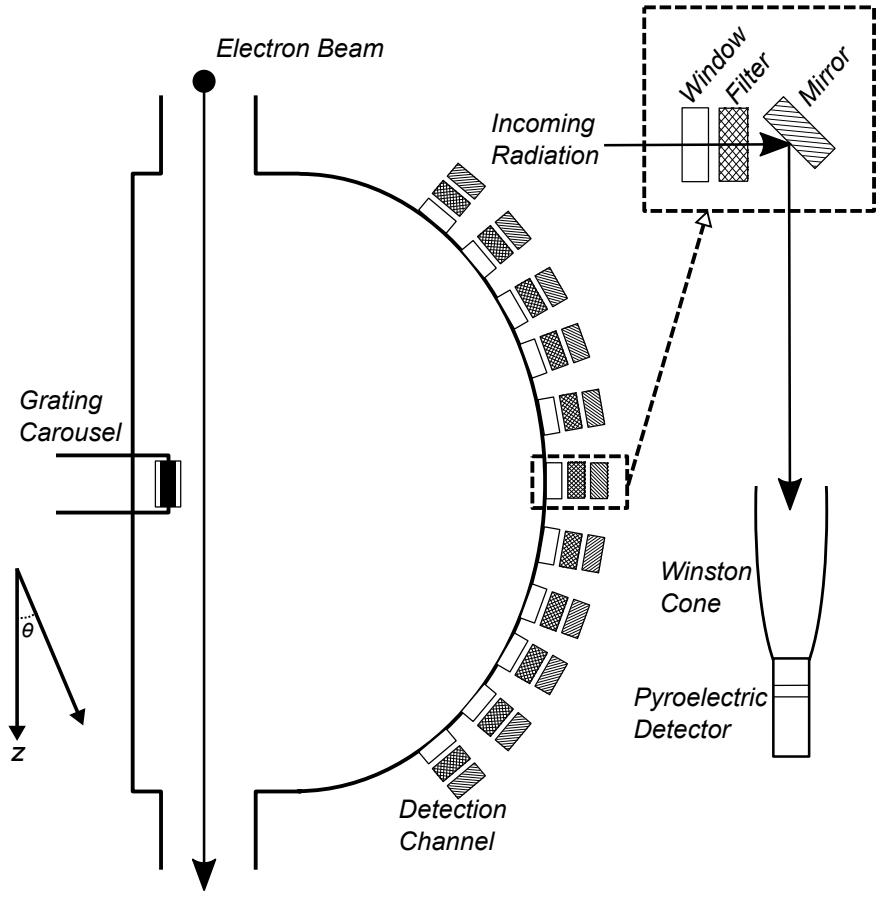

Figure 3.2: Cross-sectional schematic of the multi-shot cSPr monitor. There are 3 periodic gratings and a blank attached to the carousel. The monitor has 11 detection channels which are located at varying angles of θ - from 40° to 130° in 10° intervals - around the interaction region. The inset shows a typical detection channel in more detail. The z and θ axes are indicated on the diagram.

carousel. This is a smooth block of metal, with the same dimensions as the other gratings. The lack of a periodic surface structure ensures that the blank does not generate cSPr. The blank was used to take background measurements, required due to the high levels of noise in the high-energy environment at FACET. All the radiation measured by the detectors when the blank is in use is considered to be background radiation. This includes: diffraction radiation, noise caused by other equipment in the accelerator tunnel and reflected radiation inside the beampipe. As the device was inherently multi-shot, both the measurements with the periodic gratings and the blank had to be taken over several hundred bunches to improve statistics. Background subtraction was performed using the averaged measurements for each grating and the averaged measurements from the blank.

The optics used in the detection channels (shown in the inset of Fig. 3.2) are also crucial to the operation of the cSPr monitor. As the generated radiation is in the THz frequency range, the optics had to be selected appropriately. Working in this frequency region presents some difficulties, due to to the "THz gap", which refers the lack of sources, optics and detectors in the far infrared (THz) region. Although this frequency range is the subject of increased interest and development in recent years [65, 66], there are only a limited number of commercial optics and detectors. The lack of available THz sources presents difficulties for the calibration of optics and detectors.

The radiation is extracted from the vacuum chamber via 11 high resistivity crystalline silicon windows, which have high transmission in the THz frequency region [67]. The radiation also passes through a waveguide array plate (WAP) filter, designed to have a passband close to the expected frequency of the cSPr for that detection channel. This effectively removes the low frequency background radiation as well as suppressing high frequency background and any higher order modes of cSPr. This type of filter was developed by Ulrich [68] and the THz transmission properties were investigated by Winnewisser *et al.* [69, 70, 71]. The E203 monitor required an unique set of WAP filters for each of the gratings, as changing the period of grating changes the desired passband for each detection channel. The mechanism for changing the WAP filters remotely is labelled in Fig. 3.1. Subsequently, the filtered ra-

diation is incident on a plane mirror, which directs the radiation towards the detector. The mirror induces a 90° bend in the optical system, which provides space for the screening of the electronics from any x-rays radiation emanating from the beamline [61].

The extracted radiation is then directed to a custom-designed concentrator (Winston cone). The Winston cones increase the intensity of the radiation incident on the detector [61]. Pyroelectric detectors were used in the multi-shot monitor, these are broadband, thermal detectors which operate at room temperature. Further discussion of THz range detectors can be found in Section 4.2.2.

3.2 Challenges of Multi-shot to Single-Shot

With the success of the proof-of-principle experiments using a multi-shot cSPr monitor, the next step in the project is to design a device with single-shot capabilities. The key limitation of the E203 multi-shot monitor is the necessity of inserting the three gratings and the blank sequentially. The ideal longitudinal diagnostic would be able to extract all the information required for the profile reconstruction on a bunch-by-bunch basis. This would give users the ability to detect fine structure, instabilities and trends in the longitudinal profiles of their bunches. The shift to a single-shot cSPr monitor, however, presents a number of challenges. In this section, the two most challenging design tasks of the single-shot monitor are discussed.

3.2.1 The Use of Multiple Gratings

Accurate reconstructions of the longitudinal profile of a bunch require the measurement of the cSPr spectrum over a broad frequency range. Several gratings, with varying periodicity, provide access to a significantly larger range of frequencies than a single grating. If measurements with each grating must be taken from every bunch, then several fixed gratings and detection systems are required. The multi-shot experiment used three gratings, resulting in 33 measurements. It is proposed to incorporate three fixed gratings, with associated

detection systems, into the new single-shot design.

The difficulty with this concept is how to arrange the three gratings, and associated detection systems, with respect to each other whilst minimising the insertion length in the beamline. As shown in Fig. 3.1, the multi-shot monitor takes up approximately 0.60 m of beamline, of which 0.33 m is spanned by the detection arc (the other 0.27 m is beampipe connections). Three detection systems placed in series would require 1.00 m of beamline and an insertion length of around 1.30 m. Such a large diagnostic would be impractical in spatially limited accelerator facilities.

An alternative solution is provided by exploiting the strong directionality of cSPr in the azimuthal (ϕ) direction (see Figs 2.6 and 2.8). The gratings can be positioned at varying azimuthal positions around the electron beam and the narrow intensity distribution of cSPr means that the radiation associated with each grating is spatially separated. If the gratings and their individual detector arcs are rotated azimuthally around the electron beam, then the detector arcs can be overlapped longitudinally along the beam line reducing the total length of the monitor.

Fully overlapping the detector arcs would reduce the length of three detection systems to 0.33 m, however, in practice this is not possible. Using three gratings spaced at 120° around the electron beam as proposed, their physical dimensions would prevent them from being brought close enough to the beam for cSPr generation simultaneously. It is necessary to slightly offset each grating and associated detector arc longitudinally along the beam line, increasing the overall length of the system. When spacing the gratings it is necessary to consider the vacuum connections into the beampipe required for each element. Each grating and each detector arc will require separate vacuum ports, sufficiently separated for practical manufacturing. Taking these constraints into account and by minimising the length of the beampipe connections, a cSPr monitor with three periodic gratings spaced at 120° of length 0.64 m has been designed.

The azimuthal rotation model makes a considerable reduction in the insertion length in the beamline compared to the simple “in series” model.

3.2.2 Background Elimination

The E203 experiment observed significant background radiation when operating at FACET. This was attributed to the high-energy accelerator environment, 20.35 GeV electron energies. It is expected that background radiation will continue to be an issue for the single-shot monitor, although the levels will vary depending on the accelerator at which it is installed and its location on the beamline. In the multi-shot device a "blank" was used to sample the intensity of the background radiation, however, this method presents some difficulties when considering the single-shot design.

It is a requirement of the single-shot cSPr monitor design that the background radiation be measured on a bunch-by-bunch basis. To satisfy this requirement, whilst using a blank for background subtraction, requires a permanently installed blank with its own detector arc. As separate background radiation measurements are needed for each periodic grating, for a three grating monitor the use of blanks would double both the length and cost of the proposed system. Additionally, there is some doubt as to the reliability of measuring the background radiation present at one set of detectors using another set of detectors located in a different position along the beamline.

These considerations prompted the development of a new method for distinguishing between the cSPr signal and background radiation. The successful operation of a single-shot cSPr diagnostic depends on the ability to eliminate the background component of the measured signal on a bunch-by-bunch basis.

Previous research has suggested that cSPr is highly polarized [55] parallel to the grating grooves (DoP = 1) and that polarization can vary with frequency [32]. The simulations carried out using the GFW simulation code for cSPr predict a high degree of polarization orientated parallel to the grating grooves for a range of electron energies, bunch charges and grating profiles (see Section 2.4.1). Based on this information, it was proposed to use the distinctive polarization of cSPr to distinguish it from background radiation on a shot-by-shot basis.

To assess the linear polarization of the incoming signal, the signal must be split into two orthogonal components for measurement, for example, the components polarized parallel ($M_{\parallel}$) and perpendicular ($M_{\perp}$) to the grating grooves. The measured intensities contain both the cSPr signal (S_i) and the background radiation (B_i) polarized in each direction, as shown in Eq. 3.1.

$$M_{\parallel} = S_{\parallel} + B_{\parallel} \qquad M_{\perp} = S_{\perp} + B_{\perp} \tag{3.1}$$

The measured intensities can be separated into their constituent parts, given that the expected DoP of the cSPr signal (D_s) and the background radiation (D_b) are known.

$$D_s = \frac{S_{\parallel} - S_{\perp}}{S_{\parallel} + S_{\perp}} \qquad D_b = \frac{B_{\parallel} - B_{\perp}}{B_{\parallel} + B_{\perp}} \tag{3.2}$$

By rearranging the expressions in Eqs. 3.1 and 3.2, a value for the cSPr signal can be evaluated, as shown in Eq. 3.3.

$$S_{\parallel} = S_{\perp}\left(\frac{D_s + 1}{1 - D_s}\right) = \frac{M_{\parallel} - M_{\perp}\left(\frac{D_b+1}{1-D_b}\right)}{1 - \left(\frac{1-D_s}{1+D_s}\right)\left(\frac{D_b+1}{1-D_b}\right)} \tag{3.3}$$

This proposal requires the inclusion of a polarizer in each detection channel to select the incoming radiation along a predetermined orientation. Knowledge of the DoP of the background radiation would be provided by calibration measurements at the installation site of the monitor. Simulations, carried out with the GFW code, would calculate the expected value of the DoP of the cSPr signal.

Before this method for the elimination of background radiation can be used, it is necessary to investigate further the polarization properties of cSPr. To date, there are only a limited number of experimental studies investigating this feature of the radiation [55, 32]. Furthermore, the theoretical predictions of DoP made by the SCM, and calculated using the GFW code, have not been rigorously tested against experimental results.

3.3 Design of the Single-Shot Monitor

As viable solutions to the major challenges of designing a single-shot cSPr monitor have been identified, confirming the feasibility of such a device, it is possible to proceed with the conceptual design. This provides an overview of the features of the diagnostic, while some components are generalised to enable installation across a wide range of facilities. The conceptual design will be used to build a first prototype of the single-shot monitor. In Fig. 3.3, a cross-sectional schematic of the device, showing one grating and its corresponding detector arc, is shown. This can be compared to the multi-shot schematic shown in Fig. 3.2. Note the replacement of a grating carousel with a fixed grating and the changes made to the detection channels.

The changes to the layout of the detection channel are required to introduce a polarizer which will be used to separate the signal into two linear orientations. Splitting the signal into two constituent parts requires an additional detector (and associated concentrator). Depending on the type of detector used, this increases the cost per detection channel and could result in a more expensive monitor.

This schematic uses the general labels “concentrator” and “detector” instead of referring to specific components. The type of detector used depends on the beam parameters and the type of concentrator depends on the type of detector. In a high-energy (GeV) machine, with short bunches (fs) and high charge (nC), the Winston cone and pyroelectric detector are appropriate. At a facility with lower energy (MeV electrons), with longer bunches and lower charge, however, a more sensitive diode type detector might be required (see Section 4.2.2). The properties of the accelerator at which the monitor is installed will have a significant effect on its technical design and cost. The cross-sectional schematic (Fig. 3.3) shows that all other elements of the detection channel optics - the quartz windows, WAP filters and mirrors - remain unchanged from the multi-shot scheme.

The conceptual design for the single-shot cSPr monitor incorporates three gratings and detector arcs. The layout shown in Fig. 3.3 is used for each and they are orientated with

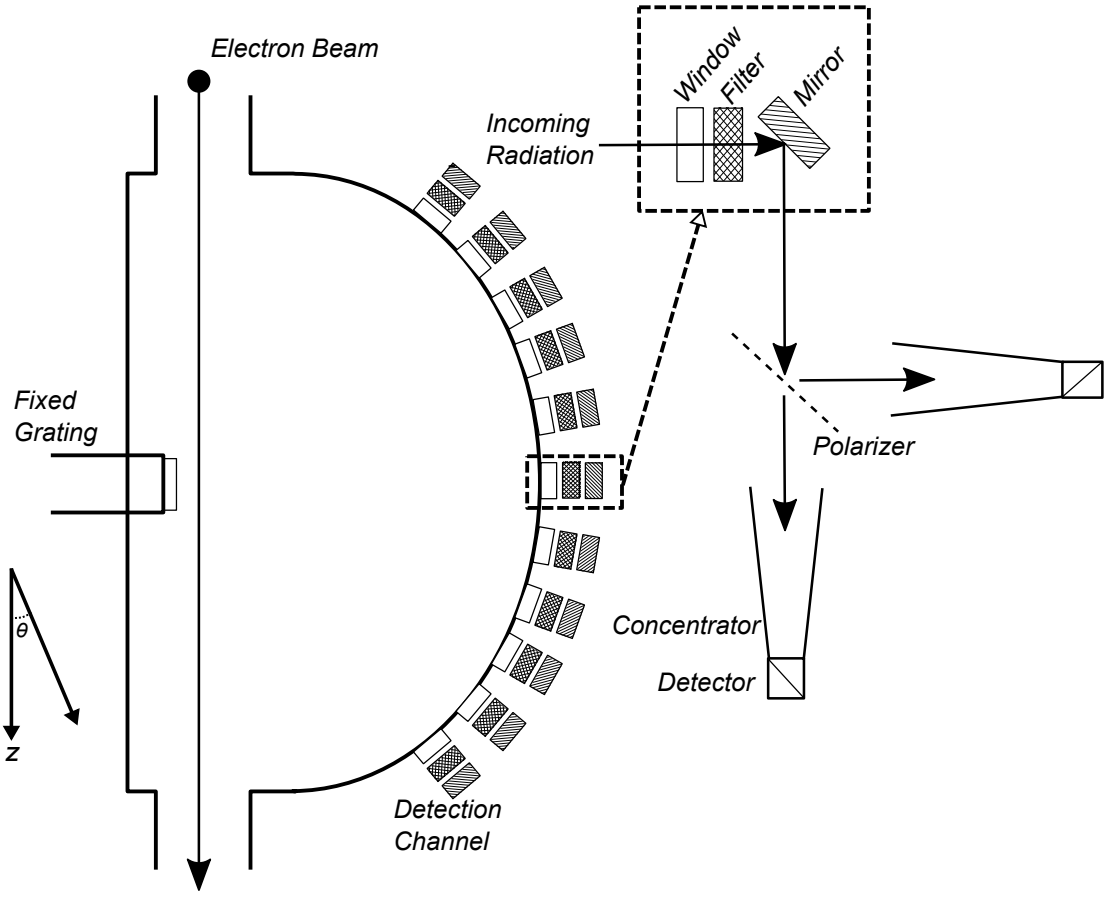

Figure 3.3: Cross-sectional schematic of the single-shot cSPr monitor. This schematic shows the layout of the monitor for one periodic grating and the corresponding detector arc. As in the multi-shot monitor (see Fig. 3.2), the detector arc consists of 11 detection channels located at varying angles of θ - from 40° to 130° in 10° intervals around the interaction region. The inset shows one detection channel in more detail. Note the polarizer used to split the incoming radiation, this creates a requirement for two detectors per channel. The z and θ axes are indicated on the diagram.

respect to each other using the azimuthal rotation model. In Fig. 3.4 two 3D models of the completed single-shot monitor design are shown.

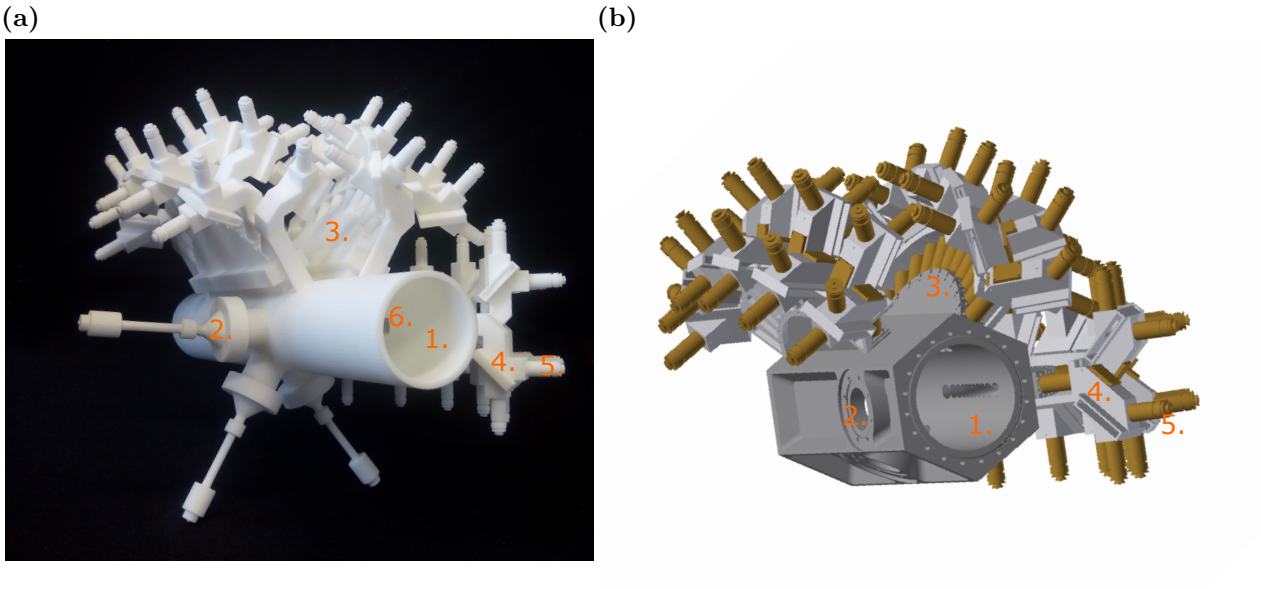

Figure 3.4: 3D models of the proposed single-shot cSPr monitor. The monitor is represented by (a) a photograph of a 3D printed model (scaled by a factor of 0.25 for printing)and (b) a 3D autocad model. The components in both are labelled as follows: 1. Beampipe, 2. Vacuum Port for Grating (in (b) a motor for adjusting the grating with respect to the beam is included), 3. Detector Arc, 4. Metal Holder for Detection Channel Optics, 5. Detectors, 6. Vacuum Port for cSPr Signal. The following differences between the two models should be noted: the inclusion in (a) of the motion control systems for the periodic gratings (see label 2. in the figure above), providing an idea of the space required by the monitor, and the altered shape in (b) of the beampipe and metal holders for the detection channels, which takes into account the practicalities of machining these metal components.

The overall design consists of the central beampipe and vacuum chamber, 3 periodic gratings (with motion stages), 3 detector arcs, 33 detection channels and 66 concentrators and detectors. In order to arrange the large number of components efficiently over the short length (0.64 m) of the design, certain adjustments were required. It is necessary to alternate the direction of the 90° bend along the detector arc, this allows for two detectors per detection channel but makes any required shielding of the electronics more difficult. It is also necessary to make the monitor easy to manufacture; the shapes of the beampipe and the metal holders in Fig. 3.4(b) were optimized for easy machining. In Fig. 3.4, Winston cones and pyroelectric detectors are shown as placeholder components, but could be easily substituted on the condition that the new components were of a similar size or smaller.

3.4 Design Aspects Covered in this Thesis

The remaining chapters of this thesis are concerned with the investigation of various elements of the conceptual design of the single-shot cSPr monitor for longitudinal profile reconstruction. The aim is to investigate the feasibility of certain aspects of the conceptual design and, where possible, suggest options for improvement.

3.4.1 Using Polarization to Eliminate Background Radiation

The most urgent aspect of the conceptual design of the single-shot cSPr monitor that requires investigation is the proposed scheme to use the inherent polarization of cSPr to separate the signal from the background radiation. This method of background elimination, although theoretically robust, in practice it requires a good working knowledge of the polarization of both the cSPr and the background radiation.

In the case of the background radiation it has been proposed to calibrate the system using "blanks" (as previously used in the multi-shot scheme), in order to measure the polarization of the background radiation. It is assumed that this remains relatively constant over the period of the measurement. This would need to be done at each accelerator at which a monitor was installed and would have to be repeated if the beam parameters were altered.

Knowledge of the polarization of cSPr is a more difficult issue to address. Although previous studies show that cSPr is generally highly polarized [55, 32], there have not been any rigorous studies over a range of cSPr parameters nor have the measured values been successfully compared to simulations. In order to make predictions about the polarization of cSPr, it is necessary to have evidence that the simulations used agree with experimental measurements.

Chapters 4, 5 and 6 cover an investigation into the polarization of cSPr for a selection of THz frequencies and periodic gratings at the LUCX accelerator facility.

3.4.2 Distribution of Detection Channels

Once the frequency spectrum has been measured it is necessary to extract the desired information about the longitudinal bunch profile. The process of reconstructing the profile from a measured frequency spectrum is complex and is an active area of research in its own right [72, 73]. The accuracy of the profile reconstruction depends on many features of the monitor, including the number and distribution of detection channels, as well as the properties of the bunch. The relationship between the accuracy of the longitudinal profile measurement and these parameters is complex and currently is poorly understood.

For the design of the single-shot cSPr monitor, 33 detection channels were chosen simply because this had been shown to be sufficient during the E203 experiments. The distribution of the detectors was based on simplicity in design; the array of 11 detector channels are placed at 10° intervals along the detector arc, providing ample channel separation for manufacturing. It is reasonable to assume that the number and distribution of the channels could be optimised for profile reconstruction at individual accelerator facilities, providing improved performance and reduced cost.

In Chapters 7 and 8, the relationship created by the reconstruction process between the monitor design, the bunch properties and the accuracy of the reconstructed profile will be investigated. Chapter 7 provides an introduction to the research associated with the reconstruction process, giving the reader an understanding of the difficulties and complexities involved in obtaining a profile with confidence. In Chapter 8 the premise, methodology and results of an optimization study aimed at improving the design of the single-shot monitor are presented.

3.5 Summary

This chapter covers the design considerations of the single-shot cSPr monitor intended for use as a longitudinal beam profile diagnostic.

The work focusses on the changes required to move from a successful multi-shot, proof-of-principle experiment to a single-shot diagnostic. Issues including the incorporation of multiple fixed gratings, the handling of high levels of background radiation and the optimal distribution of detection channels are discussed. The concept of using the polarization of cSPr to separate it from background radiation is introduced and the impact of this solution on the design demonstrated. The conceptual design is presented as a schematic and also in a variety of 3D models.

The links between the conceptual design presented in this chapter and the research carried out in subsequent chapters are stated. An overview of the rest of the thesis is given from the perspective of the single-shot monitor design.

Chapter 4

The LUCX Accelerator

To investigate the polarization of cSPr required an accelerator facility which fulfilled the following criteria:

1. Available vacuum chamber in which gratings could be installed for the generation cSPr
2. Provision to extract the cSPr from the chamber for detection (in the accelerator tunnel)
3. Sufficient laboratory space to develop a multi-component detection system
4. Supporting equipment available to monitor bunch (for example, charge measurements)
5. Beam availability for the development of methodology
6. Stable electron bunches with appropriate parameters (required sub-ps bunch lengths)

The LUCX facility (KEK, Japan) was identified as satisfying all the criteria for these experiments. In addition, there were ongoing research activities involving the generation of Smith-Purcell and transition radiation in the THz frequency range, by other research groups, prior to the commencement of this study [74]. This meant that existing experimental apparatus could be used during the study, including: a Michelson interferometer, motion stages to control the detector position and a manipulator in the beamline to which gratings could be attached. Additionally, support and expertise in using the LUCX facility, in particular

concerning the generation and detection of THz radiation, was provided throughout the experiments.

This chapter gives an overview of the LUCX accelerator and the experimental apparatus for the generation and detection of cSPr. The capabilities and limitations of the experimental apparatus at LUCX are detailed, justifying the use of certain devices, such as the detector used to measure the cSPr signal. Baseline studies, conducted to calibrate the detector and confirm the presence of cSPr, are presented. Preliminary polarization measurements are analysed and compared to predictions made using the simulations. Key problems in the methodology used for the preliminary measurements are identified and potential solutions discussed.

4.1 Overview of the Accelerator

The LUCX accelerator is an 8 MeV linear electron accelerator, it is one of several facilities located at the KEK research park in Tsukuba, Japan. A variety of experiments have been carried out at this facility including research into Compton scattering [75] and THz generation experiments [76]. Other experiments involving the generation of THz radiation have investigated the interaction of the electron beam with a variety of structures, including, periodic metal gratings [77] and dielectric capillaries [78]. Within these studies the mechanisms for diffraction, transition and Smith-Purcell radiation at THz and sub-THz frequencies have been investigated [77, 79]. In one case, the generated Smith-Purcell radiation was used to measure the separation of micro-bunches [80], demonstrating the diagnostic capabilities of this type of radiative process.

The LUCX accelerator occupies a tunnel which measures approximately 15 m in length, however, for THz generation experiments only the first few metres of the facility are used, as shown in Fig. 4.1.

The LUCX accelerator generates short (≈ 100 fs) electron bunches, which are generated as single bunches or as a series of microbunches (maximum of four) depending on the user

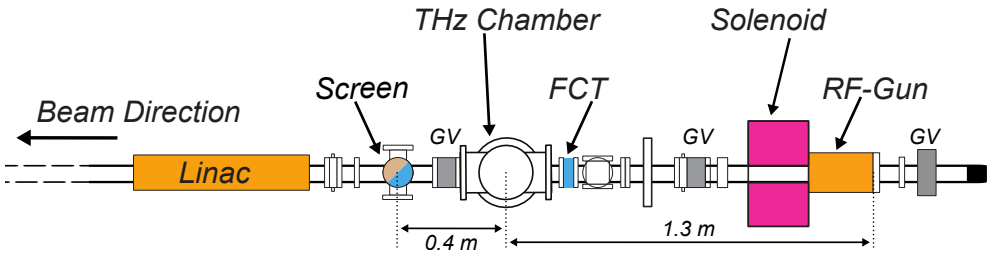

Figure 4.1: The layout of the first section of the LUCX accelerator including the THz chamber. Key aspects of the accelerator - which are discussed in the text - are labelled. Beam direction is from right to left and is indicated by an arrow. The grey rectangles, labelled GV, indicate gate valves which can be used to isolate different sections of the beamline.

requirements. The cSPr experiments described in this thesis are all carried out using the single bunch mode. The basic properties of the LUCX linear accelerator and the beam parameters at the THz chamber are given in Table 4.1.

Parameter	**Expected values**
Beam energy, typical	8 MeV
Charge per bunch, typical	50 pC
Bunch length	0.15 to 10 ps
Repetition rate, max	$12.5\,\mathrm{s}^{-1}$
Normalized emittance ($\epsilon_x \times \epsilon_y$)	$4.7 \times 6.5\pi$ mm mrad

Table 4.1: LUCX, Beam Parameters

4.1.1 Bunch Generation and Propagation

The electron bunches are generated by illuminating a CsTi photocathode with a ultrashort (fs) pulse from a TiSa laser [79]. An optical system, developed to split and shape this pulse, can produce electron trains of up to four microbunches. During the experiments investigating the polarization of cSPr, one bunch with a charge of approximately 50 pC was produced for every pulse of the laser. The length of the bunches was determined by the duration of the laser pulse; a typical bunch length is around 300 fs.

After emission at the photocathode, the electrons are accelerated to 8 MeV by a 3.6 cell S-band RF gun [81, 79]. Subsequently, as shown in Fig. 4.1, the bunches pass through a focusing solenoid; the strength of the solenoid is adjusted to minimise the emittance of the

bunch as it travels downstream. Structures, such as periodic metal gratings, are placed in the THz chamber where they interact with the electron bunches. When the accelerator is used for Compton scattering, the bunches do not have any interaction in the THz chamber but are accelerated to higher energies by a Linac (see Fig. 4.1); the layout of the accelerator beyond the THz chamber is not relevant to the polarization study. More information about the LUCX accelerator development and operation can be found in literature [75, 81, 79].

4.1.2 Charge Measurements

During experiments at an accelerator, the charge of the bunches is one of the most important parameters. Monitoring the charge is necessary to understand the operation and stability of the machine. Measuring the charge can also provide useful information about the coherent generation of cSPr. The experiments, carried out at LUCX, are expected to generate Smith-Purcell radiation in the coherent regime (using $\lambda >> l_B$ as defined in Section 2.2.1). In this regime, the intensity of cSPr has a quadratic dependence on the charge of the bunch. Comparing measurements of the charge and the intensity of cSPr can be used to test this dependence, providing evidence of coherence and the experimental stability. Furthermore, if there is significant bunch to bunch charge variation, it may be appropriate to normalise the cSPr signal with respect to the square of the charge.

At LUCX the charge is monitored using the fast current transformer (FCT), located between the focussing solenoid and the THz chamber (see Fig. 4.1). An FCT is a non-destructive charge monitor, used in a wide variety of accelerators. Non-destructive charge monitors detect the beam without intercepting it; this type of instrument is sensitive to the electromagnetic fields caused by the motion of the charged particles. It consists of a primary winding, which interacts with the magnetic field generated as a bunch passes through it, and a secondary winding, in which a current is induced [82]. These type of charge monitors are very popular as their design parameters - including the number of primary and secondary windings, the core material and the cross sectional area - can be adjusted to optimise performance for different accelerators.

4.1.3 γ Detection

Experiments which generate cSPr require information about the relative positions of the grating and the beam. The intensity of cSPr is highly dependent on the distance between the beam and the grating, reducing exponentially as they are separated. Conversely, when a fraction of the beam intersects the grating, the signal intensity is reduced - as any electrons which collide with the grating (or the grating holder) are lost. At the LUCX facility, the intersection of the beam and the metal structures in the THz chamber can be monitored, using a downstream photon monitor to measure the γ rays produced by this interaction.

The monitor, an Aerogel Cherenkov detector, is a custom design which uses an aluminium plate to convert the energetic γ rays into electron-positron pairs. The pairs radiate Cherenkov radiation as they travel through an aerogel. An aerogel is microporous solid with a very low density, its unique refractive index making it ideal for the generation of Cherenkov radiation [83]. The radiation is then extracted using a photomultiplier tube which converts the detected photons to a measurable voltage. Similar custom detectors are found in literature [84].

4.1.4 Imaging the Transverse beam

To fully understand the operation of the LUCX accelerator, it is important to consider the transverse dimensions of the beam and their variation during an experiment. The transverse beam size is crucial, when determining appropriate relative positions of the beam and the grating, for optimal cSPr production. Monitoring the transverse beam dimensions also provides information about the accelerator operation, for example, a substantial increase in the transverse dimensions could be due to space-charge forces and may indicate a significant loss of beam.

At the LUCX facility, the transverse dimensions of the beam, typically $300\,\mu m \times 300\,\mu m$, are observed using a scintillating screen. This is located in the beam pipe downstream from the THz chamber, as shown in Fig. 4.1. Scintillating screens are commonly used for transverse beam profile measurements in low energy electron accelerators, to measure the

transverse profile of the beam. When the accelerated electrons cross through the screen they deposit some of their energy, which is converted into visible light. The light emitted from the screen is detected by conventional optical detectors, providing a direct image of the two-dimensional transverse beam profile [85]. As the electrons pass through the scintillating screen they lose a significant fraction of their energy, therefore, this method of transverse beam profile measurement is destructive. At LUCX, this is mitigated by locating the screen downstream from the THz chamber, where the interactions of interest occur. This method provides not only the transverse dimensions of each bunch, but is also used as a beam position monitor as it can provide visual evidence of the intersection between the beam and the grating. It was frequently used during experiments as a guide when adjusting the grating position relative to the beam.

4.2 THz experiments at LUCX

As well as the features of the LUCX accelerator and the available diagnostics, it is also necessary to discuss the pre-existing experimental apparatus for the generation and detection of THz radiation. In particular, the capabilities of each piece of apparatus is discussed in relation to the generation of cSPr.

4.2.1 The THz Chamber

The THz chamber, at LUCX, is located directly after the FCT and is approximately 0.4 mm upstream from the scintillating screen (see Fig. 4.1). This chamber is specifically designed for experiments which use the electron beam to generate THz radiation. The dimensions of the chamber are approximately 200 mm × 200 mm × 200 mm and it has an incorporated motion stage with a holder for a metal plate. Plates which fit the holder are manufactured for specific experiments and have the targets, such as the periodic gratings for the generation of cSPr, attached. The motion stage has four degrees of freedom, which allows movement of the target with respect to the beam. The motion stage is manipulated remotely, allowing

for extensive repositioning during an experimental run. The generated radiation is extracted from the beamline via a window, outside of which an optical bench is provided to install apparatus for THz detection. In Fig. 4.2, the THz chamber is shown with a metal plate installed. The plate shown in the photograph has several gratings attached, which can be used for generating cSPr.

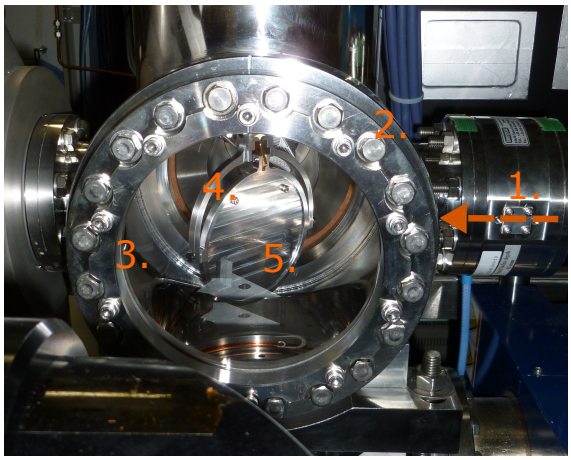

Figure 4.2: A metal plate with several periodic gratings attached is shown after its installation in the THz chamber. Key features of the are labelled as follows: 1. Electron Beam Trajectory, 2. THz Chamber Flange, 3. Sapphire Vacuum Window, 4. Holder (attached to motion stage), 5. Metal Plate.

Two windows were used throughout the series of experiments at LUCX. A quartz window and a sapphire window, both considered to be transparent at THz frequencies. The quartz window is slightly smaller (radius = 75 mm) and was replaced by the sapphire window (radius = 100 mm) during the experimental work discussed in Chapters 5 and 6. The larger window was considered superior, as it allowed the extraction of radiation from the chamber at a wider variety of angles. Both windows are approximately 10 mm thick and are wedged ($\approx 1^{\circ}$) to avoid etalon effects (which produce a frequency dependent pathlength).

Quartz (SiO_2), in its crystalline form, is popular as a window material for the extraction of THz radiation. It has a low absorption (and high transmission) for frequencies below 3 THz. Typical quartz optical elements are cut perpendicular to the crystal axis, referred to as a z-cut, as this eliminates any polarization dependence for radiation at normal incidence to the window [86].

Sapphire (Al_2O_3) is less transparent than quartz in the THz, however, its absorption is considered to be low for frequencies up to 2 THz. This is significantly higher than the maximum frequency (0.5 THz) used in the cSPr experiments carried out at LUCX. Like quartz, z-cut sapphire has no polarization dependence for radiation at normal incidence [86]. In the photograph, Fig. 4.2, the THz chamber is shown with the sapphire window installed.

It should be noted that, it has not been possible for our collaborators at LUCX to confirm that either of the windows used have been manufactured in z-cut form. At the time of window installation this parameter was not considered to be important. As it is standard preparation of this type of optical element, it is reasonable to assume that they are both z-cut and that they have no polarization dependence for radiation at normal incidence to the window.

4.2.2 THz Detectors

To measure the generated cSPr signal at the LUCX facility an appropriate detector is required. There are two key considerations, the sensitivity of the detector and its operational frequency range. Pyroelectric detectors use temperature sensitive crystals to detect incoming radiation in the infra-red and far infra-red frequency regions. They are an attractive choice due to their broadband detection range [86] but have relatively low sensitivity. They are "integrating" detectors, this means that the voltage detected is due to the cumulative effect of the radiation. In a cSPr experiment the cumulative effect is considered per bunch and the detector requires a "cool down" between bunches.

Previous experiments, involving cSPr in the THz region, have had success using pyroelectric detection systems [31, 32]. In this case, as the charge and energy of the electron bunches at LUCX is relatively low, the intensity of cSPr produced is below the sensitivity threshold for pyroelectric detectors.

Schottky Barrier Diodes (SBDs) were proposed as alternative to pyroelectric detectors for this study. Their high sensitivity to the incoming electric field makes them ideal for

the detection of low intensity radiation. They are well established as detectors in the sub-THz and THz frequency ranges, however, unlike pyroelectric detectors, they have limited operational frequency ranges.

SBDs produce an output signal which depends on the instantaneous incident power of the incoming radiation ($|\vec{E}|^2$), as opposed to the integral signal from a pyroelectric detector. The output signal is generated by the diode, typically made of GaAs or InGaAS; when an oscillating field (within a specified frequency range) is incident on the diode a DC voltage is produced. The devices have a non-linear I-V curve, it is usually required to apply a bias (constant voltage) to the diode to reach the optimum operation point on this curve. Recently zero-bias SBDs have become commercially available, these have an optimum operating point at the origin of their I-V curve (V = 0 V). Zero-bias SBDs can be operated without the application of a bias, this results in lower noise levels than typical SBDs.

SBDs have a frequency dependent response and are usually only used to detect radiation in a narrow frequency range. While they have sensitivity over a broad frequency range (on the order of 100 GHz to 3 THz [86]), their performance fluctuates and typically decreases as the frequency of the incident radiation increases. Commercial devices have limited operational ranges over which an approximately flat frequency response can be expected. The radiation accepted by an SBD is restricted to the operational range by a waveguide or other filtering component. Typical frequency ranges of commercially available SBDs are 10s to 100s of GHz [10]. SBDs have a strong polarization dependence as the diode only detects radiation with the electric field orientated in the same direction as the receiving antenna. For low intensity radiation it is often necessary to include an optical system - which could include components such as a horn antenna or lens - to increase the radiation incident on the diode.

The detector used in the studies described in this thesis was the Virginia Diodes Inc. model WR2.2ZBD. It is a zero bias SBD detector, with a stated operational range from 0.325 to 0.500 THz [87]. The detector was housed with a waveguide and horn antenna structure, with a lower cut-off frequency of 0.268 THz [88]. The aperture of this horn has dimensions of 3.5 mm × 3.5 mm (diagonal of 5.0 mm). All radiation incident on the aperture

of the horn is assumed to be detected equally. A photo of the detector is shown in Fig. 4.3, it is referred to as "the SBD detector" for the rest of this thesis.

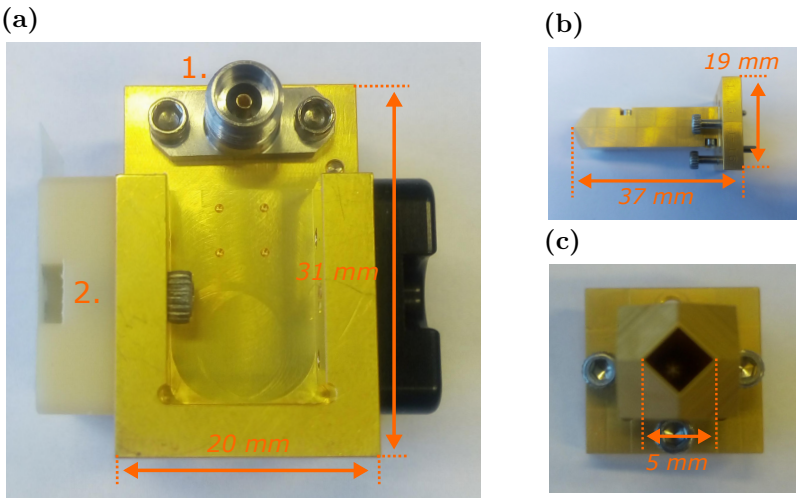

Figure 4.3: Photographs of the SBD detector (VDI model WR2.2ZBD) and its horn antenna. In (a) the SBD detector is shown with key features labelled: 1. the port from which the signal is extracted as a voltage and 2. the location of the RF port (covered by a white dust cover). The dimensions of the detector (height and width) are labelled, the depth (not shown) is 20 mm. The horn antenna is shown from (b) the side and (c) the front with key dimensions labelled. The antenna is affixed to the main detector (placed over the RF port) during experiment.

A series of calibration studies of this and other similar THz range SBDs, carried out as part of an investigation into the coherent synchrotron radiation (CSR) produced by micro-bunches, was published in 2016 [10]. The results of the study show that it is advantageous to characterise each detector individually, as significant variation in sensitivity across the operational frequency is observed. As only one detector is used throughout this study and intensity comparisons between different frequencies of cSPr are not required, the lack of an in-depth calibration study is not critical.

In the preliminary cSPr polarization investigation, the inherent polarization sensitivity of the SBD detector is used to resolve the observable THz signal into two linear polarizations. The diode is aligned with detector casing, accepting radiation polarized parallel to the grating grooves in a horizontal alignment and radiation perpendicular to the grating grooves when rotated 90° to a vertical alignment (see Fig 2.4 for definitions of parallel and perpendicular orientation definitions).

4.2.3 cSPr Generation

To generate cSPr, periodic gratings are placed alongside the beam path as shown in Fig 2.1. The wavelength of Smith-Purcell radiation is approximately equal to the grating periodicity, as defined by the dispersion relation (see Eq. 2.1). The wavelength must be much larger than the length of the bunch, to meet the criteria for coherent generation. At LUCX, with typical bunch durations of 300 fs (or lengths of 100 µm), this condition is easily satisfied for grating periodicities of 0.5 mm and above.

A set of gratings, manufactured specifically for this experiment, were attached to a metal plate and placed inside the THz chamber before it was sealed and evacuated. The motion stage to which the metal plate was attached and then manoeuvred remotely is discussed in Section 4.2.1. During this experiment, the metal plate had three gratings and a blank attached to it; the blank was used for measuring background radiation or generating transition radiation. The three gratings used are as follows:

(i) 1.00 mm period sawtooth grating
(ii) 0.70 mm period sawtooth grating
(iii) 0.70 mm period strip grating

Schematics showing one facet of a sawtooth and a strip grating respectively are given in Figs. 4.4 (a) and (b). In addition to the periodicity of each grating several other parameters must be considered, such as the blaze angle of the sawtooth gratings and the depth of the non-extruding section of the strip grating.

A photo of the metal plate, with the gratings attached, before it was placed in the beamline is shown in Fig. 4.5. All the gratings had the same macro dimensions, 20 mm × 65 mm (width × length), their length is made up of 60 mm of periodic surface and 2.5 mm of blank (smooth surface) at either end. The gratings are positioned with their long axis placed parallel to the electron beam when generating cSPr (see Fig. 4.5(b)). The blank has the same dimensions as the gratings (20 mm × 65 mm), but has a flat surface with no protrusions.

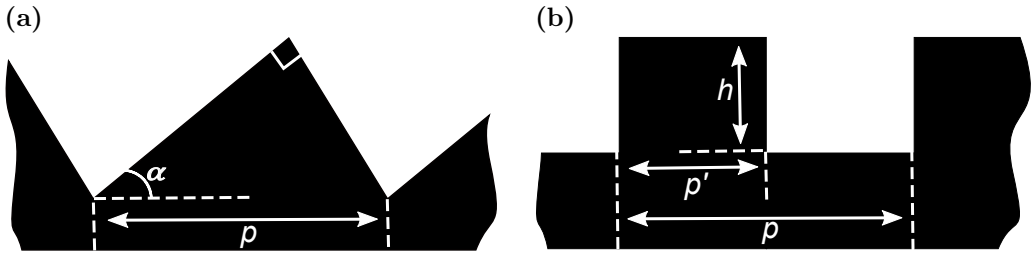

Figure 4.4: Grating profiles showing one facet of (a) sawtooth and (b) strip gratings. The experiments described in this thesis used two sawtooth gratings with periodicity (p) of 0.70 mm and 1.00 mm, both with a blaze angle (α) equal to 30°. The strip grating used had a periodicity (p) of 0.70 mm, an equal ratio between the extruding and non-extruding section ($p' = \frac{p}{2}$) and a facet depth (h) of 0.25 mm.

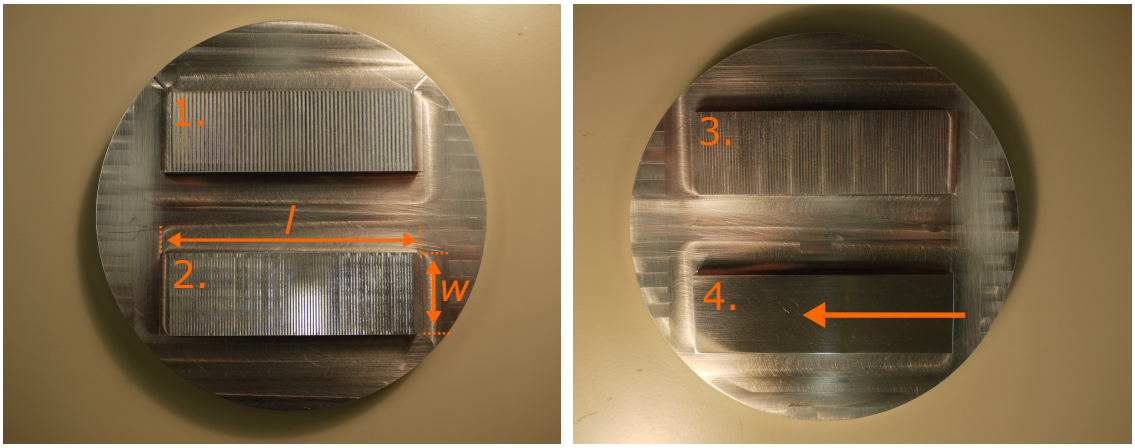

Figure 4.5: Photos of the gratings on the metal plate (both sides), before it was placed in the THz chamber. The gratings are labelled as follows: 1. 0.7 mm period sawtooth 2. 1 mm period sawtooth 3. 0.7 mm period strip 4. Blank (smooth surface). The dimensions, w=20 mm and l=65 mm, are the same for all four gratings. In experiments, the beam traverses the grating as marked by the arrow.

4.2.4 Michelson Interferometry Scheme

An interferometer was required to measure the frequency of the radiation extracted from the beamline, during the study. As the cSPr dispersion relation (see Eq. 2.1) is distinctive and is well confirmed, the detection of radiation in the expected frequency range at a specified observation angle can be used to confirm its presence. This is essential when working in an unfamiliar accelerator environment, where a large number of variables affect the generation and detection of cSPr. Initially, a Michelson interferometer (Mi) was used to measure the frequency of the signal at the LUCX facility.

The Mi, originally developed by Michelson [89], became a well known optics device following its use in the Michelson-Morley experiment (1887) demonstrating that the speed of light is a constant [90]. The Mi uses a beamsplitter to split the incoming radiation along two arms and then to recombine the two components. Measuring the output intensity of the Mi, whilst varying the length of one of the arms (see Fig. 4.6), provides an interferogram of the radiation. A Fourier transform, of the interferogram, gives a frequency spectrum of the radiation [91, 86].

A schematic of the Mi used at LUCX is given in Fig. 4.6 and a photo of it installed on the optical bench in the accelerator tunnel is shown in Fig. 4.7. This Mi has a close to zero path difference, hence, it is able to measure a broad range of frequencies. To take an interferogram one of the plane mirrors (M_1 in Fig. 4.6) is moved incrementally and the output signal is measured at each position. The size of the increments and the total change in path length while measuring the interferogram determines the measured frequency range and frequency resolution. The Mi used is appropriate for measuring frequencies up to 1.5 THz and has a resolution of 0.01 THz. The scheme in Fig. 4.6 comprises of an n-doped silicon wafer (BS), two plane mirrors (M_1 and M_2) and three parabolic mirrors. The first two parabolic mirrors (PM_1 and PM_2) are used to collimate the radiation and the last (PM_3) focuses the radiation onto the detector.

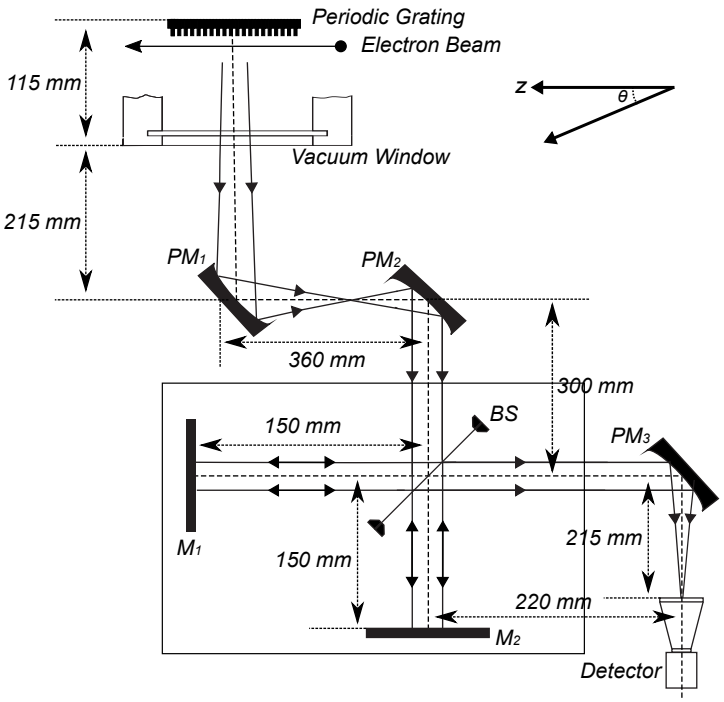

Figure 4.6: Diagram showing the layout of the Mi used at LUCX. The abbreviation PM refers to the parabolic mirrors, M to the plane mirrors and BS to the beamplitter. The component M_1 is used to vary the path difference, it is mounted on a motorized stage controlled by the accelerator control system. The definition of θ the observation angle is shown with relation to z the direction of beam propagation.

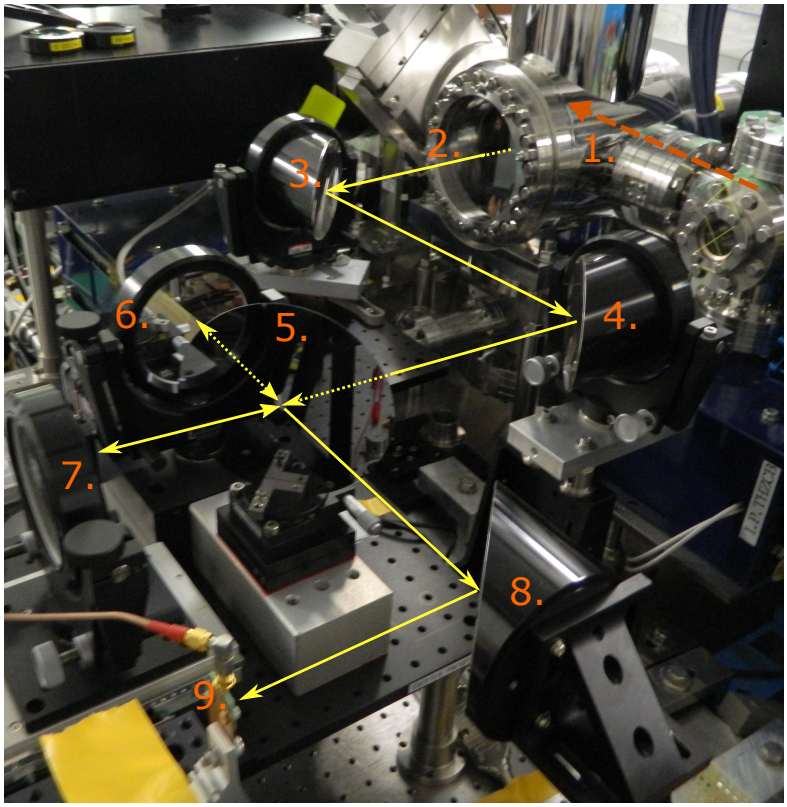

Figure 4.7: The Mi installed on the optical bench at the LUCX facility. The labels refer to the following components: 1. Electron Beam Trajectory, 2. Vacuum Window, 3. PM_1, 4. PM_2, 5. BS, 6. M_1, 7. M_2, 8. PM_3 and 9. SBD detector. PM refers to the parabolic mirror and BS to the beamsplitter. The component M_1 is used to vary the path difference, it is mounted on a motorized stage controlled by the accelerator control system. The yellow arrows indicate the optical path traversed by the radiation from the THz chamber, dashes are used when the path is behind a component in the photograph.

4.2.5 Moving Detector Scheme

An additional experimental setup, referred to as the moving detector scheme, was used to measure the THz signal directly from the window, without the use of any additional optics. For the wavelengths of radiation generated in this experiment, a distance of 230 mm from the grating placed the detector in the far-field zone, in which the grating can be considered as a point source. A schematic of this experimental layout is shown in Fig. 4.8.

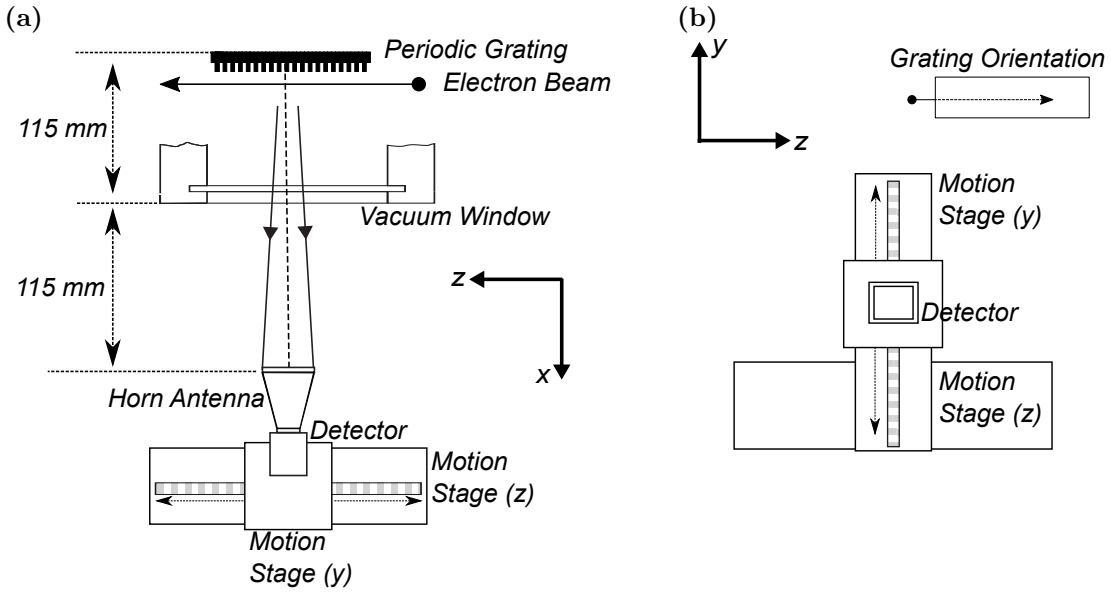

Figure 4.8: Schematic of the moving detector scheme from two different orientations. In (a) the experimental arrangement is shown from above and the motion of the detector along the z-axis is shown. In (b) the scheme is shown as seen from the grating, demonstrating the motion of the detector along the y-axis. In both schematics the axis directions are labelled.

The SBD detector was placed on a motorized stage, which was located approximately 0.23 m from the grating (along the x-axis). This stage has two degrees of freedom (along the y and z axes), so that the intensity of the radiation could be measured as the position of the detector was varied. The motorized stage was positioned so that the detector was at an observation angle of θ =90° and aligned so that the aperture was perpendicular to the incoming radiation. The motion of the stage along the y and z axes allowed small variations from the 90° observation angle, up to ± 5°. The alignment of the detector remains the same as it is moved, so its orientation varies with respect to the grating position.

This moving detector scheme was used to measure the intensity of the signal from the

THz chamber, over a range of y and z positions. This type of measurement is referred to as a spotsize scan in the upcoming discussion. Spotsize scans were used for the preliminary polarization studies, one was taken for each orientation of the SBD detector. The scans measured with the two orientations of the detector were then compared in order to estimate the DoP.

4.3 Preliminary Simulations

Simulations predicting the expected intensity and DoP of cSPr, using the LUCX accelerator parameters as outlined in Table 4.1, were carried out to assess the feasibility of these experiments. The simulations were carried out using the GFW code, which is described in Chapter 2 (Section 2.4.1). The expected intensity and DoP, for a range of observation angles (variations along both the θ and ϕ axes), are shown in Fig. 4.9 (a) and (b) respectively. The simulations were carried out for the 1 mm period sawtooth grating.

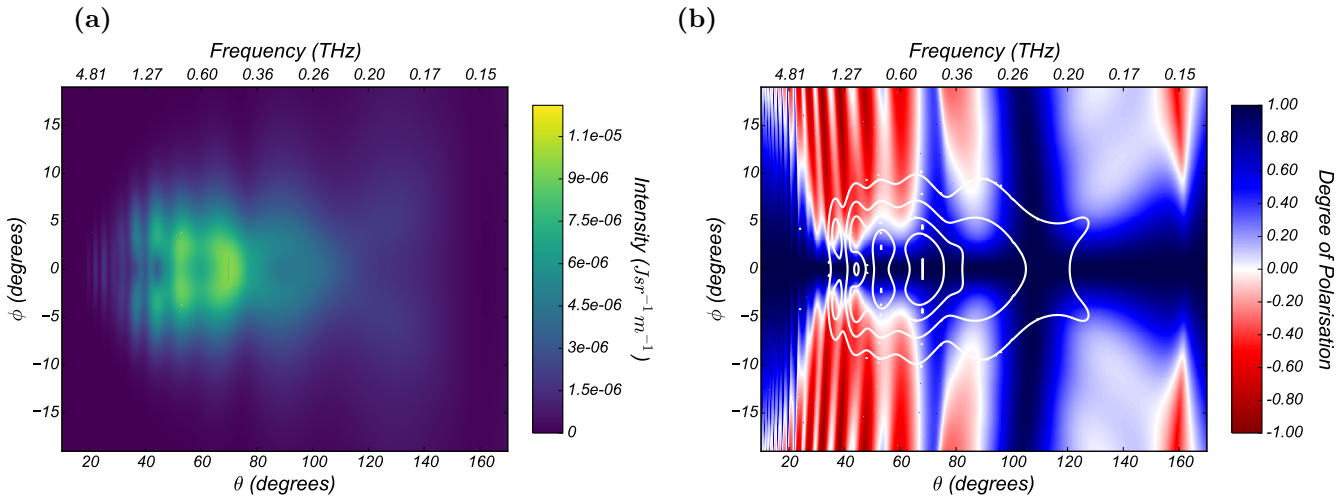

Figure 4.9: These figures show the (a) intensity and (b) DoP over a range of θ and ϕ values. In (a) the intensity is given in $\mathrm{J\,sr^{-1}\,m^{-1}}$, in (b) the DoP is given in a range from -1 to 1 where 1 indicates linearly polarized radiation with the electric field perpendicular to the grating grooves. The contours plotted on (b) indicate the distribution of the radiation, they show the radiation intensity levels from the lowest to highest value in 15% intervals.

In Fig. 4.10, the intensity and DoP of the cSPr is calculated for a range of detector positions. The radiation reaching the detector is determined by the aperture of the detector

and the distance between the grating and the detector. In this simulation the aperture of the SBD detector and the moving detector scheme distance (0.23 m) are used. Each value of the intensity, given in Fig. 4.10(a), has been integrated over the aperture of the detector. The DoP values, shown in Fig. 4.10(b), are a weighted average over the detector aperture (see Eq. 2.26), accounting for the variation in the intensity of the radiation as well as the polarization of the radiation. During the preliminary experiments the detector will be positioned at $\theta = 90°$ and $\phi = 0°$.

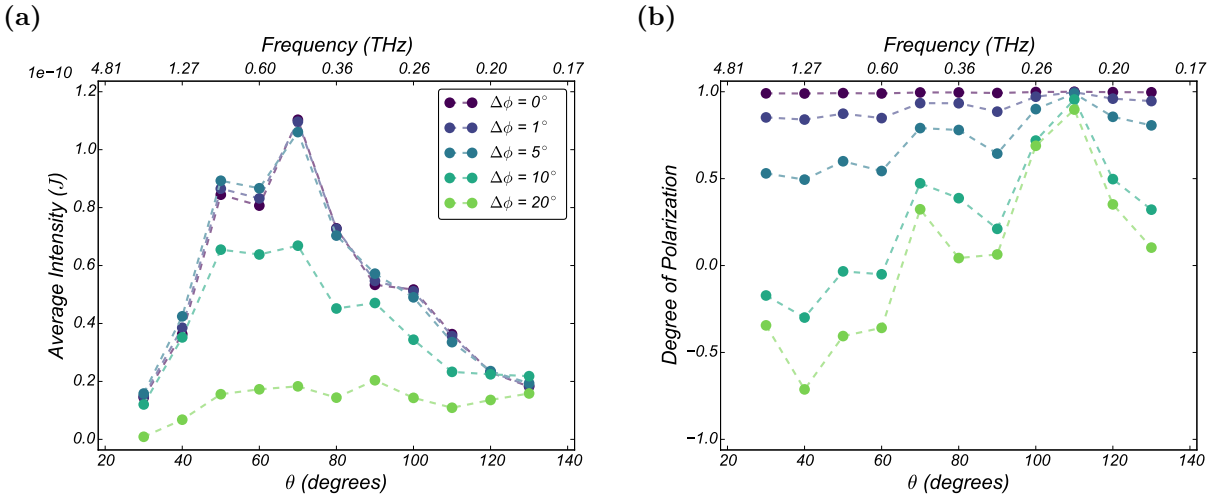

Figure 4.10: Simulations giving calculated (a) intensity and (b) DoP for cSPr generated using a 1.0 mm period sawtooth grating. The values for both are given at a variety of observation angles along the θ axis and are calculated for a variety of displacements along the y-axis. At a displacement of 0 mm the detector is aligned with the grating. The ϕ coordinate of the observation angle for each detector position is $\phi = 0°$.

The variation of the detector position along the y and z axes d, at a distance D from the grating, shifts the observation angle OA (along θ and ϕ respectively) as shown in Eq. 4.1.

$$OA_{\theta/\phi} = \arctan\left(\frac{d_{z/y}}{D}\right) \tag{4.1}$$

A displacement along the y-axis, $d_y = 5$ mm gives an angular shift of approximately 1°, when the detector is located, $D = 0.23$ m, from the grating. In Figs. 4.10 (a) and (b), the intensity and DoP are given for a range of displacements (from $\phi = 0$) along the ϕ axis. In principle, by taking measurements at different positions along the y-axis, the predicted

dependence of the DoP on the ϕ coordinate of the observation angle can be observed. Similarly, the relationship between the DoP and the θ coordinate can be explored by taking measurements at different positions along the z-axis. It should be noted, however, that as the detector is moved the alignment between the SBD detector and the grating is changed and the intensity of the radiation is expected to drop of rapidly. The effect of this loss of alignment is not accounted for in the simulations.

The predicted values, at a range of detector locations, demonstrate that the intensity of cSPr is not sensitive to small shifts in ϕ. The DoP, on the other hand, is predicted to have a dramatic change for small shifts in ϕ at the observation angle, $\theta = 90°$, used in the preliminary experiments. This demonstrates the need for good alignment of the detector with respect to the grating. The predicted sensitivity to alignment should be considered when rotating the detector during polarization measurements.

4.4 Initial Investigations

The following section discusses the preliminary set of results, from experiments at the LUCX facility. cSPr was generated using the 1 mm period sawtooth grating and the emitted radiation was measured using both the Mi scheme and the moving detector scheme. The data was taken over the course of two experimental runs in June and November 2016.

Before investigating the polarization, it is necessary to demonstrate the generation of cSPr and show agreement with the Smith-Purcell dispersion equation (see Eq. 2.1). This step verifies the experimental setup for the production of cSPr at the LUCX facility and provides information about the normal operation of the accelerator. In the following section, the results of several measurements taken to verify the presence of cSPr are presented. Once successful generation has been confirmed, preliminary measurements of the DoP of cSPr are carried out.

4.4.1 Detecting cSPr

The 1 mm period sawtooth grating was placed in the THz chamber and positioned next to the electron beam path to generate cSPr. The distance between the grating and the beam was varied, to maximize the production of cSPr. As cSPr is known to exhibit an exponential decrease in intensity as the beam-grating separation increased (see Eq. 2.13), observation of this phenomena confirms expected behaviour. Monitoring the γ signal, as the grating position is varied, indicates the presence of bremsstrahlung radiation, caused by the collision of the beam with the grating.

The intensity of the detected THz signal and the intensity of the γ signal were monitored over a range of grating positions along the x-axis. The optimal position of the grating along the x-axis will have a high THz (maximising cSPr generation) and low γ signal intensity (avoiding collision between the beam and the grating). The results of this measurement are shown in Fig. 4.11.

Figure 4.11 is used to assess the best position of the grating along the x-axis for cSPr production; in this case the peak in THz signal intensity occurs before significant γ signal is seen (corresponding to an x position of 7.5 mm). The γ signal rises dramatically as the grating intersects the main body of the beam, the low rise before the peak is caused by the grating interacting with the beam halo (not considered problematic at a low energy facility). The THz signal rises steeply as the grating approaches the beam, this is expected due to the exponential dependence of cSPr on the beam-grating separation. The THz signal drops sharply after the target crosses the beam, as in this region the electrons are absorbed by the metal and do not generate cSPr.

Beam-grating separation scans were performed periodically over the course of the experiments. This ensured that any shifts in beam position, which are expected over a period of several days, were monitored and the grating position adjusted to compensate.

In the moving detector scheme, the detector is moved in both the x and y directions to get an initial estimate of the spotsize of the THz signal and to identify the position with

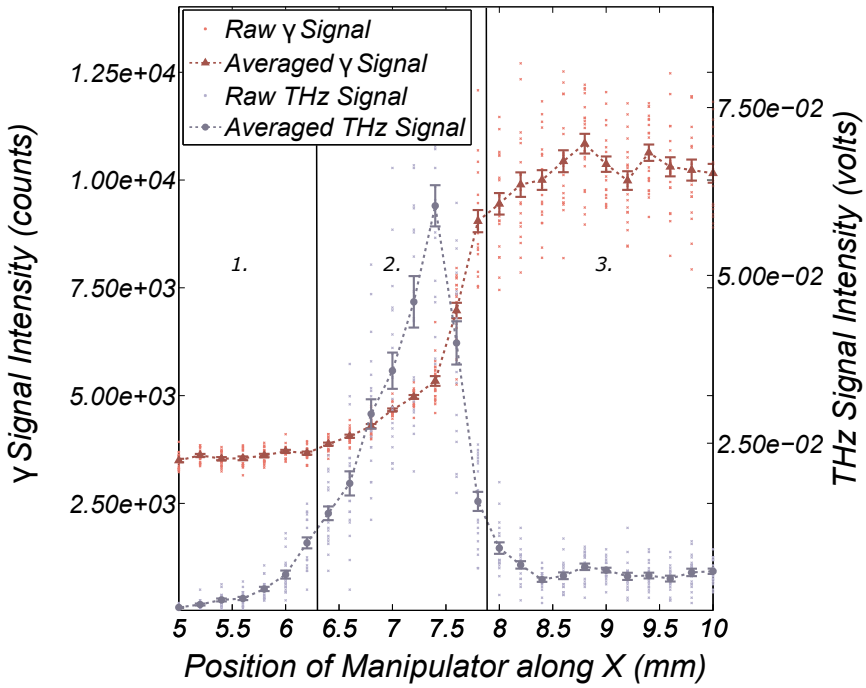

Figure 4.11: The THz signal and the γ signal are plotted for a scan of grating position along the x-axis, which varies the distance between the grating and the beam. Optimal cSPr production occurs at the peak of the THz signal intensity, which indicates that the beam is in close proximately to the beam. Positions with high levels of γ signal intensity must be avoided, as this indicates collision of the beam and the grating. The plot is split into three sections, which indicate regions of different interaction between the grating and the beam, by solid black lines. In (1) there is no interaction between the beam and the grating, in (2) the beam is close enough to the grating for cSPr generation and in (3) the beam is completely intersected by the grating.

the highest intensity radiation. A y scan is shown in Fig. 4.12, which shows the variation in intensity during a 130 mm scan along the y-axis.

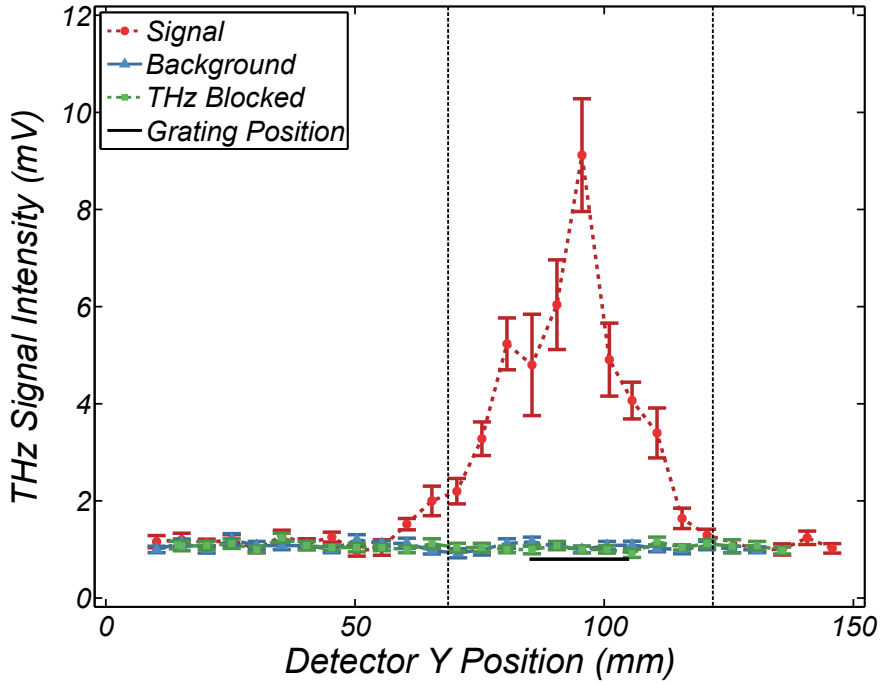

Figure 4.12: The intensity of the THz signal detected as the position of the SBD detector is varied along the y-axis. The intensity of the THz signal at each position is compared to the intensity measured with the blank in place of the periodic grating (background radiation) and the intensity measured with eccosorb between the window and the detector (THz blocked). The dashed lines are placed 28 mm either side of the peak intensity measured, this corresponds to the range $\phi = 0° \pm 7°$, the range of ϕ within which almost all of the cSPr is expected to be found.

The broadening of the intensity distribution, with relation to the grating position, represents a spread of intensity along the ϕ axis. In Fig. 4.9, almost all the radiation is shown to be found within the range $\phi = 0° \pm 7°$. Using Eq. 4.1, this suggests that all the measured radiation should be found within 28 mm of the peak intensity. The dashed lines, in Fig. 4.12, show this region and demonstrate that the expected ϕ distribution is observed.

The measurement was repeated with the blank, in place of the grating, to measure the background radiation (also shown in Fig. 4.12). Potential sources of background radiation include: THz radiation generated by other accelerator components and diffraction radiation

caused by the interaction of the beam with the edges of the grating.

It is clear, from examination of Fig. 4.12, that other THz generation mechanisms produce a negligible signal compared to the cSPr signal. A third measurement was carried out, again using the 1 mm period sawtooth grating, with eccosorb (a THz absorber) placed between the detector and the vacuum chamber window. The eccosorb measurement excludes any THz signal from the THz chamber, isolating any radiation, in the frequency range of the detector, due to other components present in the tunnel. This measurement shows there is no significant THz signal, generated elsewhere in the accelerator tunnel, reaching the detector.

The results, shown in Fig. 4.12, demonstrate that the LUCX accelerator is a low noise environment for experiments in the THz frequency range. This makes it an ideal environment for detailed analysis of low intensity THz generation mechanisms, including investigation into the polarization properties of cSPr.

The measurements discussed confirm that the THz signal is caused by the proximity of the periodic grating to the electron beam. To prove that the measured signal is cSPr, it is necessary to check the agreement with the Smith-Purcell dispersion relation (see Eq. 2.1) and demonstrate that the measured signal is coherent.

It is predicted by the Smith-Purcell dispersion relation (Eq. 2.1) that for p =1 mm and $\beta \approx 0.98$, the frequency of cSPr emitted at θ=90° is 0.298 THz. The frequency spectrum was measured using the Mi (described in Section 4.2.4) and is shown in Fig. 4.13(a). The peak frequency is (0.300 ± 0.014) THz, the error on this value is determined by the resolution of the frequency spectrum.

A frequency spectrum of coherent transition radiation (CTR) - produced by intersecting the beam with the face of the blank - was also taken using the Mi. CTR is used in the experiments at LUCX because it generates a broad spectrum, this is used to characterise the behaviour of the SBD detector. In particular, as shown in Fig. 4.13(b), the CTR frequency spectrum is used to define the frequency range of the SBD detector. The detector is shown to be operational within the range 0.300 to 0.500 THz, as stated by Virginia Diodes [87].

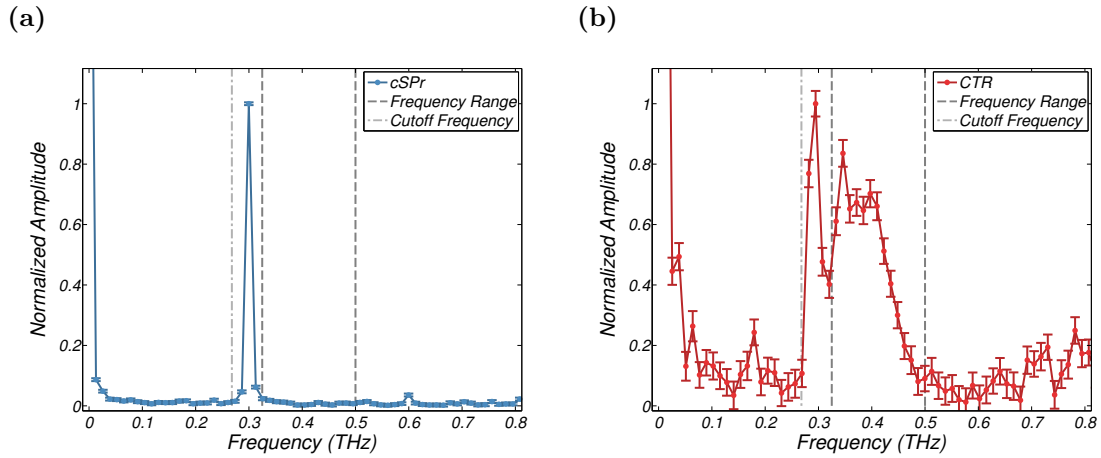

Figure 4.13: Frequency spectra of (a) cSPr and (b) CTR calculated from interferograms taken with the Mi scheme at the LUCX facility. The cSPr is generated using the 1 mm period sawtooth grating and the CTR is produced by interaction of the face of the blank with the beam. The accelerator parameters during both these interferograms are as stated in Table 4.1. The stated range of the SBD detector (0.300 to 0.500 THz) and the cut-off frequency of its waveguide (0.268 THz) are marked on both plots.

However, significant variation in sensitivity is seen over this frequency range. Detection is also observed between the lower frequency cut-off of the waveguide (0.268 THz [88]) and the lower end of its stated range (0.300 THz).

To show that the Smith-Purcell radiation measured is generated in the coherent regime, a quadratic dependence between the measured THz signal and the bunch charge must be demonstrated. At LUCX, it is possible to vary the charge of the bunches by varying the intensity of the laser pulse that reached the cathode. In Fig. 4.14 a typical charge scan is shown.

A fit of the form $y = ax^b + c$ was carried out using the data from the charge interval 0.025 to 0.065 nC; the three coefficients have the values of $a = (2.19 \pm 0.56) \times 10^4$, $b = 2.05 \pm 0.10$ and $c = -3.40 \pm 1.30$. For coherent radiation the relationship is expected to be quadratic and the value of b to be close to 2. The value of b from the fit agrees with a quadratic relationship, between the signal and the charge, within the given uncertainty. Very high and low charge values are excluded, as in these regions the THz signal falls outside of the dynamic range of the detection system. This results in detector saturation for high charge

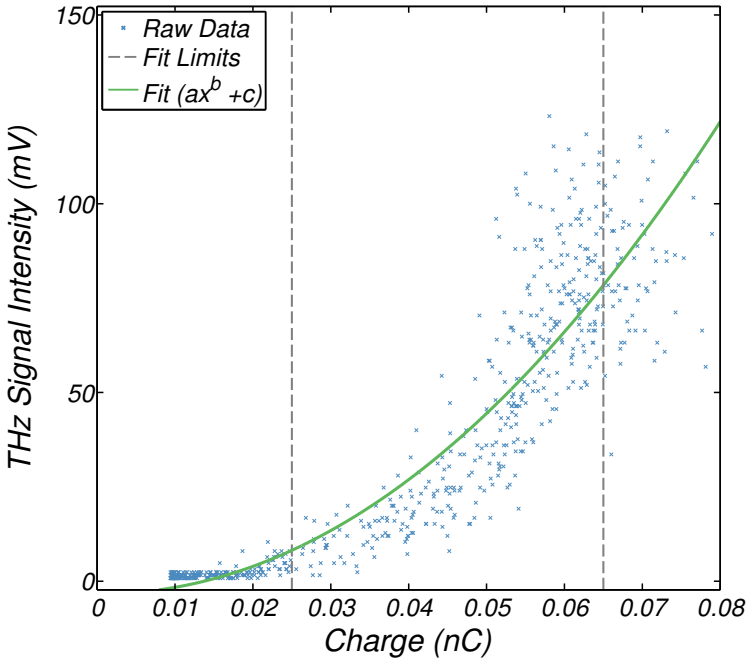

Figure 4.14: Charge dependence of the THz signal generated by interaction of the electron beam with the 1 mm period sawtooth grating at the LUCX facility. A fit of the form $y = ax^b + c$, using the data from the charge range 0.025 to 0.065 nC, is plotted alongside the raw data. The coefficients of this fit are a $= (2.19 \pm 0.56) \times 10^4$, b $= 2.05 \pm 0.10$ and c $= -3.40 \pm 1.30$.

values and a lack of sensitivity for low charge values.

The charge fit does not account for the changes to beam size and position caused by changing the bunch charge, this may cause deviation from the expected quadratic relationship. Significant variation in the THz signal is seen around the fit line, particularly in the high charge region. The variation is likely to be a symptom of significant bunch to bunch variation, with parameters such as position, shape and charge changing on a shot-by-shot basis. It is variation such as this which is driving the development of longitudinal diagnostics - such as the single-shot, cSPr monitor.

The combination of the results given in Fig. 4.11, Fig. 4.12, Fig. 4.13(a) and Fig. 4.14 sufficiently demonstrates that this experimental scheme is generating and measuring cSPr. The observed radiation has a strong dependence on the distance between the periodic grating and the electron beam (Fig. 4.11). Furthermore, the radiation measured is shown to be generated by a periodic grating, not generated by the blank and is blocked by a THz absorber (Fig. 4.12). Additionally, measurements with the Mi show that the observed frequency agrees with the dispersion relation of Smith-Purcell radiation (Fig. 4.13(a)). Charge scans (Fig. 4.14) indicate that the THz signal has a quadratic dependence on the charge, which provides evidence of coherence. The following experiments proceed based on this assessment of the successful generation of cSPr at the LUCX facility. The measurements discussed in this section were carried out regularly, providing continuous evidence for the presence of cSPr.

4.4.2 Preliminary Polarization Measurements

After confirming the presence of cSPr, investigations into the properties of the observed cSPr signal can begin. Using the moving detector scheme, spotsize scans were carried out around the observation angle $\theta = 90°$, $\phi = 0$. For this measurement the 1.0 mm period, sawtooth grating was used. In order to analyse the linear polarization, the spotsize scans were carried out for both orientations of the SBD detector. The polarization sensitivity of the detector enabled the isolation of the radiation polarized parallel to and perpendicular to the grating

grooves, in horizontal and vertical orientations respectively.

Each spotsize scan is composed of several z-scans. The detector is at a fixed location along the y-axis, and the position is varied along the z-axis. Ten measurements are taken at each position, from which the mean and standard error are calculated. After completing the z-scan, the position of the detector along the y-axis is changed and the measurement repeated.

In order to mitigate the variation seen in the charge measurement (Fig. 4.14), it was proposed to normalize each signal measurement with respect to the charge squared prior to calculating the mean. In the coherent regime this removes the dependence of the results on the charge, and eliminates an systematic error introduced by the charge variation. Analysis of the correlation between the THz signal and charge over several spotsize scans indicated that charge normalization is not appropriate for cSPr experiments at LUCX, hence, it is not used for the results presented in this section or in subsequent chapters. Discussion of this investigation into the dependence between the signal and the charge can be found in Appendix A.

The data is combined in colour plots which give the mean and standard error of the THz signal measured in every position; in Fig. 4.15 spotsize scans for both polarizations (parallel and perpendicular to the grating grooves) are given.

Figures 4.15(a) and (c) show the spotsize scans taken with the SBD detector in the horizontal and vertical orientations (isolating the parallel and perpendicular polarizations) respectively. These scans have been scaled, so that the highest intensity value (over the two scans) is equal to one. This allows for easy comparison between the intensity values at the same position for the two orientations.

In Figs 4.15(b) and (d), the standard errors on the intensity values at each position are given for the horizontal and vertical orientations respectively. The standard error values have been scaled in line with the intensity values in Figs 4.15(a) and (c). The errors are generally proportionate to the value of intensity measured, with an average percentage error

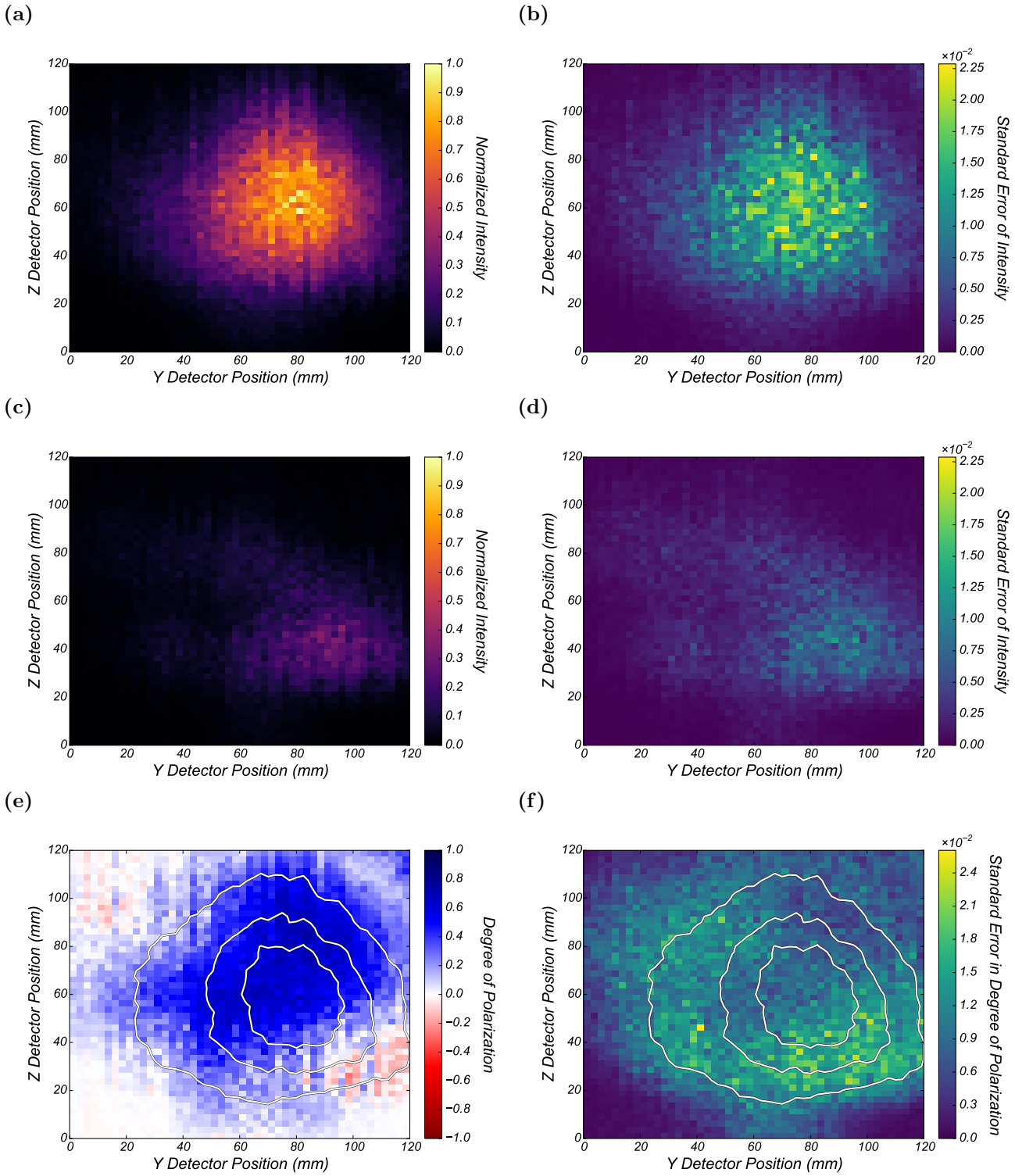

Figure 4.15: The measured THz signal is given for both orientations of the SBD detector, corresponding to the radiation polarized (a) parallel and (c) perpendicular to the grating grooves. The THz signal intensity is scaled so that the highest value measured over both spotsize scans is equal to 1. The associated standard error is given in (b) and (d) respectively, these have been scaled so that they correspond to the values given in (a) and (c). The two spotsize scans have been compared to give the (e) DoP and (f) the associated standard error. A contour of the intensity distribution from (a) is overlaid on the distributions in (e) and (f) to aid visual interpretation, they indicate the intensity levels from the lowest to highest value in 25% intervals.

on the intensity measurements of 2%.

The maximum intensity measured in the spotsize scan of the radiation parallel to the grating grooves (Fig. 4.15(a)), is approximately three times higher than the maximum intensity measured in the scan of the perpendicular polarization (Fig. 4.15(c)). This demonstrates a high level of linear polarization, with the majority of radiation polarized parallel to the grating grooves, as predicted by the GFW simulations.

The spotsize scan of the radiation polarized parallel to the grating grooves (Fig. 4.15(a)), shows an intensity distribution over a roughly circular area with a radius of 25 mm. At a distance of 0.230 m from the grating, this corresponds to a variation in observation angle of $\approx \pm 5°$. The GFW simulations, shown in Fig. 4.9 predict a spread in the intensity along the ϕ axis of around $\pm 8°$ and covering a wide range of θ (from 20° to 110°). This suggests that the measurements are limited by the loss of alignment between the detector and the grating, rather than by reaching the edge of the cSPr distribution.

The spotsize scan of the radiation polarized perpendicular to the grating grooves (Fig. 4.15(c)), however, is considerably different in shape and the maximum of intensity appears to be shifted slightly in comparison. This could be caused by the quartz (a material which exhibits birefringence in some orientations) window which the radiation travels through to exit the THz chamber. When radiation travels through a birefringent material the two polarizations have different paths and experience a different refraction index. This can result in the two orientations being shifted, in time (introducing a phase lag) or in direction of travel (shifting the resulting intensity distribution), relative to each other. As previously mentioned in Section 4.2.1, the quartz window is assumed to be z-cut (cut along an axis which prevents the effects of the birefringence), however, this is not confirmed.

The shift in the position of maximum intensity could also be caused by the uncertainty in the detector position. There is an uncertainty in the relative position, on the order of ± 5 mm, after changing the orientation.

The final possibility is that the effect could be due to the variation in polarization ex-

pected for different observation angles (see Fig. 4.10). This seems unlikely, however, as all changes are expected to be symmetric around the ϕ axis.

The spotsize scans of the radiation polarized parallel and perpendicular to the grating grooves (Figs. 4.15(a) and (c)), are analysed to calculate the DoP of cSPr generated. Using Eq. 2.22 and assuming that the two polarizations of the radiation have been completely isolated in this measurement, the DoP can be calculated for the measured radiation. The spotsize scans are compared on a point by point basis and it is assumed that there is no shift in detector position between them. The calculated DoP and associated standard error are shown in Figs. 4.15(e) and (f) respectively. A contour showing the position of the cSPr intensity distribution from the spotsize scan of the parallel polarization (Fig. 4.15(a)) is overlaid on this plot to aid visual interpretation. Most positions have a DoP value close to one, showing cSPr which strongly polarized parallel to the grating grooves. The DoP at the position of the highest intensity of measured cSPr is 0.8 ± 0.1.

There is agreement with the predictions made with GFW (Fig. 4.10), insofar that the cSPr is expected to be hightly polarized parallel to the grating grooves. Potential for disagreement arises in the extent to which this polarization was observed. In the ideal case - with perfect alignment between the detector and the grating, an SBD which behaves as expected and an output window with no birefringence effects - the DoP measured at this position is expected to be 0.95. Disagreement between the experimental results and the predictions from simulation could be due to systematic error.

It is important for the design of the single-shot cSPr monitor that accurate predictions of the DoP can be made; these preliminary measurements show general agreement with the simulation predictions. Given the limited number of experiments which have focussed on the polarization properties of cSPr, making accurate measurements and developing the expertise is crucial to developing understanding in this field.

4.4.3 Improving the Polarization Measurements

Given the success of the preliminary measurements, it is proposed to refine the methodology in order to expand the scope of the polarization study. Before looking at ways to modify the experimental setup, it is important to identify its problematic features. In particular, there are several issues with the preliminary polarization investigation which need to be addressed.

The first is the assumption, first outlined in Section 4.2.2, that the SBD detector is able to isolate the two polarizations of the cSPr. This is based on knowledge of the SBD detector, a diode with a linearly polarized response to incoming radiation. The diode was assumed to be aligned with the detector casing, so that the vertical and horizontal orientations of the SBD detector allow independent measurements of the radiation polarized parallel and perpendicular to the grating grooves. Although this assumption about the SBD detector is reasonable, there is no information from the manufacturer about either its polarization dependence or the alignment of the diode with respect to the detector casing.

Secondly, it was assumed that the manual realignment of the SBD detector, after changing its orientation, is sufficient to ensure a constant position for all the measurements. Although a lot of care was taken with the realignment, the available precision (on the order of $\pm 5\,\mathrm{mm}$) during the experiment was a limiting factor. The shift in intensity distribution seen between the two spotsize scans (Fig. 4.15(a) and (Fig. 4.15(c)) could be, at least in part, due to poor detector alignment.

Another concern is the possibility that the quartz window exhibits birefringence effects. Ideally, the window would be replaced with another material (such as silicon) or a calibration study would be carried out with another THz source. Unfortunately, this was not done for the experiments carried out at the LUCX facility, as the window was installed prior to the experimental run and no suitable THz sources were easily available. Alternatively, any systematic effect caused by the birefringence effects of the window could be observed and analysed over a range of observation angles. The current experimental setup only allows measurements around one observation angle (θ=90°, $\phi = 0°$). Developing a system able to

measure the polarization of cSPr at a range of observation angles, and hence frequencies, will enable the detection of trends and systematic errors.

Several recommendations are made for the continuation of the polarization study. Firstly, any future work requires that the polarization dependence of the SBD detector be eliminated from the analysis. This could be done by conducting a rigorous calibration study or by using passive polarization optics suitable for the frequency range. Secondly, it is required that the position of the detector does not change between the measurements of the two orientations of radiation. This requires either increased realignment precision or alternatively that an experimental scheme is devised in which the detector is not required to be rotated to select different polarizations. Finally, in order for a reasonable quantitative comparison of the results of the polarization study with the values predicted by simulation, it is considered necessary to extend this work so that a range of observation angles can be included. Ideally, this study would also consider different grating profiles and different grating periodicities to identify areas of agreement and disagreement with simulation.

4.5 Summary

In this chapter, the LUCX accelerator environment is introduced and the first experimental setup used during the investigation into the polarization proprieties of cSPr is detailed. Key features of the accelerator, the THz chamber and the detection system are discussed and their use in experiment is outlined. Initial results that demonstrate the successful production of cSPr are analysed and the results of a preliminary experiment to measure the polarization of cSPr are presented. The results show high levels of linear polarization (parallel to the grating grooves) at one observation angle, however, the DoP measured was significantly lower than that predicted by simulations.

The knowledge and data generated during the preliminary studies will be used to modify the method for measuring the DoP of cSPr. To thoroughly test simulation predictions, the experiment must be redesigned to eliminate the polarization dependence of the SBD detector

and the uncertainty in the detector position. Measurements at a range of observation angles are required to monitor trends and detect any systemic error. The design of an experiment which fulfils these criteria is discussed in the next chapter.

Chapter 5

Experimental Design and Interferometer Study

To progress from the preliminary studies, measurement of the polarization of cSPr at different spectral points is required. The measurement of the polarization of cSPr at LUCX required an experimental scheme that could measure the radiation at a range of different frequencies. As discussed in Chapter 4, the setup has to be able to measure both the frequency and polarization of cSPr at a range of angular positions and in the THz frequency range. The apparatus has to be easy to convert between the setup for measuring polarisation and the setup for measuring frequency. To achieve this freestanding, wire grid polarizers (WGPs) were used to select the polarization of the radiation and as beamsplitters for an interferometer.

The second part of this chapter discusses the configuration of a Fabry-Pérot interferometer (FPi), for taking frequency measurements, in more detail. The properties of this FPi are examined and compared to those of the existing Michelson scheme. The use of WGPs as beamsplitters in the FPi scheme is also considered; their performance is compared to silicon wafers. The development of this experimental scheme and the results presented in this chapter form a strong foundation for the measurements of the polarization of cSPr discussed in the following chapter. The work presented in this chapter, however, is also important for the

development of instrumentation appropriate for work with THz radiation, with particular relevance to researchers measuring THz radiation in accelerator environments.

5.1 The New Experimental Scheme

As previously discussed in Section 4.4.3 a new experimental setup was required in order to take high quality polarization measurements of cSPr at LUCX. The initial experimental results had demonstrated several inadequacies in the first setup. Specifically, it was impossible to uncouple the polarization of the radiation from the polarization dependence of the detector and it was not possible to take measurements of more than one frequency for each grating. The experimental design presented in this chapter will address these two concerns and take into consideration the constraints placed on the experiment by its location in an accelerator tunnel.

In a linear accelerator experimental environment, it is necessary to consider the typically limited space and access. The size of the optical bench on which the interferometer was placed and moved around was limited, therefore, compact apparatus was essential. As the polarization experiment is in a remote access accelerator tunnel, which cannot be entered while the accelerator is running, it was essential that moving, re-aligning and modifying the apparatus was a quick, accurate and reproducible process. The experiment was also required to be remotely operable so that data could be collected whilst the accelerator was operating. Finally, all the components were selected to ensure a flat, or at least well understood, frequency response across the range of interest (0.3 to 0.5 THz).

In Fig. 5.1 the experimental scheme designed to meet all these criteria is shown. Firstly, in Fig. 5.1(a), is the designed experimental layout for the polarization measurements. Whilst in the previous experiment a single WGP was used, in this version two are used. WGP_1 is attached to a rotation mount and during a polarization measurement is rotated by 360°, scanning all possible orientations of radiation which enter the system. WGP_2 is on a fixed mount, so does not rotate, and eliminates the polarization dependence of the SBD detector

from the measurements.

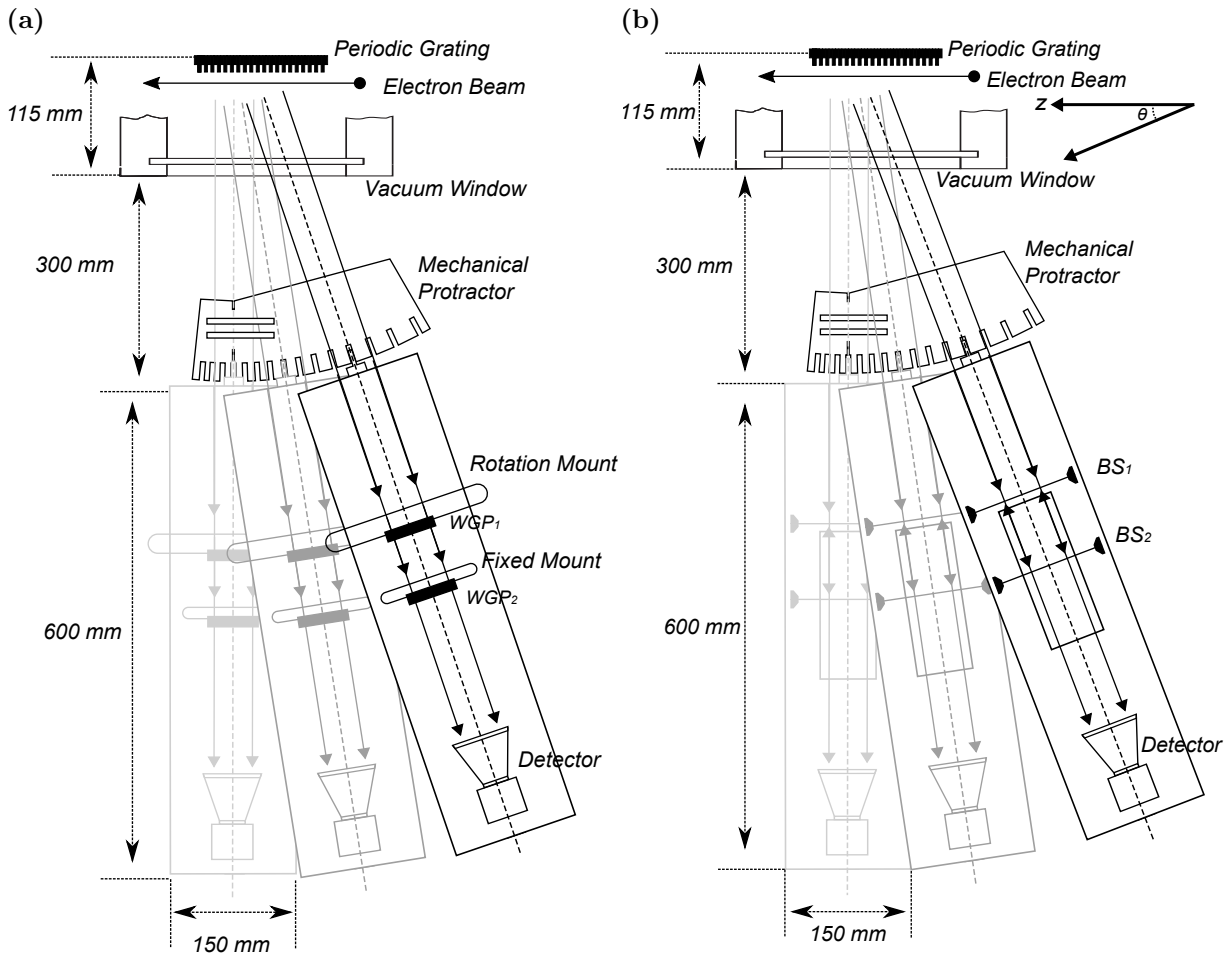

Figure 5.1: Diagrams showing the layout of the experimental setup for measuring (a) the polarization and (b) the frequency of cSPr (BS refers to a beamsplitter). In the schematics shown, WGP_1 is rotated to measure the polarization of the incoming radiation and BS_2 is moved to create the varying path difference necessary for a frequency measurement. Each of the moving components is controlled by a motorised stage operated by the accelerator control system. The definition of θ the observation angle, which is used in relation to both interferometer schemes, is shown with relation to z the direction of the beam propagation and corresponds to the axis definitions given in Fig. 2.3.

In Fig. 5.1(b) the design of a FPi, which can be used alongside the scheme for polarization measurements, is shown. It is designed to allow for frequency measurements to be made with only minimal adjustments to the experimental apparatus. If WGPs are used as beamsplitters (BS in Fig. 5.1(b)), then the adjustments required are further minimised. During the experiment, the WGP on the fixed mount (WGP_2 in Fig. 5.1(a)) was the first beamsplitter (BS_1 in Fig. 5.1(b)) and a third WGP is used as a second beamsplitter (BS_2 in Fig. 5.1(b)). In order to shift between experimental configurations, the only change required was to add the additional fixed mount WGP to shift to the frequency setup and remove it

to return to the polarization setup. This WGP is mounted on a motion stage and moved during frequency measurements to create an interferogram.

The overall design (both the polarization configuration in Fig. 5.1(a) and the frequency scheme in Fig. 5.1(b)) includes a "mechanical protractor" which is used to align the whole detection system at varying angles with respect to the beamline. The protractor is designed to keep the distance between the source and the detector constant for different observation angles; its uneven spacing allows for equal steps in detected frequency (of cSPr, see Eq. 2.1) between each position. For a grating with a period of 0.70 mm, the difference in frequency between each slot is 12 GHz. As the rest of the scheme is assembled on a plate, it is possible to move between the angular positions without breaking the alignment of the system. The plate on which the experimental apparatus is assembled covers an area of 600 mm by 150 mm (length by width) on the optical bench, such that the detector is located approximately 1 m away from the source of radiation. The design leaves space along the optical path for additional components if required, for example, lenses for collimation. In other experiments, where space is very limited the length could be further reduced.

It was possible to access the range of angles from 85° to 118° with the experimental arrangement depicted in Fig. 5.1. The angles available were limited by the finite dimensions of the sapphire window (as described in Section. 4.2.1) and the restricted space on the bench. Given the periodicities of the gratings available (0.7 mm and 1 mm) and the Smith-Purcell dispersion relation (Eq. 2.1), the frequencies emitted in this angular range are 0.203 THz to 0.465 THz. The frequencies that can be detected are further constrained by the range of the detector which, as described in Section 4.2.2, has a detection range from 0.325 THz to at least 0.500 THz [87] and a lower cut-off frequency of 0.268 THz [88].

The experimental configuration described meets all the design requirements which were placed upon it. All the components were taken to LUCX and assembled for experimental runs in November 2016 and May 2017. The results of the polarization study can be found in Chapter 7. The rest of this chapter is concerned with the design and operation of the FPi; as the design was unusual for an experiment in the THz region, it was necessary to confirm its

ability to make accurate frequency measurements. The general properties of FPi's, the use of WGPs as beamsplitters and the properties of silicon wafer beamsplitters are all discussed in this chapter. The configuration of the FPi used will also be compared to the Mi scheme outlined in Section 4.2.4. These comparisons will be examined experimentally through a compilation of results which will demonstrate the capabilities of the FPi scheme.

5.2 Design of the Fabry-Pérot Interferometer

5.2.1 Interferometer Layout

The FPi has been in use for over a hundred years [92, 93]; it uses two partial reflectors to create a resonant cavity within which some of the light is trapped. Transmission is highest on, or close to, resonance and away from resonance, the device exhibits increased reflectivity and the transmission is reduced. The theory of the FPi at THz frequencies is well understood [94] and there have been several experiments carried out using FPi's in the THz and sub-THz frequency ranges [95, 58, 96, 97, 98, 99]. The detrimental effect of incidentally creating Fabry-Pérot resonances by placing components with beamsplitting properties in the optical path has also been noted in this spectral region [100, 101]. Additional resources, providing an overview and history of the Fabry-Pérot interferometer [91, 102] and details of the use of interferometers in the THz spectral region [86], can be found in literature.

The FPi was an attractive choice for the experimental configuration as it creates a linear optical path between the source and the detector, which simplifies the alignment of components compared to a setup with two axes (such as an Mi). The FPi requires two plane-parallel beamsplitters displaced along the optical axis allowing for the experimental setup to be moved to different observation angles without breaking the alignment.

The conventional Mi, as described in Section 4.2.4 (see Fig. 4.6), remained available at the LUCX facility throughout the cSPr polarization investigation. The Mi provided an alternative scheme which could be used to benchmark the FPi. A quick comparison of the

schematics of the two interferometers (Fig. 4.6 and Fig. 5.1(b)) shows several key differences. Firstly, the larger size and complexity of this Mi scheme makes it much more difficult to move and align at different positions on the optical bench. The Mi has three parabolic mirrors (for collimating and focusing the radiation) which were not included in the FPi design. The FPi and Mi schemes also have different angular acceptances meaning that the frequency ranges covered in a single measurement with each are not identical; the acceptance of the FPi is determined by the aperture of the mounts to which the WGPs are attached whilst the aperture of the Mi is determined by the first parabolic mirror (PM_1). The two interferometers also have different measurement properties; an Mi with a close to zero path difference (as shown in Fig. 4.6) is able to measure a broad range of frequencies, whereas an FPi can only measure a finite range of frequencies at once, which is a limitation when dealing with broadband sources [91, 102]. In a cSPr experiment, however, only narrowband radiation is measured, so this is not seen as problematic.

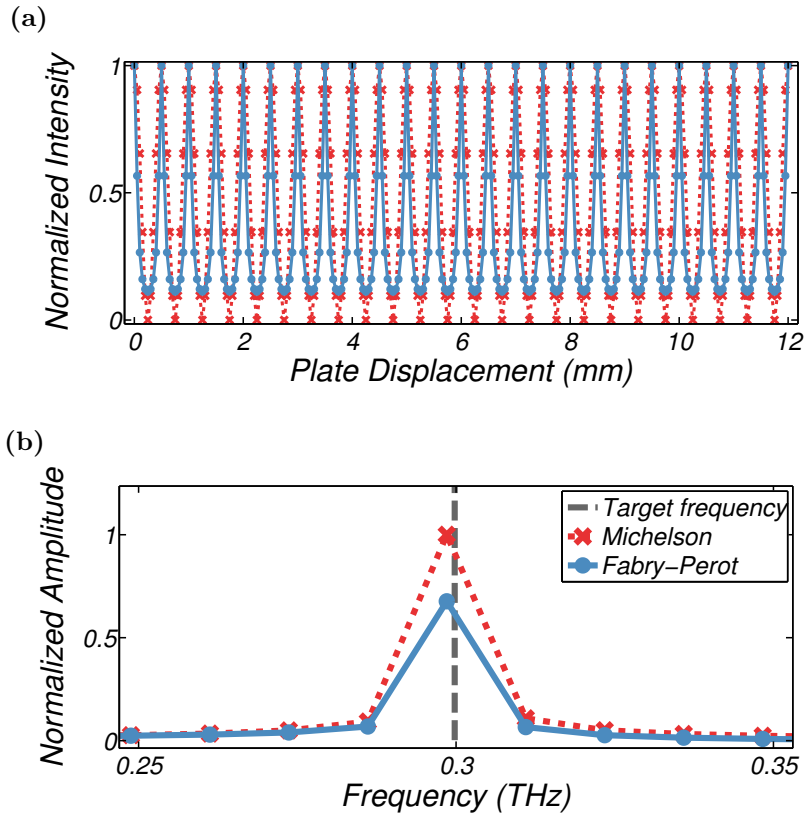

Figure 5.2: Calculated (a) interferograms and (b) the resulting frequency spectra that could be obtained using both an FPi and an Mi to measure cSPr at 0.3 THz. The FPi in this simulation uses two ideal WGPs with a relative angular displacement of 45°.

Calculations were carried out to compare the expected interferograms from both the FPi and the Mi (see Fig. 5.2(a)); both of these calculations assume a single frequency source (0.3 THz) and an ideal experiment with no noise or absorption. For example, the window and the parabolic mirrors are treated as perfect transmitters and reflectors respectively. An ideal Michelson is in theory able to give perfect 0 to 1 modulation for a single frequency throughput as shown. In contrast, the degree of modulation observed from an FPi depends on the reflectivity (R) of the beamsplitters used [102]. For a system with a reflectivity less than 1, some baseline transmission is seen. The calculation used for the prediction in Fig. 5.2 uses a reflectivity of equal to 0.5 (further discussed in Section 5.2.2). Although the FPi has reduced modulation compared to the Mi, the modulation is sufficiently pronounced to measure and analyse the frequency spectrum, as shown in Fig. 5.2(b).

5.2.2 Discussion of Beamsplitters

Fig. 5.1(b) shows the positions of the two beam splitters (BS_1 and BS_2) used to create the Fabry-Pérot cavity, which provides the path difference in this interferometer. In the experiment discussed, it was advantageous to use freestanding WGPs as they have a flat response in the frequency range of interest and could also be used for the measurements of the polarization of cSPr. Using the same components, in both the frequency and polarization measurements, reduced the overall number of components and allowed for quick changes between the two experimental configurations. WPGs are well established components used in a wide variety of settings. Their behaviour is well understood theoretically and has been confirmed experimentally [103, 104].

To create a Fabry-Pérot cavity, it is necessary to rotate the second WGP with respect to the first. This creates a relative angle between the orientation of their wires. In Fig. 5.3 the interferograms and corresponding frequency spectra are calculated for varying relative angular displacements of the two WGPs. Increasing the angle between the two WGPs increases the reflectivity of the FPi and this in turn increases the modulation of the resultant interferogram. On the other hand, as the angle between the two WGPs becomes larger, the

reflectivity of the system increases, leading to a decrease in the overall transmission of the system. Figure 5.3(b) shows that a relative angular displacement of 45° results in the most distinct frequency spectrum. With a reflectivity of R = 0.5, this displacement is a good compromise between high modulation and high transmission. This is the configuration that was used to compare the predicted behaviour of the FPi and Mi schemes in Fig. 5.2.

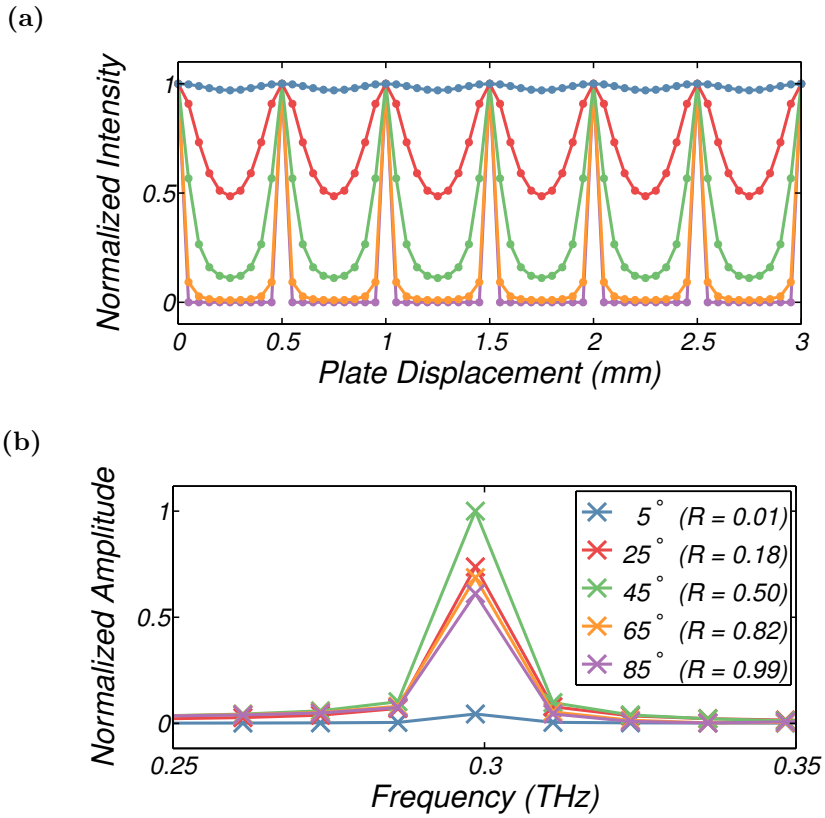

Figure 5.3: Calculated (a) interferograms and (b) the resulting frequency spectra that could be obtained using an FPi - with WGPs as beamsplitters - to measure cSPr at 0.3 THz. The angles in the legend refer to the relative angular displacement of the two WGPs used to create the Fabry-Pérot cavity. The values of the reflectivity, R, at the second WGP are also given.

WGPs are commonly used as passive components for selecting polarization in THz systems [86, 65, 100] (including as beamsplitters for Martin-Puplett interferometers [105]) and as polarizing beamsplitters in the optical region [106]. Various "one and two dimensional grids" have been used as beamsplitters for FPi's in the THz region previously [94]. In particular, attention should be drawn to FPi designs using aluminium strips deposited on crystal quartz [98], copper wires glued to crystal quartz, polyethylene foil or without substrate [99] and diffraction gratings [107] as beamsplitters. There has previously been discussion about

the relative expense and difficulty of using WGPs as polarizing beamsplitters in the THz region [108], however, nowadays commercially available freestanding WGPs appropriate for use up to 5 THz, are neither prohibitively expensive nor too fragile for use in an accelerator environment. In the absence of a supporting substrate, their frequency response is largely governed by the interaction of the wire grid with the incident radiation [103, 104] and not by the frequency response of a substrate.

Tungsten wire polarizers with a wire thickness of 10 µm and a wire periodicity of 30 µm were installed in the locations indicated by BS_1 and BS_2 in Fig. 5.1(b) [109]. To illustrate the transmission properties of this WGP, a calculation was carried out which is shown in Fig. 5.4. The model used for these calculations was developed in 1898 [110] and takes into account the periodicity of the wires and the thickness of the wires, but not any material properties [111]. In Eqs 5.1 and 5.2 the expressions for the reflection and transmission coefficients for radiation polarized parallel and perpendicular to the wire grids are given, where a is the radius of the wire, d is the spacing between the wires and λ is the wavelength of the radiation.

$$R_{\perp} = 1 - T_{\perp} = \frac{\left(\frac{2\pi^2 a^2}{\lambda d}\right)^2}{1 + \left(\frac{2\pi^2 a^2}{\lambda d}\right)^2} \tag{5.1}$$

$$R_{\parallel} = 1 - T_{\parallel} = \frac{1}{1 + \left(\frac{2d}{\lambda} \ln \frac{d}{2\pi a}\right)^2} \tag{5.2}$$

The transmission coefficients, for frequencies up to 1 THz, are plotted in Figs 5.4(a) and (b), for radiation polarized parallel and perpendicular to the wire girds respectively. The DoP of the resulting field, assuming the incident field is unpolarized, can be calculated as shown in Eq. 5.3.

$$DoP = \frac{T_{\perp} - T_{\parallel}}{T_{\perp} + T_{\parallel}} \tag{5.3}$$

This value of the DoP is shown in Fig. 5.4(c), again for frequencies up to 1 THz.

In Fig. 5.4(a) a gradual decrease in transmission is seen over the frequency range of interest, however, at 1 THz transmission is still above 99 % and the resultant degree of polarization is 0.9998.

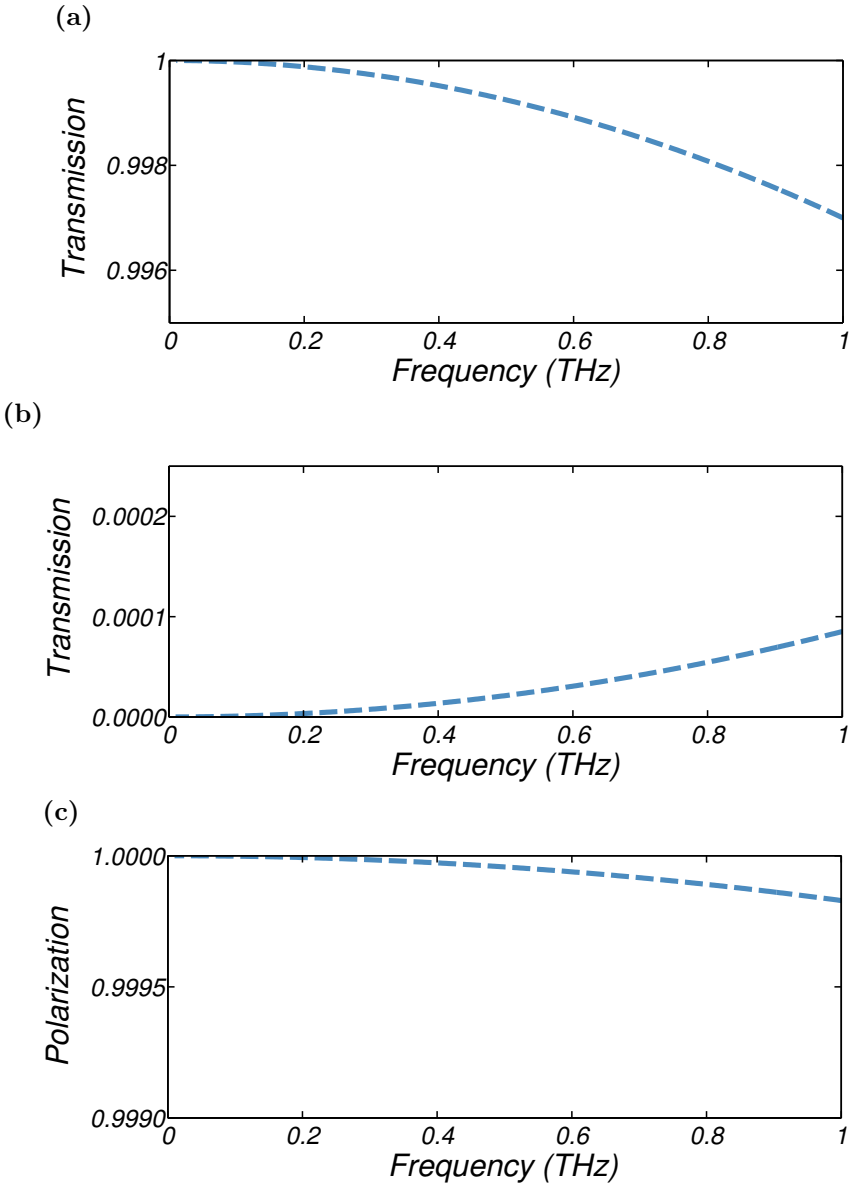

Figure 5.4: Calculations showing the transmission of a WGP with a wire thickness of 10 µm and wire periodicity of 30 µm. The transmission of incident radiation with electric field vector orientated (a) perpendicular and (b) parallel to the wire grids is shown. The (c) resultant degree of polarization of the transmitted radiation across the frequency range is also given.

The beamsplitter used for the Mi shown in Fig. 4.6 was an n-doped silicon wafer. The behaviour of doped silicon wafers can be modelled and the transmission properties can be calculated using the Cole-Davidson distribution (a modified Debye spectral response)

[112, 113]. The calculation of the transmission depends on several parameters including the density of the doping, the thickness of the wafer and the angle of incidence of the radiation.

In Fig. 5.5 the predicted response of an n-doped silicon wafer of doping density $1 \times 10^{15}\,\mathrm{cm}^{-3}$, thickness 300 µm and for an angle of incidence equal to 45° is shown. The doping density and thickness are specific properties of the wafer used; the angle of incidence is due to the position of the beamsplitter in the Mi scheme as shown in Fig. 4.6. The beamsplitter efficiency is given; this is a measure of how well a beamsplitter converts s or p polarized light into equally reflected and transmitted components. Here it is defined as $BE_{S,P} = 4R_{S,P}T_{S,P}$, (where R is the reflectivity and T is the transmission) and has a value between 0 and 1.

The n-doped silicon wafer is shown to have a variable response over the range of frequencies used in the experiments. While this is not problematic for single narrowband frequency measurements, it could hinder experiments and the subsequent analysis if a range of frequencies is used.

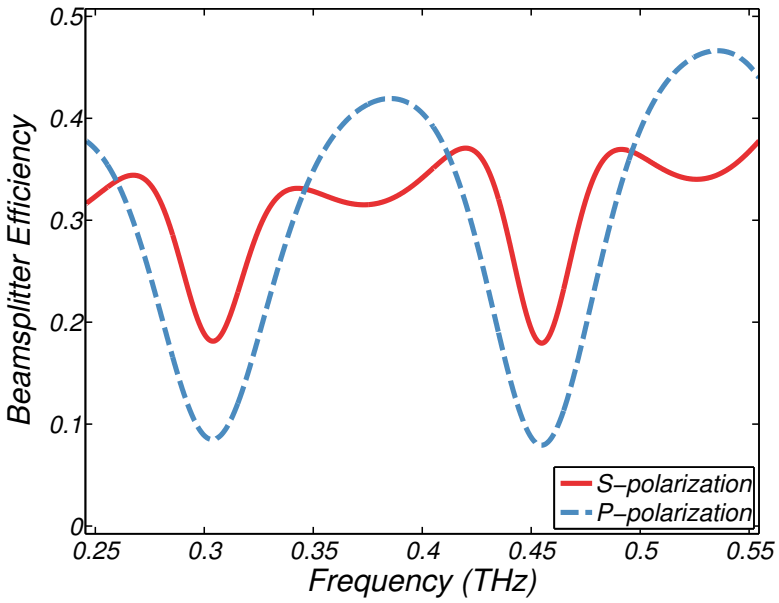

Figure 5.5: Beamsplitter efficiency of the n-doped silicon wafer used in the Mi. The calculation was done for a 300 µm thick, n-doped silicon wafer (n $=1 \times 10^{15}\,\mathrm{cm}^{-3}$) with an incidence angle of 45°.

High resistivity, $\rho \approx 5\,\mathrm{k}\Omega\,\mathrm{cm}$, silicon wafers were also used as beamsplitters in the FPi as

part of this study. They were used to examine the behaviour of the FPi with an alternative beamsplitter with a different frequency response. Transmission properties of the wafers used are shown in Fig. 5.6; the beamsplitter efficiency of a high resistivity wafer of thickness 300 µm at an angle of incidence equal to 0° is shown.

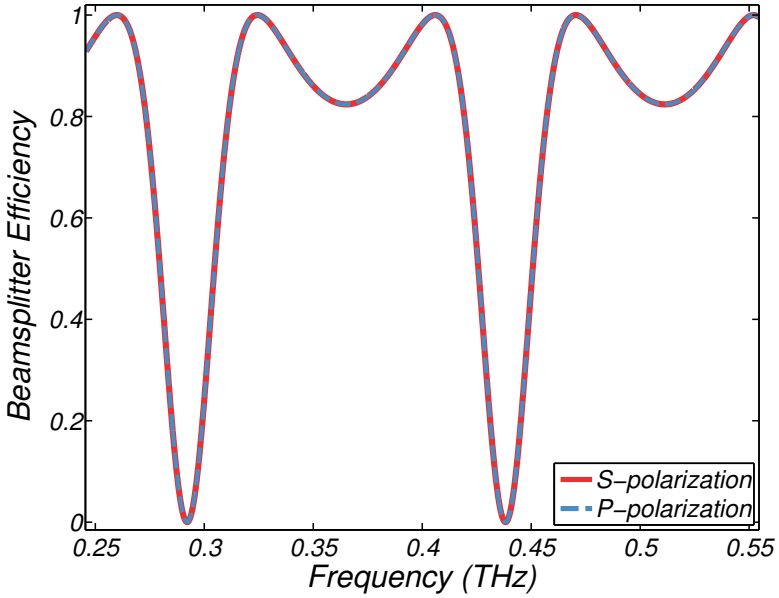

Figure 5.6: Beamsplitter efficiency of a high resistivity silicon wafer used in the FPi. The calculation was done for a 300 µm thick, $\rho \approx 5\,\mathrm{k\Omega\,cm}$ silicon wafer with an incidence angle of 0°.

The calculation, shown in Fig. 5.6, considers the beamsplitter efficiency of one wafer, however, it should be noted that two were used to form the Fabry-Pérot cavity. Similarly to the n-doped silicon wafer, a frequency dependent response is seen across the frequency range of interest. The beamsplitter efficiency of this type of wafer, however, is independent of the polarization of the radiation (for an incidence of 0°) with the result that the two components (S and P) are equal.

The silicon wafers used in both the Mi and FPi schemes are seen to exhibit highly variable beamsplitter efficiency across the frequency range of interest (0.3 to 0.5 THz). The calculated response predicts that there will be large variations in transmission across this range. In particular, there are gaps in transmission around 0.29 THz and 0.44 THz for both. This

would present difficulties when comparing the intensity of radiation measured at different frequencies. In a high noise accelerator environment, the drop in intensity caused by the variation in transmission may make measurements in certain frequency ranges impossible.

5.3 Experimental Configuration during the Interferometer Study

In order to compare the measurements taken with the two interferometer schemes, the Mi and FPi, it is important to understand the properties of each system. Previous discussion (Section 5.2.1) has considered the inherent differences between Michelson and Fabry-Pérot schemes and the effects of the different beamsplitters used. In this section the properties common to all interferometers will be discussed in order to compare the operational use of the two schemes during the experimental runs at LUCX.

Two key properties of the interferometer are: the length of the scan x_l (the total distance that the movable part travels) and the distance Δx moved between each measurement. These two properties determine the frequency resolution (Δf) and the maximum measurable frequency (f_s) that can be calculated from the interferogram.

$$f_s = \frac{c}{2\Delta x} \tag{5.4}$$

$$\Delta f = \frac{c}{2x_l} \tag{5.5}$$

Equation 5.4 shows the maximum measurable frequency of the system (f_s), which is inversely proportional to the step (Δx). Equation 5.5 shows that the frequency resolution (Δf) is inversely dependent on the scan length (x_l) [114]. In both Eqs. 5.4 and 5.5 the speed of light is denoted by c. When using discrete Fourier transforms (such as FFTs) to calculate the measured frequency spectra, the maximum resolvable frequency is defined by the Nyquist frequency (f_{Nq}), as shown in Eq. 5.6.

$$f_{Nq} = \frac{f_s}{2} = \frac{c}{4\Delta x} \tag{5.6}$$

	Michelson	**Fabry-Pérot**
$\boldsymbol{x_l}$	$\approx$ 11 mm	$\approx$11 mm
$\boldsymbol{\Delta x}$	0.05 mm	0.1 mm
$\boldsymbol{f_s}$	3.0 THz	1.5 THz
$\boldsymbol{f_{Nq}}$	1.5 THz	0.75 THz
$\boldsymbol{\Delta f}$	$\approx$ 0.0135 THz	0.0135 THz

Table 5.1: Interferometer Comparison

Table 5.1 shows the values of these parameters during the experiments with the Mi and FPi at LUCX. While the length of the scans x_l is the same for both, the stepsize (Δx) used for the Michelson is a factor of two smaller. The stepsize used for the FPi studies was increased due to time constraints (limited beam time availability) and the maximum resolvable frequency (f_{Nq}) of 0.75 THz was considered to be sufficient for this study.

Figure 5.7 shows a photograph of the FPi installed on the optical bench. During most of the experimental study, the WGP attached to the rotation mount was installed in addition to the two beamsplitter WGPs. This is located between the sapphire vacuum window and the first polarizer of the Fabry-Pérot cavity (BS_1), to facilitate the polarization study - some of which was carried out alongside the interferometer study. The wires of the extra polarizer were aligned with the wires of BS_1 during all interferogram measurements. While this extra component would cause a reduction in signal intensity if the alignment is poor, it does not affect the frequency measurement.

5.4 Results of the Interferometer Study

In this section, results obtained using the Mi and FPi interferometer schemes at the LUCX facility are brought together. These results were obtained over a series of experimental runs during which it is possible that some of the accelerator parameters may have varied, affecting the generation of cSPr. Changes to parameters such as the beam position, average

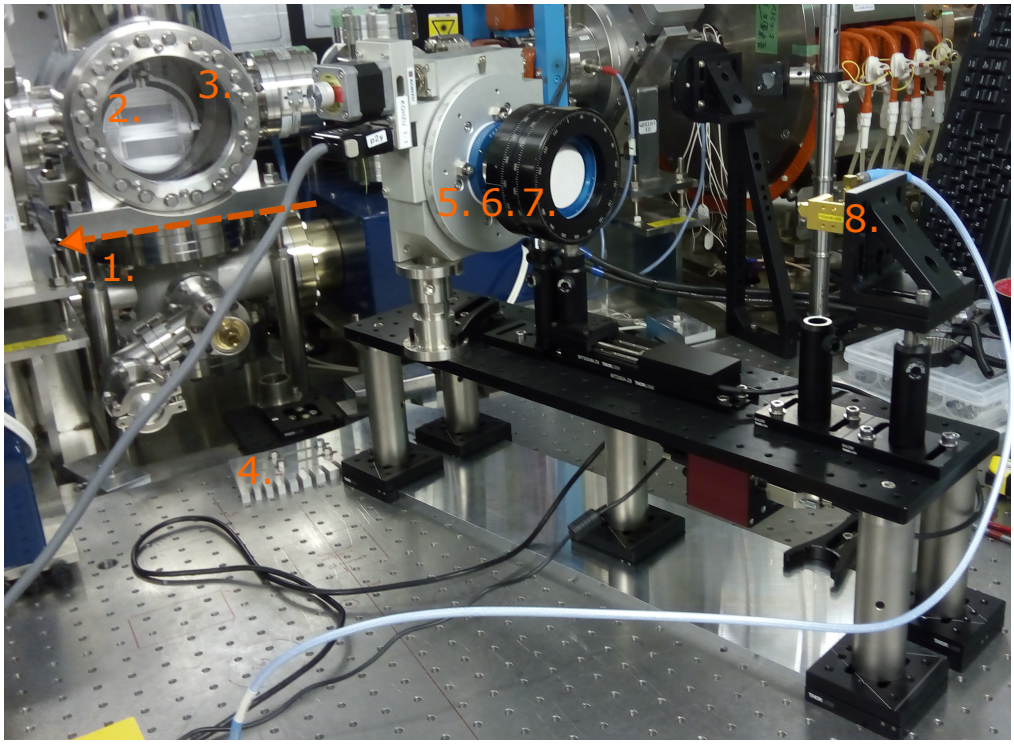

Figure 5.7: FPi installed on the optical bench at the LUCX facility. The components are as follows: 1. Electron Beam Trajectory, 2. Periodic Grating, 3. Vacuum Window, 4. Mechanical Protractor, 5. WGP on Rotation Mount, 6. BS_1, 7. BS_2, 8. Zero Bias Schottky barrier diode detector. The first WGP (5.) is aligned with BS_1 and does not affect the frequency measurement.

charge and the emittance of the bunch could have caused variation in the intensity of cSPr generated at a given frequency but would not have impacted the frequency content reaching the detector (as defined by the dispersion relation). The results presented are used to compare the frequency content measured by the interferometer schemes, but do not compare the intensity of radiation measured by each scheme. For this reason all the frequency spectra shown have been normalized to one, eliminating any dependence on the beam parameters and variation in the accelerator behaviour.

The FPi was used to measure the frequency of cSPr generated by the three gratings (0.70 mm sawtooth, 0.70 mm strip and 1.00 mm sawtooth as described in Section 4.2.3). Examples of frequency spectra of cSPr measured at different angles with the FPi (using WGPs as beamsplitters) are shown in Fig. 5.8. The graph shows results using cSPr generated by a sawtooth grating profile with a period of 0.70 mm. Frequency spectra have been observed at a set of angles ($\theta = 107.8°$, $95.7°$ and $88.4°$); the measured frequencies correspond well to the theoretical values given by the Smith-Purcell dispersion relation (Eq. 2.1).

Each of the frequency spectra are represented by points generated using an FFT - given with error bars - and a Gaussian fit. The error bars are calculated from the statistical uncertainty in the raw data from the interferograms. The FFT gives a peak frequency, with uncertainty determined by the resolution of the FFT. The amplitude of each frequency spectrum has been scaled so that the highest data point in the displayed frequency range is equal to one.

The FPi and Mi were both used to measure the frequency of cSPr generated by the 1.00 mm sawtooth grating. The results are used to compare the operation of these two interferometers. Figure 5.9 shows the measured peak frequencies - given by the maximum point of each frequency spectrum - for the two interferometers as well as the expected cSPr frequency at all positions (calculated using Eq. 2.1). As the Mi could not be rotated without affecting the alignment, the only measurements conducted with it correspond to the observation angle $\theta = 90°$. In contrast, a range of frequency measurements taken with the FPi at different observation angles are given. The error bars correspond to the known

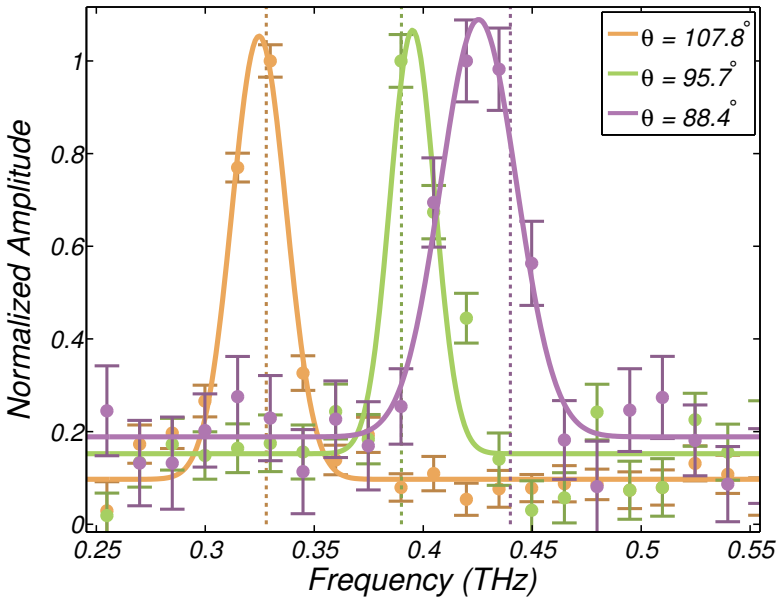

Figure 5.8: A range of frequency spectra of cSPr measured at different angular positions with the FPi. The measured frequency spectra are plotted along with a corresponding Gaussian fit (solid lines). All of the spectra are for cSPr generated using the 0.70 mm period sawtooth grating. Using the Smith-Purcell dispersion relation (Eq. 2.1) the expected frequencies of the three angular positions - 107.8°, 95.7° and 88.4° - can be calculated to be 0.33, 0.39 and 0.44 THz respectively, the dashed vertical lines represent these expected frequencies.

uncertainty in the angular alignment of the FPi; the mechanical protractor allows deviation from the designed angular position of up to ± 1.3° leading to frequency deviations of up to ± 0.01 THz. It is assumed that the Mi scheme suffered from a similar level of alignment uncertainty. In addition both interferometers are expected to have an uncertainty on the peak frequency of ≈ 0.015 THz (see Table 5.1). Using these uncertainty ranges, both sets of frequency measurements are consistent with the predicted values .

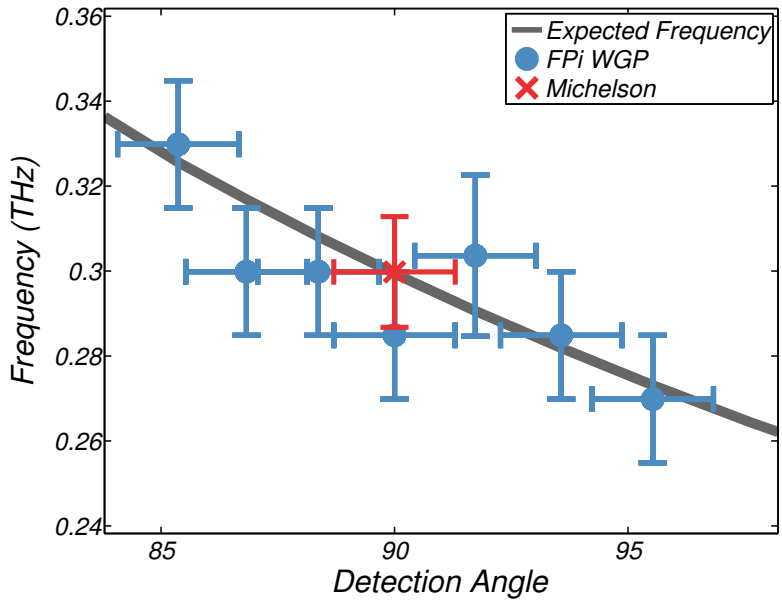

Figure 5.9: Experimental results for the FPi and Mi measuring cSPr at LUCX. The theoretical prediction of the cSPr frequency is shown by the grey line (see Eq. 2.1). The frequency is given by the peak value of the frequency spectrum and the errors are determined by the resolution of the frequency spectrum and the angular uncertainty in the interferometer alignment.

In Fig. 5.10 the results for both interferometers measuring cSPr generated by the 1.00 mm period sawtooth grating at a single observation angle ($\theta = 90°$) are given in more detail. In Fig. 5.10(a) the two interferograms are shown, these can be compared to the idealized operation predictions shown in Fig. 5.2(a). As predicted, the interferogram taken using the FPi shows reduced intensity modulation compared to the Mi. The spectral plot, in Fig. 5.10(b), shows that both interferometers measure a peak frequency close to the expected value of 0.3 THz. The lower signal to noise ratio seen for the FPi spectrum can be attributed to the reduced intensity of the radiation measured compared to that measured by the Mi.

As previously discussed, the relative angle between the two WGPs used as beamsplitters in the FPi scheme was a compromise between achieving high levels of modulation and high transmission. Variations in the accelerator parameters in the interval between the two sets of measurements could also have affected both the intensity of cSPr and the noise level measured. Gaussian fits have been plotted alongside the raw FFT in order to estimate the width and central frequency of the peaks measured by each scheme.

The Gaussian fitting gives us $\mu_{FPi} = 0.289\,\mathrm{THz}$, $\sigma_{FPi} = 0.015\,\mathrm{THz}$ and $\mu_{Mi} = 0.300\,\mathrm{THz}$, $\sigma_{Mi} = 0.007\,\mathrm{THz}$. These values show that both designs are able to measure the frequency accurately and that the spectrum produced from the interferogram measured with the FPi has a broader peak. This could be due to the larger angular acceptance of the FPi system, imperfect alignment of the two beamsplitters or a combination of both. The angular acceptance of the FPi scheme was approximately $\pm$ 2.5°, the frequency range to which this corresponds depends on the periodicity of the grating (p) and on the angle of observation (θ - see Eq. 2.1). For the range of θ and p used it is on the order of 0.01 THz. Specifically for $p = 0.70\,\mathrm{mm}$ at $\theta = 90°$, the frequencies transmitted are in the range $(0.300 \pm 0.013)\,\mathrm{THz}$. The angular acceptance of the Mi scheme is determined by the parabolic mirror (PM_1) as shown in Fig. 4.6(b). The angular acceptance of either scheme could easily be modified if it was required.

Measurements were also made with the FPi using both WGPs and high resistivity silicon wafers as beamsplitters. These were taken over a range of observation angles, using two of the available gratings to generate the cSPr. The results taken using the 0.7 mm period strip and sawtooth gratings are shown in Fig. 5.11 (a) and (b) respectively. The measurements were carried out using the same accelerator parameters and the same FPi layout as previously.

The measured frequencies are compared to the expected theoretical frequencies of cSPr at all observation angles; every measurement - for both types of beamsplitters - shows agreement with the expected value within error. This suggests that the performance of the FPi is unaffected by changing from silicon wafers to WGPs. There is little difference in the results for the strip and sawtooth gratings (as expected), demonstrating the consistency of the

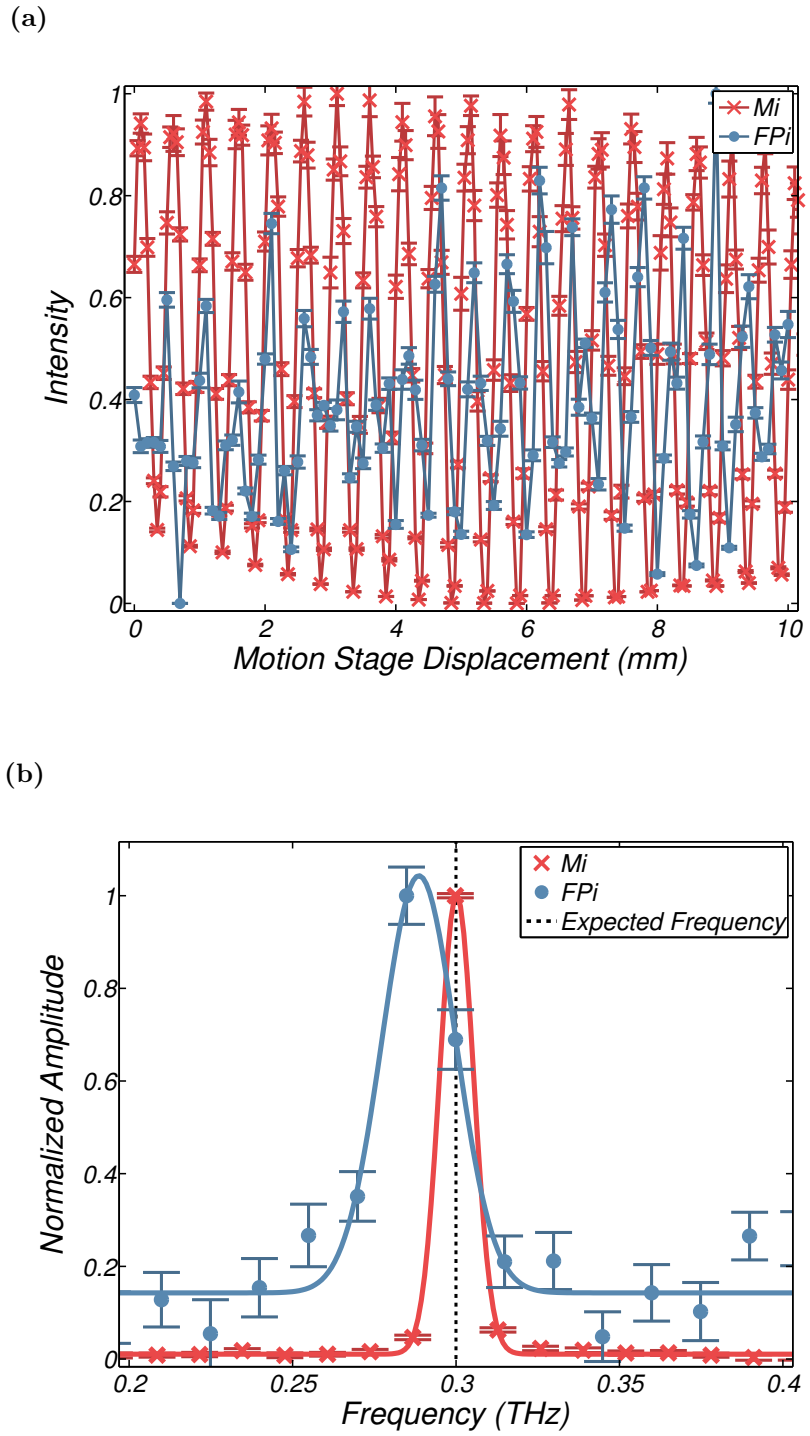

Figure 5.10: Results using the FPi and the Mi to measure the frequency of cSPr generated by the 1.00 mm period sawtooth grating and observed at 90°. Both (a) the interferogram and (b) the resultant frequency spectrum are shown for each interferometer. Solid lines in (a) are a guide to the eye and in (b) are Gaussian fits to the peaks. The expected frequency of 0.30 THz is shown by the dashed vertical line in (b). The amplitudes of both frequency spectra have been scaled so that the highest data point in the displayed frequency range is equal to one.

scheme.

In order to study these results in more depth, the frequency spectra measured at the observation angle 95.7°, using the FPi with both WGPs and silicon wafers are compared in Fig. 5.12. The data used in this comparison is drawn from the measurements of cSPr generated by the sawtooth grating with a period of 0.70 mm. It is clear from this figure that consistent frequency measurements are achieved with the two different types of beamsplitter. The small variations in peak position observed are likely due to changes in the alignment of the beamsplitters in the FPi. Gaussian fitting gives us $\mu_{WGP} = 0.395\,\mathrm{THz}$, $\sigma_{WGP} = 0.016\,\mathrm{THz}$ and $\mu_{sili} = 0.379\,\mathrm{THz}$, $\sigma_{sili} = 0.016\,\mathrm{THz}$. The central frequencies measured are in agreement within the resolution of the frequency spectra and the alignment error. The peaks are both spectra of the same width, which suggests that the beamsplitters do not have an affect on the frequency resolution.

The results presented in this section demonstrate that this FPi design works well in practice and that measurements are able determine the frequency of incident radiation in the range of interest. The frequencies measured with the FPi are shown to agree with those measured with the Mi which validates the basic operation of the device. When compared with the Mi scheme the FPi scheme has a broader spread of frequencies. However, this is likely to be due to the differences in the acceptance angles of the two systems. The slight relative broadening in spread was not seen as a limiting factor in this study. If required, it would be simple to reduce the aperture for incoming radiation, although it should be noted that the relationship between acceptance angle and frequency spread is particular to Smith-Purcell radiation.

The comparison of the operation of the FPi with WGPs and silicon wafers as beamsplitters shows no discernible difference in the frequency component measured. This validates the use of WGPs as beamsplitters when measuring the frequency of cSPr during the polarization study. The duplication of components in both configurations (as shown in Fig. 5.1) greatly simplifies the conversion between them. More generally, the similarities in response between the two types of beamsplitter make a convincing argument for the wider use of

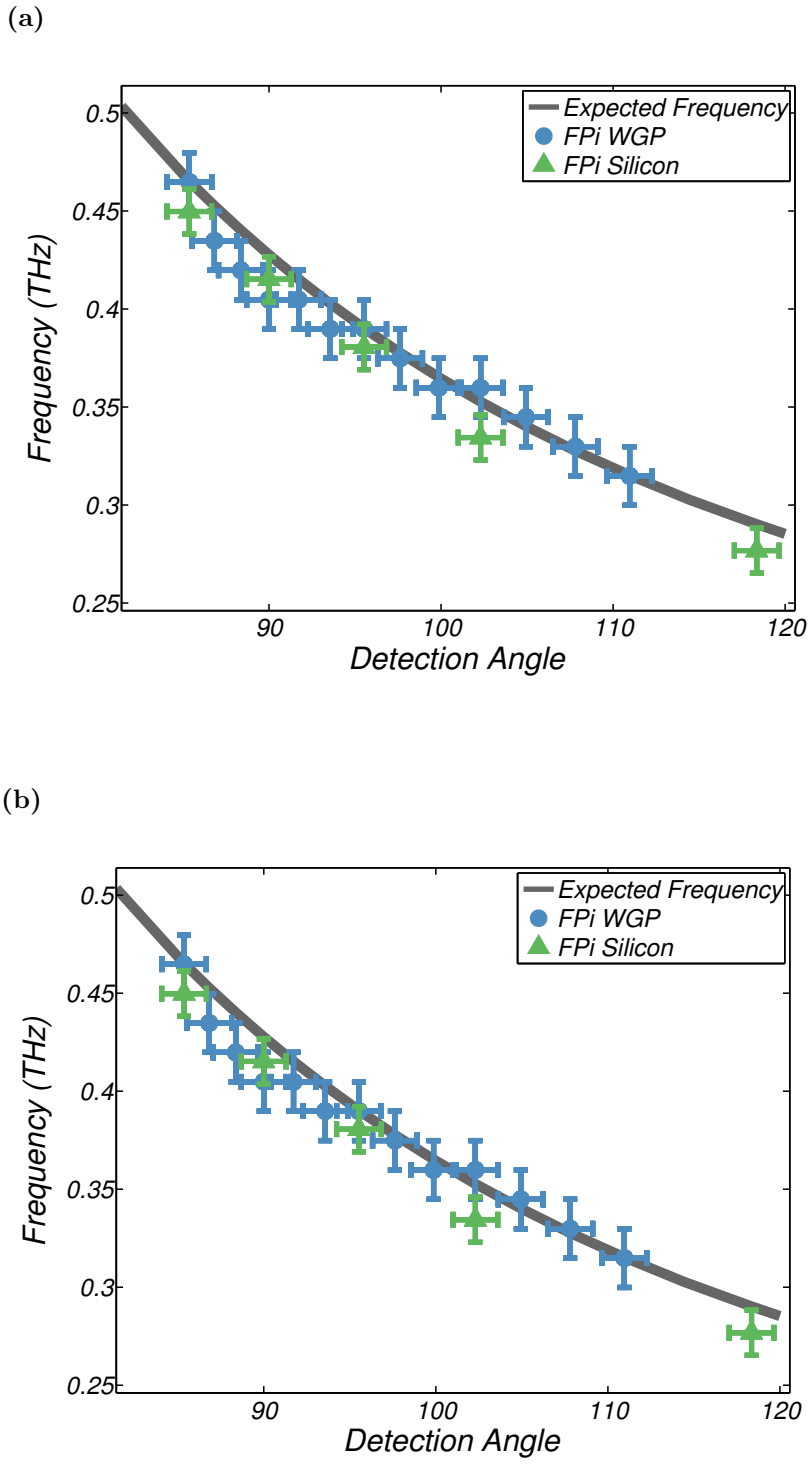

Figure 5.11: Experimental results measured using the FPi with different beamsplitters (high resistivity silicon wafers and WGPs) detecting cSPr over a range of observation angles. The cSPr was generated using a (a) strip grating, and a (b) sawtooth grating, both with a periodicity of 0.70 mm. The theoretical prediction of the frequency of cSPr (given by Eq. 2.1), is indicated by the smooth grey lines. The frequency points plotted are determined by the peak of the spectrum in each case. The errors shown are determined by the resolution of the frequency spectrum and the angular uncertainty of the interferometer alignment.

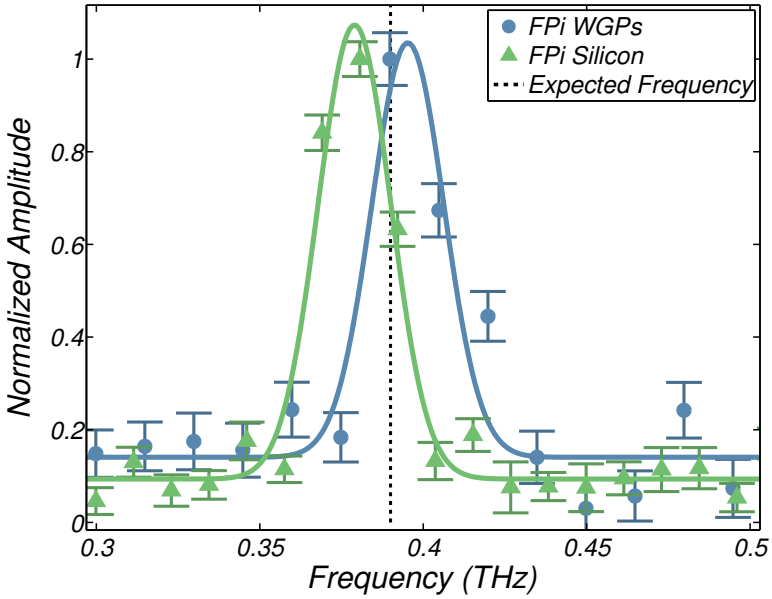

Figure 5.12: Results taken using the FPi with both WGPs and silicon wafers as beamsplitters to measure the frequency of cSPr generated by the 0.70 mm period sawtooth grating and observed at 95.7°. The solid lines are Gaussian fits of the frequency spectra. The expected frequency of 0.39 THz is shown by the dashed vertical line in (b).

WGPs as beamsplitters in the THz region. Silicon wafers are commonly used, however, they are known to have a frequency dependent response in the THz range (see Figs 5.5 and 5.6). In comparison, the WGPs have a largely flat response over a wide range and a very well understood polarization dependence making them very attractive components for use in THz radiation measurement systems.

5.5 Summary

This chapter introduces the newly developed experimental setup for the polarization study of cSPr at the LUCX facility. The final scheme has two configurations: one for measuring the polarization of incoming radiation and the other for measuring the frequency component to confirm the generation of cSPr. The experimental scheme is designed to be easy to move to different angles and to study different frequencies of cSPr; it is also compact and easy to align making it ideal for use in a restricted accelerator environment. The design of the FPi has been considered in detail as it is relatively novel in the THz frequency region. The use of WGPs as beamsplitters in this region is discussed and their predicted performance compared to more conventional silicon wafer beamsplitters. An experiment to test the performance of the FPi is described and the results from this study are presented. The FPi measurement of cSPr at 0.3 THz is shown to agree with the measurement taken with the Mi. The difference in the spread of the frequency spectra measured is attributed to the difference in aperture of the two systems. The performance of the FPi with WGPs as beamsplitters is also compared to its performance with silicon wafers as beamsplitters and no differences are noted. This study provides confirmation that the FPi scheme is reliable and can be used to verify the presence of cSPr during the polarization study which will be discussed in the following chapter. This study also make a contribution to the ongoing work in the THz field of understanding the behaviour of different components in this frequency range in order to make reliable measurements of THz radiation phenomena.

Chapter 6

Measurement and Analysis of the Polarization of cSPr

In Chapter 3 the proposed background elimination method, using the polarization of cSPr, was discussed. This method was incorporated into the conceptual design; the detection channels (as shown in Fig. 3.3) incorporate a polarizer which splits the incoming signal before measurement.The implementation of this background elimination scheme is dependent on the development of a method to measure the polarization of cSPr accurately and the demonstration of good agreement with theoretical predictions. Chapters 4 and 5 describe the experimental layout and methodology developed in order to measure the polarization of cSPr at the LUCX facility. In this chapter the results of the polarization measurements at a variety of frequencies and using several gratings are used to test the predictions of the SCM theory (using the GFW code) with respect to polarization.

The chapter begins with a brief account of the experimental acquisition of the polarization data and a description of the two analysis methods used to extract the DoP from this data. The data for all three gratings is then compared to GFW simulations of the DoP and the results are discussed. We consider possible sources of error, including the interaction of the radiation with the sapphire window and known limitations of the GFW simulation code.

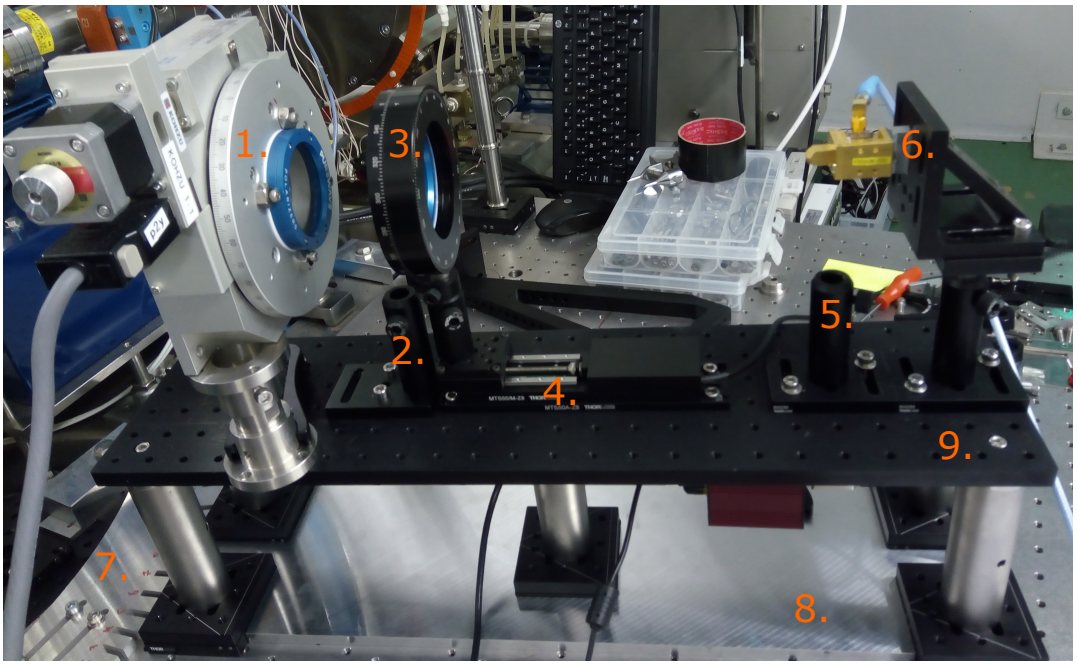

Figure 6.1: A photo of the experimental apparatus set up for polarizer-rotation scans. A schematic of this scheme can be found in Fig. 5.1(a). Incoming radiation travels from left (from the grating) to right (to the detector) in this configuration. The components are labelled as follows: 1. Rotation Mount with WGP_1 attached, 2. Post holder for fixed mount and WGP used for frequency measurements, 3. Fixed Mount with WGP_2 attached, 4. Motion Stage, 5. Post holder for optional focussing lens, 6. SBD Detector, 7. Mechanical Protractor, 8. Metal Plate Guide, 9. Portable Optical Mount.

6.1 Polarization Measurements

In the previous chapter we saw the design of the apparatus developed to measure both the frequency and polarization of cSPr generated at LUCX at a range of observation angles. Here, we give more details of the experimental procedure specific to polarization measurements.

6.1.1 Rotation Scans

The experimental apparatus for carrying out polarizer-rotation scans, used to determine the polarization of cSPr generated at the LUCX facility, is shown Fig. 5.1(a). A photograph of this apparatus, installed on the optical bench at LUCX, is shown in Fig. 6.1. The key features, including the WGP attached to the rotation mount (WGP_1) and the fixed WGP (WGP_2), are labelled

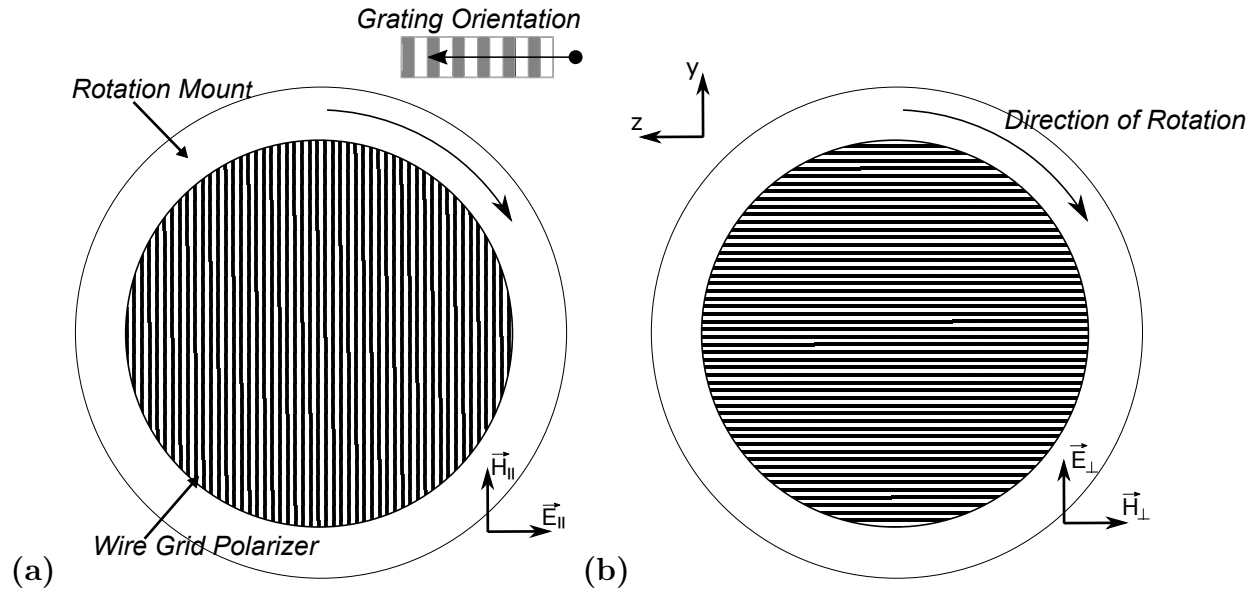

Figure 6.2: Schematic of the WGP attached to the rotation mount with different orientations of the wires: (a) 0° (180°) and (b) 90° (270°). The two orientations accept the radiation polarized (a) parallel and (b) perpendicular to the grating grooves respectively, the orientation of the field accepted by each is shown. The direction of rotation during the experiment is labelled with an arrow. A schematic shows the relative position of the grating.

During a polarizer-rotation scan WGP_1 turns through 360° in 5° intervals. Every 5° the mount stops moving and measurements are taken. At each angular position 10 measurements are taken of the cSPr intensity (using 10 different electron bunches) which are used to calculate a mean and standard error. In Fig. 6.2, a WGP is shown at two different points of the polarizer-rotation scan, in (a), with a position of 0° or 180°, the WGP would accept all radiation polarized parallel to the grating grooves and reject all radiation polarized perpendicular to the grating grooves, in (b), with a position of 90° or 270°, the opposite is true (field directions are marked on the figure). No other components, including the motion stage, are moved during a polarizer-rotation scan.

WGP_2, attached to the fixed mount, remains at an orientation of 45° throughout, halfway between the two orientations shown in Fig. 6.2. WGP_2 removes the polarization dependence of the SBD detector from the measurements, by ensuring that all of the radiation which reaches the detector is linearly polarized in the same orientation throughout the entire scan.

All three gratings (0.7 mm period sawtooth and strip, 1.0 mm period sawtooth) were used during the polarization measurements. Measurements were taken over a range of observation

angles (θ), determined by: the frequency range of the detector, the size of the sapphire vacuum window and the space available on the optical bench. The two gratings with a period of 0.7 mm were used for an observation angle (θ) range of 85° to 111° (corresponding to a frequency range of 0.465 to 0.315 THz). The grating with a period of 1.0 mm was used for an observation angle range of 85° to 97° (corresponding to a frequency range of 0.325 to 0.264 THz).

Some of the measurements at larger angles could not be completed due to the low intensity of the signal. The corresponding frequency measurements for all of the observation angles are given in Figs 5.9 and 5.11; in each case the detection of cSPr has been confirmed.

Extinction Ratio

When working with linear polarizers, such as WGPs, it is essential to consider their performance and any deviation from ideal behaviour. One measure of a polarizer's performance is its extinction ratio, which is a measure of its ability to attenuate radiation linearly polarized perpendicular to its transmission axis. It is given as the ratio of $T_\perp$ and $T_\parallel$, the transmitted radiation perpendicular and parallel to the transmission axis respectively.

The extinction ratio is expected to be very small ($<< 1$) for a commercial grade polarizer. Free standing WGPs tend to have a significantly lower extinction ratio than those with substrates, as the transmission properties of the substrates typically affect the performance.

The calculations carried out in Section 5.2.2 and shown in Fig. 5.4 demonstrate a low theoretical extinction ratio for these WGPs ($\approx 1 \times 10^{-5}$ at 0.3 THz); this is likely to be slightly higher in practise due to manufacturing limitations. WGPs typically achieve acceptable performance when the ratio of the incident wavelength λ and the wire periodicity p is sufficiently small $\frac{\lambda}{p} \geq 8$. With a wire spacing of 30 µm we can anticipate good performance for polarization measurements for wavelengths greater that $\lambda = 240$ µm or equivalently for frequencies less than 1.25 THz.

6.1.2 Analysis Procedure

In this section a selection of the experimental results from polarizer-rotation scans at LUCX will be presented and the appropriate analysis will be discussed. A fitting routine used to extract the polarization information from the data will be detailed as well as a simpler secondary analysis method used to check the veracity of the fitting routine.

Each method of analysis must extract the linear polarization of the generated cSPr at each observation angle. In addition to the cSPr, however, the method must deal with additional components present in the measured signal. In this analysis we separate the part of the signal which is not cSPr into the "background radiation" and "noise". "Background radiation" refers to non-cSPr THz radiation which is generated in the THz chamber and travels with the cSPr to the detector.

At LUCX, the background radiation was measured to be negligible (Fig. 4.12), however, this was not monitored for every scan and so a small component is allowed for in analysis. Any background radiation is assumed to be unpolarized. This assumption is based on a number of measurements carried out at different facilities, including those taken during the E203 experiments at SLAC [32].

"Noise" refers to any signal picked up at the SBD detector which did not originate in the THz chamber or distortion in the transfer line from the SBD detector to the DAQ unit. The noise is assumed to be relatively constant during a scan, but not constant over the course of the experimental run.

Both analysis methods discussed assume that all of the polarized radiation leaving the THz chamber is cSPr. Potential sources of polarized radiation in an accelerator environment include magnets (producing synchrotron radiation) and apertures (producing CDR). In all of the experiments conducted at LUCX as part of this study, no polarized radiation from any other sources has been registered. It was, therefore, not considered necessary to account for polarized radiation from other sources at the LUCX facility in the experimental design or in the subsequent analysis.

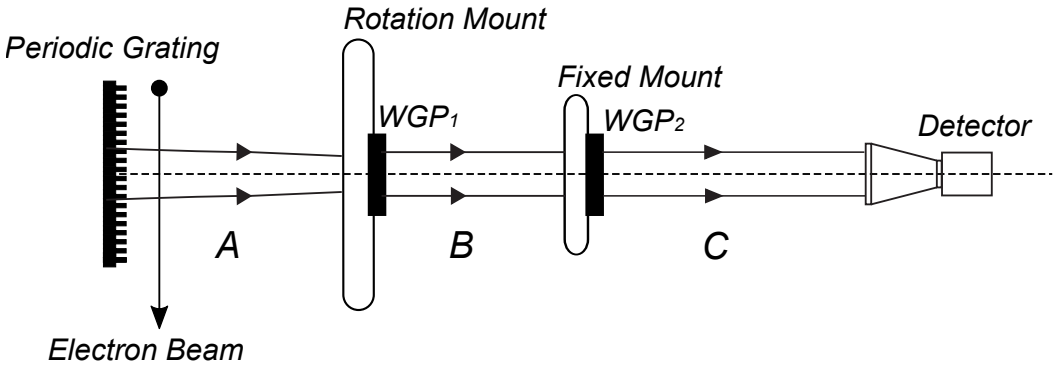

Figure 6.3: A simple schematic of the setup for polarization measurements. All apparatus used in the analysis of the polarization is labelled, apparatus which is excluded from the analysis (such as the sapphire vacuum window) is not shown in this schematic. The areas A, B and C indicate the three different intensities of the radiation as it is modified by the WGPs. This convention is used in the explanation of the analysis procedure found in the text.

Method 1: A Fitting Routine

A schematic of the experimental apparatus for the rotation scan measurements is given in Fig. 6.3. This shows the passage of the radiation from its generation via the interaction of the electron beam and the periodic grating, through the two WGPs to the SBD detector. Three areas - A, B and C - are used to demarcate regions with differing polarization properties.

In A, the polarization is determined only by the interaction between the periodic grating and the electron beam. This is the polarization that the experiment sets out to determine. In the subsequent areas, B and C, the radiation is modified by the two polarizers, WGP_1 and WGP_2 respectively, which changes the orientation of the electric field and determines its subsequent interactions. During the analysis, the measured polarization is assumed to be independent of all other factors. This includes variation in the beam parameters and any birefringent effects of the sapphire vacuum window.

The modification of the orientation of the electric field (or the change of polarization), as it passes through the two polarizers shown in Fig. 6.3, depends on the angle at which each polarizer is aligned with respect to the incoming electric field orientation. According to Malus's Law, Eq. 6.1, the degree by which the intensity of linearly polarized radiation is modified by passage through a linear polarizer depends on the relative angle, θ, between

the orientation of the field of the linearly polarized light and the transmission axis of the linear polarizer [102]. In this equation $I(0)$ is the initial intensity of the linearly polarized radiation and $I(\theta)$ is the resultant intensity after transmission through the polarizer.

$$I(\theta) = I(0)\, cos^2(\theta) \tag{6.1}$$

Using Malus's law it is possible to model the expected change in intensity of the cSPr as the rotation scan is carried out. We start by considering the intensity in region A, I_0. The radiation in this region is expected to be composed of linearly polarized cSPr (I_p) and a small amount of unpolarized background radiation (I_{up}), as shown in Eq. 6.2.

$$I_0 = I_p + I_{up} \tag{6.2}$$

After passage through WGP_1, the intensity of the radiation in region B (see Fig. 6.3) has been modified. In Eq. 6.3 the intensity of the radiation at this point is represented by I_0'. The intensities of the linearly polarized cSPr and the unpolarized background radiation will be modified differently by transmission through WGP_1. According to Malus's law the intensity of linearly polarized cSPr will depend on the cosine squared of the relative angle between the orientation of the field and the transmission axis of the polarizer, $\cos^2(a - \alpha)$, where a is the initial orientation of the linearly polarized cSPr and α is the orientation of WGP_1 (both relative to the orientation of the grating grooves). The change in intensity of the unpolarized background radiation, however, does not depend on the orientation of the transmission axis of the polarizer, so this intensity will be reduced by a constant (given here as c, where $c < 1$) for every angle α. After transmission through the first polarizer all the radiation will be linearly polarized along the same axis, determined by the angle α.

$$I_0' = I_p' + I_{up}' = I_p \cos^2(a - \alpha) + cI_{up} \tag{6.3}$$

As all the radiation is linearly polarized upon reaching the second polarizer, WGP_2, the

calculation of the intensity in region C, I_0'', is comparatively simple. The expression for the intensity in this region is given in Eq. 6.4. By again using Malus's law, the intensity of all of the radiation is reduced by the cosine squared of the relative angle between the transmission axes of the two polarizers, $\cos^2(\alpha - \beta)$, where α and β are the orientations of the transmission axes of WGP_1 and WGP_2 respectively. The angle β remains constant, at $45° \pm 2°$ with respect to the orientation of the grating grooves, throughout each rotation scan.

$$I_0'' = I_0' \cos^2(\alpha - \beta) = \left(I_p \cos^2(a - \alpha) + cI_{up}\right) \cos^2(\alpha - \beta) \tag{6.4}$$

Given the expression for the intensity of the radiation reaching the detector, Eq. 6.4, it is possible to develop a fitting function which can be used with the intensity measurements made during the rotation scans. The fitting function used in the subsequent analysis is given in Eq. 6.5. The independent variable is the orientation of the transmission axis of WGP_1, α which is varied during the scan, while the intensity measured by the SBD detector, I, is the dependent variable. This fit also requires knowledge of the angle β, the orientation of the transmission axis of WGP_2, which is constant throughout the scan.

$$I = \left(C_1 \cos^2(C_2 - \alpha) + C_3\right) \cos^2(\alpha - \beta) + C_4 \tag{6.5}$$

There are four unknowns in the fitting routine, C_1, C_2, C_3 and C_4, all of which require an initial estimate. C_1 and C_3 give the initial intensities of the linearly polarized cSPr and the unpolarized background radiation respectively. C_1 is estimated as the maximum intensity measured during the scan, as the unpolarized background intensity is expected to be a much lower, the initial value of C_3 is set at $0.1C_1$. Other initial values of C_3 were tried, including $0.01C_1$ and $0.2C_2$, with negligible impact on the fit results.

The other two unknowns, C_2 and C_4, present slightly more difficultly in providing initial estimates. C_2 is the variable of most interest, as this is the angle of orientation of the linearly polarized cSPr before interaction with the polarizers (a in Eq. 6.4). Once this parameter is obtained the polarization of the cSPr is known. The initial estimate of C_2 was varied, in

order to determine that the results were not biased; inputs of 0°, 45° and 90° were tried with negligible variation to the fit results seen.

C_4 appears in the fit equation Eq. 6.5, but is not seen in any of the equations estimating the observable intensity of the radiation at various points. This constant accounts for a non-zero baseline value, which was often observed when taking measurements. Experimentally this could be caused factors such as: background radiation from components in the accelerator tunnel, noise from the SBD detector, noise from the transport line to the DAQ unit in the control room and the extinction ratio of the WGPs.

Once a value for the angle C_2 is obtained it can be converted to the DoP. The angle is used to calculate the ratio of the intensities of radiation along the two orientations (parallel and perpendicular to the grating grooves), as shown in Fig. 2.4. Once relative values for the two intensity components have been the DoP is calculated using Eq. 2.22.

The fit was carried out using a weighted, non-linear regression model in MATLAB. The inputs were: the model given in Eq. 6.5, the value of α for each data point, the mean and standard error of the intensity for each position and the initial estimates of the four unknowns. The fitting routine is solved and returns an optimised solution for the four unknowns, along with a calculated fit uncertainty. The fit is weighted by the standard error, therefore, it places greater constraints on the fit values in areas with a low standard error and weaker constraints in areas with high standard error.

The fitting routine for the analysis of rotation scan data makes several assumptions which must be considered and, where appropriate, the effects of these assumptions is mitigated. The four unknowns in the fitting routine permit variation - in the relative levels of linearly polarized cSPr, background radiation and noise - between rotation scans. The effect of variations, in the electron bunch properties or in the general accelerator environment, on the analysis of the scans and extraction of the DoP is, therefore, minimised. On the other hand, the relatively large number of unknowns introduces a level of uncertainty into the fitting routine. In order to increase confidence in the analysis method a secondary method is used to provide a baseline comparison.

Method 2: Comparing Intensities

It is reasonable to assume, based on early measurements at LUCX (see Fig. 4.12), that the background component is negligible compared to the cSPr signal. In this case it is possible to directly compare the intensity measurements taken with the WGP_1 at the orientations: 0° (180°) and 90° (270°). These positions correspond to transmission of radiation polarized parallel and perpendicular to the grating grooves respectively.

For both orientations (parallel and perpendicular to the grating grooves) the intensity is measured twice in the polarizer-rotation scan. For example, the wires of the WGP_1 are aligned parallel to the grating grooves twice, at positions 0° and 180°. Therefore, the average of these values is obtained, which lowers the error due to variations in the accelerator environment. After taking the average to obtain a value for both intensities ($I_{\parallel}$ and $I_{\perp}$), the DoP is calculated using Eq 2.22. The comparison of intensities aided by the alignment of WGP_2 at 45°, with respect to the grating grooves, which results in equal transmission of the two orientations to the SBD detector.

The intensity of the cSPr at the two orientations, $I_{\parallel}$ and $I_{\perp}$, is related to the measured intensity at the respective orientation of WGP_1, $M_{\parallel}$ and $M_{\perp}$, as shown in Eqs 6.6 and 6.7.

$$I_{\parallel} = C_f(M_{\parallel} - M_{noise}) \tag{6.6}$$

$$I_{\perp} = C_f(M_{\perp} - M_{noise}) \tag{6.7}$$

The intensity of the cSPr is reduced via interaction with the two WGPs. The reduction in signal is denoted by a constant factor, C_f, where it is assumed that all components other than the WGPs are polarization independent. The measured signal includes the noise component M_{noise} (the equivalent of C_4 in Eq. 6.5) as well as the cSPr component. An estimate of M_{noise} is obtained by measuring the signal intensity at the point where the two polarizers have a relative angle of 90° between them (this corresponds to an WGP_1 orientation of $-45°$

and 135°). In this position all cSPr is eliminated; the measured intensity is due to other components in the accelerator tunnel or noise from the detector and transport line.

From the intensity measurements taken during the polarizer-rotation scans the values of $M_{\parallel}$, $M_{\perp}$ and M_{noise} are obtained (at respective WGP orientations of 0° (180°), 90° (270°) and −45° (135°)). These are used to calculate a value for the DoP of cSPr at the current observation angle, as shown in Eq. 6.8.

$$DoP = \frac{I_{\parallel} - I_{\perp}}{I_{\parallel} + I_{\perp}} = \frac{M_{\parallel} - M_{\perp}}{M_{\parallel} + M_{\perp} - 2M_{noise}} \tag{6.8}$$

Whilst this method is significantly simpler than the fitting routine described in the previous section, there are some clear disadvantages. Unlike the fitting routine, which uses information from the whole rotation scan to inform the final result, this method uses only a limited number of the data points collected. Using all the data collected during the rotation scan reduces random error due to variations in the electron bunch and in the accelerator environment. Systematic errors in the recorded orientation of the WGPs may also be enhanced by not making use of the full set of data. This method assumes that there is no unpolarized background radiation emanating from the THz chamber.

Given these considerations, it seems reasonable to use the intensity comparison method as a check on the fitting routine analysis. Both methods are expected to yield similar results given that the background radiation component is small compared to the cSPr signal. A large discrepancy would signal that these conditions were not being met or would draw attention to a problem with the fitting routine. In the analysis of the polarizer-rotation scans, the fitting routine is used as the primary method of analysis; the intensity comparison is used only to confirm that the fits produce sensible results.

6.1.3 Raw Measurements

In this section a selection of rotation scans are presented. These scan were taken with

different gratings and at different observation angles. A broad range of results is shown, from rotation scans which measure highly polarized radiation to scans measuring unpolarized radiation. The fitting routine described in the previous section is used to obtain a value for the degree of polarization and the fit function is plotted over the raw data allowing for a visual assessment of the accuracy of the fitting routine. Five rotation scans, representing five different polarization states are given in Fig. 6.3.

The coefficient of determination, R^2, is a goodness of fit parameter used to assess the extent to which the fit describes the data for each polarizer-rotation scan. It is calculated using the sum of squares of the residuals SS_{res} and the total sum of squares SS_{tot}, as shown in Eq. 6.9.

$$R = 1 - \frac{SS_{res}}{SS_{tot}} = 1 - \frac{\sum_{i=1}^{n}(o_i - f_i)^2}{\sum_{i=1}^{n}(o_i - \mu_o)^2} \tag{6.9}$$

In Eq. 6.9, o_i is used to denoted the observed (measured) values, μ_o to denote the mean value of the dataset and f to denote the fit values.

The WGP_1 is aligned parallel to the grating grooves at an angle of 0° (and 180°) and perpendicular at an angle of 90° (and 270°). Visual inspection of the plots can provide a general outline of the observed behaviour. For example, in Fig. 6.3(a) the intensity of radiation measured at 0° is much higher than the intensity measured at 90°. This suggests that cSPr is strongly polarized parallel to the grating grooves and has a DoP close to 1. The fitting routine gives a value of C_2 equal to $-5.64° \pm 0.96°$ and a DoP of 0.820 ± 0.028. The fit function is observed to be a good representation of the measured data and residual analysis gives the coefficient of determination, R^2, as 0.977.

Analysis of Figs 6.3 (b-e) produces the following values for the DoP, calculated using the fitting routine: 0.344 ± 0.011, 0.093 ± 0.007, -0.002 ± 0.005 and -0.238 ± 0.022, respectively. All of the fits used to obtain these values have a goodness of fit parameter, R^2, higher than 0.88, indicating that the fitting routine consistently results in functions which represent the data well. These results are supported by visual interpretation of the plots, as the DoP decreases the balance of intensities between the maxima observed near 0° and the maxima

(a)

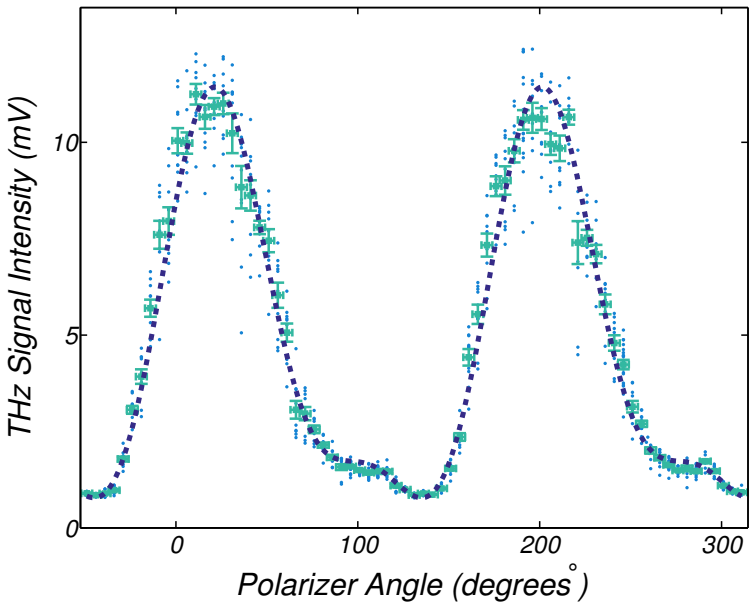
THz Signal Intensity (mV)
0
5
10
0
100
200
300
Polarizer Angle (degrees°)

(b)

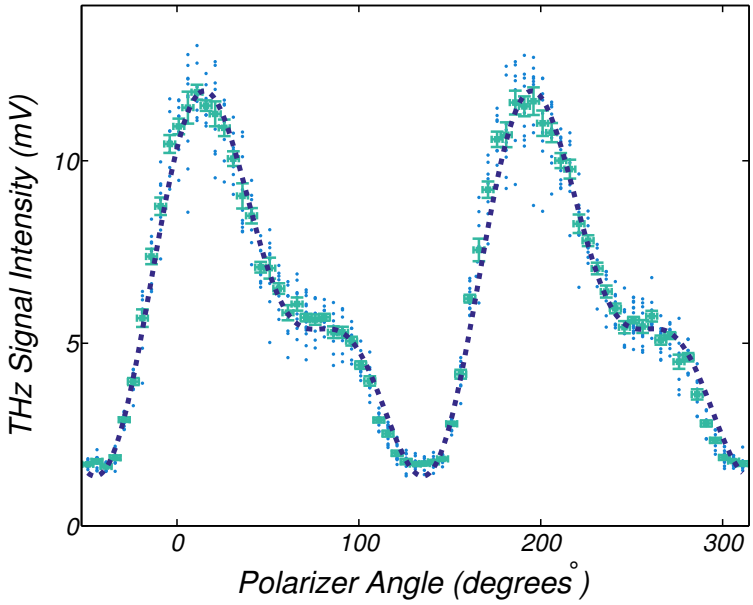
THz Signal Intensity (mV)
0
5
10
0
100
200
300
Polarizer Angle (degrees°)

(c)

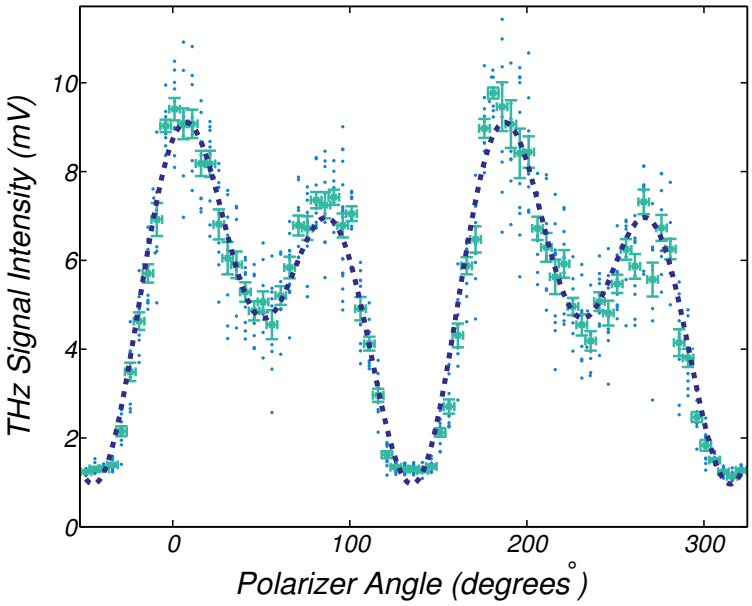
THz Signal Intensity (mV)
0
2
4
6
8
10
0
100
200
300
Polarizer Angle (degrees°)

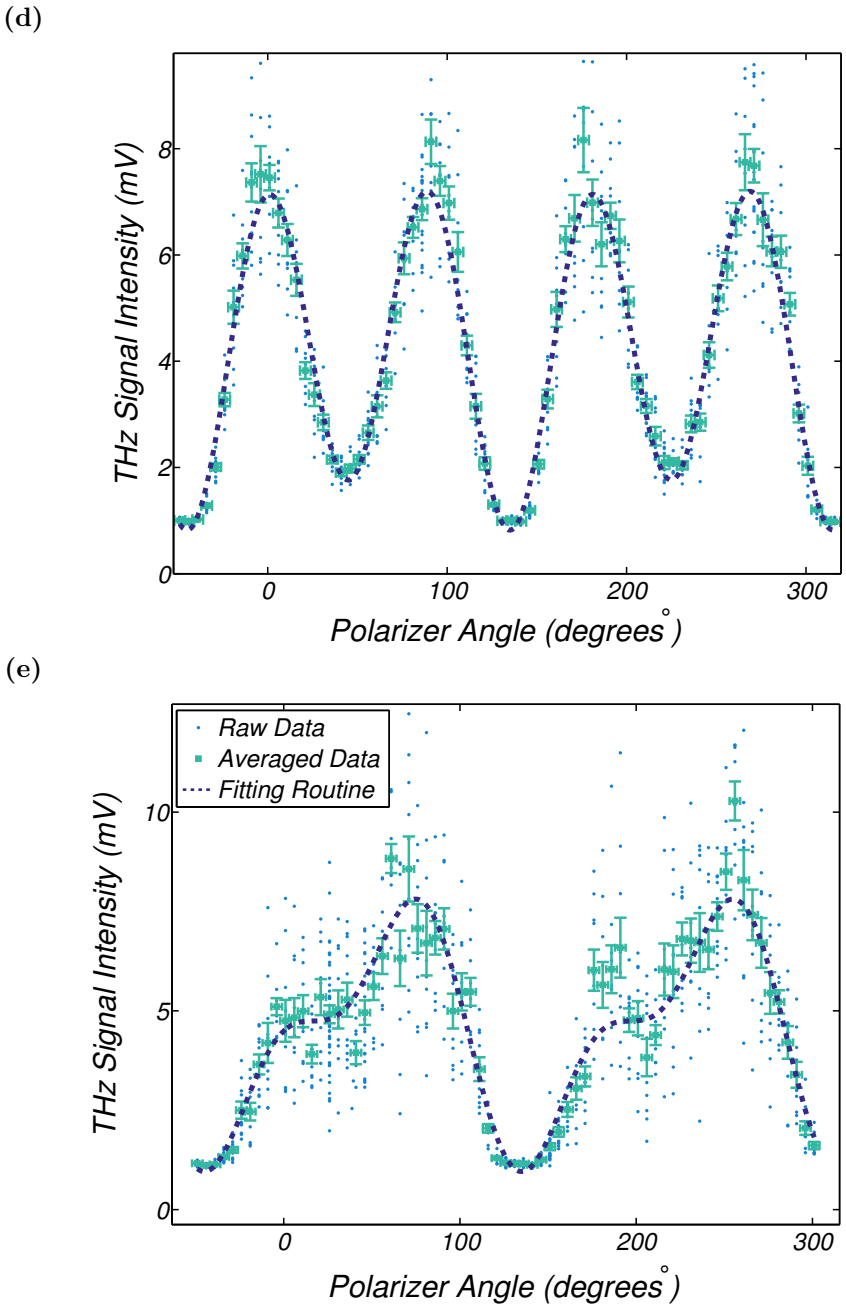

Figure 6.3: A selection of rotation scan measurements demonstrating the range of polarizations that were measured. In all of the rotation scans the wires of WGP_1 are: parallel to the grating grooves at 0° and 180°, perpendicular to the grating grooves at 90° and 270°, and perpendicular (crossed) to the wires of WGP_2 at −45° and 135°. For each position along the rotation scan 10 raw data points are given, along with the mean and standard deviation. The fitting routine described in Section 6.1.2 is also plotted. The scans presented here demonstrate measurements of a range of polarizations as follows: (a) highly polarized parallel to grating grooves (b) moderately polarized parallel to the grating grooves, (c) moderately polarized parallel to the grating grooves, (d) unpolarized and (e) slightly polarized perpendicular to the grating grooves. Calculated values of DoP given by the fitting routine are given in the main text.

observed near 90° gradually shifts.

In Fig. 6.3(d) the DoP is close to 0, indicating equal intensities of radiation polarized in both orientations (this is indistinguishable from unpolarized radiation in this experimental setup), this is supported by the observation of approximately equal maxima at 0° and 90°. In Fig. 6.3(e), the calculated DoP is below zero (-0.238 ± 0.022). This indicates that a larger proportion of the radiation is orientated perpendicular to the grating grooves, accordingly the maxima observed near 90° has a higher measured intensity than the maxima observed near 0°.

The agreement of the fitting routine results with the trends observed in Figs 6.3(a-e) provides confidence in this method of analysis for a variety of rotation scans. It is seen that good fits are found for a range of polarization results and this is supported by the coefficient of determination values, R^2, which are all close to 1. With a high level of confidence in the fitting routine it is now appropriate to proceed with analysis of the DoP results, comparing the results at different observation angles and with different gratings.

6.2 Comparison with Simulation

The overall aim of this series of experiments is to clarify whether the DoP of cSPr is distinguishable and if it is in agreement with the predictions made by the GFW simulation code, which was developed using the SCM theory of Smith-Purcell radiation. In order to achieve this aim, the experimental results are presented in this section alongside predictions of the DoP made by the GFW code.

6.2.1 Simulations with LUCX Parameters

In order to carry out simulations for the generation of cSPr at the LUCX facility appropriate input parameters are required. This ensures that the predictions of the intensity and DoP are accurate. Simulations demonstrating the code usage and providing a preliminary

assessment of the LUCX environment were carried out in Sections 2.4.1 and 4.3 respectively. In this section, the impact of key parameters is assessed systematically. The input parameters required for the GFW simulations describe the grating (periodicity, width and length), electron bunch, and the relative positions of the grating and the bunch. The post-processing code, which models specific measurement scenarios, needs the detector aperture and its relative position (with respect to the grating) as an input parameter. The dependency of the intensity and DoP measured in the LUCX experiment on these input parameters is investigated in this section. Parameters which are known to a high level of accuracy and do not vary throughout the experiment (such as the detector aperture and the grating dimensions) are not included in this investigation.

The input parameters which describe the electron bunch are the energy, charge and the bunch size (both transverse and longitudinal dimensions). The accuracy of the values used for these parameters is limited by the stability of the accelerator. The experimental response to a possible lack of stability is to take measurements over several bunches and use the mean and standard error. The average values are seen to be relatively constant over the course of an experimental run.

The energy of the bunch is relatively stable. The RF gun which brings the electrons to an energy of $\approx 8\,\mathrm{MeV}$ is well documented and its behaviour highly repeatable [81, 79]. The simulations in Fig. 2.7 (see Section 2.4.1) shows that variations in energy result in changes to both the intensity and the DoP of the resulting cSPr, however, these are small for variations on the order expected at LUCX.

The charge of the bunch is a more concerning parameter in terms of accelerator stability. As discussed in Appendix A the charge has been shown to vary significantly on a shot to shot basis. In particular, the location of a single FCT, upstream from the THz, does not provide an accurate charge measurement of the bunch generating cSPr. It is expected that some of the bunch is lost via interaction with the grating before the cSPr is generated. The fraction of the bunch lost is expected to vary over the course of the experiment as the relative position of the bunch and the grating changes. Given the lack of reliable measurements of the charge,

it is very important that its relationship with the intensity and DoP of the generated cSPr is well understood.

Whilst it is expected that the charge variation will cause significant variation to the intensity of the observed radiation, it is not expected to affect the DoP as shown in Fig. 2.9 (see Section 2.4.1). The value of charge used for the simulations in this section is 32 pC, which is representative of the typical values observed at the LUCX facility.

The transverse bunch size is measured using the scintillating screen (see Section 4.1.4), giving average dimensions of 300 µm× 300 µm. The screen is located 0.4 m downstream from the THz chamber, so a systematic error could be introduced by variation in the transverse dimensions between these positions. Changing the transverse beam size has a small effect on the simulation outcomes, but this is minimal compared to the effects of the other parameters.

The exact longitudinal bunch size is an unknown in the LUCX experiments. The current design of the single-shot cSPr monitor (see Chapter 3) requires using known values of the DoP of cSPr as part of the process of measuring the longitudinal bunch profile. It is, therefore, essential that these properties are independent of each other.

GFW was used to predict the intensity and DoP of cSPr generated by electron bunches of variable longitudinal length. The results of this simulation, carried out using typical beam parameters at LUCX, are shown in Fig. 6.4.

It is shown in Fig. 6.4 that while the variation in longitudinal bunch length effects the intensity of cSPr, the DoP remains unaltered. All subsequent GFW simulations assume a longitudinal bunch length of 250 fs and a Gaussian bunch shape as inputs.

It is more difficult to assess the relative position of the grating and the bunch, which ideally should remain stable over the course of the experiment. Variations are to be expected, as there is known to be beam drift and because of the necessity for repeated realignment of the gratings. During the experimental run it was required to move the grating plate in order to position each of the gratings next to the electron beam in turn; upon return to a previous grating realignment for optimal radiation production was required. Although the

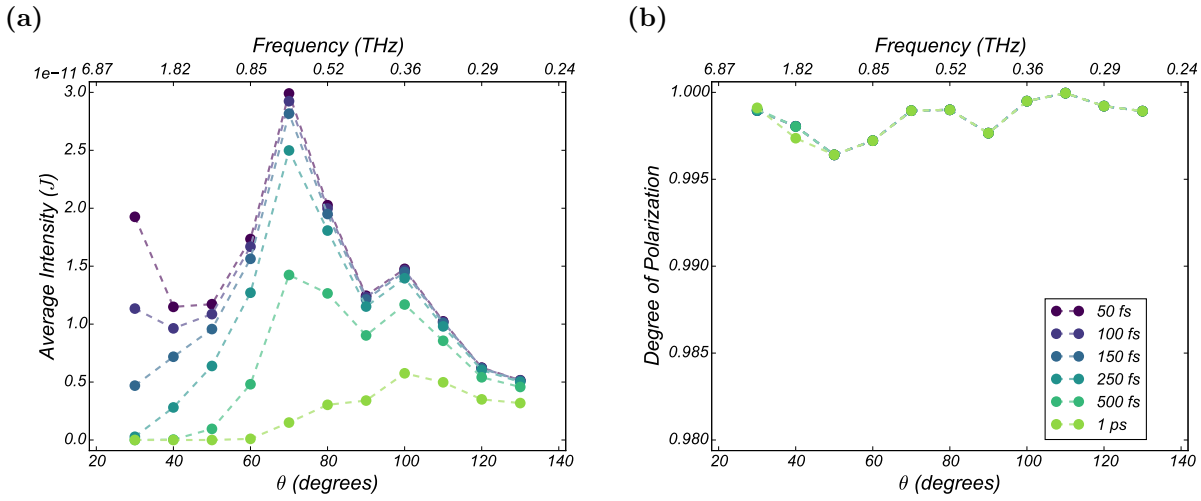

Figure 6.4: Simulations giving calculated (a) intensity and (b) DoP of cSPr generated by bunches of varying longitudinal bunch length. The results, at each observation angle considered (shown by the markers), are obtained by integrating over the detector aperture (for the setup during the polarizer-rotation scans). The central ϕ coordinate of the observation angle for each detector position is $\phi = 0°$. The cSPr is generated using a 0.7 mm period sawtooth grating. The accelerator parameters used for these simulations are given in Table 4.1 and as discussed in the text.

beam was seen to drift over the course a day, there is not thought to be a large amount of bunch to bunch variation in beam position. Variation in the beam-grating separation on a timescale longer than that of an individual rotation scan, would hinder attempts to compare the results to the GFW simulations. It is a feature of the surface current model (and other models), and shown by simulation in Fig. 6.5(a), that the intensity of cSPr drops exponentially as the beam-grating separation increases.

In Fig. 6.5(a), a peak in intensity is seen for a beam-grating separation of 1 mm, for values below this it can be assumed that a significant proportion of electrons are lost through collision with the grating plate. As the beam-grating separation is increased the intensity rapidly drops at all observation angles (θ). This was also shown experimentally at LUCX in Fig. 4.11 (see Section 4.4.1). The simulation of DoP dependence on beam-grating separation, shown in Fig. 6.5(b), predicts that variation of this parameter will have only a small effect on the polarization of cSPr. So while the uncertainty in the separation may present problems for comparative intensity measurements it should not affect the analysis of the polarizer-rotation scan results.

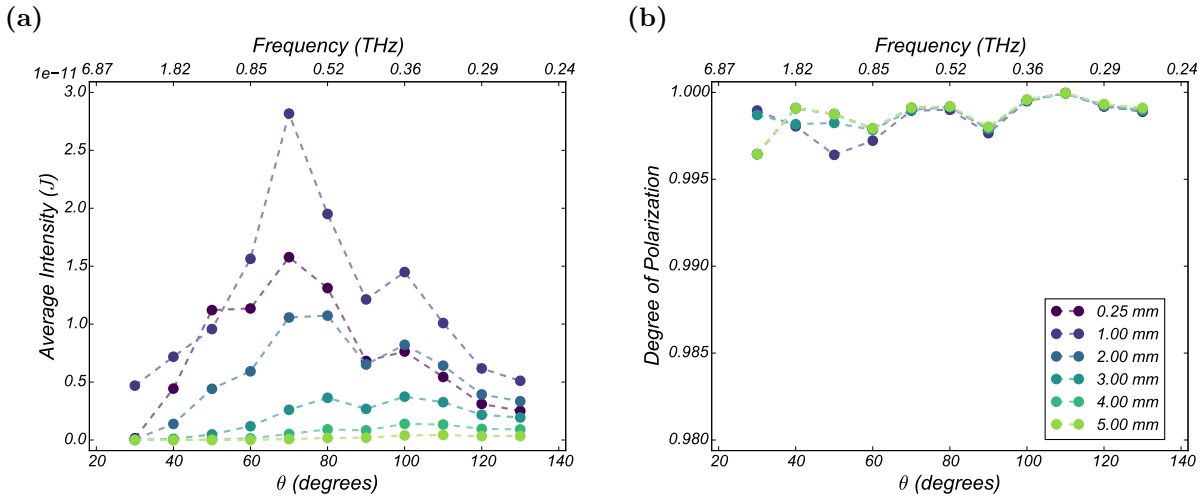

Figure 6.5: Simulations giving calculated (a) intensity and (b) DoP of cSPr generated for a range of beam-grating separations (see legend). The results, at each observation angle considered (shown by the markers), are obtained by integrating over the detector aperture (for the setup during the polarizer-rotation scans). The central ϕ coordinate of the observation angle for each detector position is $\phi = 0°$. The cSPr is generated using a 0.7 mm period sawtooth grating. The accelerator parameters used for these simulations are given in Table 4.1 and as discussed in the text.

The final simulation input parameter to be assessed is the relative position of the detector and the periodic grating. The experimental scheme, in particular the mechanical protractor, have hugely increased the reliability of the information about the position of the detector - in comparison with the measurements made in Chapter 4. The detector remains at the same height above the optical table at each observation angle, and no detector realignment was carried out during the experimental run. There is, however, some uncertainty in the observation angle, caused by the mechanical fit of the experiment plate and the mechanical protractor. This uncertainty was measured to be $\theta \pm 2.5°$, and is included in all the analysis of the experimental results.

The observation angle also has a ϕ coordinate which is determined by the relative alignment of the grating, electron beam and the detector aperture. By fixing the alignment of the detector, the variation in ϕ between the polarizer-rotation scans is reduced. However, the alignment of the grating and the electron beam with respect to the detector is difficult to monitor and has the potential to vary over time. To have an observation angle of ϕ=0°, the centre of the grating must be aligned with the detector aperture and the grating plate must be oriented in the y-z plane. At LUCX, the first can be achieved to a high level of

precision (± 1 mm), however, the second is more difficult. It is estimated that the grating plate (see Fig. 4.5) is aligned with the y-z plane to within 5° of accuracy, this gives an error on the ϕ observation angle of $\pm$ 5°. Deviation of the grating plate, on the order of 5° along the ϕ axis, would have been difficult to observe from outside the THz chamber (see Fig. 4.2). The ϕ observation angle error could also vary between the polarizer-rotation scans due to the realignment of the grating and shifts in the beam position.

It has previously been shown, in GFW simulations using LUCX parameters, that variation of the ϕ angle of observation will change both the measured intensity and DoP (see Fig. 4.10). As this uncertainty could not be eliminated from the experimental procedure, the results of the rotation scans will be presented alongside GFW simulations for a range of ϕ observation angles.

6.2.2 The Sawtooth Gratings

In Fig. 6.6 the DoP values extracted from the rotation scans measurements for both sawtooth gratings are presented. The 0.7 mm period sawtooth grating results, Fig. 6.6(a), show DoP values for 11 observation angles. These observation angles have cSPr of sufficient intensity for detection, frequencies within the range of the SBD detector and a clear path for the radiation from the grating through the vacuum window. The results from rotation scans using the 1.0 mm period sawtooth grating are given in Fig. 6.6(b). DoP values were obtained for 7 observation angles; angles greater than 95.5° (0.27 THz) corresponded to frequencies below the lower cutoff of the SBD detector.

The results from both of the sawtooth gratings were analysed using the fitting routine and a comparison of intensities, referred to in the legend of Fig. 6.6 as Method 1 and Method 2, respectively. This figure shows general agreement between the values of the DoP calculated by both methods, within the range of their uncertainty. Any differences in the results are likely due to the comparison method not accounting for any unpolarized background radiation originating in the THz chamber (the possibility of unpolarized background radiation is allowed in the Method 1 fitting routine). The general agreement between the two methods

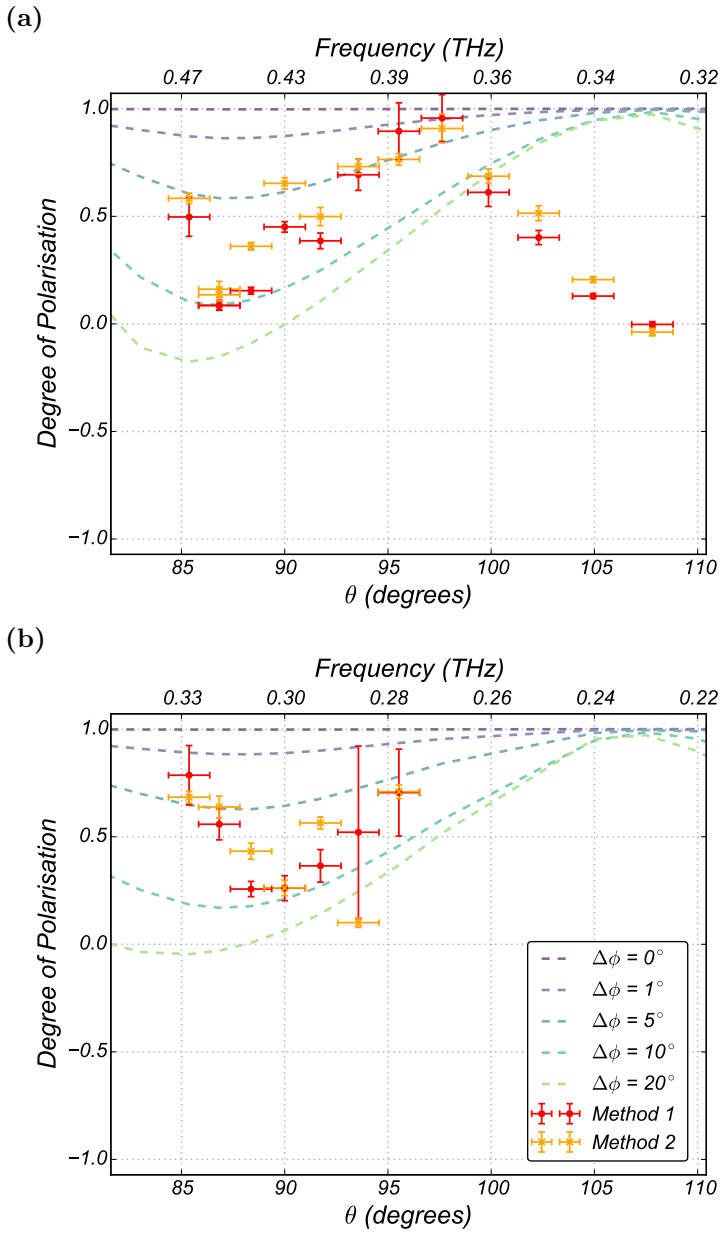

Figure 6.6: Comparison between GFW simulations and experimental measurements of the DoP of cSPr, the radiation is generated by (a) the 0.7 mm period and (b) the 1.0 mm period sawtooth gratings. Both analysis methods are used and are labelled in the legend: Method 1 refers to the fitting routine described in Section 6.1.2 and Method 2 refers to the intensity comparison described in Section 6.1.2. The results of the GFW simulations are given over the whole range of observation angles covered in the experiment. Both the (a) intensity and the (b) DoP are integrated over the detector aperture (constant for all of the polarizer-rotation scans) to give realistic measurement predictions. The simulations are plotted for varying ϕ displacement ($\Delta\phi$) from the ideal observation angle, which is centred around ϕ=0°.

increases confidence in the fitting routine and where there is disagreement, the DoP value calculated using the fitting routine is given preference.

It was discussed, in the previous section, that there is significant uncertainty in the ϕ observation angle at which the cSPr is observed during the polarizer-rotation scans. The results of the GFW simulations, also plotted in Fig. 6.6, show predicted values of the intensity and DoP over a range of ϕ observation angles (integrated over the detector aperture). In an ideal experimental scenario the detector is centred at ϕ=0°, the results are plotted in terms of deviation from this ideal position ($\Delta\phi$), exploring the effects of altering the ϕ observation angle by up to 20°.

It is clear from Fig. 6.6 that the sawtooth grating polarization measurements deviate from the values calculated by the GFW simulation for some observation angles. The simulations predict that a detector centred at $\phi = 0$, with the aperture used during the polarizer-rotation scans, would measure cSPr which is very strongly polarized in the direction of the grating grooves (DoP ≈ 1). The results show cSPr which is polarized in the direction of the grating grooves (in all but one measurement), however, the value of the DoP measured is less than is expected (<1) for an observation angle of ϕ=0° in almost all the measurements.

On the other hand, agreement can be found between the GFW simulations and the experimental results if a larger range of ϕ observation angles is considered. The values seen in the θ observation angle range from 85.4° to 97.6° could be explained by a variable ϕ observation angle, in the range of ϕ= 5° to ϕ= 10°. A systematic error in the ϕ observation angle could be due to misalignment of the grating plate in the y-z plane, is was not possible to confirm this due to constraints of the accelerator system. The ϕ observation angle could vary between scans, due to grating realignment and shifts in the beam position.

This hypothesis explains the results observed up to the observation angle of 100 , however, strong deviations from the predictions are seen in the range of θ observation angles from 100° to 107.8° (this θ range only includes measurements taken using the 0.7 mm period sawtooth grating). The results in this range show significant disagreement between the experimental measurements and the predictions made by the GFW simulations. This feature of the

experimental data cannot be explained by variation of any of the inputs to the simulation. It seems likely that some element in the experimental setup was obstructing the measurement of the polarization of cSPr over the full range of observation angles. This is discussed in more detail in the following sections of this chapter.

6.2.3 The Strip Grating

The results from the rotation scans which used the 0.7 mm period strip grating are presented in Fig. 6.7. Similarly to the 0.7 mm period sawtooth grating, these measurements come from 12 observation angles (θ) covering the range 85.4° to 111.0°. Again, both the fitting routine and intensity comparison methods were used to analyse the results and extract a value of the DoP, labelled as Method 1 and Method 2 in Fig. 6.7, respectively. As previously, general agreement is found between the results obtained using the two methods. The one considerable error, seen for the fitting routine DoP value at the θ observation angle 111.0°, is likely due to the low intensity of the cSPr signal at this position. In the absence of a strong cSPr signal, noise and background radiation will dominate the measurement, causing a poor fit with high uncertainty.

The results of the polarization measurements of the cSPr generated by the strip grating consistently show that the measured radiation has a DoP between 0 and 1. This indicates a trend of polarization parallel to the grating grooves, in line with theoretical predictions. Figure 6.7, however, shows significant discrepancies between the values of DoP predicted by the GFW simulations and the experimental results. The GFW simulations predict that the cSPr generated by a strip grating is completely polarized in the direction of the grating grooves and has a DoP of 1 for all observation angles. Only two of the 12 measurements agree with this prediction and one of these is the result at θ observation angle 111.0° which, as previously noted, has particularly high levels of uncertainty.

Unlike the analysis of the sawtooth gratings, as described in Section 6.2.3, it is not possible to explain this discrepancy by considering the uncertainty in the expected ϕ observation angle (ϕ=0°). Figure 6.7, shows even for relatively large deviations from the ideal ϕ observation

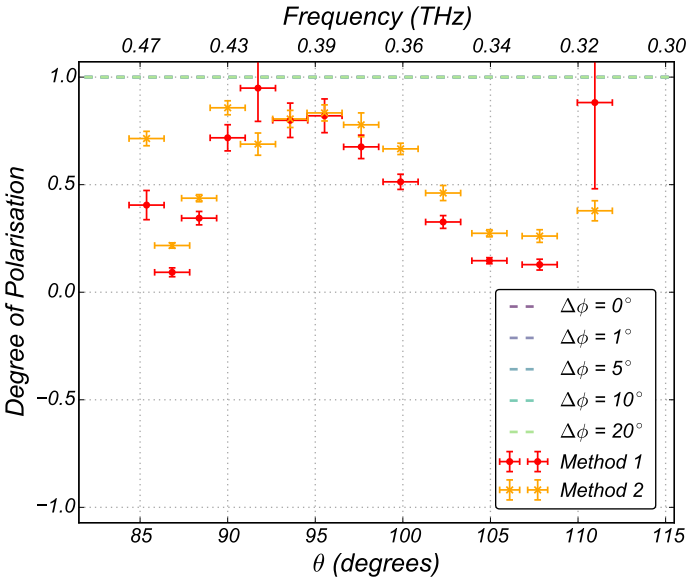

Figure 6.7: Comparison between GFW simulations and experimental measurements for the DoP of cSPr generated by the 0.7 mm period strip grating. Both analysis methods are used and are labelled in the legend: Method 1 refers to the fitting routine described in Section 6.1.2 and Method 2 refers to the intensity comparison described in Section 6.1.2. The results of the GFW simulations are given over the whole range of observation angles covered in the experiment. Both the (a) intensity and the (b) DoP are integrated over the detector aperture (constant for all of the polarizer-rotation scans) to give realistic measurement predictions. The simulations are plotted for varying ϕ displacement ($\Delta\phi$) from the ideal observation angle, which is centred around ϕ=0°.

angle ($\Delta\phi$=20°), the DoP is expected to be equal to 1.

The results presented in this section, for all three gratings, show distinctive polarization of cSPr. In particular, in almost all measurements the radiation is shown to be predominately polarized parallel to the grating grooves, showing general agreement with the GFW simulations. This distinctiveness of the measured polarization supports the proposal to use this feature of cSPr to separate it from background radiation in the single-shot monitor. In order to proceed, however, the discrepancies between the experimental results and the GFW simulations must be addressed.

.

6.3 Analysis of Discrepancy between Simulation and Experiment

It is clear, from the analysis of the experimental results for the measurement of the DoP of cSPr at LUCX, that there is significant deviation from what is predicted by GFW simulations. This section considers possible causes for this, discussing potential sources of errors in both the GFW codes and the experimental procedure.

6.3.1 Limitations of the GFW Simulations

The GFW simulations, used in this thesis to describe the intensity and DoP distributions, are based on the SCM, as outlined in Section. 2.4.1. When considering problems with these simulations it is important to distinguish between issues with the implementation, specific to the GFW code, and failings in the model itself.

There have been many previous experiments [52, 30, 58, 60, 31, 32] to test the predictions made by the SCM, these have shown high levels of agreement between the model and the measured intensity distribution of cSPr. Experimental results that show discrepancy with

the SCM have been reported [59, 115], however, the simulation of these experiments was flawed. In one instance the coherence effects were neglected and in another coherence effects were enforced on an incoherent regime. This catalogue of successful experimental evidence makes a compelling case for the validity of the SCM.

Although the SCM has been used to predict experimental results successfully, in almost all cases it has been used to predict the intensity distribution of cSPr over a range of θ observation angles. It is possible that there is a specific problem in the theory (or in its adaptation in the GFW code) with its handling of the polarization of cSPr. To test this, the predictions of DoP made by GFW simulations will be compared to the predictions made by a PIC simulation.

Simulations developed with the 3D MAGIC software were used to test the GFW simulation predictions of the DoP. MAGIC is a electromagnetic, particle in cell (PIC) software used primarily to solve problems in vacuum electronics and plasma physics. The 3D MAGIC software is used in the defence industry to design active and passive electromagnetic devices where it has been shown to be a powerful and reliable tool. It is able to handle the interactions between space-charge, electromagnetic fields and background gaseous media. Finite different, time domain (FDTD) methods are used to solve Maxwell's equations and to evolve the fields over time. The Lorentz force equation is solved to calculate the trajectories of relativistic particles and the continuity equation to obtain the charge and current densities. This approach, known as EM PIC FDTD, provides self-consistent interaction between the charge particles and the electromagnetic fields. The software also has algorithms to generate structural geometries (such as periodic gratings) making it suitable for application to cSPr generation [116, 117, 118].

As this type of PIC code requires a large amount of computational resources, the experimental setup used at LUCX could not be reproduced exactly. Instead a stripped down version of the experiment was used, with a sawtooth grating of length 10 mm (instead of 60 mm). A GFW simulation was also carried out specifically for this comparison, using a reduced length grating.

Unlike the GFW code, which estimates the intensity distribution of cSPr in the far field, the MAGIC PIC code calculates a snapshot of the electric field in the near field. By looking at the distribution of the frequencies present in the near field, accessed using a Fourier transform of the electric field, and the dispersion relation of Smith-Purcell radiation (Eq. 2.1) an estimate of the intensity distribution in the far field can be made. The intensity of the different field orientations is then used to obtain a corresponding DoP value at each position.

The MAGIC code includes features of the experimental scenario which are excluded in the idealised GFW code. For example, other radiation effects - such as the diffraction radiation caused by the interaction of the electron beam with the edge of the grating - are included in the signal. The predictions made by the MAGIC code for the strip grating in particular, consider the practical realities of this grating profile. In the GFW simulations the strip grating is treated as strips of metal separated by strips of vacuum, the effect of the recesses in the grating profile are completely ignored.

As the two simulations, GFW and MAGIC, have very different properties they cannot be expected to produced identical results. On the other hand, this means that they are also unlikely to have the same faults. In the following comparison, shown in Fig. 6.8, the results of the two simulations are compared to find the extent of the agreement between them.

The GFW code and the MAGIC, PIC code both predict that cSPr observed by a detector centred around $\phi = 0$ is highly polarized in the direction of the grating grooves. This is shown for a range of observation angles (θ) and for both strip and sawtooth gratings using parameters similar to those encountered at the LUCX facility.

Over all the observation angles (θ) shown in Fig. 6.8 the two simulation codes make predictions of the DoP of cSPr with less than 1.5% difference between the values. Additionally, the differences observed between the predictions made by the two codes are considerably smaller than the experimental error in the values obtained by experiment.

The distinction made by the GFW simulation, that the strip grating will generate cSPr

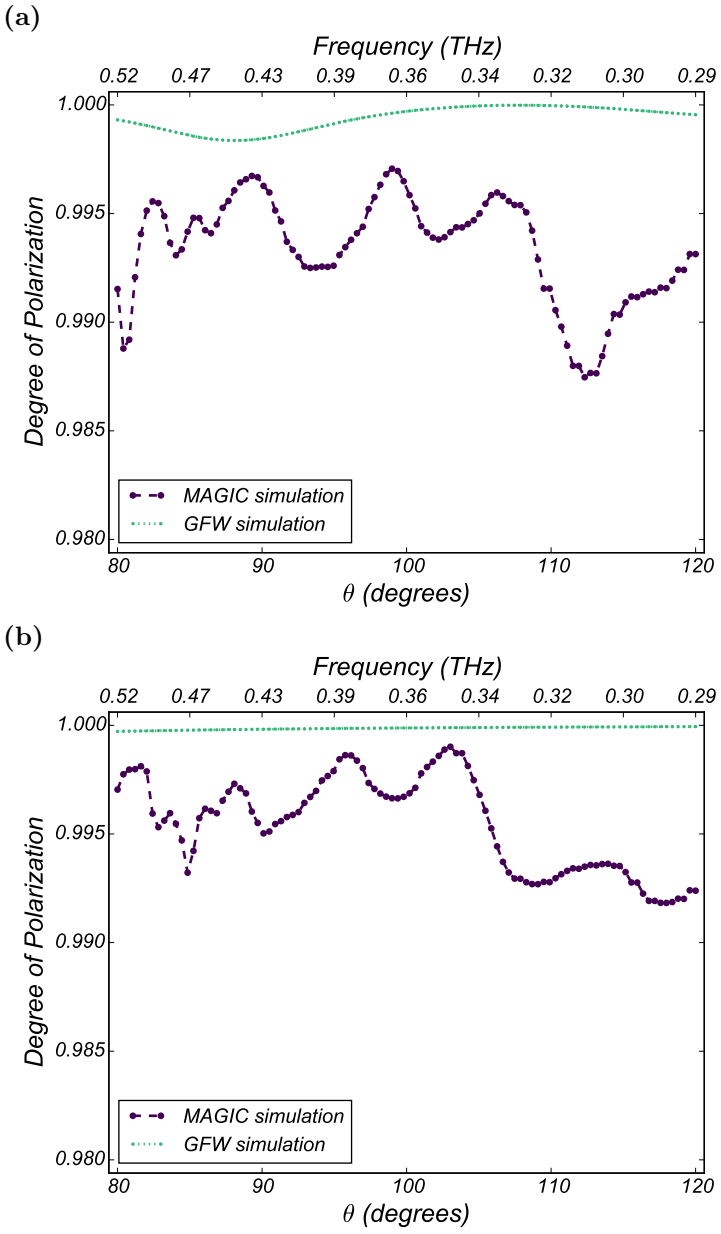

Figure 6.8: The predictions of DoP made by GFW and MAGIC simulations are compared for the 0.7 mm period (a) sawtooth and (b) strip gratings. The input parameters are similar to the LUCX experiments, but with a reduced grating length (10 mm). Both simulations use the ideal ϕ observation angle (ϕ=0°) and the results are integrated over the detector aperture (as used during the polarizer-rotation scans).

completely polarized in the direction of the grating grooves, is not observed in the PIC simulations. This is likely due to the more realistic modelling of the strip grating profile, which includes the recesses, in the MAGIC code.

The agreement shown between the two types of simulation is considerable, relative to the disagreement seen between the GFW simulations and the experimental results. The predicted DoP values for the two simulations have less that 1% different between them. The observed differences between the two simulations are small, compared to the experimental error, and can be explained by the differences in the construction of each model. The confirmation of the DOP values calculated by GFW shifts the emphasis of the investigation to the experimental setup.

6.3.2 Limitations of the Experimental Apparatus

In Fig. 6.9 the results for the DoP of cSPr, from the rotation scans carried out with both of the gratings with a periodicity of 0.7 mm, are plotted together. The results (both obtained using the fitting routine) for these two gratings illustrate similar patterns across the frequency range. In particular, although the GFW simulations predict different results for the strip and sawtooth gratings, the two gratings show similar results at most frequencies. The similarity in the DoP results suggests that systematic errors, rather than random errors, are being introduced into the system.

By excluding other components, the sapphire vacuum window (described in Section 4.2.1) has been identified as a possible source of error. This component remains in a fixed position throughout the experiment, therefore, the angle between the window and the SBD detector vary as the observation angle is changed. Additionally, there is very limited information on the interaction of polarized radiation and sapphire in the THz frequency range.

As previously mentioned in Section 4.2.1 sapphire (Al_2O_3) is a commonly used transparent material in the THz frequency range, as it remains largely transparent to up to 2 THz. Although sapphire is a birefringent material, z-cut optical components made with it do not

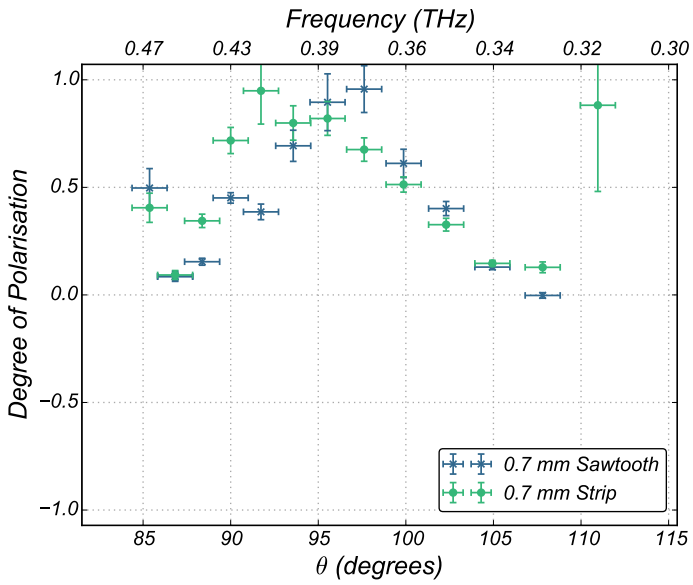

Figure 6.9: Comparing the DoP results for both 0.7 mm periodic gratings in order to better understand the patterns observed experimentally. Both sets of DoP results are obtained using the fitting routine (Method 1).

have a polarization dependence for radiation at normal incidence and in this case would transmit the two linear polarizations of interest equally.

If we assume that the window is indeed z-cut, then it is reasonable to expect that the polarization measurement will not be affected by the window. The experimental procedure, however, changes the observation angle of the detection system with respect to the window , hence, altering the incidence angle of the observed radiation on the window. Deviation from normal incidence, not a typical scenario for an optical component, reintroduces birefringence into the system.

A material that can support two different propagation vectors is considered birefringent, in practise this means that the refractive index experienced by radiation travelling through the material depends on its polarization. Two linearly polarized waves orientated perpendicular to each other will travel through a birefringent material at different speeds and emerge at different angles because of this. When the two linearly polarized waves recombine after travelling through the sapphire window a phase difference will be introduced between them [119, 102]. The phase shift could cause the polarization properties of the radiation to be altered, causing circular of elliptical polarization states that this experimental procedure is

not able to analyse.

The hypothesis that the polarization independence of the sapphire window was compromised by taking measurements at non-normal angles is supported by the experimental results. The high DoP which was predicted by the simulations is observed at observation angles close to 90°, while the results exhibit much lower DoP values at the observation angles furthest from 90°. This behaviour could not be tested or corrected within the scope of this experiment (the window is an integral part of the accelerator and cannot be easily changed), but future experiments should make changes to the vacuum window used when attempting polarization measurements.

Appropriate changes to the vacuum window could include: calibration of the results using measurements from a THz source with a known polarization, the replacement of the sapphire vacuum window with non-birefringent material such as silicon or substituting the one large window used in this experiment with a set of smaller vacuum windows so that the cSPr always has near normal incidence on the window. Indeed, the E203 multi-shot monitor and the proposed design for the single-shot monitor both have arrays of small window ports (see Fig. 3.3), each of which serves a different detection channel, so similar problems may be avoided when using these systems.

6.3.3 Conclusions of the Polarization Study

This polarization study was begun in order to demonstrate that reliable and accurate predictions of the DoP of cSPR be made for a range of frequencies and grating profiles. This is needed in order to implement polarization selection as a method for the elimination of background radiation in the proposed single-shot, cSPr, longitudinal bunch profile monitor.

This study has consistently measured cSPr which is highly polarized in the parallel to the grating grooves, in line with the predictions made by the SCM (and calculated using the GFW code). The measurement of a distinctive extrapolation supports the case for its use to differentiate between the cSPr signal and the background radiation in the single-shot, cSPr

monitor. However, within the time frame of this study it has not been possible to reconcile the detailed predictions of the SCM with the experimental measurements of the DoP.

The experimental layout designed for the polarization measurements allowed for confirmation of the presence of cSPr in each location and simplified the analysis by removing the polarization dependence of components including the SBD detector. With the removal of other unknowns from the experiments at the LUCX facility, problems with the experimental procedure were isolated to the sapphire vacuum window. It is suggested that using another material, such as silicon, or changing the configuration of the window would alleviate this problem.

This study has shown promising results and should be continued as part of the development work for the cSPr, single-shot monitor. A robust method for conducting this type of measurement has been developed and the recommendations made should be incorporated into future work.

The challenges of performing this type of experimental study in the THz frequency range, where there is a lack of sources for calibration and very little supporting research into the properties of materials, have been highlighted throughout this study. The lack of available experimental apparatus for studying the properties of THz radiation, lead to the development of a system for measuring both the frequency and polarization at a range of observation angles. The FPi design for frequency measurements, allowed for the testing of different beamsplitters and provided a new option for researchers studying THz radiation in space restricted environments.

6.4 Summary

In this chapter the results of the experiment, carried out at the LUCX facility, to investigate the polarization of cSPr are presented and discussed. An explanation of the experimental scheme, mentioned in the previous chapter, is expanded upon - providing more details about the rotation scans used to measure the DoP. The fitting routine used to analyse the results

of the rotation scans is derived and is compared to a simpler method which compares the intensities at different points in the scan. Examples are given, showing that the fitting routine can model several very different rotation scan measurements. The results of the fit are used to calculate the DoP.

GFW simulations are used to study the effect of potential sources of uncertainty in the experiment on the measured DoP. The final simulations, which take into account the uncertainty in the ϕ position of the SBD detector, are compared to the experimental results for the three gratings used. The analysis shows that there is some agreement between the results measured using the sawtooth gratings and the GFW simulations, but substantial disagreement is seen in the case of the strip grating.

Potential causes of discrepancy are considered, taking into account the limitations of the GFW simulations and the experimental procedure and apparatus. The GFW simulations are compared to PIC simulations which consider only the near field behaviour of cSPr. There is shown to be significant agreement between the two types of simulation. The properties of the sapphire vacuum window are discussed, in particular the potential for polarization dependence at non-normal incidence angles.

It is concluded that the sapphire vacuum window is the most likely cause of the discrepancy between the experimental results and the GFW simulations of the experiment. In order to obtain improved experimental results it is necessary to either calibrate the effect of the window, replace it with a non-birefringent material or redesign the experiment. A different experimental scheme could use a series of small ports at different observation angles, positioned so that all detected cSPr travelled through a vacuum window at near normal incidence.

Future investigations into the polarization of cSPr will be able to learn from the design and analysis work carried out as part of this study. In particular, the care required when selecting components (such as vacuum windows), in a frequency region with limited material studies (THz range), is highlighted.

Chapter 7

An Overview of Phase Recovery Techniques

In Chapter 2, the connection between the intensity distribution of cSPr and the longitudinal profile of the inducing electron bunch is outlined. The focus of this chapter is the process by which the information about the longitudinal bunch profile is obtained, once the intensity distribution has been measured. Successfully reconstructing the longitudinal profiles from the measured frequency spectrum, is the final step in the process of a cSPr diagnostic. This, however, is not a straightforward process and remains an area of active research.

In this chapter, the phase reconstruction problem and the challenge it creates when reconstructing longitudinal bunch profiles, are introduced. Several methods used to overcome this are introduced, their strengths and weaknesses analysed.

7.0.1 The ρ Function

The measured frequency spectrum of cSPr, generated by a particular electron bunch, contains within it information about the longitudinal profile of the bunch, as shown by Eq. 2.21. The longitudinal component can be isolated given that the single electron yield, the charge and the transverse profile of the bunch are known. The isolated component, known as the form

factor $F(\omega)$, is shown in Eq. 7.1.

$$F(\omega) = \rho(\omega)^2 = \left| \int_{-\infty}^{\infty} T(t) e^{-i\omega t} dt \right|^2 \tag{7.1}$$

The form factor is the square of the amplitude of the Fourier transform of the longitudinal distribution ($T(t)$) or the ρ function associated with the bunch profile.

In order to recover the longitudinal profile, $T(t)$, an inverse Fourier transform must be performed (as shown in Eq. 7.2). Even if perfect measurement over the whole frequency domain were possible, the frequency spectrum does not provide all the information required to do to this. As the form factor has the symmetry $F(-\omega) = F(\omega)$ the inverse transform gives only the even component of the longitudinal bunch profile. This will always result in a longitudinal bunch profile which is symmetric along the t axis [120].

$$T(t) = \int_{-\infty}^{\infty} \sqrt{F(\omega)} \cos(\omega t) dw \tag{7.2}$$

More importantly, the measured form factor $F(\omega)$ gives us information about the amplitude of the field $\rho(\omega)$ but not its phase $\psi(\omega)$. This can be shown by considering the complex form factor amplitude $\hat{S}(\omega)$ as in Eq. 7.3, where $F(\omega) = \hat{S}(\omega)\hat{S}^*(\omega) = \rho(\omega)^2$.

$$\hat{S}(\omega) = \int_{-\infty}^{\infty} T(t) e^{-i\omega t} dt = \rho(\omega) e^{i\psi(\omega)} \tag{7.3}$$

The following section will discuss various methods of obtaining the longitudinal bunch profile from the measured form factor, including solutions to the phase retrieval problem.

7.1 Reconstruction Methods

The phase retrieval problem appears in a wide variety of fields (e.g. crystallography [121], microscopy [122]) and various methods have been developed to deal with it. Although the

methods outlined in this section can provide high quality reconstructions, it should be noted that in the absence of measuring the phase it is only possible to obtain an estimate of the profile.

The true phase associated with the profile (as used in Eq. 7.3), is the sum of the minimal phase and the Blaschke phase, as shown in Eq. 7.4.

$$\psi\omega = \psi_m(\omega) + \psi_{Blaschke}(\omega) \tag{7.4}$$

The Blaschke phase contributions cannot be determined experimentally, therefore, only the minimal phase can can be obtained using the measurement of $\rho(\omega)$. When there are no zeros in the complex form factor $\hat{S}(\omega)$, the minimal phase approximation $\psi(\omega) = \psi_m(\omega)$ can be used. In many cases, the minimal phase contribution is sufficient to perform an accurate reconstruction of the longitudinal bunch profile [123].

7.1.1 The Library Search Method

Early reconstructions of the longitudinal profile using cSPr used a library of potential profiles. The measured ρ values are compared with the expected ρ function of a large number of profiles. This could be considered as multi-parameter fit, with parameters such as bunch length, overall bunch shape (for example Gaussian or triangular profiles) and asymmetry [58]. A large number of parameters would result in a larger library and more computing power would be needed [31]. Even with a very large library this method is restricted to a finite number of profiles. It can be used to confirm a known profile or as a good cross check with other methods.

7.1.2 The Kramers-Kronig Method

The Kramers-Kronig (KK) relations provide a method for linking the real and imaginary parts of a complex function using Cauchy's theorem. When applied to physical systems it

must be assumed that the systems are linear and causal [53]. A system which generates cSPr can be considered to be linear as the total electric field is proportional to the number of particles in the bunch. The causality condition is met by the fact that cSPr cannot be emitted before the electron bunch has passed over the grating [31].

The KK relations were first applied to the problem of longitudinal bunch reconstruction by Lai and Sievers in 1994 in a paper that primarily considers the reconstruction of the profile from far-infrared radiation generated by coherent synchrotron radiation [120]. The following derivation is drawn from a series of papers published by Lai and Sievers [120, 124, 123]. A mathematically rigorous derivation of this can also be found in the literature [125, 56].

Starting with the definition of the complex form factor amplitude given in Eq. 7.3 and taking logarithms gives the expression in Eq. 7.5.

$$\ln \hat{S}(\omega) = \ln \rho(\omega) + i\psi(\omega) \tag{7.5}$$

Application of the KK relations provides a solution for the minimal phase as shown in Eq. 7.6, where P denotes the principal integral value.

$$\psi(\omega)_m = \frac{-2\omega}{\pi} P \int_0^\infty \frac{\ln[\rho(\omega')/\rho(\omega)]}{\omega'^2 - \omega^2} d\omega' \tag{7.6}$$

Using the minimal phase approximation, the estimate obtained by Eq. 7.6 is assumed to be a good estimate for the true phase $\psi(\omega)$. This value is then used to calculate the longitudinal profile by taking the inverse Fourier transform of Eq. 7.3. It should be noted that this method does not distinguish between the form factor amplitude $\hat{S}(\omega)$ and its conjugate $\hat{S}^*(\omega)$ with the result that any profile is indistinguishable from its mirror image (where the profile is flipped back to front along the time axis). In many cases it may be obvious to the user which way round the profile should be. This may, however, present difficulties when working with highly variable bunch shapes.

The KK relations, with the minimal phase approximation, are generally appropriate for

carrying out the reconstruction of smooth bunch profiles with continuous derivatives (as this will avoid zeros in the complex form factor)[31]. On the other hand, this method of profile reconstruction has been shown to be inappropriate in cases where the bunch resembles a Lorentzian function or if it approximates a double Gaussian function where the two Gaussian have significant variation in width[73].

The KK method has been used experimentally to reconstruct longitudinal bunch profiles using $\rho(\omega)$ values measured from both cSPr [31, 32] and coherent transition radiation [29, 13, 126].

7.1.3 Iterative Solutions

An alternative branch of solutions to the KK method is the use of iterative methods to obtain a value for the phase. In particular, a group of iterative solutions known as projective algorithms; the estimate of the phase is obtained through a repeated cycle of Fourier transforms which alternate between the time and frequency domains. The iterative solutions, in general, require some additional constraints in order to reconstruct the profile accurately. For longitudinal bunch profile reconstruction these constraints can include requiring that the function in the time-domain, $T(t)$, is real and positive.

In 1972, Gerchberg and Saxton developed the GS algorithm, the first iterative algorithm for phase retrieval. The GS algorithm was developed principally for use in electron microscopy and X-ray diffraction techniques [127]. The algorithm is seeded using a random array of numbers as an initial estimate. Fourier transforms are used to cycle between the frequency and time domains. In each cycle, constraints are applied to the functions in both domains. The constraints placed on the profile vary depending on the physical problem being solved. This typically includes requiring the function to be real and positive in the time domain. Additionally, a condition may be applied which requires the function to go to zero outside of a pre-defined support function.

The GS algorithm can be classified as taking the error-reduction approach; each iteration

of GS reduces the error in the function estimate. Although it successfully provided an alternative solution to the phase retrieval problem, GS often stagnates and fails to search far from the initial estimate. It also often converges slowly and in some cases will converge on local minima, giving a false solution [128, 72].

Due to its known deficiencies, the GS algorithm was superseded by a class of algorithms known as the "input-output" algorithms. Unlike GS, this class of algorithm does not require that the current estimate satisfies constraints due to real world limitations. Instead of applying physical constraints such as being real or positive in the time-domain, the function is modified by an arbitrary manipulation. The most successful of the "input-output" algorithms is the hybrid input-output (HIO) algorithm [128].

The Shrinkwrap algorithm combined the HIO algorithm with the concept of adaptive support, in order to improve convergence [129]. Adaptive support requires the support function - which defines the range over which the profile can be non-zero - to shrink as the iterations progress. The Shrinkwrap algorithm was initially used to reconstruct the image of an object from its X-ray diffraction pattern. Every 20th iteration of the HIO algorithm the profile is convolved with a Gaussian function, and the result of this is used to set a threshold which determines a new support function. The width of the Gaussian is slowly decreased over time until it reaches about half its original value, as the profile converges on a solution. In 2013, the Shrinkwrap algorithm was applied the problem of longitudinal bunch reconstruction (using CTR frequency spectra), but it was found to be inadequate for this type of problem [72].

In order to find an algorithm appropriate for the reconstruction of longitudinal bunch profiles the Bubblewrap algorithm was developed [72]. The Bubblewrap algorithm drew on features of the algorithms outlined, in order to find the combination most applicable to longitudinal bunch profile reconstruction. The threshold used to determine the initial support function was adapted to deal with common features in longitudinal bunches, such as long low charge tails. The Bubblewrap algorithm implements both the HIO algorithm and the GS algorithm a number of times, gradually decreasing the arbitrary manipulation applied

by HIO, and then uses a support function constraint. The entire process is then repeated for several hundred iterations. Several of the parameters - including the number of iterations of each algorithm and the factor by which the adaptive support function is decreased - are obtained by trial and error. This means that there is no theoretical understanding of why phase reconstructions with these values are particularly successful.

The Bubblewrap algorithm was adapted in 2016 to incorporate the KK method. Both the iterative methods and the KK method have significant, but different problems. The iterative methods often produce solutions with ripples which distort the profile and are also highly sensitive to the input parameters, whereas, the KK method struggles with particular types of bunch shape, such as the double Gaussian. The new algorithm, the Phase Constrained Iterative algorithm (PCI), used the phase estimate made by the KK method as a starting condition for the iterative process. The Bubblewrap algorithm is then used, with the KK method phase estimate and the measured charge of the bunch used as constraints. The PCI algorithm has been shown to provide successful reconstructions of a range of different profiles that cannot be accessed using only the KK method or only iterative methods [73]. Nevertheless, it is still highly sensitive to the input parameters, and requires fine tuning to get accurate solutions for different types of bunch shapes.

7.2 Summary

The chapter explains that recovering the longitudinal bunch profile, from measurements of cSPr, depends on the selection of a suitable method to overcome the phase retrieval problem. Solutions to the phase retrieval problem, the Kramers-Kronig method and iterative algorithms, are described and their strength and weaknesses analysed.

Chapter 8

Optimizing the Number and Distribution of Detection Channels

Difficulties in reconstructing longitudinal profiles from finite measurements of frequency spectra are a significant obstacle to the use of cSPr (and other spectral analysis techniques) bunch profile monitors as diagnostics in operational accelerators. In particular, to achieve high quality bunch profile reconstructions, it is necessary to overcome the phase recovery problem (see Chapter 7). This effects all longitudinal bunch diagnostics which use cSPr and other similar radiative processes, including CTR and CDR. Measuring the frequency spectrum produced by these radiative processes yields the form factor (the square of the amplitude of the Fourier transform of the longitudinal distribution), so the phase component must be recovered in order to transfer the information from the frequency to time domain (see Eqs. 7.1 - 7.3). Various methods for estimating the phase have been outlined (see Chapter 7), but each method is limited and their success is dependent on the parameters of the profile being investigated.

In this chapter, the problem is approached from a different perspective. Instead of attempting to find a phase retrieval method that works for all bunch profiles, the application of a currently available reconstruction method is tested for a typical bunch profile. The eventual aim of this project is a functional cSPr monitor; accordingly in this chapter the

focus is on demonstrating the potential of this type of device from a user perspective. This study investigates the effect of the number and distribution of detection channels for the purpose of optimising the design of the single-shot cSPr monitor for specific tasks. The robustness of the reconstructions is tested by analysing their dependence on the level of noise present in the signal. These parameters are considered over a range of Gaussian-like profiles, which vary in length and shape. The results provide information about the relative importance of the various factors investigated, as well as developing a framework with which the accuracy and limitations of cSPr monitors can be assessed.

8.1 Reconstruction of the Longitudinal Bunch Profile

In this section some of the basic parameters used in this study are defined and their use is justified. Whilst developing the methodology to assess the success of reconstructions and hence the suitability of a particular monitor design, it is prescient to begin with the most basic and well understood parameters. Throughout this study, Gaussian bunch profiles and the KK method for phase reconstruction are used. The number and distribution of the detection channels is chosen to optimise the reconstruction of a Gaussian bunch.

8.1.1 Case Study of the Gaussian Profile

Gaussian (and Gaussian-like) profiles provide a simple, well understood shape, typical of the bunches delivered in many accelerator environments. Parameters, such as the length, of Gaussian bunches are easy to vary and measure. It is not, however, the only type of bunch which a longitudinal diagnostic device might be expected to deal with; the more exotic bunch shapes expected from future accelerator configurations currently pose significant diagnostic challenges. Plasma wakefield accelerators, for example, typically use a driver and a witness bunch, which would require the accurate measurement and reconstruction of a two bunch configuration (where the driver is much larger than the witness) [14]. This study sets out a baseline using Gaussian and Gaussian-like bunches, but the framework that is developed

could be adapted for other bunch shapes.

The Gaussian profile, $g(t)$, is defined over the time axis, t, by the parameters μ and σ as shown in Eq.8.1.

$$g(t) = \frac{1}{\sigma\sqrt{2\pi}} e^{-\frac{1}{2}\left(\frac{t-\mu}{\sigma}\right)^2} \tag{8.1}$$

For the purposes of this study the value of μ, which gives the bunch's position in time, is fixed and the value of σ, which is a measure of the bunch's length, can be varied. In Fig. 8.1 three Gaussian profiles and their corresponding ρ functions (as defined in Chapter 7) are shown for varying values of σ.

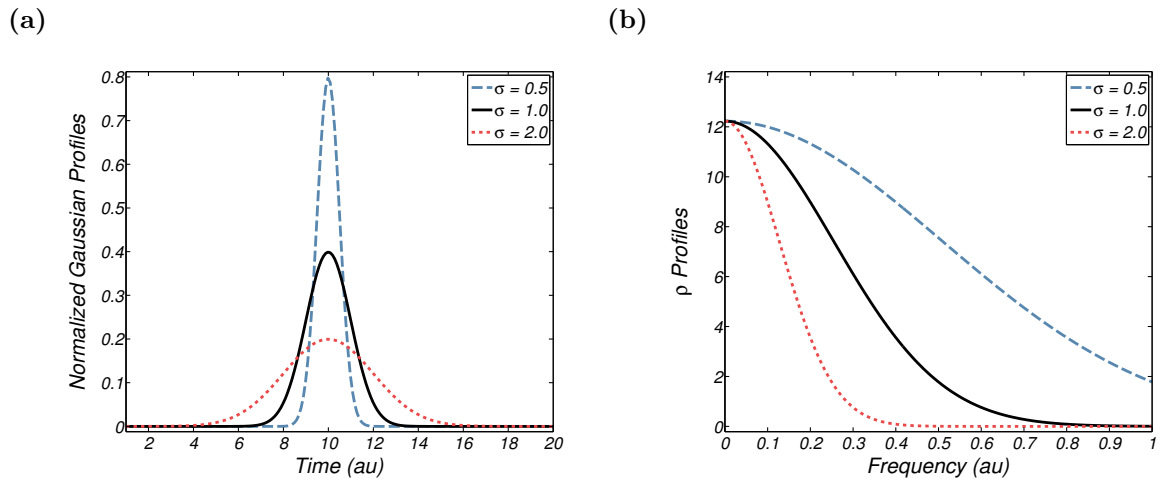

Figure 8.1: Three (a) Gaussian bunches and their (b) corresponding ρ profiles are shown for a range of bunch lengths. The bunch length is controlled by the parameter σ, and no other parameters are altered when generating the Gaussian profiles. Each bunch profile is normalized to ensure that the area under the curve remains constant, which is equivalent to a constraint requiring each bunch to have the same charge.

The shape of the bunch can also be altered by introducing asymmetry into the Gaussian profile. In order to generate an asymmetric bunch two Gaussian profiles are combined, one on either side of the value of μ as shown in Eq. 8.2.

$$g(t) = \begin{cases} \frac{1}{\sigma_1\sqrt{2\pi}} e^{-\frac{1}{2}\left(\frac{t-\mu}{\sigma_1}\right)^2}, & \text{for } t \leq \mu \\ \frac{1}{\sigma_2\sqrt{2\pi}} e^{-\frac{1}{2}\left(\frac{t-\mu}{\sigma_2}\right)^2}, & \text{for } t > \mu \end{cases} \tag{8.2}$$

The two Gaussian profiles have respective bunch lengths of σ_1 and σ_2 and the asymmetry of the bunch is defined as $A = \frac{\sigma_2}{\sigma_1}$. The overall bunch length of the asymmetric bunch profiles is $\sigma_t = \sigma_1 + \sigma_2$.

In Fig. 8.2 three Gaussian profiles and their corresponding ρ functions are shown for varying values of A. As the ρ profiles do not depend on the direction in which the bunch is orientated they remain the same when the values of σ_1 and σ_2 are exchanged. This demonstrates a limitation of this type of diagnostic, the inability to distinguish between the head and tail of any bunch.

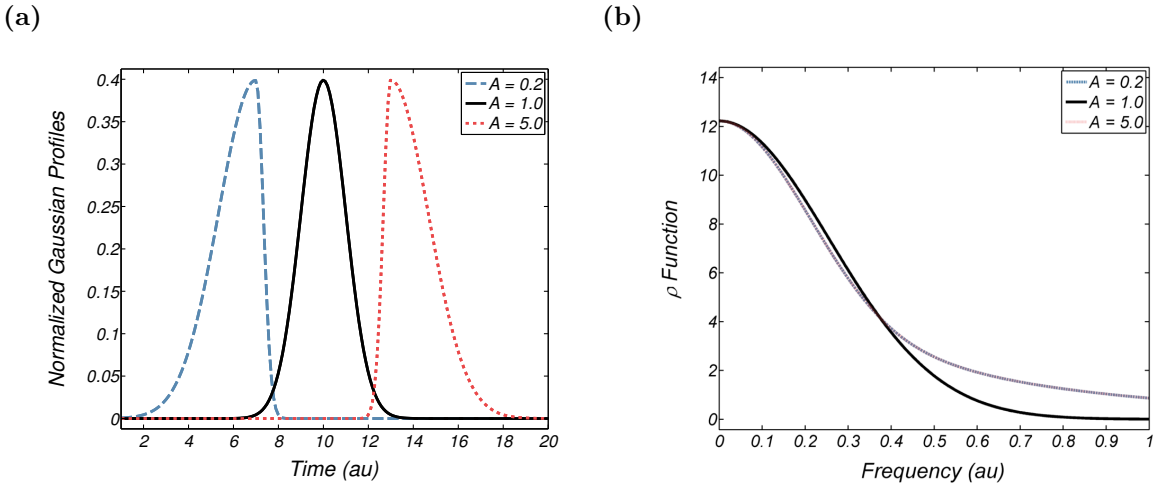

Figure 8.2: Three (a) Gaussian bunches and their (b) corresponding ρ profiles are shown for a range of asymmetries. The asymmetry of the bunches is controlled by the parameter A. The bunch length ($\sigma = 1$) is constant for all three bunches, the mean μ is slightly shifted to enable clear plotting of the bunch profiles, this has no impact on the ρ functions. Each profile is normalized to ensure that the area under the curve remains constant, which is equivalent to a constraint requiring each bunch to have the same charge. Note that the asymmetry values $A = 0.2$ and $A = 5$ give identical ρ functions, as there is no dependence on directionality.

8.1.2 Method of Reconstruction

The KK phase reconstruction method, as described in Section 7, is the phase recovery method used throughout this study. The KK method is able to reconstruct single Gaussian bunches to a high level of accuracy [31]. The KK method was selected over other methods due to its simplicity and computational efficiency. It has previously been used successfully for longitudinal bunch reconstruction in a number of studies [31, 32].

Although this study utilises the KK method for phase reconstruction, it would be relatively easy to repeat the study for different methods. The optimisation framework code, developed as part of this study, is designed to make each step of the reconstruction process easy to isolate and modify; the phase recovery method could be changed independently of the other steps.

8.1.3 Optimised Detector Layout

The position of each detection channel in a cSPr monitor (as defined by the observation angle θ) will determine the frequencies of radiation measured, for any given electron energy and grating period (see Eq. 2.1). The number and distribution of detectors will determine how the cSPr frequency spectrum is sampled, which is crucial to a successful reconstruction.

A large number of detection channels, provides a highly resolved distribution of frequency samples and will limit the loss of information due to the sampling process. Increasing the number of samples may also limit the distortion caused by background radiation or noise. Detection channels, however, are a relatively expensive part of a cSPr monitor; in the design of the single-shot monitor (Chapter 3), each channel includes two detectors, a WGP and additional optical components (see Fig. 3.3). Additionally, the number of detection channels determines the radius of the detector arc. A reduction in the number of detection channels leads to a shorter overall monitor, which would take up less space on the beamline. The balance between these competing factors, the accuracy of the reconstruction, the overall cost and size of the monitor, requires further investigation and optimisation.

The arrangement of detection channels used in the E203 multi-shot monitor and in the conceptual design of the single-shot monitor, has the channels spaced at 10° intervals along the θ axis around the grating (spanning the range $\theta = 40°$ to $\theta = 140°$). Whilst this distribution is the simplest from the perspective of monitor design and manufacture it does not necessarily provide the most effective frequency sampling. In Fig. 8.3(a) an example of the distribution of frequencies sampled by an array of 11 detectors spaced evenly around a periodic grating is given. This plot shows that sampling the frequency spectrum in this

way covers a limited frequency range. By changing the periodicity, of the gratings used, the range of frequencies sampled can be shifted. The multi-shot monitor required three gratings - each using 11 detection channels - to cover the frequency range of interest. This type of scheme, which uses fixed spatial intervals, gives dense coverage at low frequencies and sparse coverage for higher frequencies.

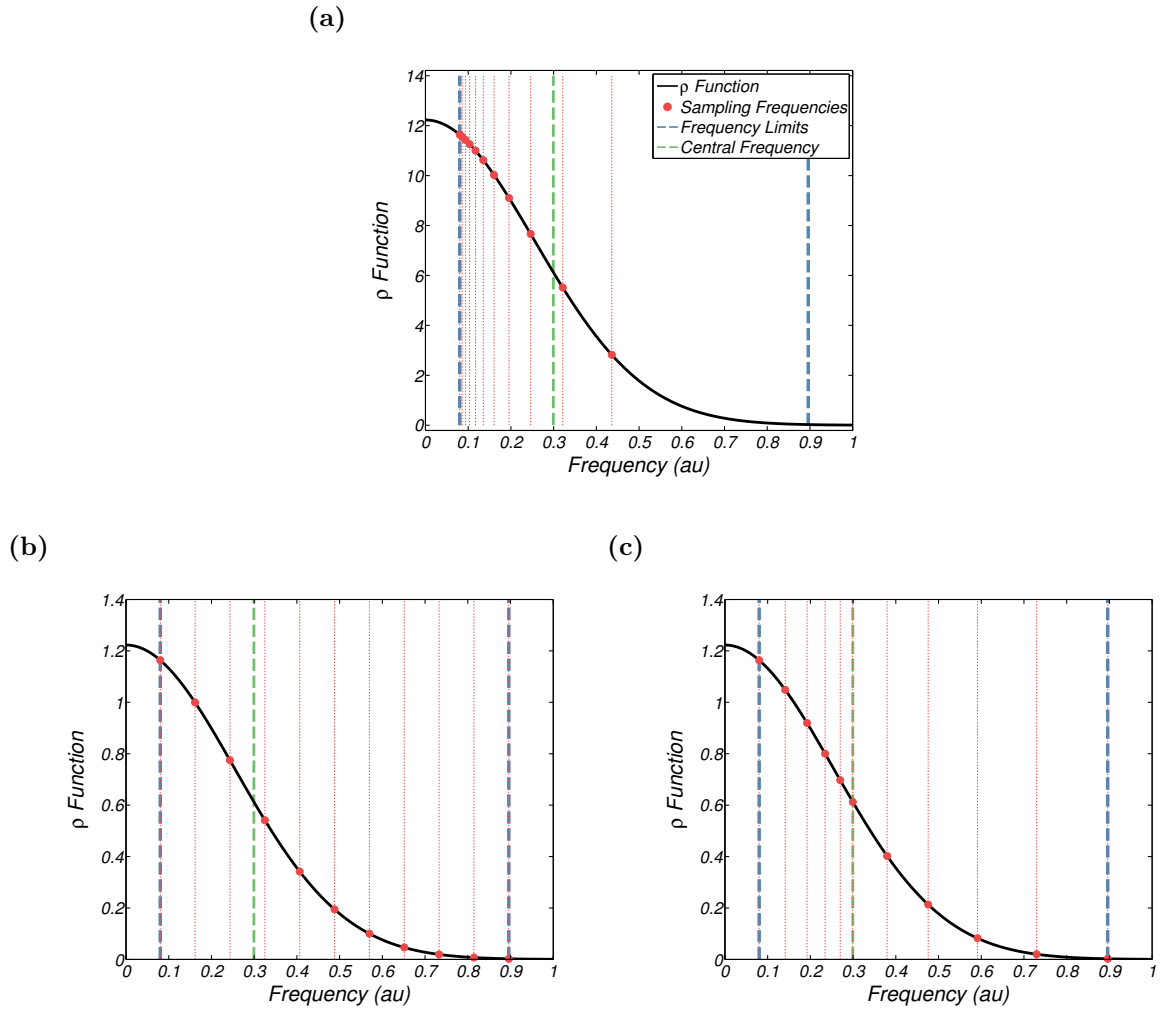

Figure 8.3: The ρ function of a Gaussian bunch ($\sigma = 1$, A=1) is sampled, modelling an experiment with a finite number of detectors. Different sampling schemes, with the same fixed frequency limits, are shown with 11 samples (equivalent to 11 detection channels) including: (a) an array of detection channels spaced at 10° intervals around one grating (spanning the range $\theta = 40°$ to $\theta = 140°$) (b) the equal frequency spacing (see Section 8.1.3) and (c) a geometric sequence around a fixed central frequency (see Section 8.1.3). In (a) the restricted cSPr detector array does not reach the upper frequency limit, more than one grating is required to span the whole range. The central frequency (shown by the green line in all three graphs), corresponds to the frequency value where the ρ function is equal to half its maximum value.

This study attempts to find an optimal distribution across the frequency range of interest

using the fewest possible detection channels. Once an appropriate frequency sampling scheme - one that fulfils the requirements of the user or resolves a particular bunch shape - has been obtained it can then be resolved into a spatial arrangement around a selection periodic gratings. This strategy will still require the use of several gratings, but may significantly reduce the number of detection channels required. Initial focus on the sampling of the frequency distribution, rather than the spatial distribution of detectors, simplifies the process of testing various configurations and makes the results applicable to other diagnostic schemes using CTR and CDR.

Equal Frequency Spacing

Perhaps the most obvious way to resolve the frequency spectrum is by sampling at equally spaced frequency intervals. The sampling range (bounded by the minimum and maximum frequencies) is selected and the spectrum is sampled at equally spaced points between these limits. The relationship between the resolution of the frequency spectrum and the number of detectors is very simple in this scheme. In Fig. 8.3(b) an equally spaced frequency sampling scheme is shown, with the ρ function of a Gaussian bunch profile used for demonstration.

It is important to set appropriate frequencies for the minimum and maximum limits of the frequency sampling range. These points should be fixed when testing a scheme, ensuring a fair comparison when varying other parameters, such as the number of detectors. The frequency limits used in Fig. 8.3 and throughout this study, are set so that all the features of the ρ function of a Gaussian bunch ($\sigma = 1$, $A = 1$) are covered. This makes extrapolation of the ρ function over the whole frequency range, after sampling, relatively straightforward.

Although the equally spaced scheme is simple and provides even coverage over the whole frequency range of interest, it is not necessarily the best frequency distribution for any particular bunch profile. The Gaussian bunch profile, for example, has a ρ function with a steep gradient in the central frequency range, which becomes much shallower close to the minimum and maximum frequencies. To optimise the reconstruction of a Gaussian bunch profile, therefore, it is beneficial to increase the number of samples in the central frequency

region and decrease them close to the minimum and maximum frequencies.

Geometric Sequence

A geometric sequence is proposed to optimise the spacing of the sampling across the frequency range of interest for Gaussian bunches. This provides a method for varying the sampling resolution over the frequency range of interest.

The defining property of the geometric series is that the ratio of successive terms is a constant [130]. It can be described by two variables, a and r, as shown in Eq. 8.3.

$$S_N = a + ar + ar^2 + ... + ar^{N-1} = \sum_{n=0}^{N-1} ar^n \tag{8.3}$$

If a is the first term, then the total sum, S_N, of a finite number of terms, N, can be found according to the expression given in Eq. 8.4.

$$S_N = \frac{a(1 - r^N)}{1 - r} \tag{8.4}$$

In this study, the geometric series is used to determine the distribution of sampling over a frequency range; the value of S_N is set equal to a frequency range and N is number of samples required in that range. The value of r controls the variation in spacing over the frequency range S_N and can be optimised by the user. Given values of S_N, N and r the value of a can be calculated using Eq. 8.4.

As previously, in the equal frequency scheme, the minimum and maximum frequencies are bounds to a fixed frequency range. A central frequency, set to the frequency value at $\frac{\rho_{max}}{2}$ for the ρ profile in question (see Fig. 8.3), is selected and two geometric sequences are computed. The first spans the central frequency to the minimum frequency and the second sequence spans the central frequency to the maximum frequency. An example of the geometric sampling scheme ($r = 1.2$, $N = 11$) is given in Fig. 8.3(c), the figure shows this frequency distribution on the ρ profile of a Gaussian bunch profile ($\sigma = 1$, $A = 1$).

In the example, shown in Fig. 8.3(c), the number of detectors in the two geometric sequences is the same, however, it would be straightforward to adjust this balance to increase the focus on either high or low frequencies. Different bunch shapes might require a different central frequency or different vales of r and N values for the two sequences.

Choosing a Detector Layout

This section highlights the myriad of choices available when deciding how to optimise the distribution of samples over the frequency range of interest for bunch reconstruction. The results presented later in this chapter only consider a small subset of these possibilities. A geometric sequencing scheme, with $r = 1.2$ and equal numbers of detectors either side of the central frequency, is used in this study. Each sampling scheme constructed is optimised for a "design profile", which represents the expected longitudinal bunch parameters in an hypothetical accelerator facility. The "design profile" is a symmetric ($A = 1$) Gaussian bunch with a length defined by $\sigma = 1$.

One aim of the study is to analyse how robust the resultant monitor would be to deviations from the "design profile" in either length or shape. In an accelerator facility where there is significant variation between the bunches, the ability of a cSPr monitor to provide accurate reconstructions over a range of parameters is crucial to its success.

8.2 Methodology

This section describes the design and development of the optimization framework used to analyse the abilities of various parameter sets with respect to profile reconstruction.

8.2.1 Generating a ρ Profile

The first step in modelling the reconstruction process is the generation of a bunch profile, here a Gaussian-like function defined by the parameters σ and A. The bunch profile is used

to generate a ρ function, this mimics the conversion of the longitudinal bunch information from the time domain to the frequency domain information measured in a cSPr experiment. It should be noted that in an actual cSPr experiment ρ values are obtained after the contribution from the transverse bunch parameters is excluded (see Eq. 2.13), here, it is assumed that this information is well known.

Once the ρ function has been generated, random noise is added to simulate the experimental conditions expected in an accelerator environment. Even for cSPr monitors in a low noise environment, with a successful background radiation elimination scheme, a fraction of the signal detected is a noise component. In Eq. 8.5 the formulation used to add a noise component to each value of the ρ function is given.

$$\rho_{noisy}(f) = \rho_{initial}(f) + n_f * \rho_{max} * R_N(f) \tag{8.5}$$

In this equation, ρ_{max} is the maximum value of the generated ρ function and R_N is the random noise component (a number between -1 and 1). A random noise component is generated for each ρ value. The noise fraction, n_f, is a user input with a value between 0 and 1. It represents the maximum potential noise contribution as a percentage of ρ_{max}. A 1% noise contribution, therefore, refers to a value of $n_f = 0.01$.

The ρ function - with the added noise component - is then sampled according to the geometric scheme outlined in Section 8.1.3, with the number of detectors N used in this scheme determined by user input. N samples from the noisy ρ function are used to estimate a full ρ function, ready for reconstruction. This is done by interpolation and extrapolation over the entire frequency domain. Basic linear interpolation is used, as this provided interpolation of sufficient quality.

Extrapolation to high frequencies is done by modelling the tail of the ρ function as a decaying exponential, requiring at least three data points to successfully extrapolate using a non linear regression model. The three highest frequency ρ samples must be in decreasing order of size, for n samples: $\rho(f_{n-2}) > \rho(f_{n-1}) > \rho(f_n)$. Large random noise contributions

can disrupt this relationship, and prevent successful extrapolation. To overcome this, the three highest frequency samples of $\rho(f)$ are compared, and any that do not obey the requirement of decreasing size are removed from the set of samples. The process is then repeated with the new three highest frequency samples, when fewer than three samples remain the reconstruction fails and the input parameter set is labelled as unstable.

The low frequency values are determined by extrapolation to zero frequency using a Gaussian model. A non linear fitting model performs the extrapolation and again requires at least three data points.

After adding noise, sampling, interpolating and extrapolation a new ρ function is ready for reconstruction into a bunch profile. The KK method is used for the phase reconstruction step. If the reconstruction fails, at any step in the process, the input parameter set used is labelled as unstable.

In addition to the reconstruction based on the new, sampled and noisy ρ function, the initial ρ function is also used to reconstruct a bunch profile. This reconstruction, subsequently referred to as the "best case" reconstruction, is used in analysis to determine variation due specifically to the process of adding noise, sampling, interpolating and extrapolating.

Due to the random component in the noise contribution, the results will vary for the same set of input parameters. To account for this the process is repeated 100 times for each parameter set, building up statistics to minimise the effect of local fluctuations caused by the random noise component. If any one of the 100 attempts for each parameter set fails, then the set will be rejected. The routine handles failure at any point in the process indiscriminately, therefore, in analysis the rejection of parameter sets for diverse reasons - including failure during the KK phase reconstruction or through elimination of frequency samples during the extrapolation procedure - will not be distinguishable.

8.2.2 Analysing the Success of Profile Reconstruction

After reconstructing the bunch profile, the problem becomes how to determine, in a way

that is meaningful to the users, if the reconstruction is "good". We have already discussed rejecting sets of parameters, due to failure at any point in the process, however, it is also important that the quality of successful reconstructions is quantified.

This study uses defined bunch profiles to generate the initial ρ function, therefore, the reconstructed profiles can be compared to the original profile to determine the accuracy of the reconstruction.

A crucial criterion for a longitudinal bunch diagnostic device is its ability to perform accurate measurements of the bunch length. Equation 8.6 gives a simple calculation that was used to estimate the accuracy of the bunch length estimate for every reconstruction, where σ_o is the observed bunch length of the reconstructed profile and σ_e is the expected bunch length used as an input when generating the initial profile. The variation between the two is expressed as a percentage difference of the expected value.

$$BL_{Err} = \frac{|\sigma_e - \sigma_o|}{\sigma_e} \times 100 \tag{8.6}$$

As well as assessing the accuracy of the bunch length measurement, it was also important to determine the accuracy of the reconstruction of the profile shape. Pearson's χ^2 test, which uses the sum of squared errors, is a statistical method used to compare the goodness of fit of dataset to a theoretical (or expected) distribution. Equation 8.7 shows how to calculate the χ^2 parameter, where O_i and E_i are data points from the observed and expected distributions respectively.

$$\chi^2 = \sum_{i=1}^{n} \frac{(O_i - E_i)^2}{E_i} \tag{8.7}$$

The χ^2 test is used to compare the reconstructed bunch profile (the observed profile) with the initial bunch profile (the expected bunch profile). The original bunch profile is used to generate the initial ρ function (which is then sampled), but has no influence on the rest of the test framework.

Additionally, the χ^2 test was used to compare the reconstructed bunch profile (the ob-

served profile) with the "best case" reconstruction carried out with the initial ρ function (the expected profile). This χ^2 test shows the deviation of the reconstructed profile from the best reconstruction that is possible using the KK phase recovery method. The differences between the reconstructed profile and the "best case" reconstruction are due to the sampling process and the addition of noise to the profile.

Finally the χ^2 test was used to compare the initial ρ function with the sampled, noisy ρ function. This provides information about the extent of the information lost due to the addition of noise, sampling, interpolation and extrapolation of the ρ profile independently of the rest of the reconstruction process.

The use of these three χ^2 tests not only provides information about the quality of the reconstruction, but also highlights the sections in the process responsible for the loss of information and hence, quality. This information helps to isolate the stage in the reconstruction process in most need of improvement.

8.2.3 Introducing Variable Parameters

The parameters used to generate and modify the ρ function are varied to investigate the dependence of the reconstruction process upon them. When designing a cSPr monitor it is important to understand the impact of a range of parameters on the performance of the monitor, in order to make informed decisions during design and operation.

The analysis, presented in the results section, looks at the effects of modifying a selection of the parameters described so far. The dependence of the quality of the reconstructions on the number of detectors and the noise level is investigated. For each scenario, a set of parameters including the number of detectors and the noise level are selected and reconstructions are attempted for a range of bunch lengths (σ) and bunch asymmetries (A). The optimization framework has been designed to "grid scan" these variable parameters. This simplistic method provides a general understanding of the effects of the variable parameters over a pre-determined range of values.

The number of detectors is varied in the range 5 to 35; note that only odd numbers of detection channels are implemented with the geometric sampling scheme. In the multi-shot monitor (E203) 33 detection channels (not optimised in sampling distribution) were sufficient for reconstruction. Here, the effects of reducing the number of detection channels in the single-shot monitor are assessed, with the potential for significant reductions in the size and cost of a cSPr monitor.

The noise levels will be varied from 0% to 50% (see Eq. 8.5), which takes into account the variation in the expected noise levels in different accelerator environments. In the multi-shot experiments at SLAC (20.35 GeV, 1 nC), the noise levels measured at some detection channels were comparable to the signal intensity, however, at the LUCX facility (8 MeV, 0.1 nC) the noise levels were negligible.

The σ value, which defines the bunch length, will be varied around the design σ value. The design σ value, used to optimise the detector layout, is set to 1, and values from 0.2 to 5 are used (variation from the design σ of a factor of 5), testing the robustness of the monitor for a range of bunch lengths.

The asymmetry value, A, used to vary the bunch profile shape, has a value of 1 for a symmetric Gaussian. The value of A is used in the range 0.08 to 12, this tests the limits of the monitor to accurately determine profile shape.

A code flow diagram outlining the basic steps of the routine described in this Section is given in Fig. 8.4. Each step shown in this diagram has been discussed in detail in the text.

8.3 Results

The results of the study are presented in this section. The effect of varying the detector number over a range of σ and A values is analysed for three different noise level scenarios.

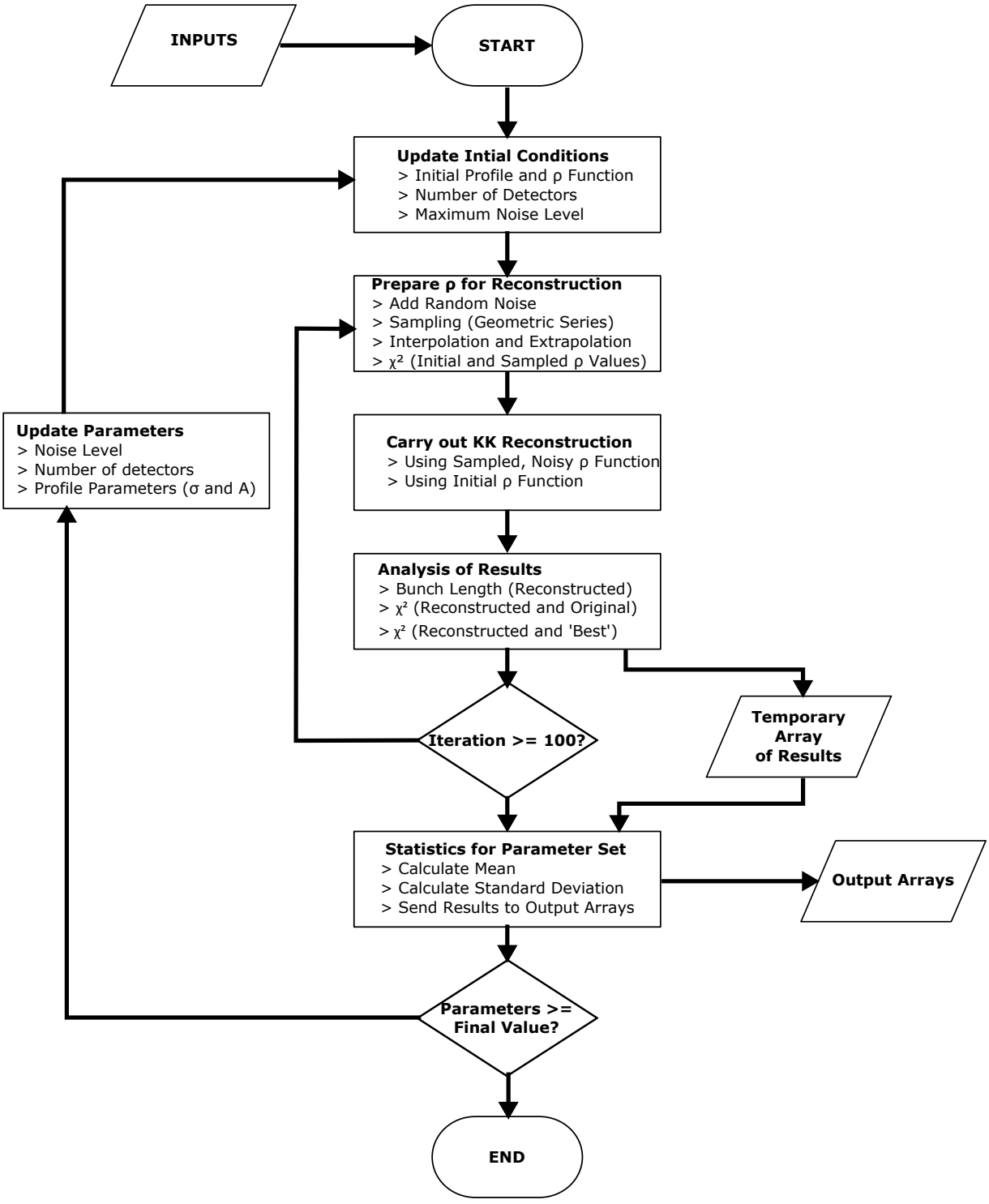

Figure 8.4: A code flow diagram outlining the steps in the routine developed to investigate the dependence between the quality of profile reconstruction and a variety of parameters. The variable parameters investigated include the noise level, the number of detectors, and the length of the initial bunch profile. The modular nature of the routine makes it simple to isolate the steps in the process introducing the most error and modify steps independently.

8.3.1 The Zero Noise Scenario

Although a zero noise system is not feasible for an actual experiment, analysis of the quality of reconstruction in this scenario provides the opportunity to study the effects of varying the number of detection channels independently of the noise contribution.

In Fig. 8.5 the analysis of bunch profile reconstructions carried out for varying σ and detection channel number are presented for a zero noise scenario. Four measures (outlined in Section 8.2.2), one shown in each of the four plots, are used to measure the quality of the reconstructions. In all four plots it is clearly shown that, in an environment without a noise contribution, increasing the number of detection channels improves the quality of the reconstructed profile. There are no failures seen in the reconstruction process for any of the parameter sets tested under the zero noise constraint.

The plots in Fig. 8.5 show that, the increase in quality of profile reconstruction seen when increasing from 5 to 11 detectors is superior to that seen when increasing the number of detectors from 11 to 17. Each successive increase in detector number causes an incrementally smaller improvement, and the effect of increasing the number of detectors above 17 is negligible. This is true for the accuracy of both (a) the bunch length measurements and (b and c) the shape of the reconstructed profile.

The accuracy of the reconstructions - in both length and shape - is also dependent on the initial bunch length with respect to the design value of $\sigma = 1$. The accuracy of the bunch length measurements, shown in Fig. 8.5(a), decreases for bunches with length both above and below $\sigma = 1$. This effect is most significant for scenarios with large numbers of detection channels (>17). The scenarios with fewer detectors show less sensitivity to the length variation, but have lower accuracy across the whole range.

The profile shape quality, assessed in Figs 8.5(b) and (c), has a marked decrease for values of σ <1. This effect is likely due to the detectors not covering an appropriate frequency range for the short bunch profiles; increasing the high frequency range would improve this. The quality of the profiles is, however, maintained for values of σ >1, with no observed reduction

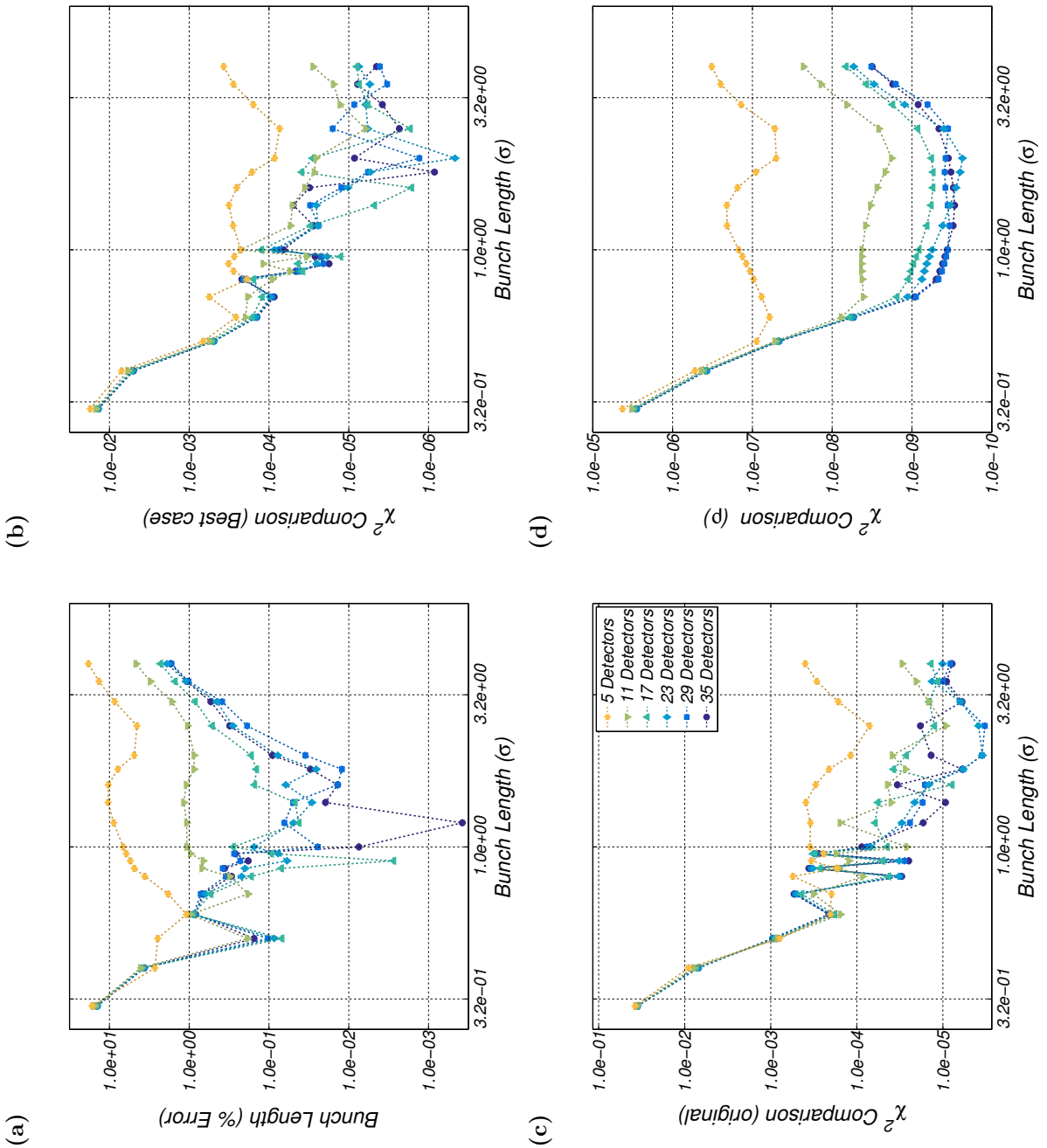

Figure 8.5: The quality of profile reconstruction is analysed for a range of bunch lengths (σ), for a varying number of detection channels with zero noise (0%) and an asymmetry of A =1. Each plot gives a different metric for profile reconstruction success, in (a) the % accuracy of the bunch length measurement after reconstruction. In (b) and (c) the accuracy of the shape of the reconstructed profile is shown using a χ^2 test on: the best (KK) reconstruction and the reconstructed profile, and the original profile and reconstructed profile respectively. In (d) a χ^2 test monitors the variation between the original and the initial ρ profile, to demonstrate the information loss due to the sampling process.

in the accuracy of the reconstructed shape over the range $1 < \sigma < 3$. This demonstrates the importance of high frequency information to the successful reconstruction of the profiles shape. The bunch length measurement, on the other hand, relies more on the low frequency information, so the same effect is not noted.

The similarities between the analysis of the the profile shape quality (Figs 8.5(b) and (c)) and the analysis of the ρ functions (Fig. 8.5(d)), demonstrates that most of the information loss occurs due to the sampling processes. This makes the sampling, interpolation and extrapolation routines the most obvious candidates for modification and improvement. There is, however, differentiation between scenarios with 17-35 detection channels seen in the analysis of the ρ functions (Fig. 8.5(d)) which is not seen in the other three plots. This reveals that although the accuracy of the ρ function measurements is increased by using more detection channels, this does improves the profile reconstruction when using the KK method.

Figure 8.6 examines the effect of bunch shape for a variety of detection channel number, via variation in A, for a zero noise environment. Again, there is a clear dependency between the quality of the reconstruction and the number of detection channels. In addition, the symmetry of the result around $A = 1$, present in all four plots, demonstrates that process is operating as expected, and the processing of the profiles is independent of their directionality. As in the case of varying σ in a zero noise scenario, there are no reconstruction failures observed.

As the number of detection channels is increased, the improvement in the quality of the reconstructions decreases; the analysis shows no improvement for the addition of more than 9 detection channels. This is less than the number recommended for the σ variation (17), suggesting that significant detection channel number reduction is possible in situations where variation in the bunch shape is expected, but the bunch length is expected to be relatively stable .

The results in Fig. 8.6 also provide information about the range of asymmetry values that can be dealt with by this type of analysis. Although the accuracy, of both length

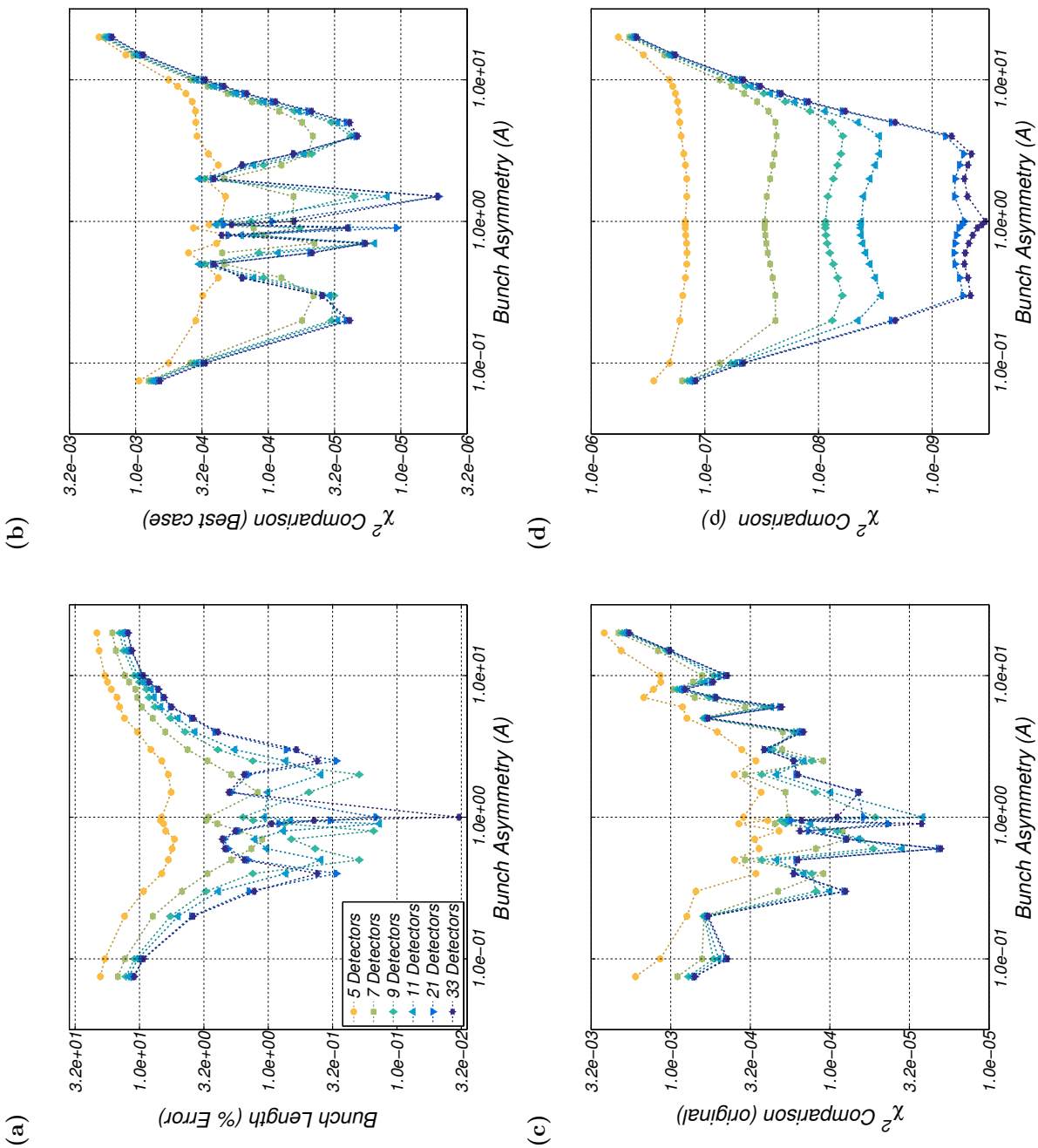

Figure 8.6: The quality of profile reconstruction is analysed for a range of asymmetry values (A), for a varying number of detection channels with zero noise (0%) and a bunch length of $\sigma = 1$. Each plot gives a different metric for profile reconstruction success, in (a) the % accuracy of the bunch length measurement after reconstruction. In (b) and (c) the accuracy of the shape of the reconstructed profile is shown using a χ^2 test on: the best (KK) reconstruction and the reconstructed profile, and the original profile and reconstructed profile respectively. In (d) a χ^2 test monitors the variation between the original and the initial ρ profile, to demonstrate the information loss due the sampling process.

and shape analysis (Figs 8.6(a), (b) and (c)), shows significant chaotic variation in the range $0.5< A <2$, it remains high and shows no overall change. All four plots show a sharp decrease in reconstruction quality around the limits of the plotted range $A = 0.1$ (and equivalently $A = 10$). This is almost certainty due to the lack of high frequency information for these profiles; not the inherent properties of the reconstruction process. The reconstructions for profiles with asymmetry values between 0.1 to 10, for scenarios with more than 5 detection channels, all have a bunch length measurement error of below 10%.

The similarities between Figs. 8.6(b and c) and Fig. 8.6(d) again demonstrate the loss of information in the sampling, interpolation and extrapolation procedures is an important factor in the reconstruction success. However, the loss of differentiation between the scenarios with a large number of detection channels (>7), also shows the loss of accuracy introduced by the KK phase recovery method.

8.3.2 The Low Noise Scenario

The best case scenario for a cSPr longitudinal bunch profile monitor is a low noise environment. This could be an inherently low noise environment - such as the LUCX facility - or it could be achieved by the successful implementation of a method for the elimination of background radiation. For the purposes of this study a noise level of 1% has been used to model a low noise environment.

Figure 8.7 shows the quality of the profile reconstructions for varying detection channel number, over a range of σ, for a low noise scenario. All four plots show a decrease in average reconstruction quality, compared to the zero noise scenario (see 8.5).

Although the dependency of the quality of the reconstructions on the number of detection channels remains observable, the addition of noise has weakened this relationship. Only the reconstructions with 5 detection channels show a non-negligible reduction in the quality of the reconstruction, compared those with more. The bunch length measurement error (Fig. 8.7(a)), in particular, shows a reduced sensitivity to the number of detection channels.

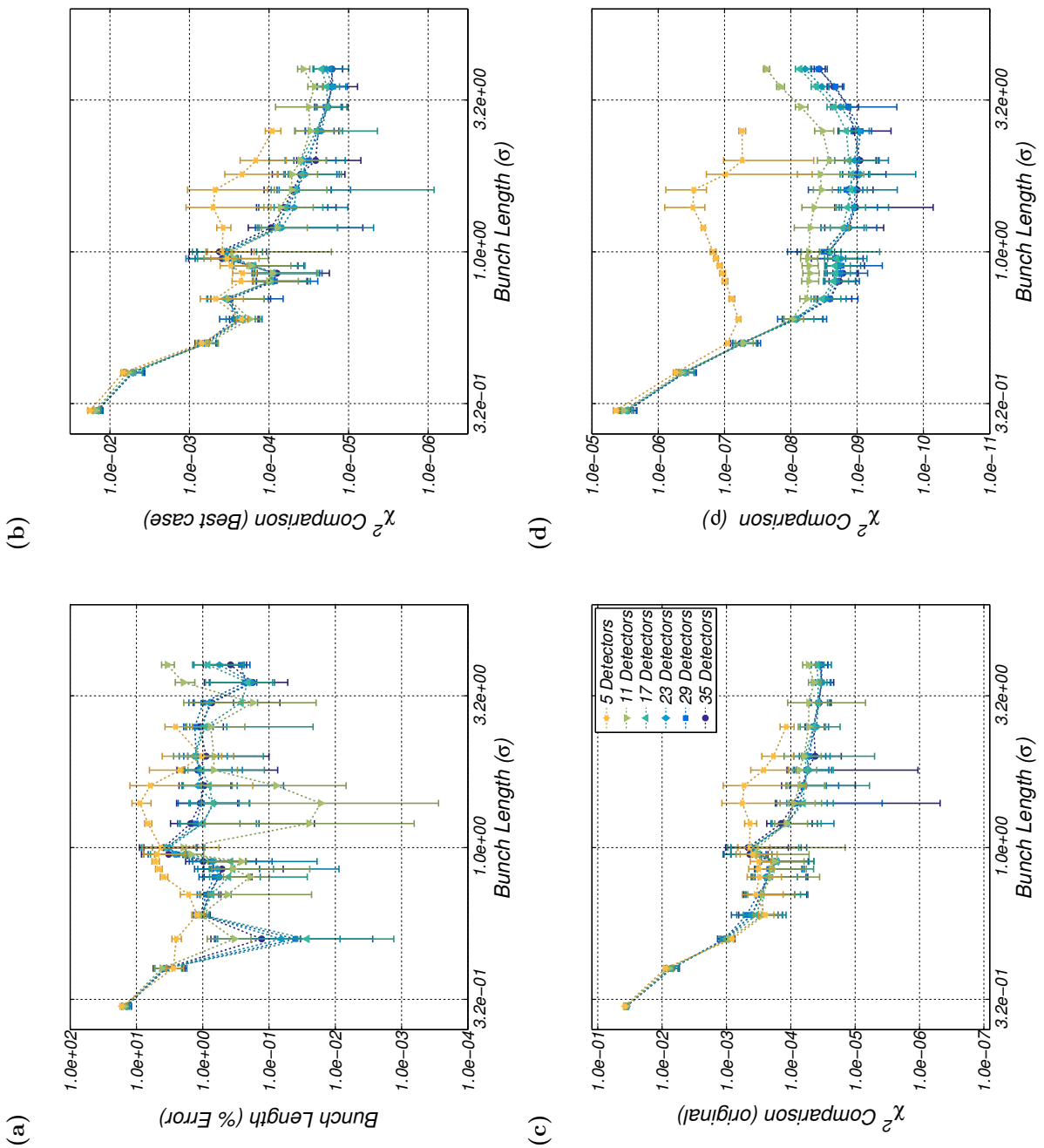

Figure 8.7: The quality of profile reconstruction is analysed for a range of bunch lengths (σ), for a varying number of detection channels with low noise levels (1%) and an asymmetry of A =1. Each plot gives a different metric for profile reconstruction success, in (a) the % accuracy of the bunch length measurement after reconstruction. In (b) and (c) the accuracy of the shape of the reconstructed profile is shown using a χ^2 test on: the best (KK) reconstruction and the reconstructed profile, and the original profile and reconstructed profile respectively. In (d) a χ^2 test monitors the variation between the original and the initial ρ functions, to demonstrate the information loss due to the addition of noise and the sampling process.

There is an average error of 1%, in the range $0.5 < \sigma < 3$, for all reconstructions using 11 or more detectors.

The addition of noise has also lead to an overall decrease in accuracy of the reconstructions - in both length and shape - over the range of σ values considered. This is especially noted close to the design bunch length $\sigma = 1$, with significant increases in both bunch length measurement error and the χ^2 values. At low values of σ ($\sigma < 0.5$), the decrease in accuracy of the shape of the reconstruction seen in the zero noise scenario (Figs 8.5(b) and (c)), still dominates the results (Figs 8.7(b) and (c)). This demonstrates that identifying the correct frequency sampling distribution is more important in this bunch length range than further reducing the noise levels.

The introduction of the random noise element (see Eq. 8.5) creates variation in the resultant profiles, as each parameters set is run 100 times the mean and standard error (represented by error bars) are plotted for each. The variation in the results, shown by the standard error, further removes the distinction between the schemes with different numbers of detection channels. In particular, the distinction in the ρ function analysis between the schemes with large numbers of detection channels (>17) which was seen in the zero noise scenario (Fig. 8.5(d)) is not seen in the low noise scenario (Fig. 8.7(d)). This indicates the noise component, even though it is small, dominates the accuracy of the ρ measurement for schemes with large numbers of detection channels.

The addition of noise has also caused the reconstruction process to fail in some parameter sets with a small number of detection channels. In Fig. 8.7, the reconstructions with 5 detection channels are seen to fail at bunch lengths of $\sigma > 2.5$. This is likely caused by the addition of noise making extrapolation to high frequencies difficult. No reconstruction failure was observed, with values going up to $\sigma = 5$, for the parameter sets with 11 or more detectors.

Figure 8.8 shows the quality of profile reconstruction for varying detection channel number, over a range of A, this time in a low noise environment. This set of results shows some sensitivity to the detection channel number, however, no improvement is seen in the quality

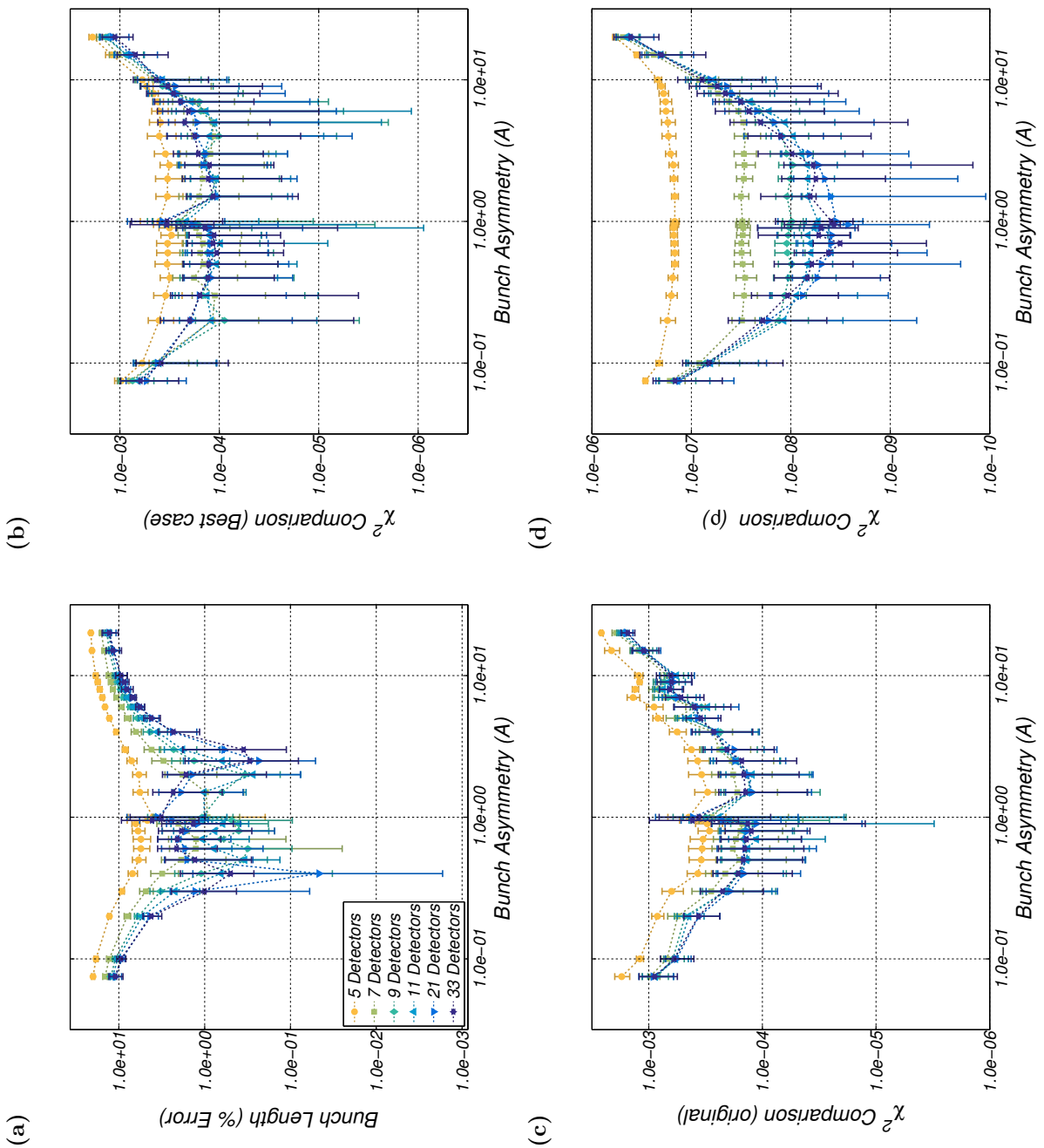

Figure 8.8: The quality of profile reconstruction is analysed for a range of asymmetry values (A), for a varying number of detection channels with low noise levels (1%) and a bunch length of $\sigma = 1$. Each plot gives a different metric for profile reconstruction success, in (a) the % accuracy of the bunch length measurement after reconstruction. In (b) and (c) the accuracy of the shape of the reconstructed profile is shown using a χ^2 test on: the best (KK) reconstruction and the reconstructed profile, and the original profile and reconstructed profile respectively. In (d) a χ^2 test monitors the variation between the original and the initial ρ functions, to demonstrate the information loss due to the addition of noise and the sampling process.

of the reconstructions for schemes with more than 5 detectors.

The addition of noise does not cause a reduction in the accuracy of reconstruction over the range of asymmetry considered. The chaotic variation in the range 0.5<A<2, seen for the zero noise scenario (Fig. 8.6), is eliminated by averaging over 100 slightly different profiles for each parameter set. The variation, or the standard error, makes the differences between the scenarios with different numbers of detection channels less distinct. In particular, the differentiation in the ρ analysis, seen in the zero noise scenario, for large numbers of detection channels (>9) is eliminated by the addition of a small noise component.

The asymmetry variation, unlike the bunch length variation, does not cause reconstruction failure in the low noise scenario. The (a) bunch length measurement errors and (b and c) the χ^2 tests of the bunch shape accuracy show similar patterns over the range of asymmetry variation.

8.3.3 The High Noise Scenario

It may not always be possible to assume a low noise environment. The experiments done at the SLAC facility experienced, for example, a poor signal to noise ratio for some detection channels. It has been proposed to use background radiation elimination schemes, to improve the performance of the monitor in a noisy environment. This section considers the reconstruction outcomes in a scenario where significant uncertainty in the measurement of the cSPr signal remains. For the purposes of this project, this high noise scenario has a noise level of 25%.

In Fig. 8.9 the quality of the reconstructions is shown for varying detection channel number, over a range of σ values, under conditions of high noise. The effect of adding noise is compounded as the noise levels increase, with the effects seen in the low noise σ variation plots (Fig. 8.7) enhanced.

As the noise level is increased it becomes difficult to distinguish between the results for different numbers of detection channels. Across the whole range of σ values, the quality of

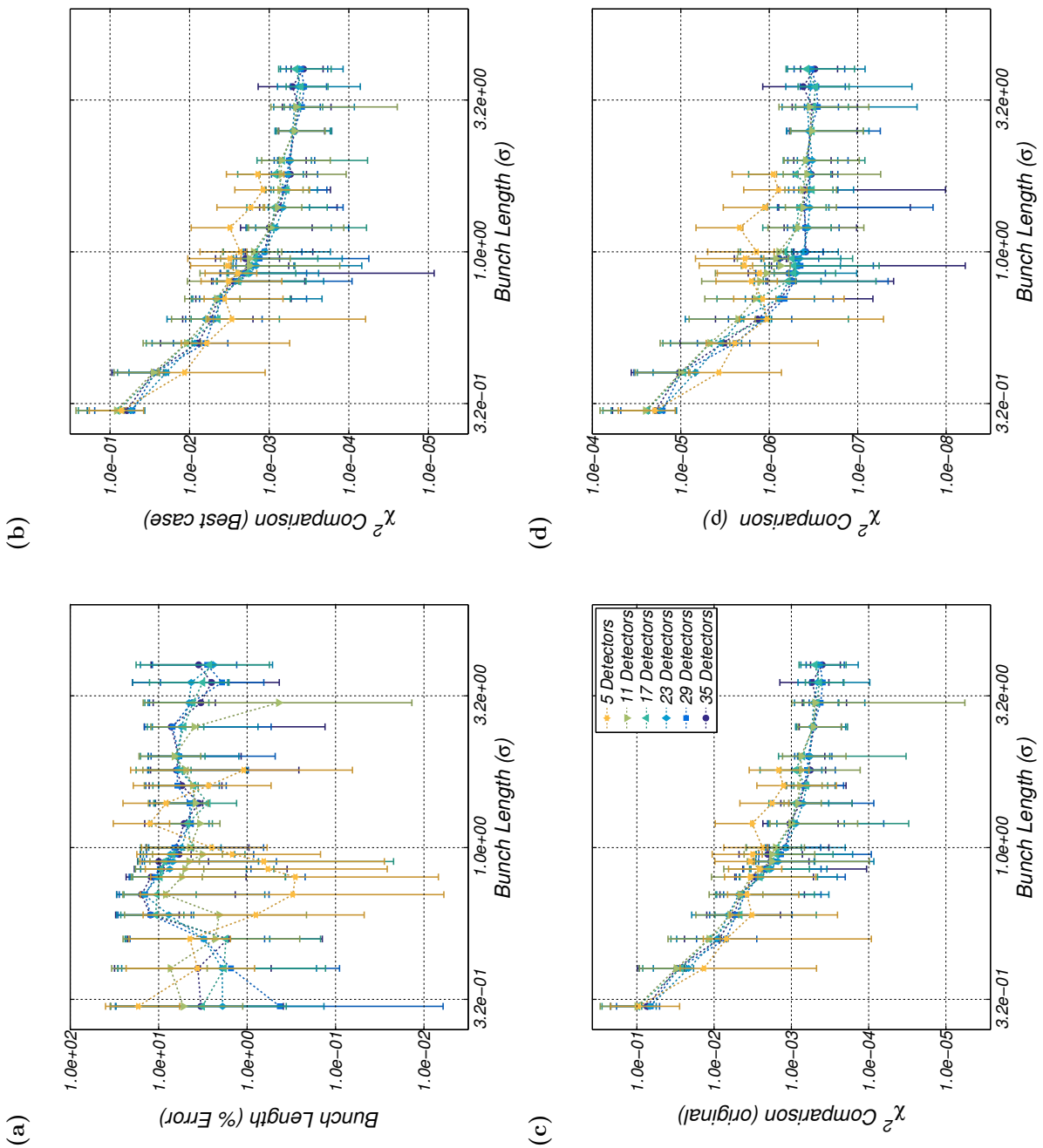

Figure 8.9: The quality of profile reconstruction is analysed for a range of bunch lengths (σ), for a varying number of detection channels with high noise levels (25%) and an asymmetry of A =1. Each plot gives a different metric for profile reconstruction success, in (a) the % accuracy of the bunch length measurement after reconstruction. In (b) and (c) the accuracy of the shape of the reconstructed profile is shown using a χ^2 test on: the best (KK) reconstruction and the reconstructed profile, and the original profile and reconstructed profile respectively. In (d) a χ^2 test monitors the variation between the original and the initial ρ functions, to demonstrate the information loss due to the addition of noise and the sampling process.

the reconstructions is reduced and large variations (given by the error bars in each plot) are recorded. In Fig. 8.9(a) the error in the bunch length measurement is up to 50% around the design bunch length ($\sigma = 1$), a significant loss of accuracy compared to the low noise scenario (Fig. 8.7(a)) .

In all four plots a decrease in sensitivity to the number of detection channels is seen for noise levels of 25%. Using all four measures of quality, there is little to distinguish the between the quality of reconstructions carried out with 5 and 35 detection channels.

The large variations in the results, caused by the random element of the now significant noise component, show that there would be significant uncertainty in any diagnostic measurement made by a scheme under the conditions of high noise. The noise now dominates the results, making the priority for improvement the reduction in the noise contribution.

Reconstruction failure is also a problem for bunches with σ values significantly higher that the design σ. The reconstructions are seen to fail for the schemes with 5 and 11 detection channels, in the case of 5 detection channels the failure is seen for a lower value of σ than in the low noise scenario. However, from 17 detection channels upwards no failure is observed over the range shown.

In Fig. 8.10 the success of the profile reconstructions is presented for a range of asymmetry values (A) in a high noise scenario. The previously observed distinction in quality of profile reconstructions with different numbers of detection channels is lost, across the range of A, with the introduction of a high level of noise.

A significant decrease in the accuracy of the profile shape reconstruction (Figs 8.10(b) and (c)) is observed, compared to the results obtained for the low noise scenario (Figs 8.8(b) and (c))). The average bunch length measurement error (Fig. 8.10(a)), however, remains similar to that measured in the low noise scenario (Fig. 8.8(a)). The increase in variation, in all four plots, shows the broad spread of the results and demonstrates a significant loss in accuracy compared to the zero and low noise scenarios.

As in the low noise scenario, no reconstruction failures are seen when varying the pa-

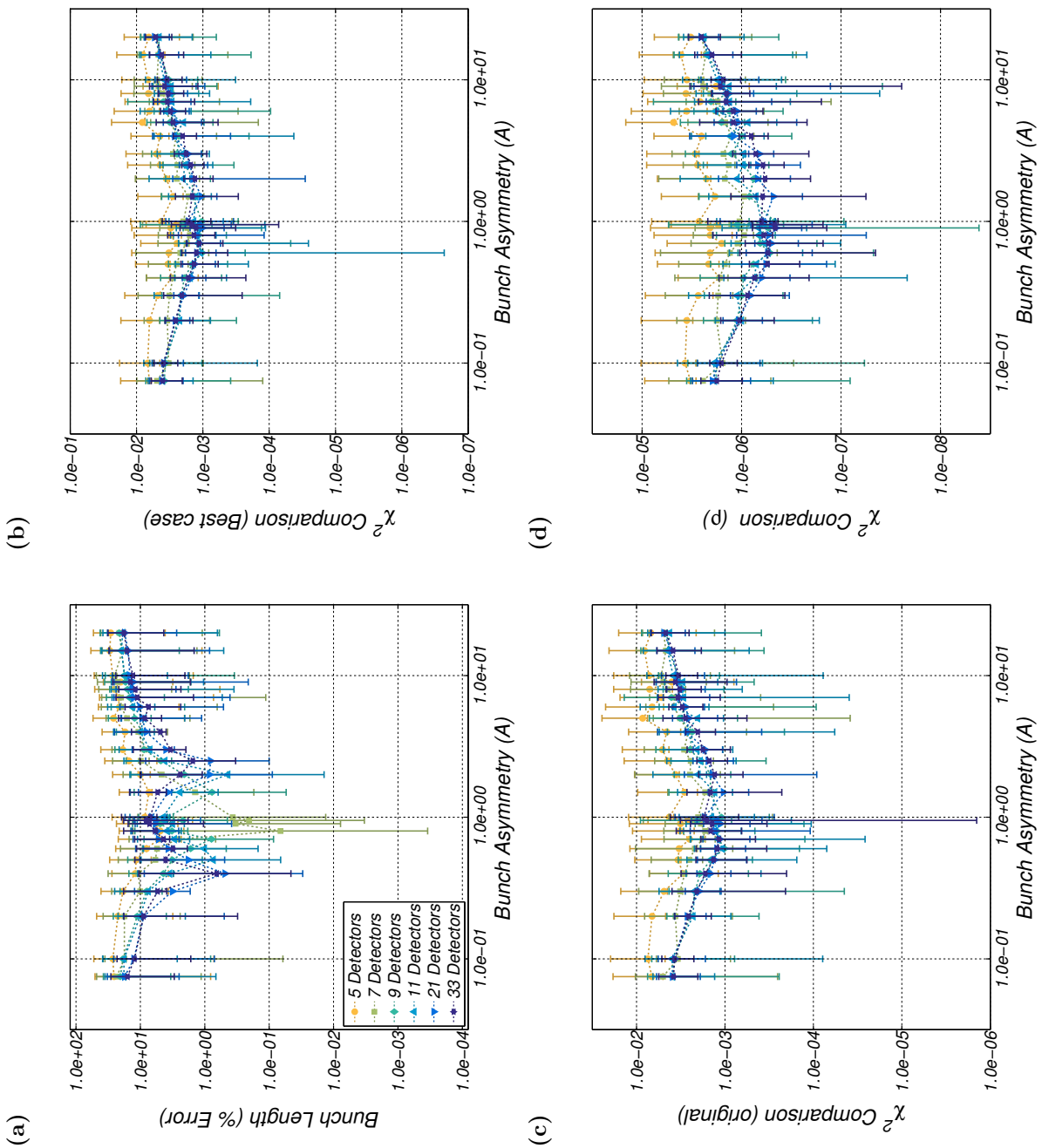

Figure 8.10: The quality of profile reconstruction is analysed for a range of asymmetry values (A), for a varying number of detection channels with high noise levels (25%) and a bunch length of $\sigma = 1$. Each plot gives a different metric for profile reconstruction success, in (a) the % accuracy of the bunch length measurement after reconstruction. In (b) and (c) the accuracy of the shape of the reconstructed profile is shown using a χ^2 test on: the best (KK) reconstruction and the reconstructed profile, and the original profile and reconstructed profile respectively. In (d) a χ^2 test monitors the variation between the original and the initial ρ functions, to demonstrate the information loss due to the addition of noise and the sampling process.

rameter A. Like in the case of σ variation, this level of noise renders all the reconstructions poor in accuracy with level of variation not acceptable for an informative diagnostic.

8.3.4 Discussion

The results of the study, looking at the number and distribution of detection channels, have demonstrated that by using prior knowledge of the expected beam parameters and noise levels, for a particular installation of the cSPr monitor, the design can be optimised. This could lead to significant savings in both the size and the cost of a monitor.

The study has shown that increasing the number of detectors will improve the quality of the reconstruction, but that the improvements are incrementally smaller with each addition. In the E203 experiment and the proposed cSPr single-shot monitor design 33 detection channels are used; this study justifies a reduction in the number of channels used. Although the exact number of channels would depend on the specifics of each installation, for a system with low noise ($\approx 1\%$) and single Gaussian-like bunches within a length in the region of $0.2 < \sigma < 5$, a monitor with 17 detection channels would be advisable and sufficient quality reconstructions could be made with fewer channels. Further reducing the number of detection channels introduces the possibility of reconstruction failure, particularly for bunches with larger values of σ.

The successful reconstruction of the Gaussian bunch over this range of lengths also gives an indication of the sensitivity of the monitor to intra-bunch features. It seems likely, that this setup would be able to resolve intra-bunch features with a length above $\sigma/5$. To resolve smaller features the frequency sampling distribution would have to be altered. The potential of this type of scheme to detect intra-bunch features should be further investigated to confirm this.

The results also cover the contribution of random noise to the reconstruction efforts. A significant noise contribution, such as a noise level of 25%, depreciates the reconstruction quality significantly even when a large number of detection channels are used. Although a low

noise scenario, such as 1% noise, causes a loss of accuracy and (in some cases) reconstruction failure, these effects are more manageable than in the high noise scenario. The priority when installing a cSPr monitor should be on the control of noise levels - using the polarization of cSPr or otherwise - in order to avoid large errors and reconstruction failure.

It is shown that reconstruction failure is likely, even when the level of noise is low, for bunches with length significantly longer than the design length (σ=1). Additionally, the quality - specifically the shape - of the reconstructed profiles deteriorated significantly for bunch lengths significantly smaller than the design length, as the sampling distribution no longer covered the frequency range of interest. In scenarios where the expected bunch variation is large, a different solution for sampling should be considered to cover a larger frequency range. For example, in a cSPr diagnostic monitor, increasing the range of grating periodicities, either by changing the gratings or by adding more gratings, would broaden the frequency range.

The number of detection channels required varies and depends on several parameters, including the range of σ and A that could reasonably be expected at a particular accelerator facility. The conditions at each facility should be carefully considered and incorporated into the design of the cSPr monitor in order to ensure high quality reconstructions.

8.4 Future Work

In experiment it can be difficult to replicate the somewhat idealised sets of parameters used throughout this chapter. Although it is possible to design a sophisticated detection channel scheme, which would sample the frequencies according to geometric or equal frequency schemes, in practise this type of design is not simple to realise. When considering the construction of a cSPr monitor it is necessary to consider additional limits. The monitor may face restricted options for detector positions or limited frequency ranges due to the availability of suitable of detectors. The study should be repeated for schemes at actual facilities, readjusting the frequency sampling to correspond with these types of experimental

limitations.

Extensions to this study were limited as in order to get sufficient statistics a large amount of computational power was required. The large number of parameters involved makes the running and analysis of this type of optimisation study significantly complex. The study described in this chapter used grid searches to scan through parameters, which although thorough, is inefficient. These factors prevented the expansion of the project to a wider variety of bunch shapes and detector configurations.

It is proposed to replace the grid search of parameters with an algorithm designed to optimise the detector configuration. This would search for detector configurations able to cope with high levels of noise, and significant variation in bunch length and shape. Determining the correct algorithm to perform this task is outside of the remit of this project, however, the interdependence of the parameters involved in the reconstruction process suggests that it may be an excellent candidate for the application of machine learning tools.

8.5 Summary

This chapter dealt with the problem of bunch profile reconstruction from radiative processes, including cSPr. Although no phase reconstruction method is ideal it was proposed to test the abilities of the KK method for a Gaussian bunch of varying asymmetry and length. It was decided to use a geometric sequence of frequencies as sampling points for the ρ values generated by Gaussian (and Gaussian-like) bunches.

An optimization framework was designed to carry out grid searches over a range of interesting parameters, testing the robustness of the reconstructions to noise, and detection channel variation. Appropriate methodology for assessing the success of the reconstructions was developed alongside this.

Although the success of the profile reconstruction, for Gaussian bunches, strongly depends on the number of detection channels, this effect is reduced as successive channels are added.

It seems possible that the number of detection channels could be significantly reduced from the 33 used in the multi-shot monitor and proposed for the single-shot design.

The noise levels had a very significant effect on the quality of the reconstructions. Although tolerable reconstruction quality is found in a low noise scenario (1%), reconstruction quality was very poor in the high noise scenario (25%). This highlights the importance of finding a suitable method to curtail the high levels of background radiation expected in many accelerator facilities.

Chapter 9

Overview and Future Work

This thesis has been concerned with the development of a conceptual design of a coherent Smith-Purcell longitudinal bunch profile monitor and an investigation into the feasibility of its basic principles. Longitudinal bunch diagnostics are important for monitoring and optimising the performance of particle accelerators, such as colliders and FELs. While conventional, destructive, longitudinal diagnostics are widely used, there is a need for continuous monitoring of the bunch profile to observe bunch-to-bunch variations and understand their relationship with the machine performance. Increasingly short bunches and interest in intra-bunch features are driving demand for higher resolution of these diagnostic tools.

A monitor based on the spectral analysis of cSPr generation is a potential candidate for the next generation of longitudinal beam diagnostics. This method is promising as it is non-destructive and has the potential to be single-shot. Previous proof-of-principle experiments have demonstrated the ability of cSPr to recover information about the longitudinal properties of electron bunches, however, all experiments to date have required measurements from multiple bunches to recover the longitudinal profile. The movement from proof-of-principle, to a conceptual design and onwards towards a functional diagnostic tool is the motivation for the work carried out in this thesis. The challenges specific to this diagnostic, including background elimination, operation in the THz frequency range and optimization of the detection channel position are discussed in this context.

9.1 The Polarization Study

The design of the single-shot, cSPr monitor requires a method for the elimination of background radiation from each detection channel. It was proposed to use the polarization of cSPr to differentiate it from background radiation. The feasibility of this proposal relies upon the demonstration that the polarization of cSPr is distinctive and can be accurately predicted by simulation. This instigated a series of experiments at the LUCX facility to investigate the polarization properties of cSPr.

A set of experiments was designed capable of measuring both the frequency and the polarization of the signal measured at the LUCX facility. As the cSPr signal generated in the THz frequency range, a region with a lack of sources for calibration and commercial optical apparatus, the design had to account for this. Additionally, the restrictions of operating in an accelerator environment were considered in the design process. An FPi, using WGPs as beamsplitters, was designed, assembled and tested at the LUCX facility. It was shown to measure the frequency of the cSPr signal accurately and with sufficient precision. Comparison between the Mi and FPi schemes showed similar results, with the Mi having a higher precision. The use of WGPs and silicon wafers as beamsplitters in the FPi scheme was compared and revealed no distinguishable differences in the frequency measurements.

An experiment was then conducted to measure the polarization of the cSPr signal over a range of detector positions using several different gratings. Analysis of the polarization results for the two sawtooth gratings showed reasonable agreement with GFW simulations for the lower range of frequencies (0.28 to 0.32 THz), but deviation at higher frequencies (0.32 to 0.39 THz). There were also discrepancies between the results from the strip grating and the the GFW simulations over the whole frequency range, which should be investigated in future projects. A near-field simulation (carried out with the MAGIC PIC code), showed overall agreement with the GFW simulations. It was, therefore, hypothesised that the disagreement between experiment and simulation was due to a feature of the experimental apparatus rather than a failing in the theoretical understanding.

The polarization study consistently measured highly polarized cSPr, oriented parallel to the grating grooves, which broadly agrees with the predictions made by the GFW simulations. The polarization of cSPr clearly distinguished it from any unpolarized background radiation. Further experimental investigation is required for a precise measurement of the DoP. This will demonstrate the feasibility of the proposed method to exclude background radiation in the single-shot, cSPr monitor and increase confidence in the predictions made by simulations. These experimental studies provide a baseline result and should be continued, either at the LUCX facility or elsewhere, in order to move the project to the next stage. All future work should use a vacuum window that either:

- Has been calibrated for birefringence effects with a THz source
- Is made of a material with no birefringent effects in the THz frequency range (for example silicon)
- Consists of several different vacuum windows, oriented so that non-normal incidence does not occur

At least one of these changes should be implemented before continuing the experimental investigation.

9.2 The Optimization Study

The proposed design for the single-shot, cSPr monitor has 33 detection channels, based on previous experiments which have demonstrated that this is sufficient to reconstruct the longitudinal bunch profile. It is suggested that optimizing the number and distribution of the detection channels could lead to a reduction in the size and the cost of the final monitor.

A code was developed to perform the optimization for Gaussian and Gaussian-like bunches, which were varied in length and asymmetry. The KK method was used for phase recovery and a geometric sequence was used to sample the frequency spectrum. The success of the

profile reconstructions was determined by the accuracy of the bunch length measurement and the similarity in profile shape to the original bunch. The study looked at the effect on the reconstruction of changing the number of detection channels and varying the noise level.

The study determined that a Gaussian bunch, close to the expected bunch length ($0.2< \sigma <5$) could be reconstructed with as few as 11 detectors. This was true even with the addition of a small noise component (1%), which had a minimal effect on the outcome. Operating in a high noise environment (25%) was shown to have a very detrimental effect on the quality of the reconstructions, this highlights the importance of finding a suitable method to eliminate background radiation.

Whilst this optimization study only considered a small set of potential longitudinal bunches, the study provides a framework to optimize the conceptual design of the single-shot, cSPr monitor (and other longitudinal bunch diagnostics using coherent radiative processes) for any accelerator facility. The results presented in this thesis have conclusively demonstrated the benefits of optimizing the design, with the potential for significant savings and a reduction in the footprint of the eventual diagnostic.

Additionally, it would be valuable to move the optimization beyond grid searching methods and explore a greater variety of parameters. The computational resources needed to perform grid scans over the selected parameter sets limited the scope of the study within this thesis. One suggestion is to develop an algorithm to further refine the frequency sampling distribution for a particular bunch shape and accelerator environment. This may provide a more efficient distribution of detection channels for the cSPr, single-shot monitor as well as informing the design of other diagnostic approaches which rely on the spectral analysis of coherent radiative processes.

Appendix A

Charge Measurements at LUCX

In Section 4.4.3 preliminary measurements of the polarization of cSPr generated at the LUCX facility were taken, using spotsize scans to compare the two orientations of the radiation. As the radiation was generated in the coherent regime, it was proposed to normalised the measured THz signal intensity by the square of the corresponding charge measurement. This normalization by the charge measurement should remove any fluctuations caused by variation in the charge of the bunch over the course of the scan. Typical fluctuations in charge are shown in Fig. 4.14. The charge is measured for every bunch using an FCT upstream of the grating, as described in Section 4.1.2. The charge normalization is carried out, for every pair of charge and THz signal intensity measurements, before the mean and standard error are calculated over the 10 bunches measured in each position.

Careful inspection of Fig. A.1(d) shows that the standard error of the measured THz signal intensity for this scan varies by a considerable amount between consecutive columns (where each column is a z-axis scan). The data in the z-axis scans with lower errors was collected before the data in the scans with higher errors. The increase in the standard error was due to an increased spread, in the charge normalized signal, over the course of the spotsize scan. Although the standard error of the measurements increases, no indication of any change in behaviour is seen for the respective mean values (Fig. A.1(c)). Separate analysis of the THz signal intensity and the charge measurements does not reveal an obvious

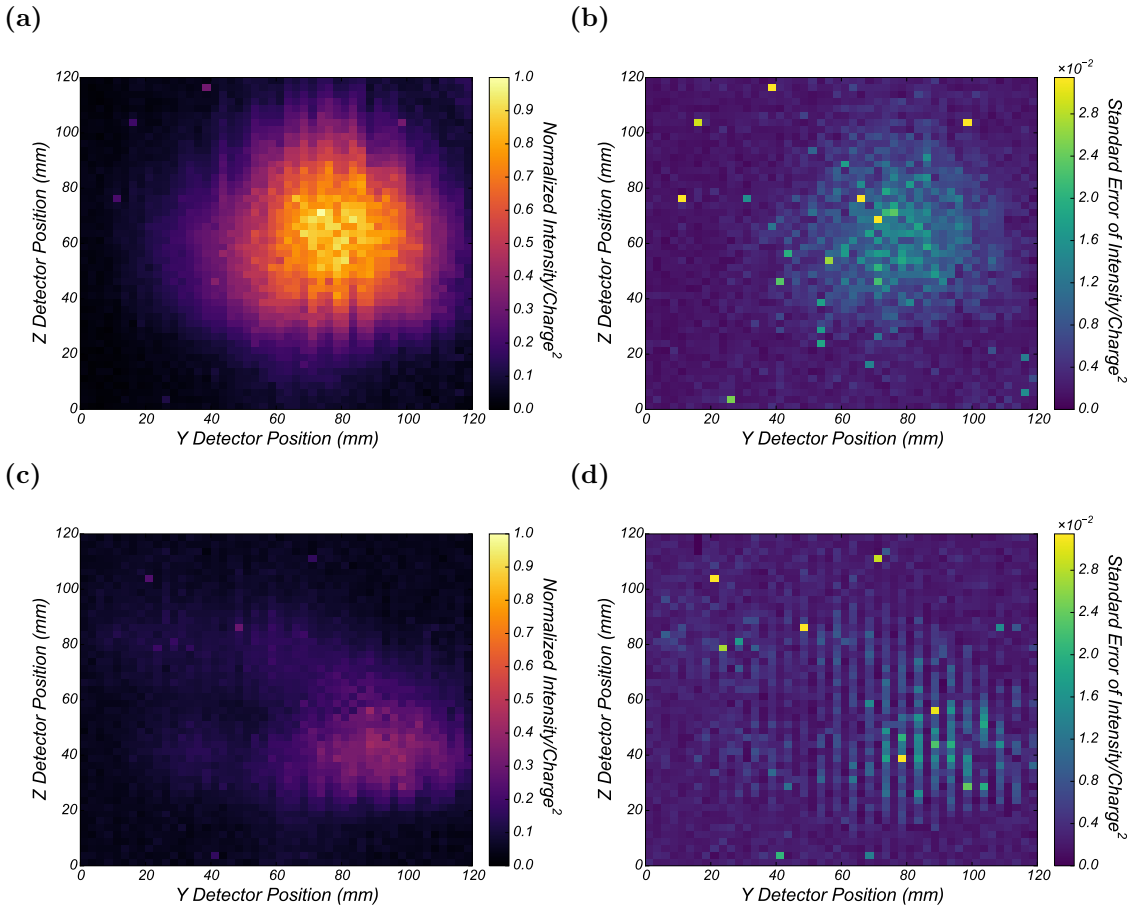

Figure A.1: The measured THz signal, normalized by the charge squared, is given for both orientations of the SBD detector, corresponding to the radiation polarized (a) parallel and (c) perpendicular to the grating grooves. The THz signal intensity is normalized so that the highest value measured over both spotsize measurements is equal to 1. The associated standard error is given in (b) and (d) respectively, these have been scaled so that they correspond to the normalized values given in (a) and (c).

cause for this observation.

The correlation between the square of the measured charge and the measured THz signal intensity was investigated to help explain the increase in standard error. The correlation coefficient, r, between two variables (x and y) for a sample of n is calculated as shown in Eq. A.1, where denotes $\mu_{x,y}$ the mean of each variable in the sample.

$$r = \frac{\sum_{i=1}^{n} (x_i - \mu_x)(y_i - \mu_y)}{\sqrt{\sum_{i=1}^{n} (x_i - \mu_x)^2} \sqrt{\sum_{i=1}^{n} (y_i - \mu_y)^2}} \tag{A.1}$$

The correlation coefficients are shown in Fig. A.2, this parameter is calculated for the set of 10 readings at every detector position and averaged for every z-axis scan. Fig. A.2(a) gives the correlation for the scans arranged according to the y position of the detector, which corresponds to the columns in Fig. A.1. Fig. A.2(b) gives the correlation chronologically to enable analysis of the relationship between the charge and the THz signal intensity over time. The results for the first spotsize scan (O1), corresponding to Fig. A.1(a), show a consistently high correlation (the correlation coefficient is close to 1) between the measured THz signal intensity and the measured charge, however, the second spotsize scan (O2), corresponding to Fig. A.1(a), shows a large variation in correlation. During the second spotsize scan the average correlation coefficient of the THz signal and the charge drops from close to 1, indicating a perfect correlation, to 0, indication no relationship between the parameters. The decrease is gradual, the average correlation slowly decreases over the course of several z-axis scans. The correlations calculated for each detector position show an increasingly large amount of variation (as the overall correlation for each z-scan decreases), with correlation coefficients ranging from -0.9 to 0.9.

The drop in correlation between the THz signal and the square of the charge during the second spotsize scan is likely due to an independent change in the accelerator environment. One possible explanation is that the beam position changed over time and more of the beam was lost due to interaction with the grating. The charge is measured in the FCT, located upstream of the THz chamber. If large amounts of the beam are lost via interaction with

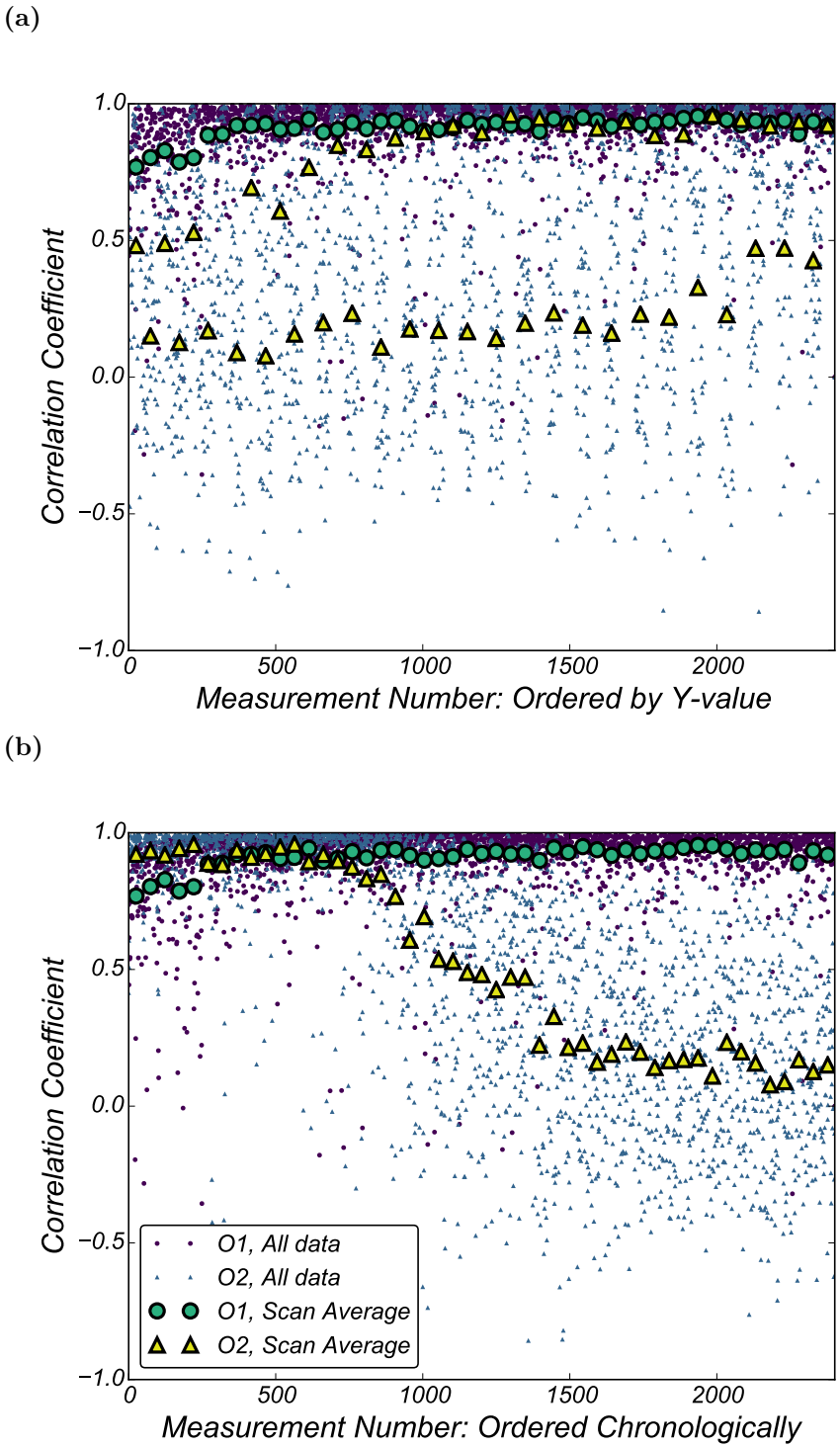

Figure A.2: Correlation coefficient of the measured THz signal intensity and the square of the charge for both spotsize scans. The correlation coefficient for both scans is presented in order of (a) position along the y-axis and (b) chronologically over the spotsize scan duration. Results are given for both of the scans - O1 corresponds to the first spotsize scan (Fig. A.1 (a)) and O2 corresponds to the second spotsize scan (Fig. A.1 (c)). For both scans the correlation coefficient is given for each detector position (all data) and as an average for each scan along the z-axis (scan average).

the grating, the measured charge will not correspond to the charge that generated the cSPr. This hypothesis is tested by analysis of the γ signal measured during the scans; gamma signal measurement is described in Section 4.1.3. If the interaction between the grating and the beams increases the γ signal should rise accordingly. The γ signal is plotted chronologically for both spotsize scans in Fig. A.3. No significant variation in the γ signal is observed over the course of the scans, in particular, no increase in γ signal is seen during the second spotsize scan. The drop in correlation between the measured THz signal intensity and the square of the charge is, therefore, unlikely to be caused by an increase in beam loss via collision with the grating.

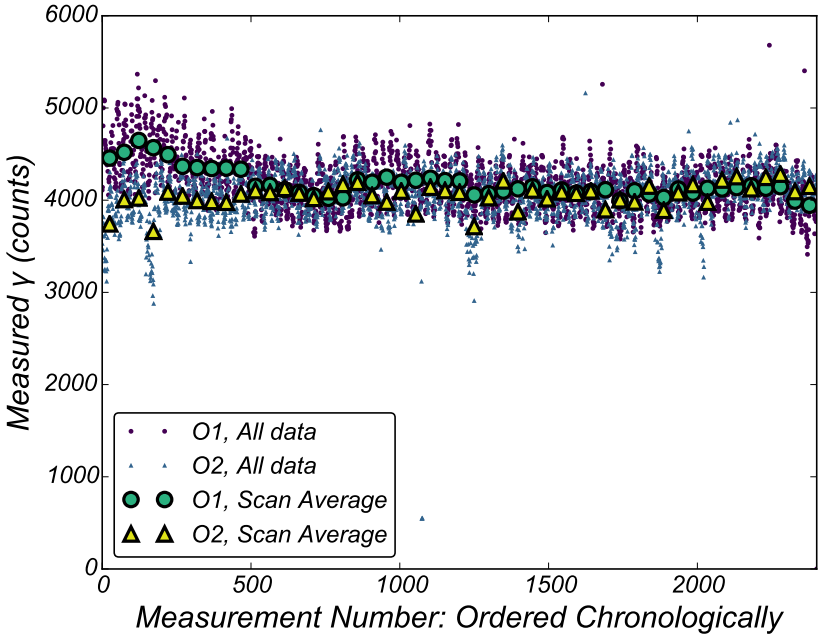

Figure A.3: The γ signal for both spotsize scans is presented in chronological order. O1 corresponds to the first spotsize scan ((Fig. A.1 (a)) and O2 corresponds the the second spotsize scan ((Fig. A.1 (c)). For both scans the average γ signal is given for each detector position is given (all data) and as an average for each scan along the z-axis (scan average).

Alternative explanations for the decrease in correlation between the measured THz signal intensity and the square of the charge should be considered. Changes to the environment, such as a rise in temperature, could affect accelerator components (for example the focussing solenoid) and change the properties of the bunch arriving at the grating. Another hypothesis is that the change in correlation is caused by a technical fault, for example, a triggering error

which led to the intensity and charge measurements for different bunches to be recorded as occurring for the same bunch. The lack of confidence in any one these explanations creates doubt over the consistency of the change measurements with respect to the THz signal intensity measurements. For this reason, the results presented in this thesis do not normalize the measured cSPr signal with respect to the charge squared.

Bibliography

[1] Amaldi, U., "The Importance of Particle Accelerators," *Europhysics News*, vol. 31, no. 6, pp. 5–9, 2000.

[2] The Institute of Physics, "Particle Physics - It Matters," *Institute of Physics Publications*, 2009. Edited by Kirby-Harris, R.

[3] P. Suortti and W. Thomlinson, "Medical Applications of Synchrotron Radiation," *Physics in Medicine and Biology*, vol. 48, no. 13, 2003.

[4] A. Marcelli, A. Cricenti, W. M. Kwiatek, and C. Petibois, "Biological Applications of Synchrotron Radiation Infrared Spectromicroscopy," *Biotechnology Advances*, vol. 30, no. 6, pp. 1390 – 1404, 2012.

[5] R. Blaustein, "Biology and Light Sources," *BioScience*, vol. 67, no. 3, pp. 201–207, 2017.

[6] L. Bertrand, *Chapter 2: Synchrotron Imaging for Archaeology, Art History, Conservation, and Palaeontology*, vol. 2 of *Physical Techniques in the Study of Art, Archaeology and Cultural Heritage*, pp. 97 – 114. Elsevier, 2007.

[7] K. Yokoya and P. Chen, "Beam-beam Phenomena in Linear Colliders," 1990.

[8] R. B. Palmer, "The Interdependence of Parameters for TeV Linear Colliders," *Conf. Proc.*, vol. C8706292, p. 80, 1987.

[9] N. Phinney, N. Toge, and N. Walker, "International Linear Collider Reference Design Report: ILC Global Design Effort and World Wide Study," vol. 3, 2007.

[10] A. Finn, P. Karataev, and G. Rehm, "Design, Development and Use of the Spectrometer for Investigating Coherent THz Radiation Produced by Micro-Bunching Instabilities at Diamond Light Source," *Journal of Physics: Conference Series*, vol. 732, no. 1, p. 012039, 2016.

[11] W. Shields *et al.*, "Microbunch Instability Observations from a THz Detector at Diamond Light Source," *J. Phys. Conf. Ser.*, vol. 357, no. 012037, 2012.

[12] R. Neutze, R. Wouts, D. van der Spoel, E. Weckert, and J. Hajdu, "Potential for Biomolecular Imaging with Femtosecond X-Ray Pulses," *Nature*, vol. 406, 2000.

[13] C. Behrens *et al.*, "Constraints on Photon Pulse Duration from Longitudinal Electron Beam Diagnostics at a Soft X-Ray Free-Electron Laser," *Phys. Rev. ST Accel. Beams*, vol. 15, p. 030707, Mar 2012.

[14] A. Aschikhin *et al.*, "The FLASHForward facility at DESY," *Nucl. Instrum. Methods Phys. Res. A*, vol. 806, pp. 175 – 183, 2016.

[15] A. Caldwell *et al.*, "Path to AWAKE: Evolution of the Concept," *Nucl. Instrum. Methods Phys. Res. A*, vol. 829, pp. 3 – 16, 2016. 2nd European Advanced Accelerator Concepts Workshop - EAAC 2015.

[16] "Beam Studies and Experimental Facility for the AWAKE Experiment at CERN," *Nucl. Instrum. Methods Phys. Res. A*, vol. 740, pp. 48 – 53, 2014.

[17] M. Litos *et al.*, "High-Efficiency Acceleration of an Electron Beam in a Plasma Wakefield Accelerator," vol. 515, pp. 92–59.

[18] G. Burt, "Transver Deflecting Cavities," *Contribution to the CAS - CERN Accelerator School: Specialised Course on RF for Accelerators*, 2012.

[19] R. Akre, L. Bentson, P. Emma, and P. Krejcik, "A Transverse RF Deflecting Structure for Bunch Length and Phase Space Diagnostics," vol. 3, pp. 2353–2355, 2001.

[20] S. Jamison *et al.*, " Femtosecond Bunch Length Measurements (TUYPA01)"," in *Proceedings of the 10th European Particle Accelerator Conference (EPAC'06)*, 2006.

[21] G. Berden *et al.*, "Electro-Optic Technique with Improved Time Resolution for Real-Time, Nondestructive, Single-Shot Measurements of Femtosecond Electron Bunch Profiles," *Phys.Rev. Lett.*, vol. 93.

[22] R. Pan, S. Jamison, T. Lefevre, and W. Gillespie, "Coulomb Field Strength Measurement by Electro-Optic Spectral Decoding System at the CALIFES Beam Line," *Nucl. Instrum. Methods Phys. Res. A*, vol. 821, pp. 8 – 12, 2016.

[23] A. Debus *et al.*, "Electron Bunch Length Measurements from Laser-Accelerated Electrons Using Single-Shot THz Time-Domain Interferometry," *Phys.Rev. Lett.*, vol. 104, no. 8, p. 084802, 2010.

[24] A. P. Potylitsyn, M. I. Ryanzanov, M. N. Strikhanov, and A. A. Tishchenko, *Diffraction Radiation from Relativistic Particles*, vol. 239. Berlin Heidelberg: Springer, 2010.

[25] M. Micheler *et al.*, "Longitudinal Beam Profile Monitor at CTF3 Based on Coherent Diffraction Radiation," *Journal of Physics: Conference Series*, vol. 236, no. 1, p. 012021, 2010.

[26] M. Shevelev *et al.*, "Sub-millimeter Bunch Length Non-invasive Diagnostic Based on the Diffraction and Cherenkov Radiation," *Journal of Physics: Conference Series*, vol. 357, no. 1, p. 012023, 2012.

[27] Y. Shibata *et al.*, "Diagnostics of an Electron Beam of a Linear Accelerator using Coherent Transition Radiation," *Phys. Rev. E*, vol. 50, pp. 1479–1484, Aug 1994.

[28] B. Schmidt *et al.*, "Longitudinal Bunch Diagnostics using Coherent Transition Radiation Spectroscopy," 2018.

[29] D. Mihalcea, C. L. Bohn, U. Happek, and P. Piot, "Longitudinal Electron Bunch Diagnostics Using Coherent Transition Radiation," *Phys. Rev. Spec. Top. - Accel. Beams*, vol. 9, p. 082801, 2006.

[30] J. Brownell, J. Walsh, and G. Doucas, "Spontaneous Smith-Purcell Radiation Described through Induced Surface Currents," *Phys. Rev. E*, vol. 57, no. 1, pp. 1075–1080, 1998.

[31] V. Blackmore *et al.*, "First Measurements of the Longitudinal Bunch Profile of a 28.5 GeV Beam using Coherent Smith-Purcell Radiation," *Phys. Rev. Spec. Top. - Accel. Beams*, vol. 12, pp. 1–12, 2009.

[32] H. L. Andrews *et al.*, "Reconstruction of the Time Profile of 20.35 GeV, Subpicosecond Long Electron Bunches by Means of Coherent Smith-Purcell Radiation," *Phys. Rev. Spec. Top. - Accel. Beams*, vol. 17, pp. 1–13, 2014.

[33] I. M. Frank, "Doppler Effect in a Refractive Medium," *Izv. Akad. Nauk USSR. Fizika.*, vol. 6, p. 3, 1942.

[34] I. M. Frank, "Einstein and Optics (From the History of Physics)," *Sov. Phys. Usp.*, vol. 22, p. 975, 1979.

[35] H. Motz, "Applications of the Radiation from Fast Electron Beams," *J. Appl. Phys.*, vol. 22, no. 1951, pp. 527–535, 1951.

[36] S. J. Smith and E. M. Purcell, "Visible Light from Localized Surface Charges Moving Across a Grating," *Phys. Rev.*, vol. 92, no. 1, p. 1069, 1953.

[37] P. M. V. den Berg, "Smith-Purcell Radiation from a Point Charge Moving Parallel to a Reflection Grating," *J. Opt. Soc. Am.*, vol. 63, no. 12, pp. 1588–1597, 1973.

[38] K. Ishiguro and T. Tako, "An Estimation of Smith-Purcell Effect as the Light Source in the Infra-Red Region," *Opt. Acta Int. J. Opt.*, vol. 8, no. January, pp. 25–31, 1961.

[39] G. Toraldo di Francia, "On the Theory of some Cerenkovian Effects," *Nuovo Cim.*, vol. 16, no. 052, pp. 61–77, 1960.

[40] P. M. van den Berg, "Smith-Purcell Radiation from a Point Charge Moving Parallel to a Reflection Grating," *J. Opt. Soc. Am.*, vol. 63, no. 12, p. 1588, 1973.

[41] P. M. van den Berg and T. H. Tan, "Smith-Purcell Radiation from a Line Charge Moving Parallel to a Reflection Grating with Rectangular Profile," *J. Opt. Soc. Am.*, vol. 64, no. 12, p. 325, 1974.

[42] G. Doucas, J. H. Mulvey, M. Omori, J. Walsh and M. F. Kimmitt, "First Observation of Smith-Purcell Radiation from Relativistic Electrons," *Phys. Rev. E*, vol. 69, no. 12, pp. 1761–1764, 1992.

[43] I. Amato, "An Everyman's Free-Electron Laser?," *Science*, vol. 258, no. 5081, pp. 401–401, 1992.

[44] G. Dattoli and A. Renieri, "Cheap Free-Electron Lasers on the Horizon," *Physics World*, vol. 6, no. 1, p. 25, 1993.

[45] O. Haeberlé, P. Rullhusen, J. M. Salomé, and N. Maene, "Calculations of Smith-Purcell Radiation Generated by Electrons of 1-100 MeV," *Phys. Rev. E*, vol. 49, no. 4, pp. 3340–3352, 1994.

[46] A. S. Kesar, S. Korbly, R. J. Temkin, and M. Hess, "Smith-Purcell Radiation from a Charge Moving Above a Finite-Length Grating," *Proc. IEEE Part. Accel. Conf.*, pp. 1496–1498, 2005.

[47] A. S. Kesar, "Smith-Purcell Radiation from a Charge Moving Above a Finite-Length Grating," *Phys. Rev. Spec. Top. - Accel. Beams*, vol. 8, no. 072801, pp. 1496–1498, 2005.

[48] S. E. Korbly, *Smith-Purcell Radiation from Femtosecond Electron Bunches*. PhD thesis, Princeton University, 2005.

[49] A. S. Kesar, M. Hess, S. E. Korbly, and R. J. Temkin, "Time- and Frequency-Domain Models for Smith-Purcell Radiation from a Two-Dimensional Charge Moving Above a Finite Length Grating," *Phys. Rev. E*, vol. 71, no. 1, p. 16501, 2005.

[50] A. S. Kesar, R. A. Marsh, and R. J. Temkin, "Power Measurement of Frequency-Locked Smith-Purcell Radiation," *Phys. Rev. Spec. Top. Accel. Beams*, vol. 9, pp. 1–6, 2006.

[51] A. S. Kesar, "Smith-Purcell Radiation from a Charge Moving above a Grating of Finite Length and Width," *Phys. Rev. Spec. Top. - Accel. Beams*, vol. 13, pp. 1–8, 2010.

[52] J. H. Brownell, J. Walsh, H. G. Kirk, R. C. Fernow, and S. H. Robertson, "Smith-Purcell Radiation from a 50 MeV Beam," *Nucl. Instruments Methods Phys. Res. Sect. A Accel. Spectrometers, Detect. Assoc. Equip.*, vol. 393, no. 97, pp. 323–325, 1997.

[53] J. D. Jackson, *Classical electrodynamics*. New York, NY: Wiley, 3rd ed., 1999.

[54] J. S. Nodvick and D. S. Saxon, "Suppression of Coherent Radiation by Electrons in a Synchrotron," *Phys. Rev.*, vol. 96, no. 1, pp. 180–184, 1954.

[55] Y. Shibata *et al.*, "Coherent Smith-Purcell Radiation in the Millimeter-Wave Region from a Short-Bunch Beam of Relativistic Electrons," *Phys. Rev. E*, vol. 57, no. 1, pp. 1061–1074, 1998.

[56] O. Grimm and P. Schm, "Principles of Longitudinal Beam Diagnostics with Coherent Radiation," *TESLA Rep.*, no. 6, pp. 1–20, 2006.

[57] S. R. Trotz, J. H. Brownell, J. E. Walsh, and G. Doucas, "Optimization of Smith-Purcell Radiation at Very High Energies," *Phys. Rev. E*, vol. 61, pp. 7057–7064, June 2000.

[58] G. Doucas, M. F. Kimmitt, *et al.*, "Determination of Longitudinal Bunch Shape by Means of Coherent Smith-Purcell Radiation," *Phys. Rev. Spec. Top. - Accel. Beams*, vol. 5, pp. 14–21, 2002.

[59] J. H. Brownell and G. Doucas, "Role of the Grating Profile in Smith-Purcell Radiation at High Energies," *Phys. Rev. Spec. Top. - Accel. Beams*, vol. 8, pp. 1–11, 2005.

[60] G. Doucas *et al.*, "Longitudinal Electron Bunch Profile Diagnostics at 45 MeV using Coherent Smith-Purcell radiation," *Phys. Rev. ST Accel. Beams*, vol. 9, p. 092801, Sep 2006.

[61] V. Blackmore, *Determination of the Time Profile of Picosecond-Long Electron Bunches through the use of Coherent Smith-Purcell Radiation through the use of Coherent Smith-Purcell Radiation.* PhD thesis, St Cross College, Oxford, 2008.

[62] G. Doucas. personal communication.

[63] The Numerical Algorithms Group (NAG), "The NAG C Library." `www.nag.com`.

[64] C. Kittel, *Introduction to Solid State Physics.* Wiley, 8th ed. ed., 2004.

[65] S. S. Dhillon *et al.*, "The 2017 Terahertz Science and Technology Roadmap," *J. Phys. D. Appl. Phys.*, vol. 50, p. 043001 (49 pp), 2017.

[66] G. P. Williams, "Filling the THz Gap - High Power Sources and Applications," *Reports Prog. Phys.*, vol. 69, pp. 301–326, 2006.

[67] J. Dai, J. Zhang, W. Zhang, and D. Grischkowsky, "Terahertz Time-Domain Spectroscopy Characterization of the Far-Infrared Absorption and Index of Refraction of High-Resistivity, Float-Zone Silicon," *J. Opt. Soc. Am. B*, vol. 21, pp. 1379–1386, Jul 2004.

[68] R. Ulrich, "Far-Infrared Properties of Metallic Mesh and Structure," *Infrared Phys.*, vol. 7, pp. 37–55, 1967.

[69] C. Winnewisser, F. Lewen, and H. Helm, "Transmission Characteristics of Dichroic Filters Measured by THz Time-Domain Spectroscopy," *Appl. Phys. A Mater. Sci. Process.*, vol. 66, pp. 593–598, 1998.

[70] C. Winnewisser, F. Lewen, J. Weinzierl, and H. Helm, "Transmission Features of Frequency-Selective Components in the Far Infrared Determined by Terahertz Time-Domain Spectroscopy," *Appl. Opt.*, vol. 38, no. 18, pp. 3961–3967, 1999.

[71] C. Winnewisser, F. T. Lewen, M. Schall, M. Walther, and H. Helm, "Characterization and Application of Dichroic Filters in the 0 .1 3 THz Region," vol. 48, no. 4, pp. 744–749, 2000.

[72] S. I. Bajlekov *et al.*, "Longitudinal Electron Bunch Profile Reconstruction by Performing Phase Retrieval on Coherent Transition Radiation Spectra," *Phys. Rev. Spec. Top. - Accel. Beams*, vol. 16, pp. 1–14, 2013.

[73] F. Bakkali Taheri *et al.*, "Electron Bunch Profile Reconstruction Based on Phase-Constrained Iterative Algorithm," *Phys. Rev. Accel. Beams*, vol. 19, p. 032801, 2016.

[74] A. Aryshev *et al.*, "Development of Advanced THz Generation Schemes at KEK LUCX Facility," in *Proc. 10th Annu. Meet. Part. Accel. Soc. Japan (August 3-5, 2013, Nagoya, Japan)*, pp. 873–876, 2013.

[75] M. Fukuda *et al.*, "Upgrade of the Accelerator for the Laser Undulator Compact X-Ray Source (LUCX)," *Nucl. Instruments Methods Phys. Res. Sect. A Accel. Spectrometers, Detect. Assoc. Equip.*, vol. 637, no. 1, pp. S67–S71, 2011.

[76] M. Shevelev *et al.*, "Coherent Radiation Spectrum Measurements at KEK LUCX Facility," *Nucl. Instruments Methods Phys. Res. Sect. A Accel. Spectrometers, Detect. Assoc. Equip.*, vol. 771, pp. 126–133, 2015.

[77] G. Naumenko *et al.*, "Monochromatic Coherent Grating Transition Radiation in Sub-THz Frequency Range," *Nucl. Instruments Methods Phys. Res. Sect. B Beam Interact. with Mater. Atoms*, vol. 402, pp. 153–156, 2017.

[78] K. Lekomtsev *et al.*, "Sub-THz Radiation from Dielectric Capillaries with Reflectors," *Nucl. Instruments Methods Phys. Res. Sect. B*, vol. 402, pp. 148–152, 2017.

[79] A. Aryshev, A. Potylitsyn, *et al.*, "Monochromaticity of Coherent Smith-Purcell Radiation from Finite Size Grating," *Phys. Rev. Accel. Beams*, vol. 20, pp. 1–8, 2017.

[80] H. Zhang *et al.*, "Non-Destructive Measurement and Monitoring of Separation of Charged Particle Micro-Bunches.," *Appl. Phys. Lett.*, vol. 111, no. 4, 2017.

[81] A. Deshpande *et al.*, "Experimental Results of an RF Gun and the Generation of a Multibunch Beam," *Phys. Rev. ST Accel. Beams*, vol. 14, p. 063501, Jun 2011.

[82] R. C. Webber, "Charged particle beam current monitoring tutorial," *AIP Conference Proceedings*, vol. 333, no. 1, pp. 3–23, 1995.

[83] M. Tabata, I. Adachi, M. Kawai, H.and Kubo, and T. Sato, "Recent Progress in Silica Aerogel Cherenkov Radiator," *Proc. TIPP 2011*, vol. 37, pp. 642–649, 2011.

[84] S. T. Boogert *et al.*, "Micron-Scale Laser-Wire Scanner for the KEK Accelerator Test Facility Extraction Line," *Phys. Rev. Spec. Top. - Accel. Beams*, vol. 13, pp. 1–16, 2010.

[85] B. Walasek-Höhne *et al.*, "Scintillating Screen Applications in Accelerator Beam Diagnostics," *IEEE Trans. Nucl. Sci.*, vol. 59, no. 5, pp. 2307–2312, 2012.

[86] M. Naftaly, *Terahertz Optics*. Boston: Artech House, 2015.

[87] Virginia Diodes, "Zero Bias Detectors - VDI Model: WR2.2ZBD." `http://vadiodes.com/index.php/en/products/detectors?id=122/`, 2016. [Online; accessed 21-April-2016].

[88] Virginia Diodes, "Virginia Diodes Inc. Waveguide Band Designations." `http://vadiodes.com/VDI/pdf/waveguidechart200908.pdf`, 2016. [Online; last modified [29-June-2010].

[89] A. A. Michelson, "Visibility of Interference-Fringes in the Focus of a Telescope," *The London, Edinburgh, and Dublin Philosophical Magazine and Journal of Science*, vol. 31, no. 190, pp. 256–259, 1891.

[90] A. A. Michelson and E. W. Morley, "On the Relative Motion of the Earth and the Luminiferous Ether," *American Journal of Science*, vol. s3-34, pp. 333–345, November 1887.

[91] W. H. Steel, *Multiple-beam Interferometers*, ch. 9.3: The Fabry-Pérot Interferometer. Cambridge, United Kingdom: Cambridge University Press, 2nd ed., 1983.

[92] C. Fabry and A. Pérot, "Sur les Franges des Lames Minces Argentes et Leur Application a la Mesure de Petites Épaisseurs dAir," *Ann. Chim. Phys.*, vol. 12, p. 459, 1897.

[93] C. Fabry and A. Pérot, "Thorie et Applications dune Nouvelle Mthode de Spectroscopie Interfrentielle," *Ann. Chim. Phys.*, vol. 16, p. 115, 1899.

[94] E. Baker and B. Walker, "Fabry-Perot Interferometers for Use at Submillimetre Wavelengths," *J. Phys. E*, vol. 15, pp. 25–32, 1982.

[95] D. Jahn *et al.*, "Fabry-Perot Cavity for Sensing Polar Liquids at Terahertz Frequencies," *Int. Conf. Infrared, Millimeter, Terahertz Waves, IRMMW-THz*, pp. 1–6, 2017.

[96] A. Doria *et al.*, "Can Coherent Smith-Purcell Radiation be Used to Determine the Shape of an Electron Bunch ?," *Nucl. Instr. Meth. Phys. Res. A*, vol. 483, pp. 263–267, 2002.

[97] R. Braakman and G. A. Blake, "Principles and promise of Fabry-Perot Resonators at Terahertz Frequencies," *J. Appl. Phys.*, vol. 109, 2011.

[98] T. Hori, T. Matsui, K. Araki, and H. Inomata, "Variable-Finesse Wideband Fabry-Perot Wavemeter for Far-Infrared and Millimeter Waves," *Opt. Lett.*, vol. 14, no. 6, pp. 302–4, 1989.

[99] R. Ulrich, K. F. Renk, and L. Genzel, "Tunable Submillimeter Interferometers of the Fabry-Perot Type," *IEEE Transactions on Microwave Theory and Techniques*, vol. 11, pp. 363–371, Sep 1963.

[100] A. Ferraro *et al.*, "Flexible Terahertz Wire Grid Polarizer with High Extinction Ratio and Low Loss," *Opt. Lett.*, vol. 41, no. 9, pp. 2009–2012, 2016.

[101] A. Isozaki, T. Kan, K. Takano, M. Hangyo, and K. Matsumoto, "Double-Layer Wire Grid Polarizer for Improving Extinction Ratio," no. June, pp. 530–533, 2013.

[102] E. Hecht, *Optics*. San Francisco, USA: Addison Wesley, 4th ed., 2002.

[103] G. R. Bird and M. Parrish, Jr., "The Wire Grid as a Near-Infrared Polarizer," *J. Opt. Soc. Am.*, vol. 50, no. 1954, p. 886, 1960.

[104] P. Yen, "A New Optical Model for Wire Grid Polarizers," *Opt. Commun.*, vol. 26, no. 3, pp. 289–292, 1978.

[105] W. Liu *et al.*, "Terahertz Frequency Measurement of Far-Infrared Laser with an Improvement of Martin-Puplett Interferometer," *Nucl. Instruments Methods Phys. Res. Sect. A Accel. Spectrometers, Detect. Assoc. Equip.*, vol. 614, no. 2, pp. 313–318, 2010.

[106] M. Xu, H. Urbach, D. de Boer, and H. Cornelissen, "Wire-Grid Diffraction Gratings Used as Polarizing Beam Splitter for Visible Light and Applied in Liquid Crystal on Silicon," *Opt. Express*, vol. 13, pp. 2303–2320, Apr 2005.

[107] V. Y. Balakhanov, V. K. Zhibotov, and A. V. Titov, "Coupled Fabry-Perot Microwave Interferometers," *Journal of Applied Spectroscopy*, vol. 11, pp. 831–833, Jul 1969.

[108] C. W. Berry and M. Jarrahi, "Broadband Terahertz Polarizing Beam Splitter on a Polymer Substrate," *J. Infrared, Millimeter, Terahertz Waves*, vol. 33, pp. 127–130, 2012.

[109] Purewave Polarizers, "10 Micron Wire Grid Polarizer: PW010-030-075." `http://www.purewavepolarizers.com/wire-grid-polarizers`, 2017. [Online; accessed 14-August-2017].

[110] H. Lamb, "On the diffraction in transmission of electric waves by a metallic grating," *Proc. London Math. Soc.*, vol. 29, pp. 523–544, 1898.

[111] T. Larsen, "A Survey of the Theory of Wire Grids," *IRE Trans. Microw. Theory Tech.*, vol. 10, pp. 191–201, 1962.

[112] T. Jeon and D. Grischkowsky, "Nature of Conduction in Doped Silicon," *Phys. Rev. Lett.*, vol. 78, pp. 1106–1109, 1997.

[113] T. Jeon and D. Grischkowsky, "Observation of a Cole-Davidson Type Complex Conductivity in the Limit of Very Low Carrier Densities in Doped Silicon," *Appl. Phys. Lett.*, vol. 72, pp. 2259–2261, 1998.

[114] G. W. F. Drake, *Infrared Spectroscopy*, ch. 40.4.3: The Operation of Spectrum Determination. New York City: Springer, 2006.

[115] G. Kube *et al.*, "Observation of Optical Smith-Purcell Radiation at an Electron Beam Energy of 855 MeV," *Phys. Rev. E - Stat. Physics, Plasmas, Fluids, Relat. Interdiscip. Top.*, vol. 65, p. 15, 2002.

[116] Northrop Grumman, "MAGIC Tool Suite." `http://www.northropgrumman.com/Capabilities/PICCodeSoftware/MAGIC/Pages/default.aspx`, 2018. [Online; accessed 17-July-2018].

[117] B. Goplen, L. Ludeking, D. Smith, and G. Warren, "User-Configurable MAGIC for Electromagnetic PIC Calculations," *Computer Physics Communications*, vol. 87, no. 1, pp. 54 – 86, 1995.

[118] A. J. Woods and L. D. Ludeking, "MAGIC3D Electromagnetic FDTD-PIC Code Dense Plasma Model Benchmark," in *2009 IEEE Pulsed Power Conference*, pp. 533–536, June 2009.

[119] A. Lipson, S. G. Lipson, and H. Lipson, *Optical Physics*. New York, USA: Cambridge Univeristy Press, 4th ed., 2011.

[120] R. Lai and A. J. Sievers, "Determination of a Charged-Particle-Bunch Shape from the Coherent Far Infrared Spectrum," *Phys. Rev. E*, vol. 50, no. 5, pp. 3342–3344, 1994.

[121] R. W. Harrison, "Phase Problem in Crystallography," *J. Opt. Soc. Am. A*, vol. 10, no. 5, p. 1046, 1993.

[122] A. Walther, "The Question of Phase Retrieval in Optics," *Opt. Acta Int. J. Opt.*, vol. 10, no. 1963, pp. 41–49, 1963.

[123] R. Lai and A. J. Sievers, "On using the Coherent Far IR Radiation Produced by a Charged-Particle Bunch to Determine its Shape: I Analysis," *Nucl. Instruments Methods Phys. Res. Sect. A Accel. Spectrometers, Detect. Assoc. Equip.*, vol. 397, pp. 221–231, 1997.

[124] R. Lai and A. J. Sievers, "Phase Problem Associated with the Determination of the Longitudinal Shape of a Charged Particle Bunch from its Coherent Far-IR Spectrum," *Phys. Rev. E*, vol. 52, pp. 4576–4579, Oct 1995.

[125] S. P. Wooten, F. and Davis, "Optical Properties of Solids," *Am. J. Phys.*, vol. 41, pp. 939–941, 1973.

[126] D. Pelliccia and T. Sen, "A Two-Step Method for Retrieving the Longitudinal Profile of an Electron Bunch from its Coherent Radiation," *Nucl. Instruments Methods Phys. Res. Sect. A Accel. Spectrometers, Detect. Assoc. Equip.*, vol. 764, no. 2, pp. 206–214, 2014.

[127] R. W. Gerchberg and W. O. Saxton, "A Practical Algorithm for the Determination of Phase from Image and Diffraction Plane Pictures," *Optik*, vol. 35, 1972.

[128] J. R. Fienup, "Phase Retrieval Algorithms: a Personal Tour ," *Appl. Opt.*, vol. 52, no. 1, p. 45, 2012.

[129] S. Marchesini *et al.*, "X-ray Image Reconstruction from a Diffraction Pattern Alone," *Phys. Rev. B*, vol. 68, p. 140101, Oct 2003.

[130] K. F. Riley, M. P. Hobson, and S. J. Bence, *Mathematical Methods for Physics and Engineering*. Cambridge, UK: Cambridge University Press, 3rd ed., 2006.